



5-2018

Performance Improvement of Wide-Area-Monitoring-System (WAMS) and Applications Development

Jiecheng Zhao
University of Tennessee

Recommended Citation

Zhao, Jiecheng, "Performance Improvement of Wide-Area-Monitoring-System (WAMS) and Applications Development. " PhD diss., University of Tennessee, 2018.
https://trace.tennessee.edu/utk_graddiss/4921

This Dissertation is brought to you for free and open access by the Graduate School at Trace: Tennessee Research and Creative Exchange. It has been accepted for inclusion in Doctoral Dissertations by an authorized administrator of Trace: Tennessee Research and Creative Exchange. For more information, please contact trace@utk.edu.

To the Graduate Council:

I am submitting herewith a dissertation written by Jiecheng Zhao entitled "Performance Improvement of Wide-Area-Monitoring-System (WAMS) and Applications Development." I have examined the final electronic copy of this dissertation for form and content and recommend that it be accepted in partial fulfillment of the requirements for the degree of Doctor of Philosophy, with a major in Electrical Engineering.

Yilu Liu, Major Professor

We have read this dissertation and recommend its acceptance:

Lee D. Han, Fangxing Li, Hairong Qi

Accepted for the Council:

Dixie L. Thompson

Vice Provost and Dean of the Graduate School

(Original signatures are on file with official student records.)

Performance Improvement of Wide-Area-Monitoring-System (WAMS) and Applications Development

A Dissertation Presented for the
Doctor of Philosophy
Degree
The University of Tennessee, Knoxville

Jiecheng Zhao

May 2018

Copyright © 2018 by Jiecheng Zhao
All rights reserved.

ACKNOWLEDGEMENTS

First and foremost, I would like to express my deepest appreciation to my advisor, Dr. Yilu Liu, for her patient guidance, insightful suggestions, and continuous encouragement throughout this study and my career. I would also like to thank Dr. Fangxing “Fran” Li, Dr. Hairong Qi, and Dr. Lee D. Han for serving on my committee. I appreciate their interest, precious time and insightful comments.

I would like to thank Jose Gracia, Paul Ewing, Allen Goldstein, Dr. Lingwei Zhan, Dr. Jin Tan, Dr. Wenxuan Yao, Dr. Shutang You, Dr. Ling Wu, Dr. He Yin, Yinfeng Zhao, and Dr. Yong Liu for their collaboration, discussion and suggestions. This work would not be possible without their help. I am greatly appreciative to the help and friendship from my colleagues in the Power Information Technology Labs. I would also like to thanks staff members in EECS department for their generous help in many ways.

Last but not least, with my deepest love and appreciation, I would like to thank my father, Buhui Zhao, and my mother, Jianping Ji for their consistent love and support. Special thanks to my fiancée Dr. Ziwen Ling for her endless love, encouragement, and insightful discussions and suggestions.

ABSTRACT

Wide area monitoring system (WAMS), as an application of situation awareness, provides essential information for power system monitoring, planning, operation, and control. To fully utilize WAMS in smart grid, it is important to investigate and improve its performance, and develop advanced applications based on the data from WAMS. In this dissertation, the work on improving the WAMS performance and developing advanced applications are introduced.

To improve the performance of WAMS, the work includes investigation of the impacts of measurement error and the requirements of system based on WAMS, and the solutions. PMU is one of the main sensors for WAMS. The phasor and frequency estimation algorithms implemented highly influence the performance of PMUs, and therefore the WAMS. The algorithms of PMUs are reviewed in Chapter 2. To understand how the errors impact WAMS application, different applications are investigated in Chapter 3, and their requirements of accuracy are given. In chapter 4, the error model of PMUs are developed, regarding different parameters of input signals and PMU operation conditions. The factors influence of accuracy of PMUs are analyzed in Chapter 5, including both internal and external error sources. Specifically, the impacts of increase renewables are analyzed. Based on the analysis above, a novel PMU is developed in Chapter 6, including algorithm and realization. This PMU is able to provide high accurate and fast responding measurements during both steady and dynamic state. It is potential to improve the performance of WAMS. To improve the interoperability, the C37.118.2 based data communication protocol is curtailed and realized for single-phase distribution-level PMUs, which are presented in Chapter 7.

WAMS-based applications are developed and introduced in Chapter 8-10. The first application is to use the spatial and temporal characterization of power system frequency for data authentication, location estimation and the detection of cyber-attack. The second application is to detect the GPS attack on the synchronized time interval. The third application is to detect the geomagnetically induced currents (GIC) resulted from GMD and EMP-E3. These applications, benefited from the novel PMU proposed in Chapter 6, can be used to enhance the security and robust of power system.

TABLE OF CONTENTS

Chapter 1	Introduction.....	1
1.1	Overview.....	1
1.1.1	Wide Area Monitoring System	2
1.1.2	FNET/GridEye: A WAMS Case.....	3
1.2	Dissertation Outline	5
Chapter 2	Literature Review: Phasor and Frequency Estimation Methods.....	8
2.1	Introduction.....	8
2.2	Phasor and Frequency Estimation Methods.....	10
2.2.1	Zero-crossing Detection.....	11
2.2.2	Discrete Fourier Transform.....	12
2.2.3	Demodulation Method	15
2.2.4	Newton Type Method	16
2.2.5	Least Square Method	18
2.2.6	Phase-Locked Loop	19
2.2.7	Kalman Filter Method.....	21
2.2.8	Other Methods	22
2.3	Techniques	22
2.3.1	Three-Phase and Single-Phase.....	23
2.3.2	Filter.....	23
2.3.3	Deal with DC Offset and Harmonics	24
2.3.4	Dynamic Signal Model	24

2.3.5	Hybrid	25
2.3.6	Other Techniques	26
2.4	Performance Comparison.....	26
2.4.1	Accuracy	26
2.4.2	Estimation Speed	28
2.4.3	Computation Complexity.....	30
2.5	Proposed Area for Future Research	31
2.6	Conclusion	32
Chapter 3	PMU Error Impact	33
3.1	Introduction.....	33
3.2	Methodology	34
3.3	PMU Error Analysis	35
3.3.1	PMU Measurement Error.....	35
3.3.2	Transducer Error	36
3.3.3	Error Assumption.....	37
3.4	Event Location	37
3.4.1	Event Location Algorithm	37
3.4.2	Analysis and Result.....	38
3.5	Oscillation Detection	40
3.5.1	Oscillation Detection Algorithm.....	40
3.5.2	Analysis and Result.....	40
3.6	Dynamic Line Rating.....	42
3.6.1	Dynamic Line Rating Algorithm	42
3.6.2	Analysis and Result.....	43

3.7	Islanding Detection	45
3.7.1	Islanding Detection Algorithm	45
3.7.2	Analysis and Result.....	46
3.8	Conclusion	47
Chapter 4	PMU Error Model	48
4.1	Introduction.....	48
4.2	Methodology	49
4.3	Data	50
4.4	Result: Steady State Error Model	51
4.4.1	Frequency Deviation	51
4.4.2	Magnitude Deviation	54
4.4.3	Harmonics Distortion.....	55
4.4.4	Interharmonics Distortion	55
4.5	Result: Dynamic Error Model.....	56
4.5.1	Frequency Ramp Change	56
4.5.2	Amplitude Modulation.....	56
4.5.3	Phase Modulation.....	58
4.5.4	Amplitude Step Change	58
4.5.5	Phase Step Change.....	59
4.6	Discussion	61
4.7	Conclusion	61
Chapter 5	PMU Accuracy Analysis.....	62
5.1	Introduction.....	62
5.2	Accuracy Limitation Analysis	62

5.2.1	Error Source Analysis	63
5.2.2	Accuracy Limitation Calculation	66
5.3	Impact of Converter-based Energy Sources	71
5.3.1	Converter-based energy sources analysis	71
5.3.2	Model Construction	72
5.3.3	Impact Analysis	74
5.4	Conclusion	74
Chapter 6	Fast Response PMU Development	76
6.1	Introduction.....	76
6.2	Fast Response Algorithm Design.....	77
6.2.1	Dynamic Analysis of DFT Algorithm	77
6.2.2	Analysis of PLL Algorithm	77
6.2.3	Improvement of PLL Algorithm.....	79
6.2.4	Testing Result	81
6.3	High Reporting Rate Design.....	87
6.4	PMU Realization.....	93
6.5	Performance Testing	96
6.6	Conclusion	98
Chapter 7	C37.118.2 Standard Complied FDR/UGA	102
7.1	Background	102
7.2	Data Package Design	104
7.2.1	Common Fields.....	104
7.2.2	Data Frame.....	107
7.2.3	Configuration Frame.....	107

7.2.4	Header Frame.....	107
7.2.5	Command Frame.....	110
7.3	Realization and Testing.....	110
7.4	Conclusion	113
Chapter 8	PMU Measurement Application for Authentication and Cyber Security ...	114
8.1	Introduction.....	114
8.2	Methodology	115
8.2.1	Spatial Feature Extraction and Pattern Recognition	115
8.2.2	Temporal Feature Extraction and Pattern Recognition.....	117
8.3	Spatial Feature Based Data Authentication	118
8.4	Temporal Signature Based Data Authentication.....	120
8.5	Conclusion	121
Chapter 9	Time Synchronization Interval Attack in Smart Grid: Impact and Detection	122
9.1	Introduction.....	122
9.2	TSIA Model	123
9.2.1	Time Synchronization Interval Overview.....	123
9.2.2	Attack Strategy.....	124
9.3	Impact Analysis	124
9.3.1	Measurement Error Derived from TSIA.....	124
9.3.2	Synchrophasor Based Applications Vulnerability to TSIA	127
9.4	TSIA Detection	127
9.5	Conclusion	130
Chapter 10	Power System Measurement for GIC Detection.....	132
10.1	Introduction.....	132

10.2	GIC Signature Analysis	134
10.2.1	Effect of GMD /EMP on Transformer.....	134
10.2.2	Harmonics Analysis	134
10.3	Non-contact Transducer.....	136
10.4	GIC Detection Algorithm Design	137
10.4.1	Accurate Harmonics Detection Algorithm	138
10.4.2	GIC/EMP-E3 Detection Algorithm	139
10.4.3	Testing and Result.....	140
10.5	Conclusion	142
Chapter 11	Conclusions and Future Works	144
11.1	Conclusions.....	144
11.2	Future Works	146
References	147
Appendix	163
Appendix A	Dynamic Line Rating of Overhead Transmission Line	164
A.1	Conductor Temperature and Resistance	165
A.2	Solar Heating.....	165
A.3	Convective Cooling.....	165
A.4	Radiative Cooling	166
Appendix B	Implementation of CRC-CCITT.....	168
Appendix C	Time Accuracy and Reliability of Synchrophasors	169
C.1	Introduction	169
C.2	Problems.....	169
C.3	Mitigation.....	170

Appendix D FDR Troubleshooting.....	172
D.1 GPS Issue	172
D.2 Ethernet Issue	173
D.3 Power Issue	175
D.4 Display Issue	176
D.5 Input Signal Issue	176
D.6 Troubleshooting Chart	178
Appendix E FDR Time Delay Issue and Impact	181
Appendix F Specification of Universal Grid Analyzer.....	183
F.1 General Requirements	183
F.2 Functional Requirements	183
F.3 Communication Requirements	184
F.4 Data Format	184
Vita.....	187

LIST OF TABLES

Table 2.1. Performance during steady state	27
Table 2.2. Dynamic performance during modulation and frequency ramping	27
Table 2.3. Dynamic performance during step change	28
Table 2.4. Group delay of algorithms	29
Table 2.5. Computation complexity.....	31
Table 3.1. Effect of worst-case measurement errors on synchrophasor-based applications	47
Table 4.1. Coefficients of error in harmonics distortion.....	55
Table 5.1. Harmonic components of electrical signals from four different outlets	69
Table 5.2. Measurement accuracy limitation results.....	70
Table 5.3. Harmonics of voltage and current in wind turbine system	75
Table 5.4. Simulation result of measurement error from PV and wind turbine.....	75
Table 7.1 Data frame of the FNET/GridEye protocol	103
Table 7.2 Common fields of the C37.118.2-2011 frames.....	105
Table 7.3 Bit definition of leap second and time quality of FRACSEC[31..24]	106
Table 7.4 Definition of the time quality indicator	106
Table 7.5 Data frame design for FDR/UGA.....	108
Table 7.6 Configuration frame 1 and 2 design for FDR/UGA	109
Table 7.7 Header frame design for FDR/UGA.....	110
Table 7.8 Command frame design for FDR/UGA.....	111
Table 7.9 Command sent to FDR/UGA.....	112

Table 9.1 Vulnerability of synchrophasor based applications to TSIA	127
Table F. 1 Measurement accuracy specifications	184
Table F. 2 Configuration Frame of UGA.....	185
Table F. 3 Data Frame of UGA	186

LIST OF FIGURES

Figure 1.1. Structure diagram of WAMS.....	3
Figure 1.2. Structure diagram of the FNET/GridEye	4
Figure 1.3. Hardware diagram of FDR	5
Figure 2.1. Overview of phasor and frequency estimation methods	11
Figure 2.2. Basic diagram of phase-locked loop (PLL).....	20
Figure 3.1. Typical instrumentation channel for a PMU [163].....	36
Figure 3.2. The processed phase angle curves measured by FDRs in a generation trip event.....	38
Figure 3.3. Phase angle curves of four generation trip events. The red horizontal line represents the preset threshold.	39
Figure 3.4. Phase angle curves of a generation trip. The red horizontal line represents the preset threshold. (a). No error added; (b) $\pm 0.6^\circ$ error added.....	41
Figure 3.5. Cumulative distribution plot of phase angle tolerance in one year.	41
Figure 3.6. Phasor measurement unit error impact on oscillation signal.....	42
Figure 3.7. Overall framework of phasor measurement unit (PMU)–based dynamic line rating technology.	43
Figure 3.8. Dynamic line rating error on 1 day in summer.....	44
Figure 3.9. Maximum DLR error respect to PMU phase angle error and instrumentation channel phase angle error in a low temperature and wind speed day. The error is in percentage. PMU error is positive and negative boundary.	44
Figure 3.10. Frequency measured by frequency disturbance recorders in the Hurricane Sandy case shows the Sussex FDR operating in an island.	46
Figure 4.1. The application of the framework tool to evaluate synchrophasor	49
Figure 4.2. Voltage magnitude error of phase A in frequency range test	52

Figure 4.3. Fitting of magnitude a_1 using sinusoidal function.....	52
Figure 4.4. Fitting of offset a_2	53
Figure 4.5. Voltage magnitude error in magnitude range test	54
Figure 4.6. Voltage magnitude error in interharmonics test	56
Figure 4.7. (a) Magnitude and (b) phase angle error in frequency ramp test	57
Figure 4.8. Voltage magnitude error in amplitude modulation test	57
Figure 4.9. Voltage magnitude error in amplitude step change test	58
Figure 4.10. ROCOF error and curve fitting in phase step change test	60
Figure 5.1. GPS PPS signal output	63
Figure 5.2. Diagram of error estimation simulation	67
Figure 5.3. Power spectrum density of electrical signals from different 120 V outlets ...	68
Figure 5.4. System model with PV	72
Figure 5.5. System model with wind turbine.....	73
Figure 5.6. Wind turbine model.....	73
Figure 5.7. 3p oscillation of RMS value of voltage output by wind turbine	75
Figure 6.1. Structure of the PLL algorithm.....	78
Figure 6.2. Frequency range test, (a) frequency, (b) TVE.....	82
Figure 6.3. Amplitude modulation test, (a) frequency, (b) TVE	83
Figure 6.4. Actual magnitude vs. estimated magnitude.....	83
Figure 6.5. Phase modulation test, (a) frequency, (b) TVE	84
Figure 6.6. Frequency comparison.....	84
Figure 6.7. Frequency ramp test, (a) frequency, (b) TVE.....	85
Figure 6.8. Comparison of frequency estimation response during frequency ramp change	86
Figure 6.9. Magnitude step test, (a) frequency, (b) TVE.....	86

Figure 6.10. Phase step test, (a) frequency, (b) TVE.....	88
Figure 6.11. Comparison of phase angle estimation response during angle step change .	88
Figure 6.12. Phase angle of 60.5 Hz waveform at 60 Hz reporting rate.....	90
Figure 6.13. Phase angle of 60.5 Hz waveform at 120 Hz reporting rate.....	91
Figure 6.14. Phase angle of 60.5 Hz waveform at 120 Hz reporting rate after compensation	92
Figure 6.15. Diagram of UGA hardware	93
Figure 6.16. Picture of UGA hardware.....	94
Figure 6.17. DSP software diagram.....	95
Figure 6.18. ARM software diagram	96
Figure 6.19. Steady state testing result	97
Figure 6.20. Magnitude result in magnitude step change testing: (a). true value and testing result of fast responding PMU; (b). testing results of a commercial PMU; (c), testing results of another commercial PMU.	99
Figure 6.21. Result in magnitude step change testing: (a). phase angle error, the two green lines correspond to the equivalent 1% TVE; (b). TVE, the orange line corresponds to 1% TVE.	100
Figure 6.22. Frequency measurement in magnitude step change testing: (a). true value and testing result of fast responds PMU, the green lines correspond to the ± 0.005 Hz error range allowed by PMU standard; (b). testing results of a commercial PMU; (c), testing results of another commercial PMU; (d), testing results of yet another commercial PMU.	101
Figure 7.1. Comparison of phase angle estimation response during angle step change .	105
Figure 7.2. Procedure to responding to the command frame	111
Figure 7.3. Diagram of the C37.118.2 communication module	112
Figure 8.1. FDRs in North American power system	115
Figure 8.2. STFT based spatial feature extraction	116
Figure 8.3. Neural network based pattern recognition.....	116

Figure 8.4. Diagram of spatial signature based data authentication using a machine learning method	117
Figure 8.5. Illustration of recursive temporal signature extraction.....	118
Figure 8.6. Data source locations of Case A. Yellow marks are the locations where measurement units are installed.	119
Figure 8.7. Data source locations of Case B. Red dots are the locations where measurement units are installed.	119
Figure 8.8. Match accuracy comparison of different ENG segments length and sampling rate.....	120
Figure 8.9. Two cases of the ENF measurement in the same building.....	120
Figure 8.10. Example of temporal signature based authentication.	121
Figure 9.1. Sampling rate changed due to PPS error	125
Figure 9.2. Phase angle error regarding different PPS errors	126
Figure 9.3. Frequency error regarding different PPS errors	126
Figure 9.4. Frequency error and the time to achieve specified TVE regarding to different PPS error	128
Figure 9.5. TSIA detection method diagram based on frequency deviation	129
Figure 9.6. Frequency deviation of onboard oscillator	130
Figure 9.7. TSIA detection method diagram based on internal oscillator	131
Figure 10.1. Harms of GMD/EMP-3	133
Figure 10.2. DC causes half-cycle saturation of the transformer core.....	135
Figure 10.3. Amplitude of harmonics during transformer half-cycle saturation [209] ..	135
Figure 10.4 Diagram of the amplifier circuit for the non-contact transducer	137
Figure 10.5 Structure of PSD algorithm	138
Figure 10.6 Waveform (upper) and power spectrum density (lower) of a signal with 1% 6 th harmonic and -30 dB density	140

Figure 10.7 The relation between harmonic amplitude estimation error and detection time under sampling rate of (a) 1,440 Hz and (b) 14,400 Hz. Harmonics distortion is 1% and SNR = -30 dB.....	141
Figure 10.8 Laboratory experiment setting.....	142
Figure 10.9 A signal sampled with 1% 6 th harmonic.....	142
Figure D. 1. Troubleshooting Chart 1	178
Figure D. 2. Troubleshooting Chart 2.....	179
Figure D. 3. Troubleshooting Chart 3.....	180
Figure E. 1. Frequency of a generation trip in EI with 2 clusters of FDR units with different time stamp shift.....	181

CHAPTER 1 INTRODUCTION

1.1 Overview

Power system is becoming more and more complex, mainly due to the increase of new technologies and the demand of using clean energy. First of all, with the increased concern of carbon emission and the development of material and power electronics, more wind turbine and photovoltaic (PV) are connected to the power grid. Secondly, the structure of load changes with the increasing efficiency of lights, expansion of power electronic devices, and the expected growing of Electric-Vehicles (EV). Thirdly, the unbalanced distribution of the renewable energy and the demand center calls for large power transmission capability. As a result, ultrahigh voltage transmission and high-voltage dc (HVDC) are more and more used in the power system.

While the increased complexity of power system is getting more difficult to keep safe and reliable, the demand of reliability is ever increasing. As nowadays more and more work and life depends on electricity, a blackout would cause much more severe impact than decades ago. E.g., the economic loss of the New York City 1977 blackout is about $\$13.28 \times 10^6$ /hour, while in the Northeast 2003 blackout it boosted to $\$179.17 \times 10^6$ /hour. Even when there is no blackout, the power quality problem triggered by the power system events could also result considerable loss as large amount of equipment is sensitive to voltage/current magnitude, root-mean-square (r.m.s) value, harmonics, transient oscillation, etc.

Due to these two reasons, it is important to understand the wide interconnected power grids, and provide proper planning and operation to maintain the safety and reliability of the power system. Theories and tools are developed to model and analyze the power system, and applications are created to control the system and maintain it in the stable area. To ensure these tools and applications work, it is essential to know the operation situation and states of the system. Situation awareness serves this role in power system. Situation awareness is defined as “the perception of the elements in an environment within a volume of time and space, the comprehension of their meaning, and the projection of their status in the near future” [1]. According to this definition, the situation awareness in power system includes three steps [2]:

1. Perception: achieve the information of key elements of the power system, including generation data, transmission planned outages, load forecast, real-time measurements, breaker status, etc.
2. Comprehension: use the perceived data to obtain status of equipment, deviation between actual and planned states, etc.
3. Projection: forecast the future system state and behavior.

Wide area monitoring system (WAMS) is an important application of the real-time situation awareness system. It is able to provide abundant information of the system operation status over the wide area synchronously, accurately, and timely. Based on this

more efficient and reliable protection and control can be implemented [3]. WAMS has been widely used in the energy management systems (EMS) of power system [4].

1.1.1 Wide Area Monitoring System

As an application of the situation awareness system, the concept of WAMS mainly includes two parts: spatial and temporal, which corresponds to the definition of situation awareness. It covers the wide area of the whole power grid, and the information of different buses, transmission lines, generators and loads are collected by sensors. The wide spread sensors transmit the information to the data center through high-speed communication channels. The carefully deployed sensors and the estimation algorithms guarantee the observability of the whole grid. More importantly, synchronized measurement technology (SMT) is used in WAMS. Data from sensors are measured synchronously and tagged with accurate time tag. The information obtained by tools processing these data are therefore able to reflect the situation of the power grid in each time point, just like the snap shots of the system. This is essentially useful, since in the wide area system, many events involve a chain of large number of small events in sequence. The time tag of high accuracy and resolution helps to locate the event source and prevent the disturbance from spreading out to the whole grid, especially for the cascading failures.

The WAMS mainly includes phasor measurement units (PMUs), phasor data concentrators (PDCs), applications software, and communication networks. A generic structure of WAMS is shown in Figure 1.1.

PMU is the fundamental sensor of WAMS. It is a device for synchronously measuring the current and voltage of the ac lines. To guarantee the synchronization, a common time reference, usually the global positioning system (GPS) is used to timestamp the measurements. In this way, the parameters of the ac voltage and current are measured in terms of phasors, complex numbers represented by their magnitude and phase angle.

PDC is a mass storage which collects data from remote PMUs and transmits to control center. In multi-level WAMS, measurement data from PMU may go through multiple PDCs before reaching the control center. Local PDCs collect data directly from PMUs and transmitted to a super PDC. Super PDCs collect the data from multiple local PDCs and send to the control center. They can also send the data back to local PDCs so each power utility can understand the status of the power grid outside its regional area [3].

In the control center, the data from PDC are archived, and used for different applications, online or offline. Online applications are usually used for real-time operation. Some developed applications include real-time visualization, state estimation, early warning, congestion management, oscillation monitoring and damping control [5, 6], voltage stability, adaptive protection, etc. Off-line applications include post-event analysis, data statistics and operation portfolio analysis, etc.

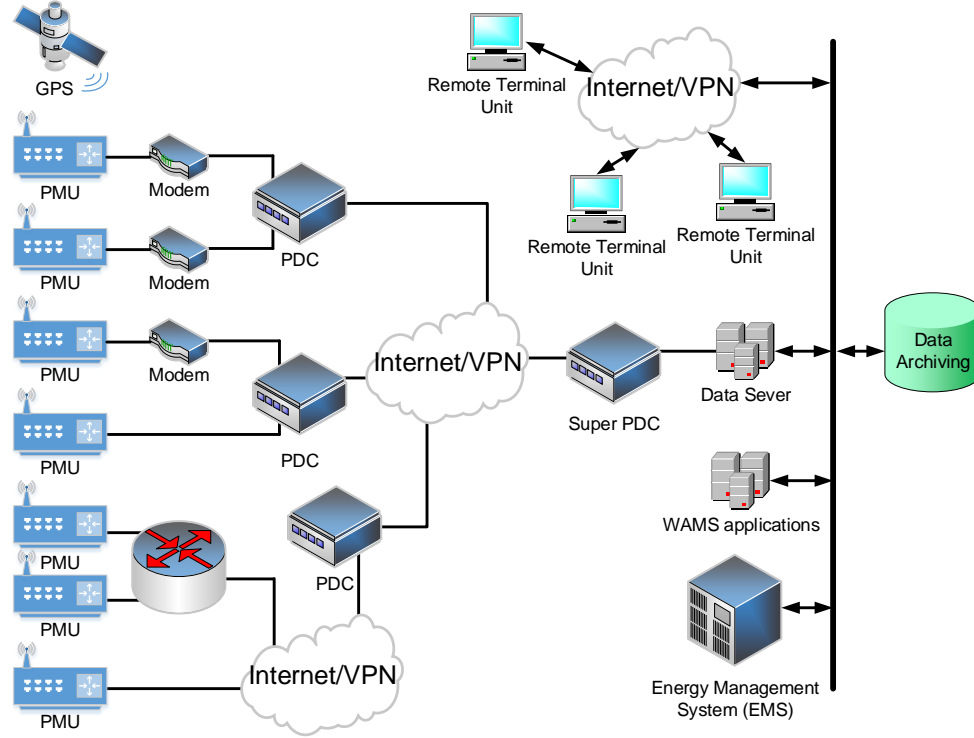


Figure 1.1. Structure diagram of WAMS

WAMS has been built up and used in various power grids over the world [7-10], including but not limited to Brazil, China, Central European, India, Mexico, Nordic Countries, North America, and Russia [8]. It is acknowledged that WAMS is an effective tool for power system situation awareness, and provides abundant real-time information of the power system, in both steady and dynamic state. It allows new algorithms and applications to be developed and used to leverage the stability, security, and the effectiveness of the power system. As the number of deployed PMUs increasing, the number of applications being used for power system operation is still limited. There is few commercial off-the-shelf applications available in the market. Meanwhile, it has not been proved that all the PMUs and WAMS applications are in full compliance with industry standards and the requirement of power system operation. Effort is required to investigate and improve the performance, interoperability, and reliability of the WAMS.

1.1.2 FNET/GridEye: A WAMS Case

The frequency monitoring network (FNET/GridEye) is the first WAMS deployed at the distribution level. Since operating in 2003, it has been providing the synchronized real-time measurements of North American power grid and many other power grids worldwide continuously for over a decade [11-14]. As a pilot and independent WAMS system in distribution level, it is beneficial to the future implementation of WAMS, as it can provide valuable operation experience and evaluate the system effectiveness.

As many other WAMSs, FNET/GridEye includes remote sensors, the data center, and the communication network. A structure diagram of the FNET/GridEye is shown in Figure 1.2. The phasor and frequency data are first collected by Frequency Disturbance Recorders (FDRs) deployed in different places of the grid, and then transmitted to the data center through Ethernet using TCT/IP communication protocol. The data center uses a 3-layer structure. In Layer 1, the data concentrator collects the real-time data from FDRs and stream to the real-time applications component and data storage component in Layer 2. The real-time applications process the real-time data and send the result to data storage, non-real-time applications, and application users. The data storage restore the real-time data and the processing results from the real-time applications, which can be used by the non-real-time applications in Layer 3[15].

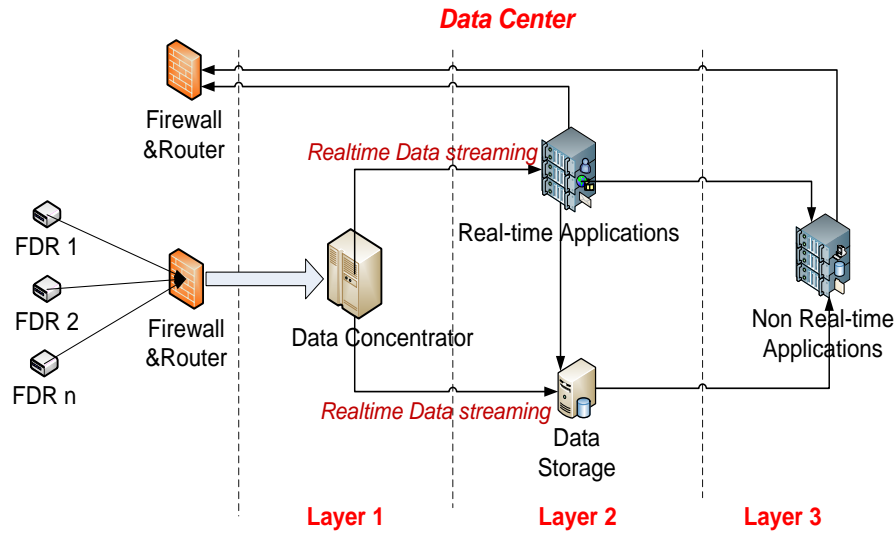


Figure 1.2. Structure diagram of the FNET/GridEye

FDR is used to collect power grid data, including voltage magnitude, phase angle, and frequency. FDR is a single-phase distribution level PMU of low cost and high accuracy. Compared with transmission level PMUs, the FDRs face the following challenges. First of all, more distortions and harmonics exist in distribution level, which impacts the accuracy of the phasor and frequency estimation. Meanwhile, while 3-phase signal is usually available for transmission level PMU and can be used to cancel triplen harmonics, there is only one phase available for FDR, making the harmonics rejection even harder. Thirdly, the cost of FDR should be significantly reduced to get widely deployed.

The structure of the FDR hardware is shown in Figure 1.3. The voltage signal from wall outlet is fed into the device, preconditioned, and sampled by ADC. The ADC sampling action is controlled and synchronized by GPS through GPS receiver and a digital signal processor (DSP). Therefore, the samplings and hence the estimation results are aligned among difference FDRs. The phasor and frequency are obtained in the DSP and

transmitted to a microprocessor (MCU), in which the results are packaged with Coordinated Universal Time (UTC) time and send to the FNET/GridEye data center through Ethernet. A LCD on the front panel of FDR also shows the device operation status and results for monitoring.

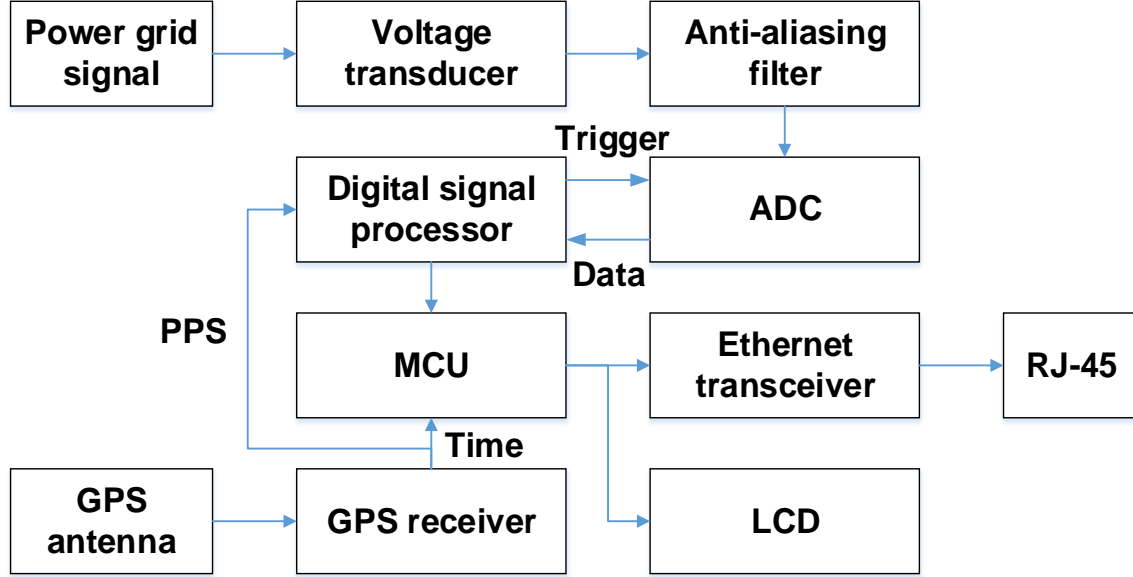


Figure 1.3. Hardware diagram of FDR

Nearly 300 FDR units are deployed over the world, in which over 200 are in North America. These FDRs stream the measured voltage phasor and frequency to the data center at the data rate of 10 Hz.

Based on the data provided by FDRs, several real-time and non-real time applications have been developed. The real-time applications are those with critical requirement of response, and they use short periods of data cached in memory. These applications include event trigger, oscillation trigger, islanding trigger, line trip trigger, ambient mode analysis, and real-time data visualization. Non-real-time data are applications with less time constraints, and offline applications, including event localization, frequency response analysis, oscillation mode analysis, event video replay, online report, etc. [14, 16, 17].

1.2 Dissertation Outline

This dissertation is organized in following chapters.

Chapter 2 reviews the phasor and frequency estimation methods. The algorithms to estimate the phasor and frequency are the core function of PMUs, and they are critical for the accuracy and responding speed of the PMU performance. To understand the algorithms is fundamental of investigate and improve the performance and interoperability of the WAMS. Different PMU algorithms are categorized and analyzed.

Then the key techniques of different algorithms are extracted and illustrated. The performances of different algorithms are compared, in aspects of accuracy, estimation speed, and computation complexity.

Chapter 3 investigates the impact of the PMU measurement error on various PMU-based applications. The target of the study is to reveal the worst possible cases the PMU measurement error is possible to cause to the applications. Firstly, the range of PMU measurement error, including both the error sourced inside the PMU and outside the PMU, i.e. the transducers and the cable to connect the transducers and the PMU, are given using reasonable assumptions. Using the error range, four PMU-based applications: event localization, oscillation detection, islanding detection, and dynamic line rating, are investigated. The worst case of each application and the related probability are given. The mitigation of each application is also discussed.

Chapter 4 proposes a PMU measurement error model, serving as core of an open-source framework tool which is used to evaluate the impact of PMU data quality on different PMU-based applications. To enable the target application being evaluated as working in the real operation condition, the measurement error model needs to mimic the error behavior of real PMU regarding each specific operation parameter and input signal. The final model is able to accurately describe the measurement error of one type of PMU in different operation conditions and with different input signals.

Chapter 5 addresses the highest accuracy a PMU can achieve, and the factors which influence the accuracy limitations. The factors are mainly divided into two groups: internal and external. The internal group includes PMU algorithm and hardware; the distortions included in the input signals, such as white noise and harmonics are attributed to the external group. The accuracy limitation of Discrete Fourier Transform (DFT) based PMU algorithm is investigated, and the contribution from different factors are analyzed. Based on this, a specific topic is studied. In this topic, the impact of converter-based energy on PMU measurement is analyzed.

Chapter 6 proposes the development of a fast response PMU. The target of this work is to improve the dynamic performance of PMU, and leverage the implementation of PMU in power grid dynamics, especially the transient instability detection. The proposed PMU needs to response to the dynamics in a timely manner and provide precise estimation of phasor and frequency. To achieve this goal, the dynamic analysis of conventional algorithms are investigated. Based on this, a fast response algorithm is proposed. A PMU is developed based on this algorithm. Multiple techniques are developed to improve its performance in realization.

Chapter 7 focuses on the work to furtherly enhance the situation awareness capability of power system by improving the interoperability of synchrophasors. The C37.118.2 Standard compliance FDR/UGA was developed. With this improvement, the FDR/UGA can work with conventional PMUs using the same PDC. This can leverage the synergy of

transmission and distribution synchrophasors and provide comprehensive information for system operation and planning.

Chapter 8 proposes applications which utilize the PMU measurements for authentication and cyber security. Firstly, the spatial and temporal signal of electric network frequency (ENF), and the possibility to use them for authentication and cyber security is discussed. Then the method to extract the spatial and temporal characters of ENS is proposed. Based on the characters, applications of spatial and temporal bad data authentication and correction are developed. Finally, the detection of GPS time interval manipulation is developed.

Chapter 9 proposes applications to detect the time synchronization interval attack. The mechanism and impact of time synchronization interval attack are first analyzed. Then two detection methods are proposed, depending on the amount of the timing error introduced by the attack. These methods, do not need extra hardware, can be easily implemented in current PMUs or data center and effectively detect the attack.

Chapter 10 explores the implementation of phasor measurement on GIC/EMP detection. The effect of GIC/EMP on transformer saturation is analyzed and used as the signature. Based on this signature, a synchronous phase detection based algorithm is proposed. Using this algorithm, the GIC/EMP can be detected with high sensitivity and accuracy.

Chapter 11 concludes the dissertation and proposes the future work.

CHAPTER 2 LITERATURE REVIEW: PHASOR AND FREQUENCY ESTIMATION METHODS

2.1 Introduction

Phasor and frequency of voltage and current are vital parameters of alternating current power systems. The phasor at a power system bus, which includes magnitude and angle of the voltage or current sinusoidal signal, represents the direction and amount of the power flow at this bus, and is a key indicator of stability [18, 19]. The frequency, which is the change rate of the phase angle, reflects the balance between power generation and load. When they are unbalanced, the kinetic energy of the generator turbines is consumed or stored to balance the energy of the whole system. As a result, the rotor speed, hence the power system frequency increases when the power excess, and decreases at the power deficit [20, 21]. Therefore, the estimation of phasor and frequency of power system is an essential and effective approach for power system monitoring. The information directly from phasor and frequency, or derived from various application using them, is critical to many applications of power system monitoring, protection and control [22-25].

In the early years, the phasor are mainly estimated by digital relays, and most of them provide frequency estimation [26, 27]. Phase angle changes fast over time, therefore the phase at one location provides rare information, and it is difficult to obtain the phase of multiple locations at one time. In 1983, Phadke, Thorp, et al. developed phasor measurement unit (PMU), an instrument specialized for phasor and frequency estimation [28, 29]. Using synchronous technique such as global positioning system (GPS), the phasor and frequency measurements from different locations in the wide area are synchronized and given the uniformed time stamp [30]. Since then, the phasor and frequency estimation methods experienced a fast development with the increasing interest in synchrophasor measurement technology. The improving of phasor and frequency estimation provides the basis for accurate PMUs, and hence makes a number of novel applications for power system monitoring, protection, and control possible. On the other hand, the effectiveness of applications require accurate and reliable estimation, especially in the real power system with distortion and sudden changes. As a result, the IEEE Standard C37.118 serial for synchrophasors was compiled and revised [31-35].

In [33], the phasor and frequency are defined. The sinusoidal signal in ac power system can be described in (2.1):

$$x(t) = X_m \cos(\omega t + \phi) \quad (2.1)$$

The phasor is represented as shown in (2.2):

$$\mathbf{X} = (X_m/\sqrt{2})e^{j\phi} \quad (2.2)$$

The phasor definition includes two parts: the root-mean-square (r.m.s) value, $X_m/\sqrt{2}$, and the initial phase angle ϕ . Here the phasor is defined for the angular frequency ω . To give a uniform definition of the phasors regardless of the frequency changing, the waveform in (2.1) is rewritten as a relative to the nominal system frequency synchronized to Coordinated Universal Time (UTC):

$$x(t) = X_m(t) \cos(\omega_0 t + \phi(t)) \quad (2.3)$$

where ω_0 is the nominal angular system frequency ($2\pi \cdot 50$ rad/s or $2\pi \cdot 60$ rad/s). The synchrophasor is defined as:

$$\mathbf{X} = (X_m(t)/\sqrt{2})e^{j\phi(t)}. \quad (2.4)$$

Hence the phasor at different places of the system are synchronized to UTC, a uniform reference.

The frequency is usually defined as the number of periods in one second. According to this definition, it needs at least one cycle to estimate and update the frequency. In the power system, the system frequency corresponds to the rotational speed of electrical generator, and hence the instantaneous frequency can be defined with physical meaning. The harmonics and noise are excluded, and the frequency is defined as the derivative of fundamental phase angle respect to time [21, 33]:

$$f(t) = \frac{1}{2\pi} \frac{d(\omega_0 t + \phi(t))}{dt} \quad (2.5)$$

Various estimation methods for phasor and frequency have been proposed, such as zero-crossing detection, discrete Fourier transform (DFT), least square fitting, phase-locked loop, and Kalman filter. Meanwhile, distortions, both steady and dynamic, exist in power grid voltage and current signal. The unbalance between power demand and supply will cause system frequency and voltage to deviate from the nominal value and fluctuate over time. The power inverters increase with the proliferation of high-voltage direct current (HVDC), flexible ac transmission systems (FACTS), and renewable generations. Harmonics introduced by these devices therefore have been increasing rapidly. Both inter-area and intra-area oscillation usually exist in multiple modes, and are significant when not damped adequately. When system events such as generation trip or load shedding happen, the frequency will suffer a ramping, and sometimes together with an oscillation. During the system fault, dc decaying is generated in the current signal. In addition, white noise exist in almost all parts of the power system, and are mixed into the signal. All of these effects are able to pollute the power system signal and influence the performance of the phasor estimation algorithms. Hence, each method group is researched and improved by using different techniques, tuned parameters, and combinations to enhance its performance in accounting to one or more system disturbances.

Besides the requirement of accuracy, the responding speed is another criterion for phasor and frequency estimation algorithms. Most monitoring, control, and protection application requires the detection of any event in a timely manner. The fault detection needs to be detected in time to address the issue. A late detected islanding threatens the safety of line workers and could cause device damage. Real-time applications to predict the future stability will be ineffective if the estimated values have a large time delay. In voltage stability control, timely detecting of the critical status is essential to prevent the system from voltage collapse, and potential cascading failures.

Another concern is the complexity of the estimation methods. A method with less computational effort is easier to be realized in microprocessors or FPGAs, and can be applied to more economic hardware. This could lower the cost of the measurement device, and hence enable the device to be widely deployed for a better awareness of the power grid.

This chapter presents a review of the phasor and frequency estimation methods. This review will mainly focus on the algorithms targeting the PMUs, since they became the most accurate and fast instrument to provide phasor and frequency estimation of power system in the past decades, and are the platform for most advanced phasor and frequency estimation algorithms. The remainder of this paper is organized as follows. In Section 2.2, the basic ideas and improvements of main methods for phasor and frequency estimation are presented. Section 2.3 describes the key techniques to deal with the distortion in the power grid signal. The performance of the phasor and frequency estimation methods in terms of accuracy, responding time, and complexity are compared in Section 2.4. Section 2.5 overviews the key challenges to estimation methods and recommends possible future research. Section 2.6 concludes the review.

2.2 Phasor and Frequency Estimation Methods

Numerous methods for phasor and frequency estimation have been proposed, such as zero-crossing detection, discrete Fourier transform (DFT), least square fitting, phase-locked loop, Kalman filter, and Newton type method. Generally, these methods can be classified to frequency domain or time domain, as shown in Figure 2.1. The frequency domain methods transform a period of time serial signal into frequency domain, and analyze and calculate the phasor and frequency. On the other hand, most time domain methods directly analyze the signal waveform and convert the estimation into an optimization problem. With error or squared errors as an objective function, the algorithms are designed to minimize the objective function by tuning the estimation recursively.

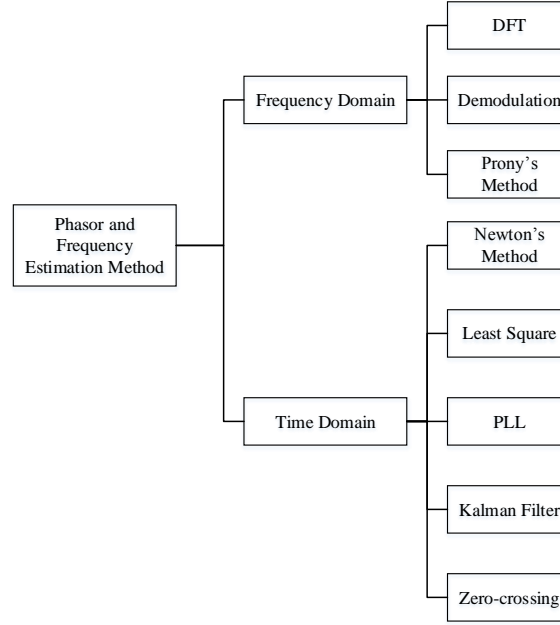


Figure 2.1. Overview of phasor and frequency estimation methods

2.2.1 Zero-crossing Detection

Zero-crossing is the most straightforward method. It determines the period between two consecutive zero crossings of the signal, and hence obtain the frequency of the signal. It is robust to frequency change. However, it is sensitive to distortions such as voltage/current sag and swell, noise, harmonics, and DC component. Furthermore, it is detectable only every half a period, hence degrades its dynamic performance.

Some studies are conducted to eliminate its sensitivity to distortion. Least square fitting method can be used fit half cycle samples into a polynomial function [36]. The roots of this function are solved to represent the zero-crossing time, and hence the frequency is estimated. The polynomial fitting suppresses noise and harmonics distortion. However, for transient signals, this method could generate large error. In [37] zero-crossing is expanded to various non-zero voltage level crossing. With the interpolation and weighing approach, this algorithm is able to estimate the frequency at every sample and immune to amplitude variation. Filter is an option to reduce the noise from the input signal before fed into the estimation algorithm. In [38] a median filter and a predictive filter are cascaded to effectively remove impulses and the white noise. This approach however, cannot tolerate large frequency variations. An enhanced phase-locked loop (PLL) is used as an adaptive filter in [39]. PLL can extract the fundamental component from the input for zero-crossing detection. In [40] voltage and current from two phases are used to reconstruct the voltage waveform for zero crossing. Although methods [38-40] are intended to obtain firing angle for converters, they can be utilized for phasor and frequency estimation.

2.2.2 Discrete Fourier Transform

Discrete Fourier Transform (DFT)-based phasor and frequency estimation algorithm is the first algorithm to estimate the positive sequence component of power system, and hence arouse the invention of PMU [28]. The main idea of DFT algorithm is to transform the time domain signal into frequency domain, and calculate the Fourier series at the fundamental frequency. Then the phasor of the fundamental component can be obtained. A serial of signal samples can be represented by

$$x(k) = \sqrt{2}X \sin\left(\frac{2\pi}{N}k + \phi\right) \quad (2.6)$$

where X is the magnitude, N is the sampling number in each cycle, k is the index of data samples, and ϕ is the initial phase angle. Taking samples from one cycle, the DFT at signal frequency is given by

$$\mathbf{X}_1 = \frac{2}{N} \sum_{k=0}^{N-1} x(k) e^{-j\frac{2\pi}{N}k} = \sqrt{2}X \sin \phi - j\sqrt{2}X \cos \phi. \quad (2.7)$$

The synchrophasor defined in (2.4) can be represented by

$$\mathbf{X} = \frac{1}{\sqrt{2}}j \mathbf{X}_1. \quad (2.8)$$

The synchrophasor can also be obtained by a recursive form

$$\mathbf{X}^{(r)} = \mathbf{X}^{(r-1)} + j \frac{1}{\sqrt{2}} \frac{2}{N} (x_{N+r} - x_r) e^{-j\frac{2\pi}{N}(r-1)}. \quad (2.9)$$

For a three phase system, the positive sequence voltage can be obtained by a similar equation.

$$\begin{aligned} \mathbf{X}^{(r)} = \mathbf{X}^{(r-1)} + j \frac{1}{\sqrt{2}} \frac{2}{N} \frac{1}{3} & \left[(x_{a,N+r} - x_{a,r}) e^{-j\frac{2\pi}{N}(r-1)} \right. \\ & + (x_{b,N+r} - x_{b,r}) e^{-j\frac{2\pi}{N}(r+5-1)} \\ & \left. + (x_{c,N+r} - x_{c,r}) e^{-j\frac{2\pi}{N}(r+9-1)} \right]. \end{aligned} \quad (2.10)$$

When the signal frequency changes from the nominal value ω_0 to $\omega_0 + \Delta\omega$, (2.9) becomes

$$\mathbf{X}^{(r)} = \mathbf{X}_0^{(r)} \cdot \frac{\sin \frac{\Delta\omega}{120}}{\sin \frac{\Delta\omega}{120N}} e^{j\frac{\Delta\omega}{60N}r} \quad (2.11)$$

where $\mathbf{X}_0^{(r)}$ is the phasor from a signal at nominal frequency having the same magnitude as the $(\omega_0 + \Delta\omega)$ signal. Denote the phasor factor by $e^{j\psi_r} = e^{j\frac{\Delta\omega}{60N}r}$, the frequency deviation can thus be calculated by

$$\Delta f = \frac{(\psi_r - \psi_{r-1}) \cdot 60N}{2\pi} \quad (2.12)$$

In (2.7) DFT is applied on a window with N samples from one cycle. Actually, as long as the window covers integer number of cycles, the equation always fulfills. Multicycle DFT approach is potential to improve accuracy in steady state condition [29]. Harmonic components, if exist in the input signal, will be eliminated during DFT [41]. However, the window, which is a finite interval, causes some problems.

First of all, when distortion components, including interference signal and noise, are mixed in the input signal, they cannot be fully eliminated as harmonics. This is known as the spectral leakage due to the finite measurement interval, i.e. the window length, cannot cover the whole period of the distortions. As a result, the energy of each spectral component is spread over the whole frequency axis and impacts the spectral of the fundamental part [42, 43].

Secondly, since the window length is integer times of the nominal frequency cycle, spectral leakage happens when the fundamental frequency deviates from the nominal frequency. At this circumstance, the phasor and frequency estimation error will increase with the deviation. The error of magnitude and phase angle includes two parts: dc part and ac part. The dc part is a constant error, and the ac part is the fluctuating part which equals to twice the input ac frequency [44].

One mitigation approach is to change the window form by introducing weighting coefficients. The window used in (2.7) is a rectangular window in which every sample remains unchanged. Adding weights coefficients to the window is equivalent to use a filter for the signal. To best reject the interference and fit for the off-nominal fundamental frequency, the spectral of the window should have a relatively flat mainlobe and small sidelobes. Some classic windows include triangle window, $\cos^\alpha(X)$ window, Hamming window, Blackman window, Hanning window, Nuttall window and some constructed window [45, 46]. They mainly show low sidelobes or fast decaying sidelobes, however, their mainlobe is not flat enough to deal with the spectral leakage. To deal with this issue, flap window [47] and raise-cosine filter [48, 49] are proposed. These windows, with flat mainlobe and small sidelobes, improved the accuracy of estimation. Several windows are compared in [42]. In [50] an optimal window technique is proposed based on the theoretical analysis on the error in off-nominal conditions. It generates a cluster of

cosine-class windows whose window parameters are adjusted to minimize the error according to the window length and the number of terms of the window.

Another approach is to design adaptable filters. These filters can self-tune the fundamental frequency, and have very small error over a wide frequency range. When applying, accurate frequency is first estimated from a separate algorithm or feedback from the output, and then used to tune the adaptive filter. Phasors are estimated using the filtered signal. The reported filters include FIR bandpass filter derived from the exponentially modulated filter bank [51], and adaptive Kalman filter, which suits for narrow band applications with changing harmonics and sub-synchronous phenomena [52, 53]. One issue of the filter is that filters brought group delay. It could influence the responding speed of the algorithm. Another issue is that, even carefully designed, it may still include attenuation and phase shift to the fundamental component and will influence the accuracy. Magnitude and phase compensation are thus needed to fix this issue.

The third approach is interpolation or resampling. The main idea is to adjust the measurement values according to the actual frequency so that the window always covers integer cycles. The first type is to adjust the measurement values so that the sampling rate is tuned to be a fixed integer time of the actual frequency. Adjustment is implemented through linear interpolation [54-56]. It needs to recalculate almost all the values. A simpler method is to use a variable window whose length is tuned to cover the fraction part of the sampling time interval. Only the last value of the window needs to be determined by linear interpolation [57]. The second type is to recalculate the measurement values so that its frequency is shifted to nominal. The synchrophasor remain unchanged after the adjustment, but the influence of off-nominal frequency disappears [58, 59]. Although the ideas of these two types of algorithms are different, they are generally the same in application, since both tried to adjust the measurements into the values the phases of which correspond to an integer fraction of the nominal frequency cycle.

Similar to the adaptive filter approach, the data adjustment also requires the knowledge of the actual value of frequency. One method is use a separate algorithm to predetermine the actual frequency. Another method is to iteratively estimate the phasor and frequency until the estimation is converged or the setting iteration times is achieved [55]. Higher order interpolation may increase the accuracy but the computational complexity also raises.

Another type of interpolation is implemented in spectrum domain, usually named as IpDFT. In this method, multiple spectrum bins are obtained by DFT, and the fundamental frequency, if deviated from the nominal value, falls between two subsequent DFT bins. Interpolation can be used to determine its phasor and frequency [60-65]. To get a good frequency resolution, the window size of the IpDFT should be long enough, which is unlikely to handle dynamic situation. Furthermore, it needs to implement multiple times of DFT to get the bins, compared to once for conventional DFT. The computational amount hence increases.

The fourth approach is post-process and compensation. The error during off-nominal frequency input can be deducted by algebraic analysis, which depends on the frequency deviation [29, 43]. Based on this, methods are proposed to compensate the error. Similar to the interpolation method, the actual frequency value is required. [43] implements least-square approach to estimate the frequency deviation for compensation. Some techniques, however, do not need to know the actual frequency preliminarily. Ref [44] reveals that by choosing suitable phase difference interval, the frequency error can be suppressed to near zero. Authors of Ref [66] used the Smart Discrete Fourier Transforms (SDFT) to solve the frequency deviation by solving several phasor equations. The phasor and frequency are solved together. It suits for steady state, and the computation delay and burden quickly increase with the number of harmonic components. Filtering the estimation results is another post-processing method, such as shifting window and integration [67, 68], and notch filter [69].

Besides these four approaches, ref [70] finds that if an orthogonal signal of $x(t)$ with the same magnitude can be found, the angle estimation error brought by frequency deviation can be eliminated. Clarke transformation is used to obtain this pair of signals and high accurate estimation result is obtained.

In classic DFT algorithms, the frequency is calculated by using (2.5) on two consecutive phasors. This is based on the assumption that the frequency is steady within the window. However, during the dynamic conditions, the frequency changes from time to time, and obtain the true instantaneous frequency is important. A theoretical analysis on DFT is done in [71]. Based on the analysis, the instantaneous frequency is obtained with the correct timestamp during steady state, linear frequency changing, or nonlinear slow changing. In [36] a polynomial function is first obtained by least squares fitting using multiple phasors, and its first order derivative is calculated as the instantaneous frequency. This method smooths the effect of noise, but introduces time delay.

2.2.3 Demodulation Method

Demodulation method is actually a special type of DFT. As it is discussed by papers specifically, it is reviewed here in a separate subsection from DFT. For a sampled signal described in (2.1), it is first modulated by sinusoidal and cosine waveform at the nominal frequency.

$$y_c(t) = x(t) \cos(\omega_0 t), \quad (2.13)$$

$$y_s(t) = -x(t) \sin(\omega_0 t). \quad (2.14)$$

Both $y_c(k)$ and $y_s(k)$ includes two frequency components: $(\omega + \omega_0)$ and $(\omega - \omega_0)$. The first part can be removed by a low pass filter, and the outputs are

$$\widetilde{y}_c(t) = \frac{1}{2} X_m \cos((\omega - \omega_0)t + \phi), \quad (2.15)$$

$$\widetilde{y}_s(t) = \frac{1}{2}X_m \sin((\omega - \omega_0)t + \phi). \quad (2.16)$$

The synchrophasor can then be obtained by

$$\mathbf{X} = \sqrt{2}(\widetilde{y}_c(t) + j\widetilde{y}_s(t))e^{j\omega_0 t}. \quad (2.17)$$

For three-phase, positive and negative sequence can be obtained by using dq-transform, and each of their synchrophasor can be estimated using demodulation method separately [72].

Comparing to DFT algorithm, both algorithms use the rotation factor $e^{j\omega_0 t}$ to shift the frequency spectrum to low frequency, then filter out the high frequency components to get the phasor and frequency deviation. Both are basically a narrow band pass filter. Disturbances outside this passband are filtered. The difference is that, DFT uses a window to eliminate the disturbance and obtain a cluster of samples, shifts the frequency spectrum, and uses the integration to eliminate the residual high frequency components. Demodulation, on the other hand, shifts the frequency first and then filters the noise.

The performance of the demodulation algorithm mainly depends on the selection of the filter, including average, two-cycle Hamming filter, and Bessel filter [72]. Similar to the DFT algorithm, a filter can be implemented on the estimation results for post-process [73]. However, the response speed will be influenced. For the three-phase case, dq-transform brings advantage in performance and computation effort. For low noise and low negative sequence situation, the dq-transform saves the filter [74]. They can also assist in a harmonic trapping technique to cancel both negative sequence and harmonics [75]. However, the computational burden increases as the harmonic order increases, and it is based on the assumption that the signal is steady.

For frequency estimation, similar method used in DFT can be used here. Considering the characteristic of this method, two synchrophasors $\mathbf{X}(n-1)$ and $\mathbf{X}(n+1)$ can be used to calculate the frequency and eliminate the residual phase noise [36].

2.2.4 Newton Type Method

Newton type method uses Newton's method or Gauss-Newton algorithm to obtain the optimal solution of the non-linear equations of samples and parameters of phasor and frequency. Denote the estimation of sample $x(k)$ as

$$\hat{x}(k) = \hat{X}_m \cos(\hat{\omega}\Delta Tk + \hat{\phi}). \quad (2.18)$$

The parameters to be estimated can be denoted as the vector

$$\hat{\boldsymbol{\theta}}(k) = [\hat{X}_m \quad \hat{\omega} \quad \hat{\phi}]. \quad (2.19)$$

Due to there are 3 unknowns, at least 3 samples are required for estimation. The estimation equations are represented in matrix as

$$\mathbf{X}(k) = \hat{\mathbf{X}}(k) + \mathbf{E}(k) = h(\hat{\boldsymbol{\theta}}(k)) + \mathbf{E}(k), \quad (2.20)$$

where h is the estimation function, and $\mathbf{E}(k)$ is the vector of estimation errors $e(k)$:

$$\mathbf{E}(k) = [e(k) \quad e(k-1) \quad \cdots \quad e(k-N+1)]^T. \quad (2.21)$$

N ($N \geq 3$) is the number of samples used for each estimation. The target of estimation is to minimize the error $e(k)$ to get an accurate estimation. One example of the objective function (or cost function) is derived from the maximum likelihood function and can be represented as:

$$\varepsilon(k) = \mathbf{E}^T(k)\mathbf{E}(k) = \sum_{i=k-N+1}^N e^2(k). \quad (2.22)$$

Applying Newton's method to minimize the objective function, $\hat{\boldsymbol{\theta}}(k)$ can be recursively calculated by applying:

$$\hat{\boldsymbol{\theta}}(k+1) = \hat{\boldsymbol{\theta}}(k) - \mathbf{H}(k)^{-1} \nabla \varepsilon(k). \quad (2.23)$$

Here $\mathbf{H}(k)$ is the Hessian matrix of $\varepsilon(k)$ and $\nabla \varepsilon(k)$ is the gradient vector. For each group of input voltage/current, the iteration can be applied once or several times. Constrains of estimation error and iteration time can be set to limit the computation time [76, 77].

The inverse of Hessian matrix is complex in computation, and results this method hard to be used in real-time. To solve this issue, simplified methods are proposed.

One of the commonly used method is by using Gauss-Newton algorithm [76, 78, 79]. In this method, Hessian matrix and the gradient vector are replaced by terms of Jacobian matrix and the recursive equation of (2.23) becomes:

$$\hat{\boldsymbol{\theta}}(k+1) = \hat{\boldsymbol{\theta}}(k) - (\mathbf{J}^T(k)\mathbf{J}(k))^{-1} \mathbf{J}^T(k)\mathbf{E}(k) = \mathbf{J}^\#(k)\mathbf{E}(k), \quad (2.24)$$

where $\mathbf{J}^\#(k)$ is the left pseudoinverse of Jacobian matrix $\mathbf{J}(k)$.

Another method is to simplify the Hessian matrix. Analysis reveals that when the signal frequency to sampling frequency ratio is not 0 or 0.5, the off-diagonal terms of the Hessian matrix can be neglected. In this way, the Hessian matrix becomes a diagonal matrix and its inverse is easy to be calculated [80, 81]. Furthermore, the Hessian matrix can be updated recursively by

$$\mathbf{H}(k+1) = \mathbf{H}(k) + \nabla \varepsilon(k) \nabla^T \varepsilon(k), \quad (2.25)$$

in which $\nabla \varepsilon(k) \nabla^T \varepsilon(k)$ can also be approximated as a diagonal matrix [82].

The Newton's method, which uses the approximation of the Taylor expansion, requires the starting estimation point to be close to the true value in order to guarantee convergence and response speed. One idea is to use a separate algorithm to obtain a rough value as the initial value for Newton type method [77, 83].

To improve the tracking capability in dynamic situation, a forgetting factor λ ($0 < \lambda < 1$) is introduced [79, 81, 82]. The objective function then becomes

$$\varepsilon(k) = \sum_{i=k-N+1}^N \lambda^{N-i} e^2(k). \quad (2.26)$$

Newton type method can be used to estimate the parameters of not only the fundamental component, but also the harmonics and decaying factor of DC offset [81, 84]. To implement this function, the signal model in (2.1) is extended to

$$\hat{x}(t) = \sum_{i=1}^M \hat{X}_i \cos(i\hat{\omega}\Delta T k + \hat{\phi}_i) + \hat{X}_0 e^{-\hat{\alpha}k\Delta T}, \quad (2.27)$$

where \hat{X}_i and $\hat{\phi}_i$ ($i = 1, \dots, M$) are the estimation of the magnitude and the phase angle of i -th harmonic, respectively. $\hat{\omega}$ is the estimation of the fundamental angular frequency, ΔT is the sampling interval, and \hat{X}_0 and $\hat{\alpha}$ are the estimation of amplitude and decay factor of the DC offset.

2.2.5 Least Square Method

Least Square (LS) method, sometimes referred as Least Error Square (LES), Least Mean Square (LMS), or Weighted Least Square (WLS), is a time domain phasor and frequency estimation method. Similar to Newton type method, it tries to find an optimized guess on the parameter of the input signal, and thus obtain the estimation close to the real value. Instead of solving the nonlinear optimization problem, LS method linearizes the equation of (2.20) into

$$\mathbf{X}(k) = \hat{\mathbf{X}}(k) + \mathbf{E}(k) = \mathbf{H}f(\hat{\boldsymbol{\theta}}(k)) + \mathbf{E}(k) \quad (2.28)$$

where \mathbf{H} is the matrix of known values, $f(\hat{\boldsymbol{\theta}}(k))$ is the function of unknown variables, and $\mathbf{E}(k)$ is the estimation error. The parameter vector is estimated to get the least error square by

$$f(\hat{\theta}(k)) = (\mathbf{H}^T \mathbf{H})^{-1} \mathbf{H}^T \mathbf{X}(k) = \mathbf{H}^\# \mathbf{X}(k), \quad (2.29)$$

where $\mathbf{H}^\#$ is the left pseudoinverse matrix of \mathbf{H} . The number of samples in $\mathbf{X}(k)$ should be larger than the number of unknown variables to guarantee over estimation.

The linearization is realized by expanding the input signal in the neighborhood of the nominal frequency using Taylor series. Each term of the Taylor series is the product of two parts. The first part is the functions of the phasor and frequency, i.e. $f(\hat{\theta}(k))$, and the second part includes only known values, i.e. H . After $f(\hat{\theta}(k))$ is solve, $\hat{\theta}(k)$ can be obtained [85].

Another type of LMS algorithm utilize the relation of

$$\begin{aligned} \frac{1}{2} [V \sin(\omega t + \phi) + V \sin(\omega(t + 2\Delta T) + \phi)] \\ = V \sin(\omega(t + \Delta T) + \phi) \cdot \cos(\omega\Delta T). \end{aligned} \quad (2.30)$$

The $\cos(\omega\Delta T)$ is solved by LMS algorithm, and the frequency can be calculated [86].

The performance of the LS method mainly depends on the selection of data window size, the sampling frequency, and the frequency deviation. Large data window could reduce the effect of noise, but also decreases the responding speed. High sampling frequency also improves the noise immunity characteristic, but increases the computational complexity [85]. As the frequency deviates from nominal value, the error brought by the truncation in Taylor series increases. One mitigation method is to iteratively update the linearization point of the Taylor series with the actually estimated frequency [87]. Large data window cannot eliminate the effect of periodical disturbances, such as harmonics, therefore they need to be filtered [88]. A window can be used as the weighting matrix \mathbf{W} to suppress the noise [89]. The pseudoinverse matrix then becomes

$$\mathbf{H}^\# = (\mathbf{H}^T \mathbf{W} \mathbf{H})^{-1} \mathbf{H}^T \mathbf{W}. \quad (2.31)$$

Similar to the Newton type method, LS method can also estimate the parameters of harmonics and decaying DC offset by expanding the signal model [86, 87].

2.2.6 Phase-Locked Loop

Phase-locked loop (PLL) is used to synchronize power electronic devices with power system before being used for PMU algorithm. It severs as phase angle tracking component for converters. The basic diagram of PLL is shown in Figure 2.2. PLL is comprised of a phase detection (PD), a loop filter (LPF), and a voltage-controlled oscillator (VCO). The VCO outputs a sinusoidal signal which is compared with the input signal in PD. The error between them is input into LP to generate a control signal for VCO, and tune the output of VCO the same as input.

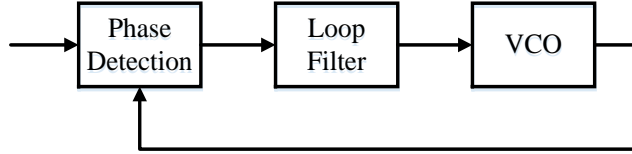


Figure 2.2. Basic diagram of phase-locked loop (PLL)

When used for measurement and phase tracking, each of the three components is digitalized. The input signal is converted by dq-transform in PD, and then multiplied by the output of VCO to obtain the error signal $U \sin(\theta^* - \theta)$ where U is the peak value of voltage/current, θ is the actual phase angle, and θ^* is the estimated phase angle. When difference between estimated and actual angle is small, the error signal is approximately linear to the angle estimation error. The error signal is input into the loop filter, and the estimated angular frequency ω^* is obtained. This value is used by the digitalized VCO to generate θ^* . The feedback loop continues working to eliminate the error and output the estimation of frequency and angle [90, 91].

The loop filter behaviors as a regulator and mainly determines the performance of the PLL, including the convergence speed and accuracy. A PI regulator is usually used as the loop filter. The method to determine the parameter of the regulator includes symmetrical optimum [90] and Wiener method [91]. This type of algorithm, however, is sensitive to the presence of harmonics and unbalanced conditions due to that it considers the signal as balanced and harmonic free.

In another type of PLL, the instantaneous value is estimated and directly compared with input signal to generate the error signal. Both magnitude and frequency are estimated by the loop filter, and the phase angle is determined by the integration of frequency. The estimated signal could be either in the quadrature term [92] or direct term [39]. In this method, the square of error is usually set as the cost function, and is the target to be minimized. Gradient descent method is used for estimation. This method, originally developed for single-phase, can estimate the positive sequence by combining four units [93], or extended to estimate unbalanced three phase directly [94]. It can also be used for harmonics and interharmonics estimation by cascading [95], or combining with filter bank and down sampling module [96]. DC component mixed in the input signal may influence the performance of the PLL algorithm. By introducing a bandpass filter [97] or adding a dc estimation branch, this issue can be solved [94].

The gradient method based PLL algorithm is similar to Newton type method and LS method in type of utilizing the gradient of the cost function to minimize the estimation error. Different from the latter two, PLL algorithm uses only one input value for each estimation, and there are no iterations for each estimation. Therefore, its structure is simpler and computational burden is smaller. However, it is therefore more sensitive to the disturbance and interference in the input signal. Similar to LS method, it needs several estimations to converge after starting. Another concern of PLL algorithm is its

stability, due to its close loop structure. The parameters in loop filter should be chosen carefully to ensure that the algorithm is stable [91, 92].

2.2.7 Kalman Filter Method

Kalman filter is an optimal response digital filter [98]. Due to its ability to automatically tune its response to minimize the estimation error, it can be used for phasor and frequency estimation. The Kalman filter is based on a state space model of the system and the Kalman gains. The model includes state transition and output equations. In the application of phasor and estimation, the real and image part of the phasor are selected as the state variable. The state transition equation is built to estimate the phasor at time $(n + 1)\Delta T$ in terms of the phasor at $n\Delta T$ [99]

$$\mathbf{X}(n + 1) = \mathbf{A}\mathbf{X}(n) + \mathbf{w}(n). \quad (2.32)$$

Here $\Delta\mathbf{X}(n)$ is the change in phasor from time $(n + 1)\Delta T$ to $n\Delta T$, $\mathbf{w}(n)$ is the process noise, and \mathbf{A} is the transition matrix which can be determined according to the sampling rate. The output equation is the relation between the sampled values and the phasor, i.e.

$$x(n) = \mathbf{H}\mathbf{X}(n) + v(n), \quad (2.33)$$

where \mathbf{H} is the relationship between the instantaneous sample and its phasor representation, and $v(n)$ is the measurement noise at time $n\Delta T$.

The Kalman gains, which are the time varying coefficients, are updated for each input to minimize the square of the expected estimation error. They can be calculated by the three equations below.

$$\mathbf{K}(n) = \mathbf{P}^-(n)\mathbf{H}^T[\mathbf{H}\mathbf{P}^-(n)\mathbf{H}^T + \mathbf{R}]^{-1}, \quad (2.34)$$

$$\mathbf{P}(n) = [\mathbf{I} - \mathbf{K}(n)\mathbf{H}]\mathbf{P}^-(n), \quad (2.35)$$

$$\mathbf{P}^-(n + 1) = \mathbf{A}\mathbf{P}(n)\mathbf{A}^T + \mathbf{Q}. \quad (2.36)$$

In these equations, $\mathbf{K}(n)$ is the Kalman gains, $\mathbf{P}^-(n)$ is the *a priori* estimate error covariance, \mathbf{R} is the covariance of the measurement noise $b(n)$, $\mathbf{P}(n)$ is the *a posteriori* estimation error covariance, \mathbf{I} is an identity matrix, and \mathbf{Q} is the covariance of the process noise $\mathbf{w}(n)$. The phasor is therefore estimated by Kalman filter equation

$$\hat{\mathbf{X}}(n) = \mathbf{A}\hat{\mathbf{X}}(n - 1) + \mathbf{K}(n)[x(n) - \mathbf{H}\mathbf{A}\hat{\mathbf{X}}(n - 1)]. \quad (2.37)$$

In the frequency estimation, the relation between state variables and the measurement is no longer linear, and (2.33) is changed to

$$x(n) = h(\mathbf{X}(n)) + v(n) \quad (2.38)$$

The \mathbf{H} in (2.34), (2.35), and (2.37) is replaced by the Jacobian matrix of partial derivatives of h with respect to $\mathbf{X}(n)$, i.e.

$$\mathbf{H}(n) = \frac{\partial h(\mathbf{X}(n))}{\partial \mathbf{X}(n)} + v(n) \quad (2.39)$$

This is also named as the extended Kalman filter (EKF). Using EKF, the phasor and frequency can be estimated together [100].

In application, the Kalman gain is updated in each iteration, then the phasor is estimated once the latest measurement $x(n)$ is obtained. The matrices \mathbf{A} , \mathbf{H} , \mathbf{Q} , and \mathbf{R} can be deemed as constant and be estimated offline [99]. Matrices \mathbf{Q} and \mathbf{R} , which related to the noise statistics, can be obtained by either analyzing the power system data and measurement device, or by simulation using EMTP [101]. In the presence of unknown or nonstationary noise statistics, the noise statistics can be adaptively calculated on-line. Hence, the matrices \mathbf{Q} and \mathbf{R} are updated in each iteration [102].

Kalman filter based method is dependent on the signal model and sensitive to the initial conditions [92]. A reasonable initial value could increase the convergence speed of the algorithm. The noise and sampling rate also influence the convergence overshoot and speed [100].

2.2.8 Other Methods

There are some other methods developed for phasor and frequency estimation. Prony's method, which is widely used for oscillation mode detection, can be used to estimate the fundamental frequency and phasor [103, 104]. However, it is sensitive to harmonics [66]. Neural network method can also be used for estimation [105, 106], but it is not capable of dealing with polluted signals.

Taylor method uses only three consecutive samples to calculate the frequency [107, 108]. However, it is based on the assumption that the signal is very stable and the peak value is known. Also, the estimation accuracy decreases fast as the frequency deviates from the nominal value.

2.3 Techniques

Although the phasor and frequency estimation algorithms are in different types, they share the same target and faces similar challenges such as input phase number and disturbances. At as result, some techniques can be used for various algorithms. In this section, some common problems and solutions are summarized and analyzed.

2.3.1 Three-Phase and Single-Phase

Most algorithms can be used in both three-phases and single-phase. Over the years, research on three-phase are more popular, and methods are developed to deal with the negative sequence distortion.

Taking the advantage of the symmetric of three-phase, some techniques can be used to simplify the phasor and frequency estimation, and even improve the algorithm performance. The most used technique is Clarke transform, which convert the three-phase signal into the two-phase orthogonal frame, and Park transform, which change the orthogonal signal pair from stator coordinator into a rotating reference. Authors of [109] claim that estimation error of DFT algorithm on the positive sequence components of the signal is less than that when directly estimated from the three-phase signal itself; the window size can even be minimized to half cycle without introducing addition error when the DC term in each phase is equal. Clarke transform can also eliminate the triplen harmonics [74]. It is also found that the one part of the phase angle error derived from off-nominal frequency in DFT algorithm is canceled in the positive sequence of a balanced three-phase signal [110]. However, in three-phase the algorithms also need to exclude the influence of negative sequence when the three-phase voltage/current is unbalanced [75].

Single-phase is gaining focus nowadays as the synchronous monitoring and smart grid technique of power grid is expanding to the distribution level. Single-phase PMU is also used in transmission level because of cost or availability of signals. At this circumstance, some additional error may exist compared to the positive sequence of three-phase. The DFT method shows a second harmonics component error in single phase and unbalanced three phase [29, 110]. Average filter, Blackman-Harris filter, and least-squares fit are proposed to eliminate this error in post-processing [29, 111]. Quasi-positive-sequence DFT is developed to simulating a three-phase signal from single phase and hence decrease the phase angle error [70, 110].

2.3.2 Filter

Filter is an important tool in signal processing. Phasor and frequency estimation is generally implemented in two steps, in both of which the filter is used. The first step is to sample the signal, and convert continuous analog signal into discrete digital signal. In this step, the anti-alias filter is used before sampling to filter out the frequency components higher than half of the sampling rate. It can be avoided if the sampling frequency is much higher than the highest spectrum component contained in the signal [60, 65]. When used, it is usually included in the analog-to-digital converter (ADC) so it is out of the scope of this paper. However, it may bring up to -24° phase shift, which should be compensated [53].

The second step is to estimate the phasor and frequency. In this step, filter is also used in a lot of algorithms, before, during, or after the estimation. The main purpose is to reserve

the fundamental component and eliminate the disturbance, including harmonics, inter-harmonics, and noise.

Filter usually brings attenuation and phase shift, which will influence the accuracy of estimation. One mitigation is to design a filter which has a flat band with zero attenuation and phase shift at fundamental frequency. However, when the frequency deviates from the nominal value, the error increases. Although a wide passband filter can be designed, it usually brings the tradeoff of high sidelobes, which cannot effectively eliminate the out-of-band disturbance. Another method is to compensate the attenuation and phase shift. This needs knowledge the signal frequency.

2.3.3 Deal with DC Offset and Harmonics

To improve the accuracy of phasor and frequency estimation, eliminating of disturbance is an important approach. One disturbance attracting attention is the decaying dc offset. It usually happens during the power system fault or transformer transients, and includes relatively wide range of frequency spectrum with larger distribution at lower frequencies [29]. For the sake of this, normal filters used in DFT algorithm can hardly filter it out, and it can result up to 15.1% magnitude error [112]. Methods to deal with this issue includes prefiltering [112], least square error based method [113], modified Fourier algorithms [114, 115], DC delaying effect compensation [41, 116-118], partial-sum-based algorithm [119], iteratively determination [120, 121], and integrating and subtracting [122, 123].

Another kind of disturbance is harmonics, which are mainly generated by the increasing usage of power electronic devices in power system, such as HVDC, FACTS, renewable energies, and energy storages. LMS fitting is an effective filter for harmonics [36]. Shifting window average method (SWAM) can be used on the estimation results from DFT to eliminate the impact of harmonic components [68]. By taking harmonics into signal model, the algorithm can be designed to eliminate their influence, or even calculate the phasor of harmonics [66, 75]. Resampling or interpolation method adjusts the data window of DFT back to an integer times of the signal cycle, and DFT at this circumstance is immune to harmonics [57, 59].

For time domain algorithms, extending the signal model by including the decaying dc and harmonics is a good way to reject their influence on the estimation of the fundamental component [81, 87, 94, 99]. Furthermore, the parameters of decaying dc and harmonics can be estimated.

2.3.4 Dynamic Signal Model

When using phasor and frequency, some applications such as protections in power system, require fast measurement response. To achieve this goal, a method is to treat the phasor and frequency as the time-varying parameters instead of a constant in each estimation. Here we rewrite the equation (2.3):

$$x(t) = X_m(t) \cos(\omega_0 t + \phi(t)) \quad (2.40)$$

The magnitude $X_m(t)$ and synchrophasor $\phi(t)$ are treated as a time dependent signal. As a result, the estimation of each will not be a constant value, but a time dependent formula. This is a more generic form of signal. When $X_m(t)$ is a zero-order formula, the magnitude becomes a constant value. If $\phi(t)$ is a first-order polynomial function, its derivative is the frequency deviation. Only at this circumstance, the frequency can be calculated by the following equation with no error.

$$f = f_0 + \frac{\phi(t + \Delta t) - \phi(t)}{2\pi\Delta t}. \quad (2.41)$$

To solve these time-dependent formula, a commonly used method is Taylor series expansion. First rewrite the waveform using

$$x(t) = \text{Re}[a(t)e^{j\omega_0 t}], \quad (2.42)$$

where $a(t) = X_m(t)e^{j\phi(t)}$. Then implement Taylor expansion on $a(t)$ around the reference time t

$$a(t) \approx \sum_{k=0}^K \frac{1}{k!} a^{(k)} t^{(k)}. \quad (2.43)$$

Here K is the maximum derivative order of the Taylor expansion. Considering the $x(t)$ as a bandlimited signal, K is not necessary to be very large to ensure the Taylor error is negligible. Usually $K = 2$ is enough to represent the dynamic behavior of the signal, and $K = 1$ can be used for most steady state to decrease the computational complexity. This model was used by DFT method [124, 125], IpDFT [89], LMS method [89, 126], and is potential to be used in many others.

2.3.5 Hybrid

Each algorithm has its own advantage and disadvantage; therefore, it cannot beat every other method. However, combining multiple algorithms may generate a new one benefiting from the advantages of each.

Newton type method and PLL method usually need a few iterations to converge. With an accurate initial value, the convergence time can be minimized. Recursive DFT and zero-crossing can be used to estimate the amplitude and frequency respectively as the initial value for Gauss-Newton method [77, 83]. In [127] the DFT is used to obtain an initial estimation, then PLL algorithm is used to estimate phasor and frequency of fundamental, harmonics, and interharmonics components.

In DFT method, the correction of off-nominal effect usually needs the knowledge of the frequency deviation preliminary. Algorithm which estimates the frequency without the

knowledge of phasor, such as zero-crossing can be used to provide the frequency estimation [54].

In [70] and [56], the phase angle is calculated by DFT method, while LMS algorithm is use to obtain frequency and ROCOF, to eliminate the disturbance from noise.

Some methods use one algorithm as a filter, and another for estimation. In [103], DFT is used to extract the fundamental part of the signal, and Prony's method is implemented for estimation. In [39] PLL is used as a filter for zero-crossing method.

2.3.6 Other Techniques

When the PMU measures all the currents injecting into a bus, the Krichhoff's Current Law can be used as a constrain to improve the accuracy [128].

2.4 Performance Comparison

The accuracy, responding time, and computation complexity are important performance of the phasor and frequency estimation methods. An accurate algorithm provides the confidence for the applications which use the estimated phasor and frequency. Responding time is critical for time sensitive applications which require fast detection and operation. Computation complexity decides whether the estimation method can be realized easily in a specific hardware, and its cost.

2.4.1 Accuracy

Accuracy is one of the most important criterias to evaluate the phasor and frequency estimation methods. In the latest PMU standard, total vector error (TVE) are used to define the phasor error, defined as the following equation:

$$TVE(n) = \frac{|\hat{X}(n) - X(n)|}{|X(n)|} \quad (2.44)$$

In the standard, the requirement of accuracy is divided into two groups: steady state and dynamic state. In steady state, the TVE is required to be within 1%, and the frequency error to be less than 0.005 Hz. In dynamic state, the TVE should be less than 3%.

It is generally hard to give a complimentary comparison of accuracy among all the algorithms, since 1), not every reference applies the same testing, and only a few test following the synchrophasor standard; 2), the reporting rate each algorithm uses may be different, which influence the accuracy, especially in dynamic testing. Here the accuracy reported by references are generally compared in Table 2.1 to Table 2.3.

Table 2.1. Performance during steady state

Algorithms	Frequency Deviation (10% deviation except explained)		Harmonics	Inter-harmonics
	<i>Phasor</i>	<i>Frequency</i>		
Zero-crossing [38]	0.0314 rad for 2% Δf_0	-	-	-
DFT with optimized window [50]	0.2%	-	-	-
IpDFT [65]	0.03%	0.001 Hz	-	-
SWAM + DFT [68]	0.001%	0.000,5 Hz	-	-
DFT + post filter [69]	0.07%	0.002,5 Hz	0.005%, 2.8×10^{-15} Hz	-
ZC + IpDFT [54]	0.028%	0.000,4 Hz	0.035%	0.000,7 Hz
Adaptive filter DFT [53]	0.1%	-	0.02%	0.010,9 Hz
Smart DFT [66, 129] ¹	<0.001 pu, 0.001 degree	< 0.01 Hz	-	-
Clarke Transform DFT [70]	$2 \times 10^{-11}\%$	2×10^{-13} Hz	$9 \times 10^{-13}\%$, 1.1×10^{-10} Hz	1.146%
Newton method + LMS [78]	-	-	0.0013%, 0.000,2 Hz	-
PLL [94]	<0.5%	<0.1 Hz	-	12%
LMS [130]	-	1.289×10^{-9} Hz	-	-

1. 59.5 Hz for nominal frequency of 60 Hz

Table 2.2. Dynamic performance during modulation and frequency ramping

Algorithms	Amplitude Modulation (10% amplitude, 5 Hz)		Phase Modulation (0.1 rad, 5 Hz)		Frequency Ramping (± 1 Hz/s)	
	<i>Phasor</i>	<i>Frequency</i>	<i>Phasor</i>	<i>Frequency</i>	<i>Phasor</i>	<i>Frequency</i>
DFT with optimized window [50]	0.15	-	-	-	-	-
IpDFT [65]	1%	0.1 Hz	-	-	0.04%	0.001 Hz
Dynamic signal model + STFT [124]	0.059% (2 Hz modulation)	-	-	-	0.013% (2 Hz/s ramping rate)	-
DFT + post filter [69]	0.006%	0.000,35 Hz	0.004%	0.001,5 Hz	0.04%	0.000,268 Hz
Zero crossing + IpDFT [54]	0.45%	0.003 Hz	0.3%	0.08 Hz	0.03%	0.001 Hz
Adaptive filter DFT [53]	0.216%	0.000,018~0.016 Hz ¹	0.122%	0.004,034~0.008,013 Hz	0~0.7%	-
Smart DFT[66, 129] ²	-	-	< 0.01%	< 0.01 Hz	~0.1%	<0.01 Hz
Clarke Transform DFT [70]	0.025%	0.001,47	0.025%	0.001,47	0.028%	0.000,06
Newton method + LMS[78]	-	-	-	-	-	0.1 Hz
PLL [94] ³	1%	-	-	-	0.02%	-

1. 11% modulation

2. 1 Hz modulation frequency

3. 1% amplitude modulation with modulation frequency of 15 Hz

Table 2.3. Dynamic performance during step change

Algorithms	Amplitude Step Change (10% amplitude)				Phase Step Change (0.1 rad)			
	Overshoot	TVE Responses Time (sec)	Frequency Response Time (sec)	Delay Time (sec)	Overshoot	TVE Responses Time (sec)	Frequency Response Time (sec)	Delay Time (sec)
Zero crossing + IpDFT [54]	6.56%	0.028	0.082	0.002	5.77%	0.056	0.102	negligible
Adaptive filter DFT ¹	0~0.2443 %	0.0181~0.0651	-	0.01~0.04	0.0044~10.2772 %	0.0194~0.1785	-	0.01~0.45
PLL [94] ¹	10%	0.02	0.04	-	4%	0.02	0.03	-

1. The phase step change uses 10 degree

Zero-crossing method does not provide magnitude estimation, so TVE cannot be applied for evaluation. Reference suggested that the phase angle accuracy is equivalent to 3% TVE. The conventional DFT suffers from the frequency deviation. When the fundamental frequency is close to nominal value, the harmonics distortion is almost 0. Using window or filter, the error is decreased, but is still sensitive to the frequency deviation. Post filter and interpolation methods can generally eliminate this sensitivity, and provide good steady state performance. They also show good dynamic performance together with the adaptive filter method. The reported C37.118 compliance of Newton type method and LS method is rare. However according to the test, they show very good noise rejection performance, together with high accuracy during harmonics distortion. The PLL method shows good performance for both steady state and dynamic. However it is sensitive to interharmonics. Signal may need to go through a filters before being fed into the algorithm for estimation.

2.4.2 Estimation Speed

Estimation speed is another focus of the phasor and frequency estimation method performance. Especially when estimation is used for generator synchronous, system protection, and automatic control, responding time is a critical factor to influence the effectiveness and performance of applications.

The estimation speed depends on two parts: responding speed and group delay. The responding speed means when the change takes place in the input signal at timestamp t_0 , how long the change will be reflected in the estimation. The responding speed is mainly evaluated by the delay time in the standard. Some testing results are summarized in Table 2.3. The group delay refers to the delay between the input time of a sample and the output time of its corresponding estimation, ignoring the computation time. The reported group delay and comments are listed in Table 2.4.

Table 2.4. Group delay of algorithms

Algorithms	Reported Latency	Comments	Group Delay
Zero-crossing	-	The response delay could be half or one term, depending on the algorithm setting.	Long
Conventional DFT	-	The response delay could be half to several cycles, depending on the window size.	Long
DFT with optimized window [50]	-	Half cycle to one cycle.	Long
Adaptive filter DFT [53]	0.028~0.079 s group delay	The filter introduces group delay. The group delay of EKF is lower than FIR.	Long
IpDFT [65]	0.02 s	The IpDFT needs at least 3 bins for interpolation. Therefore, the window length is at least two cycles, result a minimum delay of one cycle.	Long
Dynamic signal model + STFT [124]	-	Needs 3 phasor from conventional DFT for calculation. Therefore the delay is one cycle and a half at least. Phase-shift is used to get the estimation of the report time, but that is based on the assumption that the phasor behavior is unchanged.	No delay if the phasor dynamic behavior unchanged; long otherwise.
SWAM + DFT [68]	-	Needs one cycle phasor from conventional DFT using shifting window for post-processing. The delay is one cycle more than conventional DFT.	Long
DFT + post filter [69]	-	Needs several phasor from conventional DFT for post filter process. The furthest is 5 estimation periods away. When using a shifting window, the minimum delay is 5 samples more than DFT.	Long
ZC + IpDFT [54]	0.1 s (M class) 0.03 s (P Class)	Latency is caused by zero-crossing algorithm for frequency estimation and interpolation. M class uses a longer window and results more latency.	Long
Smart DFT[66, 129]		Since the estimation needs phasor from several conventional DFT calculation, the delay is relatively large.	Long
Clarke Transform DFT [70]	0.039,2 s	Filter, quasi-Clarke transform, and DFT contributes the latency together.	Long
Newton method + LMS [78]	-	As long as the index is the last data of the window, there is no group delay.	Short
PLL [94]	-	No group delay for this algorithm.	Short
LMS [130]	-	As long as the index is the last data of the window, there is no group delay.	Short
Kalman	-	No group delay for this algorithm.	Short

Zero-crossing algorithm usually includes half cycle to one cycle delay, due to its intrinsic character. The estimation speed of DFT method mainly depends on the window length. Long window tends to average the dynamic change of input signal. Although it improves the noise immunity, it also decreases the responding speed. Furthermore, the estimated phasor and frequency usually corresponds to the center point of the window, so the group delay equals to half the window length. Pre and post filters also introduce the group delay. Similar to the DFT method, the responding speed of the Newton type method and LMS method also depends on the window length. Using forgetting factor can eliminate the average influence of the older samples. Furthermore, they can effectively eliminate the group delay as long as they are designed to estimate the phasor and frequency of the latest input sample. PLL method shows fast response speed, which generally depends on the coefficients it uses for estimation. There is also a trade-off between responding speed and overshoot. High responding speed usually brings large overshoot. Kalman filter and adaptive notch filters can have a fast response, but with a filtering delay, which is not a constant [124].

2.4.3 Computation Complexity

The algorithm complexity decides if it can be realized in most processors, and the cost of the estimation device. For each estimation, the data storage occupation, and the number of multiplications and additions are importation factors of complexity. A complex algorithm requires more storage space, and needs many calculations to be done within a specific time length. Therefore, the processor needs to provide abundant registers, multipliers, or higher clock rate. As a result, the available processors are limited, and the cost usually increases. For the wide area monitoring and the increasing requirement of distribution level awareness, the low cost sensors are needed for a high coverage density. The comparison of computation complexity and comments are listed in Table 2.5.

Zero-crossing algorithm uses very little hardware sources. However, since it is vulnerable to distortion and cannot estimate the magnitude, supplementary techniques are needed, and the complexity increase.

Conventional DFT is also a low computation algorithm. However, to improve its accuracy in off-nominal fundamental frequency input, filter, compensation or interpolation is added to the algorithm. The Kalman filter and interpolation usually cost a lot of computation resources. By using recursive form, the data window length has no influence on the computation complexity from the second estimation output.

The Newton type method and LS method include the pseudoinverse of matrix calculation, complexity of which is in square relation to the window length. Furthermore, the Newton type method usually needs several iterations for each estimation, and hence requires a higher speed of computation. The Hessian matrix can be simplified to a diagonal matrix so that the pseudoinverse of matrix can be transferred to non-matrix calculation. The recursive term can also be used to furtherly decrease the complexity.

Table 2.5. Computation complexity

Algorithms	Comments	Complexity
Zero-crossing	Filter and counter. For better performance, the filter is realized by PLL, or least square fitting.	Very low
Conventional DFT, DFT with window [50]	The computation effort of the recursive form is very small. $e^{-j\frac{2\pi}{N}(r-1)}$ can be calculated in advance and restored.	Low
Adaptive filter DFT [53]	Computation burden of EKF is significantly higher than FIR. The FIR is similar to conventional DFT.	Low for FIR High for EKF
IpDFT [65]	Computation burden is high, due to the requirement of at least 3 times of DFT, and interpolation. The enhanced method needs several iterations for better accuracy.	High
Dynamic signal model + STFT [124]	Using a look-up table, the computation burden is only a few more additions and multiplications than conventional DFT.	Low
SWAM + DFT [68]	The post-processing uses an average filter. Using recursive method, the computation complexity is very close to conventional DFT.	Low
DFT + post filter [69]	More complex than DFT due to the filters used before and after the DFT estimation. Average filter used before DFT uses a lot of additions since it works in high sampling rate.	Median
Zero crossing + IpDFT	Complex due to the combination of algorithm, filters, and interpolation, and compensation.	High
Smart DFT [66, 129]	The single tone term is relatively easy, since it needs only three phasor calculated by DFT. For signal with harmonics, the computation burden increases rapidly.	Low to high
Clarke Transform DFT [70]	The algorithm includes conventional DFT and LMS methods, together with three-phase signal generation, Clarke transformation and compensation.	High
Newton method + LMS [78]	Complexity of both Newton method and LMS depends on the data window length. Long data window increase the dimension of the matrix and hence the computation amount. Another factor of Newton method is the pseudoinverse of Hessian matrix. Using Jacobian matrix of simplified diagonal matrix can decrease the complexity. The third factor is the iteration for each estimation.	Median to high
PLL [94]	Very simple since it uses only the current input data instead of a data window.	Low
LMS [130]	Computation amount depends on the window length. Pseudoinverse of Jacobian matrix is also complex. Easier than Newton method since it needs only one iteration.	Median

The PLL algorithm uses only one input for each estimation, and stores only a few historical value for integration operation. Therefore, the computation amount and storage space are very small.

2.5 Proposed Area for Future Research

Estimation of phasor and frequency is the key technique for synchrophasor, which provides measurement data for a lot of wide area monitoring and control. It is also used for grid-connect converters and relays. The utilization and requirement of this technique will boost with the increasing concern of wide-area monitoring, automatic control, mega data for power system, high penetration of renewable energy, power energy storage, and microgrid. To fulfill the requirement of these applications, some of the key challenges and problems are summarized for future research.

- Noise exists in power grid voltage and current, including not only the white noise, but also decaying dc, harmonics, interharmonics, etc. With the increasing of converters used in the power grid, the noise intensity and types will become a big challenge for the phasor and frequency estimation technique, especially in the current measurement which is more vulnerable to noise distortion. Additionally, the

transducers which connect the measurement device and the power grid, and the device itself, may introduce noise. On the other hand, the requirement of the fast response to power system dynamic reduces the algorithms' noise tolerance. Although there is no requirement on the tolerance to multiple noise combination in the synchrophasor standard, it is essential for estimation algorithms to operate with enough accuracy during the noise distortion in reality.

- To provide effective information for power system monitoring and control, it is important to estimate the phasor and frequency during the power system disturbance, especially the transient, with a manner of fast responding speed and accuracy. This is a key challenge for the existing devices, since the estimation at the abrupt change of power system is usually with large error. To provide accurate estimation during the first swing of the transient will extend the resolution of power grid visibility and benefit for the system transient stability control and prediction.
- While more phasor and frequency estimation algorithms and devices are targeting the transmission level, the interest on distribution level and microgrid is increasing. For this application, more challenges are added compared to the transmission level. Generally, in distribution level and microgrid, there are higher level of noise and harmonics, and unbalanced phases. Sometimes single-phase measurement is required. Meanwhile, the small phase difference between voltage phasor of different buses demands higher phasor resolution, and microgrid usually requires the estimation to work in a wider frequency range due to the low inertia.

2.6 Conclusion

Phasor and frequency estimation is an important technology for power system sensors. It has been used for PMUs, power system synchronization, and relays. A variety of phasor and frequency estimation algorithms which have been proposed in the recent publications are reviewed in this chapter. The basic ideas of these methods are introduced, and the key techniques are discussed in detail. The methods are compared in terms of estimation accuracy, estimation speed, and computation complexity. Finally, some interesting areas for future research are proposed. As the modern power system evolving toward the smart grid, the increasing penetration of renewable energies and energy storage, and the development of microgrid, the phasor and frequency estimation will be applied to work in more severe conditions, and have a higher requirement on accuracy and speed.

CHAPTER 3 PMU ERROR IMPACT

3.1 Introduction

Synchrophasors, such as PMUs were developed to monitor and analyze power system behavior. These devices provide synchronized measurements for wide-area or local power system awareness in terms of phasor and frequency with high precision and time resolution. Many synchrophasor-measurement-based applications have been studied in recent years, including generator trip event detection and location, islanding detection and control, voltage stability, state estimation, model validation, dynamic line rating, et al [13, 17, 131-141].

To ensure the performance and reliability of the synchrophasor-based end-use applications, good quality of synchrophasor measurement data is needed, in terms of precise measurement, good synchronization, and fast and reliable network communication [142]. Frequency and phase angle, which are used by most of these applications, are subject to measurement errors from both internal and external factors, and the errors may affect the performance of applications or even cause them to fail. Measurement errors typically originate in the PMUs and the instrumentation channels which connect the high voltage transmission system and the PMUs.

Performance requirement of PMUs are specified in IEEE Synchrophasor Standard C37.118.1-2011 and C37.118.1a-2014 [33, 35]. In the standards, two performance classes of PMUs, namely the P and M class, are defined. The P class is intended for fast response, such as protection and the M class mainly for analytic measurements requiring good precision but allowing some reporting delay. Both classes have corresponding requirements for serial of tests, including steady state and dynamic state. The maximum allowed measurement error, such as total vector error (TVE), frequency error (FE), and rate of change of frequency error (RFE) are defined. The lab test of several PMU products and prototypes shows that there are noticeable inconsistency between commercial PMUs performance and the accuracy requirement specified in the standards [143].

Besides the synchrophasor device, another factor contributing to the measurement error is the instrumentation channels. The instrumentation channels, including instrument transformers, connecting control cables, and attenuators, are used to scale down the power system voltage and current to the levels proper for driving relays, fault recorders, and other monitoring devices such as synchrophasors [144]. Testing and evaluation reveal that instrument transformers could introduce phasor error [145]. The parameters of the components shift with time and subsequently cause error. Furthermore, the error becomes even larger during transients as their characteristics deteriorate at frequency deviates from the nominal frequency. The control cable which connects the instrument transformer and the attenuator also brings measurement error, as it brings time latency which is transformed into phase angle error. In addition, the cables are not normally “instrumentation class” wiring and their input could be influenced by the change of

burden (e.g., adding or replacing relays or other devices) [144]. The instrumentation channels error has not been specified by the synchrophasor standards [33, 35].

The synchrophasor measurement errors is a critical issue for synchrophasor-based applications. Without understanding how the measurement errors will impact the performance of various synchrophasor applications, the users cannot implement them for power system monitoring and operation confidently and effectively [146]. Some studies are conducted to reveal the influence of synchrophasor error on different applications. The investigations mainly focused on applications of state estimation [147-149], voltage stability assessment [150-153], and line fault and outage [154, 155]. However, quite a few synchrophasor-based applications, including those already running online, have not yet been evaluated. Furthermore, these existing works neglected the instrumentation channel error, and the synchrophasor errors are mostly represented by a fixed value or a zero-mean Gauss noise with a fixed standard deviation.

In this chapter, the impact of measurement errors on four different synchrophasor-based applications are evaluated. The measurement errors from both synchrophasors and instrumentation channels are taken into consideration. Specifically, the investigation mainly focused on the measurement errors of phase angle and frequency since they are used by most synchrophasor-based applications. Intuitively, the requirement of synchrophasor measurement accuracy may vary depending on the specific application algorithm. However, the synchrophasor standards did not consider the applications of PMUs as a factor to standardize the measurement accuracy, and this potentially could impede the applications of PMUs. In this work, four applications are evaluated as examples to compare the measurement error impact on different applications. All the possible measurement errors are studied to help the application developers and users understand the worst possible cases of each application.

The rest of this paper is structured as follows. The methodology is discussed in Section 3.2. In Section 3.3 the measurement errors from PMUs and instrumentation channels are discussed, and the assumption of measurement errors in this paper is given. Section 3.4 to 3.7 present the impact of the errors on four typical synchrophasor applications, namely power system disturbance location, oscillation detection, dynamic line rating and islanding detection. Section 3.8 concludes this chapter.

3.2 Methodology

To answer the question that how will the PMU error impact the related applications, two perspectives should be studied. The first is how much the error is, and how to evaluate it. The PMU measurement data used by different applications varies from one piece of data, to a cluster of data, to the continuous data streaming. Therefore, the data quality could include the data accuracy, availability, and the transmission delay. Here we specifically study the impact of data accuracy.

The data accuracy generally includes two parts: the transducer and the PMU itself. The transducer includes the instrumentation transformer which degrades the high voltage and current into the low range for measure, and the cable which connects the instrumentation transformers to the PMU. This type of error mainly depends on the type of the transformer and the length of the cable. The error from PMU itself is more complicated, it generally depends on the PMU hardware, the phasor and frequency estimation algorithm, and the accuracy of timing synchronous signal. The error from the algorithm usually differs on different input signal, i.e. dependent on the parameters of the voltage and current to be measured. Considering the number of models of commercial PMUs available in the market, and the tremendous possibility of the magnitude, frequency, and phase angle combination of the input signal, it is hard to give the measurement accuracy of all PMU models and all the scenarios of power system voltage and current. Considering the PMUs providing data for power system applications are supposed to fulfill the PMU standard, the largest error allowed by the standard can be used to as the maximum error to obtain the performance envelope of each application.

The second perspective is how to determine the impact of PMU measurement accuracy for a specific application? In order to produce accurate and credible results, real-time applications such as event location is likely to have more stringent requirement for measurement accuracy than slower applications such as frequency monitoring or off-line applications such as model reduction. Furthermore, the applications which generate quantified results are selected in order to compare the output using ideal data and data with error in a quantified way. To obtain the performance envelope of the applications under the influence of the measurement error, the worst case, defined as the errors in measurement that result in the application deviating to the greatest extent, is the target to be found out.

3.3 PMU Error Analysis

3.3.1 PMU Measurement Error

In IEEE Std. C37.118.1-2011[33], total vector error (TVE) is used to evaluate the measurement error of PMUs on amplitude and phase difference. According to IEEE Std. C37.118.1-2011, to evaluate the measurement error of PMUs on amplitude and phase difference, total vector error (TVE), defined in Eq. (3.1), is used.

$$TVE(n) = \sqrt{\frac{(\hat{X}_r(n) - X_r(n))^2 + (\hat{X}_i(n) - X_i(n))^2}{(X_r(n))^2 + (X_i(n))^2}}, \quad (3.1)$$

where $\hat{X}_r(n)$ and $\hat{X}_i(n)$ are the sequences of estimates given by the PMU under testing and $X_r(n)$ and $X_i(n)$ are the sequences of theoretical values of the input signal at the instant of time (n) assigned by the unit to those values.

According to this definition, a phasor angle error of 0.57° (0.01 radian) will cause 1% TVE, corresponding to a time error of $\pm 26 \mu\text{s}$ for a 60 Hz system, and $\pm 31 \mu\text{s}$ for a 50 Hz system. Meanwhile, the maximum steady-state frequency error is required to be less than 0.005 Hz. In reality, most PMUs show largest error during the dynamic inputs, such as frequency ramping and phase/magnitude modulation [69, 156]. Therefore, in the applications we investigated it is reasonable to assume that PMUs error could reach their largest corresponding range.

3.3.2 Transducer Error

The instrumentation channel refers to the circuit between the transmission system and the PMU. The instrumentation channel scales down the amplitudes of voltages and currents on the transmission system and passes to the attached PMU. Components on the channel usually include instrument transformers, cables, and attenuators, as shown in Figure 3.1.

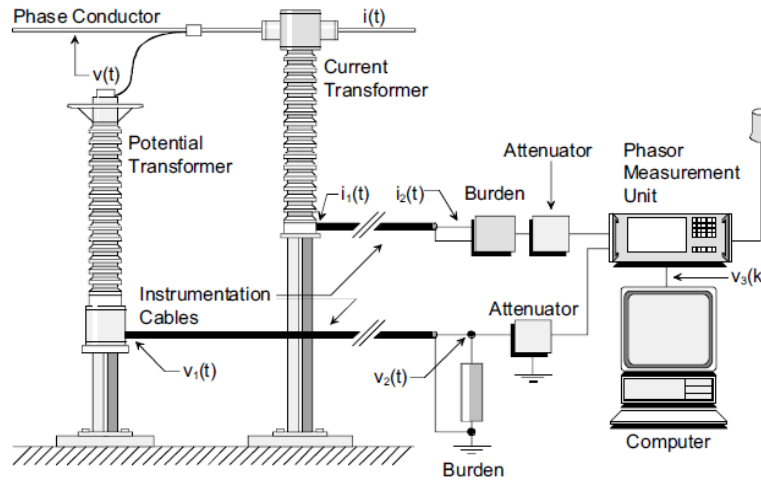


Figure 3.1. Typical instrumentation channel for a PMU [157]

An ideal instrumentation channel is supposed to output a waveform which is exactly a replica of the waveform scaled down from the high voltage power system [158]. However they are not ideal and introduce measurement errors.

The cable is the main contributor to instrumentation channel errors as the cable causes time delay that is then transformed into phase angle error. This delay is dependent on several characteristics of the cable, such as the cable material and if it is shielded. Typically a 500 ft. RG-8 cable introduces a 0.4° phase angle error. In some cases, the length of the cable can be 3,000 ft., which will cause a larger phase angle error [159]. Most used PMU transducers include current transformers (CTs), voltage transformers (VTs), and capacitive coupled voltage transformers (CCVTs). For American National Standards Institute (ANSI)-class type transformers, the maximum phase angle error allowed by the standard is between 0.26° and 2.08° , depending on the transformer type [159, 160]. Although the instrumentation channel error is generally consistent and can be

compensate, it is usually not calculated and eliminated in some installation procedures [161, 162].

3.3.3 Error Assumption

Worst-case measurement errors (measurement errors that result in the largest application errors) are conservatively assumed in the analysis for each application. For instance, the worst case PMU-based event location error locates an event in the farthest place from the actual event position.

The error range is determined based on the previous discussion. For the PMU, a phase angle error of $\pm 0.6^\circ$ and a frequency error of 0.005 Hz are used. The typical phase angle error caused by instrumentation channels varies from -0.2° to -1.0° [159, 163].

3.4 Event Location

3.4.1 Event Location Algorithm

Power system disturbance location is a PMU application used to detect and locate power grid disturbance events, such as generator loss and load shedding. The method is based on a geometrical triangulation algorithm using responding time to the disturbance from PMUs dispersed around the power grid. A disturbance in the power system, such as a generator trip or a load shedding event, causes instantaneous frequency and phase angle variations that propagate along the power network with finite and constant speeds [164]. Therefore, the variation of frequency and phase angle detected by each PMU has a unique time delay proportional to the distance from the disturbance location. Based on this, the location of the disturbance can be estimated. This application is used by the Frequency Monitoring Network (FNET) currently in service at the University of Tennessee in Knoxville and also by many electric utility operators [165]. FNET uses the frequency disturbance recorder (FDR), a single-phase distribution-level PMUs, to collect GPS timestamped voltage phasors and frequency measurements.

In the FNET/GridEye application, voltage phase angles measured by FDRs deployed in different locations are collected and processed. The angle plots are shifted to start from 0° and the slope of the plot before the event is de-trended to be 0. In this way, only the dynamic signature of different FDRs in reaction to the power system disturbance is reserved. The absolute value of these angles are then taken for event location. Figure 3.2 shows an example of phase angle movements caused by a generation trip.

Coordinated Universal Time (UTC) is used to indicate the time at which the event occurred. The legends show the names of the different FDRs used by FNET/GridEye. The red horizontal line represents the preset threshold. The earliest time when the angle measured by an FDR increases to this threshold is defined as TDOA. It can be seen from Figure 3.2 that the TDOAs of each FDR are different. The FDR with the smallest TDOA is assumed to be the nearest one to the generation trip location, the target position. A

circle with a 200-mile radius around this position is then established as the suspect area. Every suspected power plant and pumped hydroelectric storage unit within this area is then checked by linear regression with the data from the first six responding FDRs. The event plant is the plant with the least fitting residues [166].

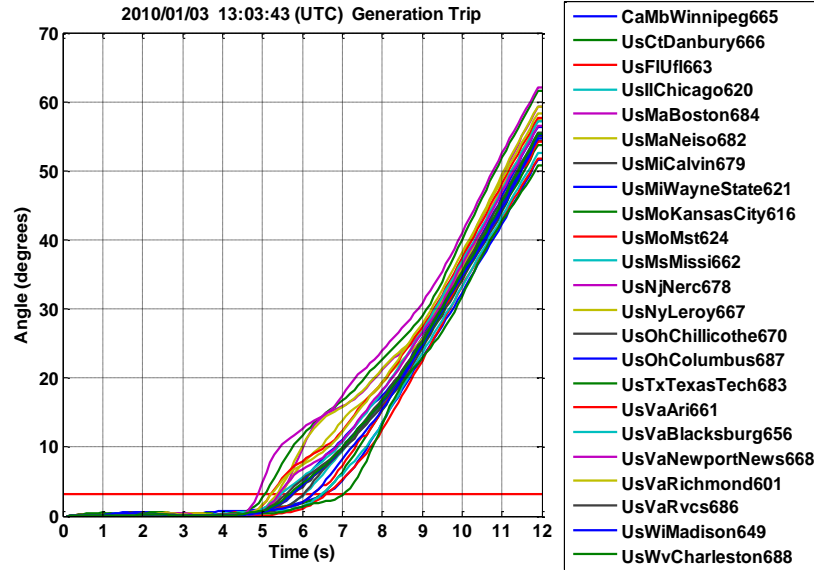


Figure 3.2. The processed phase angle curves measured by FDRs in a generation trip event.

3.4.2 Analysis and Result

Phase angle measurement errors may change the responding sequence of the FDRs. If the first responding FDR changes, the suspect area will change accordingly. If the new suspect area does not include the event location, the event location algorithm will fail. The impact of instrumentation channel error would be negligible in this case because consistent angle shifts are eliminated when relative angle values are calculated. For this analysis we assumed that for every single FDR, the measurement error that impacts the event location application is randomly distributed within a reasonable error band. Based on the assumption discussed in Section 3.3.1, $\pm 0.6^\circ$ was taken as the maximum measurement error band.

It is found in some cases that the phase angle curves are separated from each other by a relatively large interval. Therefore, the first responding unit is unlikely to change even with a $\pm 0.6^\circ$ error added. Phase angle (processed) of four generation trip events are plotted in Figure 3.3, with $\pm 0.6^\circ$ error band added to the first two responding units.

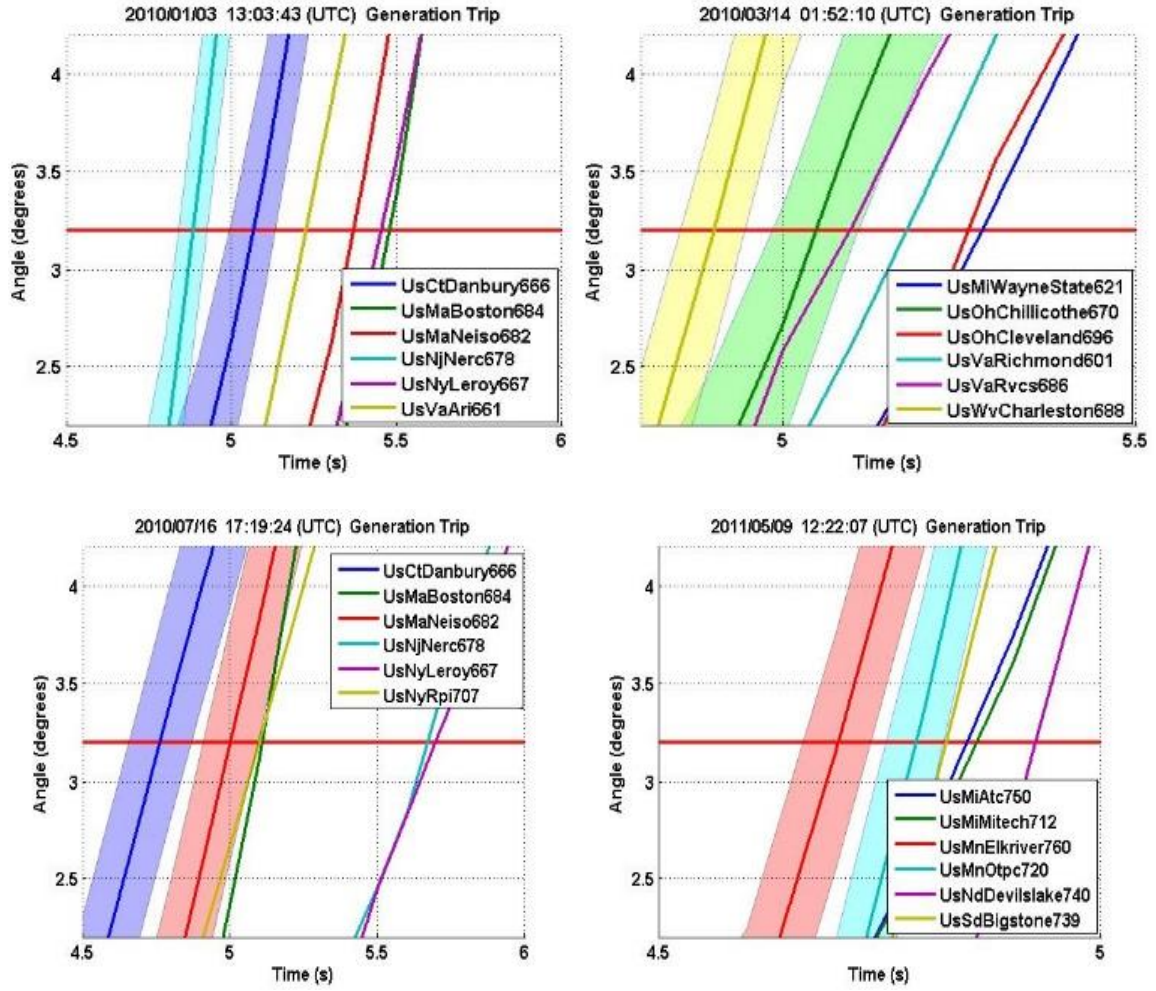


Figure 3.3. Phase angle curves of four generation trip events. The red horizontal line represents the preset threshold.

In spite of this, some cases still show that the event location has the potential to be impacted. A generation trip event that took place in West Virginia on 03/12/2010 is taken as an example and shown in Figure 3.4. In this event when $\pm 0.6^\circ$ error is added into the measurement result, the first responding FDR changed. The new ‘first responding FDR’ is 255 miles from the event location. Because of this, the event location is out of the suspect area and the event location algorithm will then fail.

The phase angle data of events in a year were investigated, and the tolerance to phase angle errors of each event was found. According to the statistic result shown in Figure 3.5, more than 55% of the event has phase angle tolerances larger than $\pm 0.6^\circ$, hence they are unlikely to be influenced by the measurement error. However, the remaining 45% are likely to produce erroneous results. If the accuracy of PMU is improved to $\pm 0.1^\circ$, 90% of the event locations will not be influenced by the measurement error.

3.5 Oscillation Detection

3.5.1 Oscillation Detection Algorithm

Small signal stability problems in the power grid can cause significant electromechanical oscillations that may lead to grid reliability issues and potentially large-scale blackouts. High-precision and time-synchronized frequency and phase angles measured by a PMU can be used for oscillation detection.

Here the angle-based inter-area oscillation detection is used as an example [167]. In this application, relative angle measurements of each PMU are obtained by subtracting a reference PMU’s measurement and shifting to start from 0° . These angle measurements remain stable when the system is operating in the steady state. During an inter-area oscillation, the relative angles form a wavy curve. If the oscillation magnitudes (peak-to-peak value, P2P) of more than one PMU exceed a certain threshold and sustained for at least one swing, an oscillation will be considered to occur. The threshold uses empirical values and is different for each power grid.

3.5.2 Analysis and Result

Similar to the event location, $\pm 0.6^\circ$ was taken as the maximum measurement error for each measurement unit. Therefore the relative angle error ranges from -1.2° to $+1.2^\circ$. For an oscillation event, the P2P with error could be smaller than the threshold, and the oscillation will not be detected. On the other hand, if a nonoscillation signal is impacted by the measurement error, and the variation magnitude is larger than the threshold, it will be recognized as an oscillation and cause a false alarm.

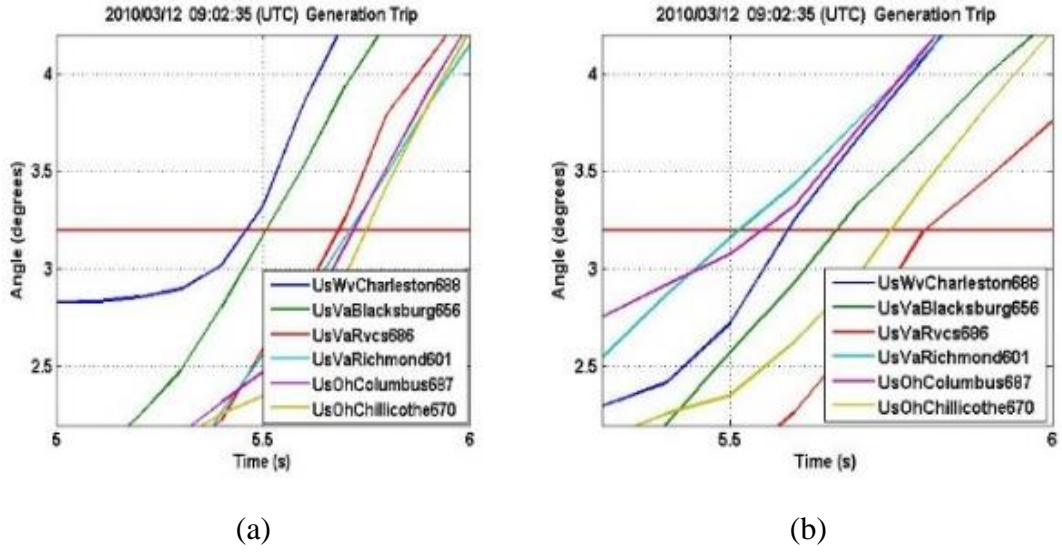


Figure 3.4. Phase angle curves of a generation trip. The red horizontal line represents the preset threshold. (a). No error added; (b) $\pm 0.6^\circ$ error added.

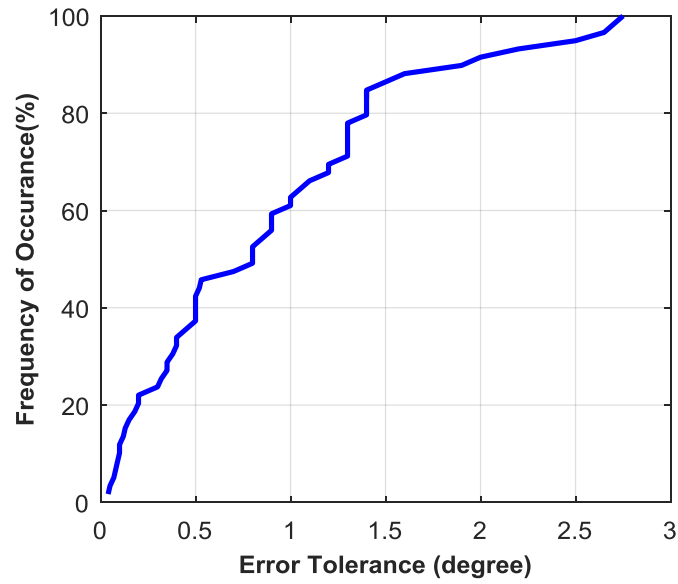


Figure 3.5. Cumulative distribution plot of phase angle tolerance in one year.

A real oscillation case in Eastern Interconnection (EI) is shown in Figure 3.6 with a 1.2° error band. The threshold for detecting oscillation in the EI is set as 3° . The oscillation magnitude is about 4° ; therefore it will be detected. However, accounting for the measurement error, the angle difference could decrease to 1.5° which is below the threshold – the oscillation would not be detected.

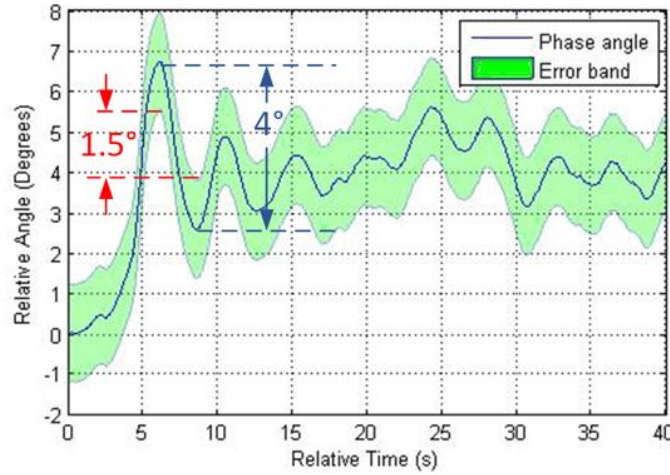


Figure 3.6. Phasor measurement unit error impact on oscillation signal.

3.6 Dynamic Line Rating

3.6.1 Dynamic Line Rating Algorithm

The rating of a transmission line indicates the highest current that the line can transfer safely and securely. Currently, the ampacity of the transmission lines are generally determined by conservative seasonal estimations of meteorological values [168]. Dynamic line rating (DLR) technology is developed to calculate this ampacity at each time unit of operation. The application of DLR can dynamically increase the transmission capacity and effectively use the thermal capacity of the transmission line (assuming there are no stability limits), especially for the overhead transmission lines. As intermittent renewable energy sources puts stress on the existing infrastructure of the power system, DLR provides a solution to accommodate the surge in installation of distributed/renewable energy sources whereas minimize or postpone the high cost power network enforcement [168].

PMU measurement data on both ends of a transmission line can be used to dynamically calculate the rating of that line. One method based on IEEE Standard 738-2012 is used here as example [140, 169, 170]. The procedure is shown in Figure 3.7. The detailed algorithm is given in Appendix A

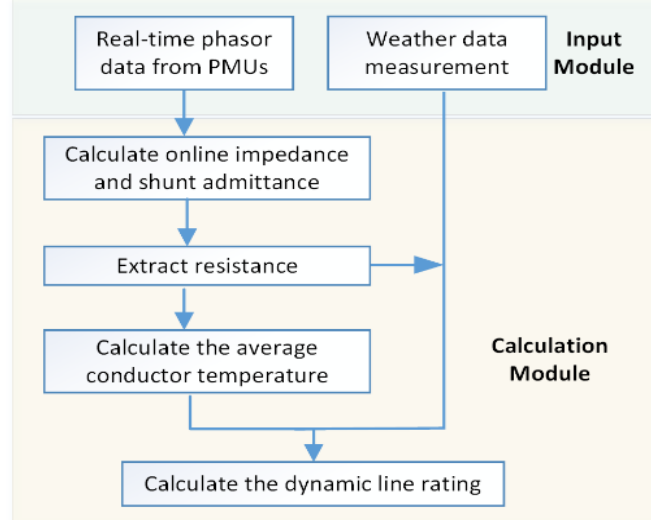


Figure 3.7. Overall framework of phasor measurement unit (PMU)-based dynamic line rating technology.

The PMU measurement error will induce uncertainty in the estimation of the transmission line parameter. Here we only consider the phase angle error as an example, which includes $\pm 0.6^\circ$ error from PMU and -1.0° to -0.2° error from instrumentation channel. In this studied case, the conductor of the transmission line is the 26/7 Drake aluminum conductor, steel-reinforced (ACSR) conductor. The configuration and the parameters of the conductor are based on [170]. The DLR model in this system is assumed to refresh every 10 min.

3.6.2 Analysis and Result

The effect of PMU measurement error depends on the weather condition. For the consistent weather parameters of ambient temperature, wind speed, and solar heat gain remain at 30°C , 1 m/s, and 12 W/m, respectively, the DLR error can be up to 27% when measurement error is introduced. The DLR error is also evaluated under various weather conditions. The result of one-day in summer is shown in Figure 3.8. In this figure, the red-circle line represents the true value of DLR, and the red shadow represents the error band. The green, brown, and purple dashed curves are the ambient temperature, wind speed, and solar heat gain, respectively. According to the calculation, the maximum error in summer with high wind speed reaches 46%. For a case with lower temperature and wind speed, the maximum will decrease to approximately 22%.

The relation between maximum DLR error and measurement error for a low temperature and wind speed day is shown in Figure 3.9. From this figure it can be seen that to limit the maximum DLR error within 10%, the PMU error should be kept within $\pm 0.1^\circ$. If the instrumentation channel error can be eliminated (e.g., by calibration), the requirement of PMU accuracy could be relaxed to $\pm 0.3^\circ$. This is an effective way to improve the

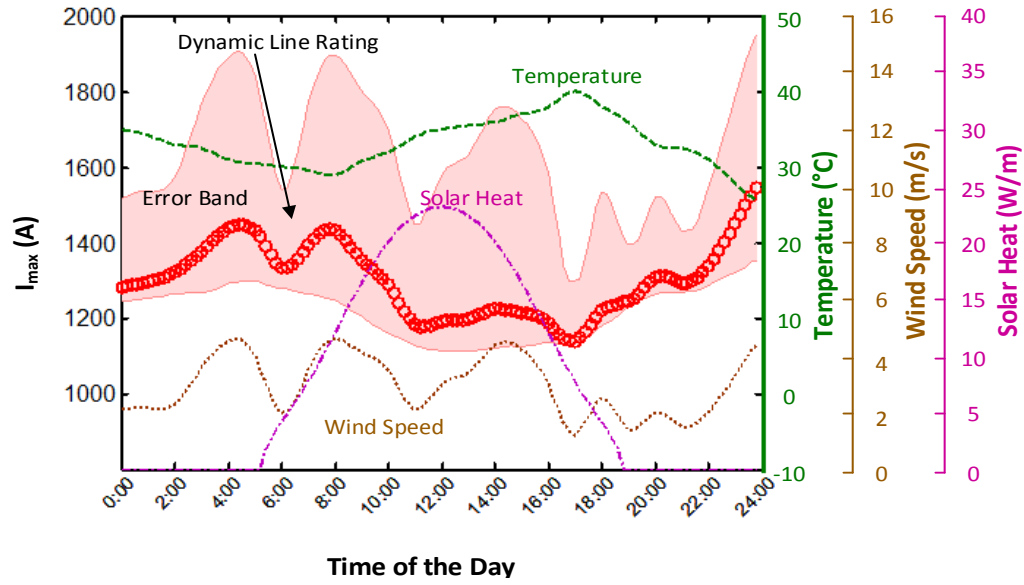


Figure 3.8. Dynamic line rating error on 1 day in summer.

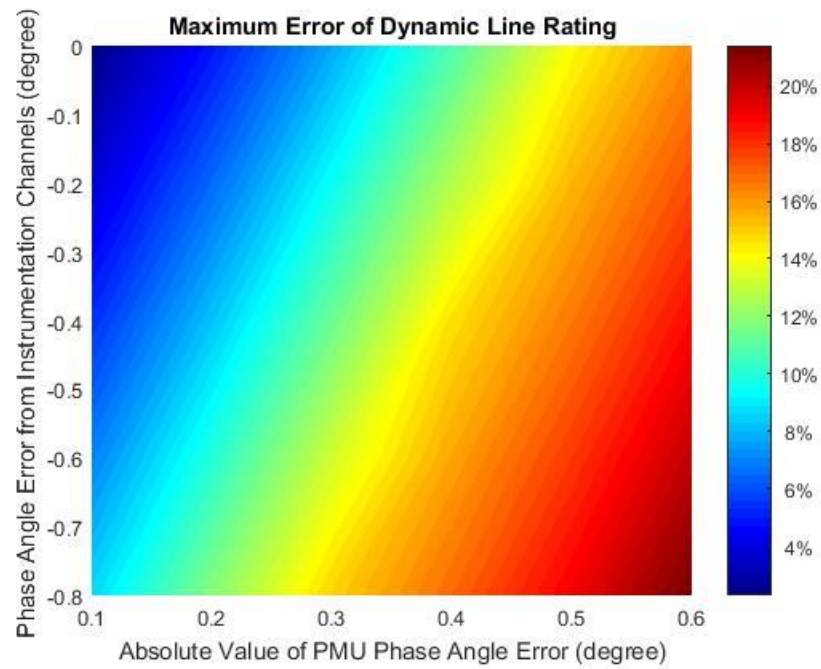


Figure 3.9. Maximum DLR error respect to PMU phase angle error and instrumentation channel phase angle error in a low temperature and wind speed day. The error is in percentage. PMU error is positive and negative boundary.

accuracy of the dynamic line rating. It should be noted that these examples are obtained from a basic method and are not intended to give a specific DLR error boundary.

3.7 Islanding Detection

3.7.1 Islanding Detection Algorithm

Distributed generation (DG) sources, which use fuel cells, photovoltaic, and other electricity generation technologies, are typically placed close to the load being served [171]. The advantages of DG are well known. However, there are some technical challenges associated with the use of DG. One of them is islanding, the situation where part of a distribution system becomes electrically isolated from the remainder of the power system while continuing to be powered by DG sources. Electrical islands are difficult to sustain and typically result in loss of service to the loads. They can also threaten the safety of line workers if the workers are not aware that the circuit is energized. Reconnecting the island to the larger system requires that both are in synchronous, but the DG sources often cause them to drift out of phase. Therefore, it is very important to detect islands quickly in order to reconnect them before the generation and load become unbalanced and the load is lost.

PMUs capture the characteristics of frequency and phase angle change during the creation of the island in a fast and accurate manner. Using PMUs in islanding detection is therefore promising. Here we take the frequency measurement based islanding detection method used by FNET/GridEye as an example [17]. In this algorithm, frequency deviations (FD) for all the FDRs are calculated by

$$FD_i(t) = |f_i(t) - f_{\text{ref}}(t)| \quad (3.2)$$

where $f_i(t)$ is the measured frequency value of the i th FDR at timestamp t and $f_{\text{ref}}(t)$ is defined as the median value of all the monitored FDRs in the same interconnection. The integration of frequency deviation (IOFD) is defined as the accumulation of the FD over a certain time, given by

$$IOFD_i = \sum_{t_1}^{t_2} FD_i(t) \quad (3.3)$$

where t_1 and t_2 are the start time and end time, respectively, for this integration time period. IOFD is used to prevent the algorithm from false alarm. For example, an abnormal frequency data point far away from the actual value will generate a large FD. Also, during a generation trip event, the grid remains intact yet the frequency in some locations may oscillate while dropping. If FD is the only criterion, this kind of phenomenon could be incorrectly recognized as an islanded situation.

When the FD_i of any FDR surpasses the first threshold, F_{th1} , an early warning is triggered, indicating possible islanding. Then $IOFD_i$ is calculated over a time period and

compared to the second threshold, F_{th2} . If it is over F_{th2} , the algorithm indicates that the system monitored by this FDR is in off-grid operation. Otherwise, the system is concluded to not be islanded.

3.7.2 Analysis and Result

When measurement error is combined with the frequency, the result of FD_i and $IOFD_i$ will be influenced, causing the islanding detection algorithm to fail to detect an island or to incorrectly indicate an islanded situation when no island exists. To demonstrate islanding detection errors, cases were selected and data collected by FDRs were fed into the algorithm to verify that the algorithm is functioning correctly. Frequency errors are then manually added to the data and the new detection result is compared with the original one to identify the impact caused by measurement error.

One case studied happened during Hurricane Sandy in 2012. During that time an FDR in Sussex, New Jersey, detected the off-grid operation. The frequencies are plotted in Figure 3.10. In the experiment, errors within ± 5 mHz are added to the data. However, due to the large frequency deviation, the added errors were not large enough to cause the islanding detection algorithm to fail. Further analysis shows that the islanding detection will not fail until the frequency error is larger than ± 0.35 Hz.

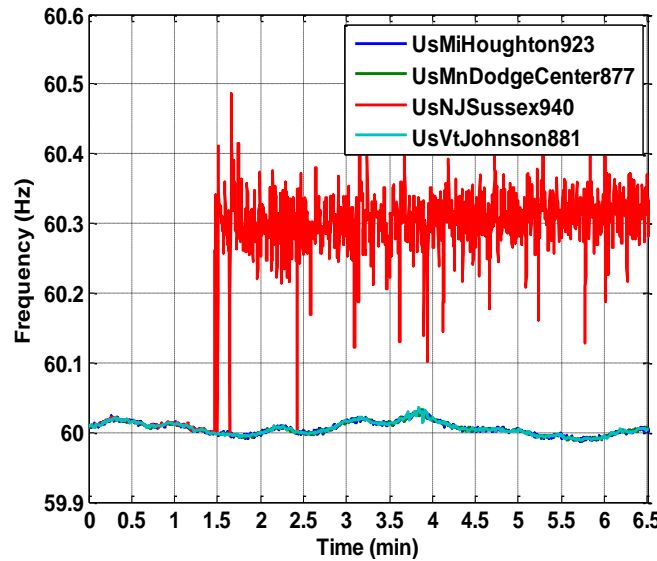


Figure 3.10. Frequency measured by frequency disturbance recorders in the Hurricane Sandy case shows the Sussex FDR operating in an island.

Several other cases were also studied by adding frequency errors and changing the integration time. The islanding detection time of this algorithm mainly depends on the integration time for calculating IOFD. Analysis shows that the ± 5 mHz error does not influence the detection accuracy on detection time of 30 s, 4 s, and 2 s. Measurement errors may affect the detection accuracy if shorter detection time is required.

3.8 Conclusion

In this chapter, the impact of synchrophasor measurement errors on several typical applications is analyzed. The measurement errors from both PMU device itself and instrumentation channel are considered. The conclusions are summarized in Table 3.1.

It can be seen from the table that the disturbance location and dynamic line rating application are vulnerable to measurement errors. As for oscillation detection, the detection could fail due to the errors. Moreover, a non-oscillation case could be mistakenly detected as an oscillation case. Islanding detection is generally robust but can be affected if the detection time is less than 2 s.

Table 3.1. Effect of worst-case measurement errors on synchrophasor-based applications

Application	Effect of Worst-Case Measurement Error	Likelihood
Disturbance location	Some cases show impact	45% are vulnerable
Oscillation detection	Possible failure to detect oscillation or incorrectly alarm when no oscillation exists	Threshold dependent
Dynamic line rating	Potential to induce very large error	Very sensitive
Islanding detection	Not likely to be influenced for detection time above 2 s	Detection time dependent

The PMU errors used in this study were the maximum errors permitted by IEEE Std. C37.118.1-2011 and IEEE Std. C37.118.1a-2104. The authors note that 1), most commercially-available PMUs, as well as the FDRs from UTK/ORNL, operate at much higher levels of accuracy; 2), the error impact could change if different application algorithms are used. However, this chapter studies the worst-case with errors allowed by the IEEE Standard in order to ensure the users know the worst case results of applications driven by phasor measurements.

CHAPTER 4 PMU ERROR MODEL

4.1 Introduction

Phasor Measurement Units (PMUs) were developed to monitor and analyze power system behavior. These devices provide a way to monitor a wide-area power system with very high precision, in both distance and time, due to the high precision and time synchronization of the data they produce. Compared to traditional power system measurement devices such as SCADA, PMUs provide accurate frequency and phasor measurement of voltage and current in a considerably fast data rate. Meanwhile, these data are synchronized by using precise timing sources such as Global Positioning System (GPS). Therefore, it provides the potential for a number of power system applications including monitoring, protection, and control. Many PMU-measurement-based applications have been developed to provide larger visibility and better control and stability for the power system, including state estimation, event location, model validation, oscillation detection and damping control, et al [13, 138, 166, 172-174].

Many PMUs have been installed in power plants and substations to provide data for the control center, and applications are increasingly been developed for power grid operation, analysis, and planning by using the PMU data. However, PMU data arriving the applications are often influenced by measurement and data transmission, and therefore include estimation error, data loss and delay [159, 175, 176]. They are potential to affect the accuracy and trustworthiness of the applications [169]. Without fully understanding the impact of the PMU data quality on applications, users may lack confidence to use an applications in the power system, especially for real-time control.

Performance and communication requirements of PMUs are specified in IEEE Std. C37.118.1-2011, C37.118.2-2011, and C37.118.1a-2014 [33, 34, 177]. Measurement compliance with the PMU standard requirements is confirmed by input signals defined in the standard into the PMU devices under testing. The compliance includes several tests which can be attributed into two categories: steady state and dynamic. A lab test on the performance of ten prototype and commercially available PMUs was conducted by National Institute of Standards and Technology (NIST). The result reveals that at least eight of them do not pass all the test [143]. In real applications, the PMU data quality could be further impacted by factors including current and potential transformer error, time synchronization accuracy, intrinsic error in the PMU device over time, high communication traffic, etc. All these suggest that there is no guarantee that different PMU-based applications would perform satisfactorily. The impact of PMU data quality is an important application issue.

PMU Application Requirement Task Force (PARTF) is formed to quantitatively determine the acceptable data quality of PMU data input into power system applications. To fully evaluate the PMU-based applications and find out the acceptable data quality, a framework tool is being developed to test applications using datasets with known data qualities. It will be able to generate both ideal and impaired data by simulating actual

power system events, and analyze the output of application fed with ideal and impaired data. The application of this framework tool is shown in Figure 4.1.

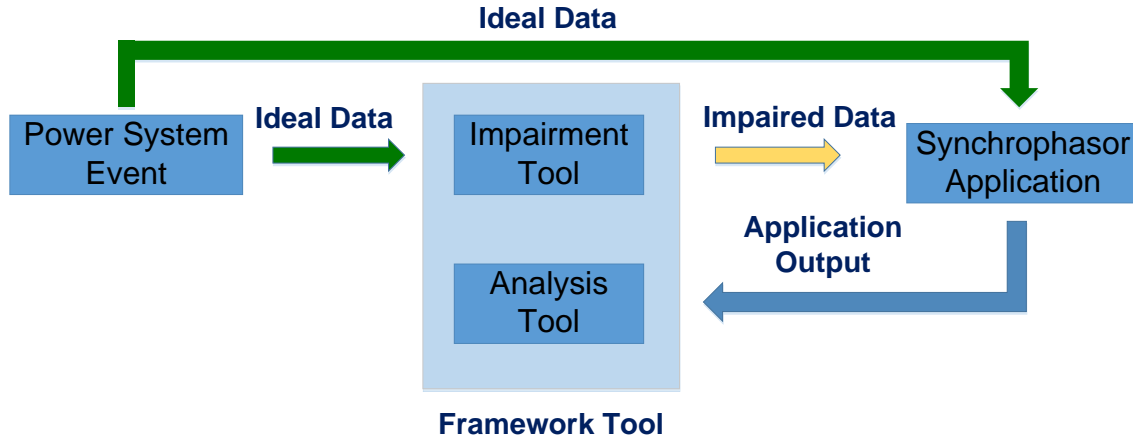


Figure 4.1. The application of the framework tool to evaluate synchrophasor

The impairment tool is to simulate the behavior of real PMU estimation and communication, and generate impaired data with the input of ideal data and the parameter of the PMU type and configuration. To realize this tool, one part of the work is to model the PMU estimation error. Factors influencing PMU errors such as the PMU type, data rate, nominal frequency/voltage, and phase angle are necessary to be parameterized in the impairment tool.

The structure of this paper is arranged as follows. Section 4.2 states the methodology to construct a model of PMU impairment. The data used for modeling is introduced in 4.3. The detailed modeling results of the Reference Signal Processing Model introduced in IEEE C37.118.1-2011 Annex C is presented as an example in Section 4.4 and 4.5.

4.2 Methodology

To simulate the estimation behavior of a real PMU and export the impaired data in a same manner of the PMU, it is essential to understand how the real PMUs' estimation error behaves under different inputs. The real inputs of PMU vary infinitely, but they can generally be divided into two groups: steady state and dynamic. The former indicates the situation in which the magnitude and frequency of the input signal remain unchanged, whereas in dynamic situation, at least one the parameters changes over time, such as the ramp of system frequency or the step changes in magnitude or phase angle.

The PMUs are first tested following the measurement compliance required in PMU standard C37.118.1-2011 [33]. The procedures and the requirement of testing equipment including test signals, timing reference, result calculations, and test system calibration, are provided in IEEE Synchrophasor Test Suite Specification [163].

Using the testing result, the estimation error of each PMU is obtained. Due to the difference of phasor estimation algorithm and implemented hardware, the estimation error behaviors are inconstant among PMUs of different class (P class and M class) and from different manufactures. Furthermore, for a specific PMU product and class, the estimation error behaviors vary depending on the nominal frequency and reporting rate. To ensure the model is able to cover all the behavior of the PMUs, the specific error behavior models are first set up for each specific product model, class, nominal frequency and reporting rate, and then the relation among them are concluded to set up generic models.

According to the test, the steady state models include frequency range, magnitude range, harmonic distortion and out-of-band interfering signals (interharmonics); the dynamic models include phase modulation, amplitude modulation, phase step change, amplitude step change, and frequency ramp change. In each test, there are four measurements, therefore each model includes four outputs, i.e. magnitude, phase, frequency, and rate of change of frequency (ROCOF).

For each part of the model, curve fitting and theory analysis are used to set up a reasonable, accurate, and simple model. Each model is in the form of algebra equations which are able to cover as much inputs as possible with outputs accurately representing the real PMU error. Meanwhile, the equations are transformed to the concise form to lower the computation burden.

4.3 Data

A lot of commercial PMUs and PMU algorithms are tested by National Institute of Standards and Technology (NIST) according to the IEEE C37.118.1-2011 standard [33, 143]. For each tested model, it includes one or both of the M class and P class. M here standards for measurement, and M class PMUs, with high precision and noise rejecting characters, are mainly used for analysis. On the other hand, P stands for protection, and P class PMUs are intended for applications requiring fast response, so they are with low measurement delay. For each class, the PMUs can work in different data reporting rate. Since the class and reporting rate highly influence the parameters used by the algorithm, the performance of PMU depends on these parameters. In the test, different combinations of class and reporting rate are treated separately, and the full test is repeated on each available combination.

As tested according to the standard, the input testing signals can be divided into two groups. The first group uses steady state signal as input. Here steady state indicates that the parameters to be estimated by the PMU, including phasor, frequency, and rate of change of frequency (ROCOF) are constant. Each subgroup of the steady state is explained below.

- (1) Frequency range: the frequency of the input signal is in different values ranging around the nominal frequency. The magnitude and phase angle remains unchanged.
- (2) Magnitude range: the magnitude of the input signal is in different values, while the frequency and phase angle remains unchanged.
- (3) Harmonics distortion: a single harmonic component is mixed into the input signal
- (4) Out-of-band interference: a signal whose frequency exceeds the Nyquist rate for the reporting rate is mixed into the input signal

In the dynamic test, one or several parameters of the input signal changes over time. Each subgroup of the dynamic state is explained below.

- (1) Frequency ramp change: the frequency of the input signal ramps respect to the time. The ramp rate is ± 1 Hz/s.
- (2) Amplitude modulation: the amplitude is modulated by a sinusoidal signal with different modulation frequencies. The modulation magnitude is 10%.
- (3) Phase angle modulation: the phase angle is modulated by a sinusoidal signal with different modulation frequencies. The modulation magnitude is 10 rad.
- (4) Amplitude step change: the amplitude of the input signal takes a step change
- (5) Phase angle step change: the phase angle of the input signal takes a step change

4.4 Result: Steady State Error Model

4.4.1 Frequency Deviation

As an initial work of this research, we studied the estimation impairment *behavior* of M class PMU algorithm provided in C37.118.1-2011 and amended in C37.118.1a-2014 [33, 177]. The modeling method is explained on the scenario in which both nominal frequency and reporting rate are 60 Hz. Here the frequency range model is used as an example to demonstrate the approach of modeling.

In this frequency range test, the input signals are at nominal magnitude at the frequency range from 55 Hz to 65 Hz with an increase of 0.1 Hz. The voltage magnitude error of phase A is shown in Figure 4.2.

Analysis suggested that the magnitude error behaves like a cosine waveform over time, shown in (4.1).

$$|V|_{err} = a_{1F} \cos(2\pi f_{verr}t + \theta_F) + a_{0F} \quad (4.1)$$

The frequency and magnitude of the waveform depends on the frequency of input signal. The constant magnitude error when input frequency equals to the nominal frequency can be considered as a cosine waveform whose frequency equals to 0 (producing a DC offset). Observation suggests that the frequency of the magnitude error over time can be represented by the formula below.

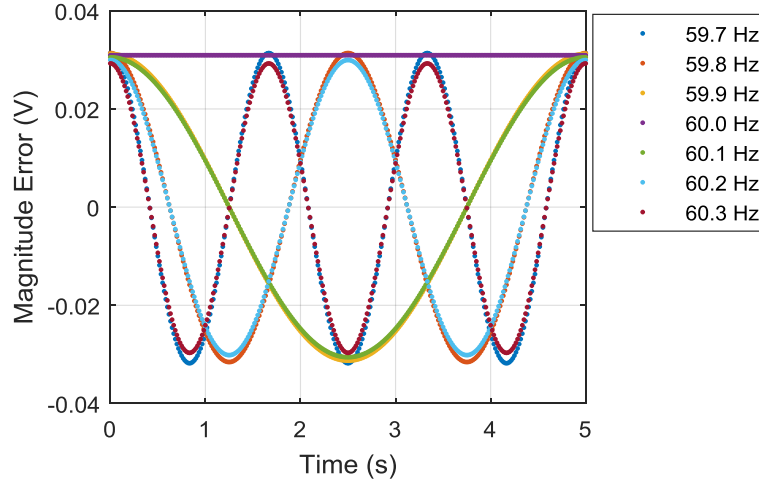


Figure 4.2. Voltage magnitude error of phase A in frequency range test

$$f_{verr} = 2 \cdot |f_0 - f| \quad (4.2)$$

Here f_{verr} is the frequency of the magnitude error, f_0 is the nominal frequency, and f is the frequency of the input signal. Using sinusoidal curve fitting on each group of testing data, the magnitude, initial phase angle, and the offset are obtained.

The magnitude a_{1F} is fitted by a sinusoidal function for all three phases. The fitting curve is shown in Figure 4.3.

$$a_{1F} = 0.03163 \sin(2\pi/11.6 \cdot (f - 56.7)) \quad (4.3)$$

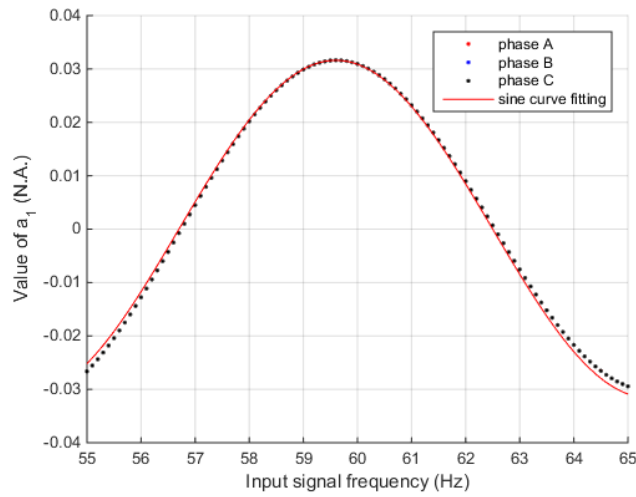


Figure 4.3. Fitting of magnitude a_1 using sinusoidal function

The offset a_{0F} is less or equal to 0, and the envelope is similar to the frequency response of the filter. Therefore, the offset a_{2F} can be described by (4). $|V|_{in}$ is the voltage of the input signal, and $|H(e^{j\omega})|$ denotes the frequency response of the filter. It fits well with the data points, shown in Figure 4.4.

$$a_{0F} = |V|_{in}(|H(e^{j\omega})| - 1) \quad (4.4)$$

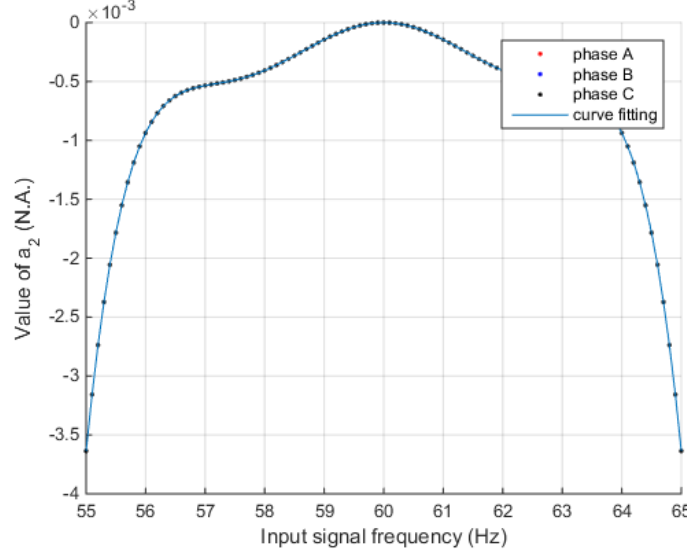


Figure 4.4. Fitting of offset a_2

Denote θ_0 as the initial phase angle of the input signal in each phase. In this test, $\theta_0 = 0, -2\pi/3$, and $2\pi/3$ for phase A, B, and C, respectively. The θ_F of each phase equals to θ_0 when $f < f_0$ and $-\theta_0$ when $f > f_0$. To simplify the model, f_{err} in (4.2) is changed to

$$f_{verr} = 2 \cdot (f_0 - f), \quad (4.5)$$

hence θ_F constantly equal to θ_0 .

Since the dependency (V_{in} , f , θ_0 , etc.) of the parameters used in the steady state frequency range tests are discrete, it is important to ensure the obtained model is generic for all the cases. In this model, there are only three values for the initial phase angle θ_0 . Further investigation using more values reveals that θ does not simply follow $\theta = \theta_0$ when θ_0 is value other than $0, -2\pi/3$, or $2\pi/3$. Instead, the generic equation should be amended to (4.6).

$$\theta_F = -2\theta_0 \quad (4.6)$$

Combining with the magnitude error of current, the magnitude error can be represented by

$$|X(t)|_{err} = a_{1F} \frac{|X|}{|V_0|} \cos(2\pi f_{err}t + \theta_F) + a_{0F}. \quad (4.7)$$

Here $|X|$ is the magnitude of the input signal, $|V_0| = 70$, and a_{1F} , a_{2F} , f_{err} and θ_F can be obtained from (4.3)-(4.6).

Similarly, the phase angle error is also modeled, and can be described by (4.5), (4.8)-(4.10).

$$\phi_{err}(t) = b_{1F} \cos(2\pi f_{verr}t + \delta_F) \quad (4.8)$$

$$b_{1F} = 0.02589 \sin(2\pi/11.6 \cdot (f - 56.7)) \quad (4.9)$$

$$\delta_F = -2\theta_0 - \pi/2 \quad (4.10)$$

The absolute value of frequency error and ROCOF error are less than 4×10^{-6} and 1×10^{-10} , respectively, hence they are deemed as 0.

When the reporting rate or the PMU class changes, the model remains unchanged but parameters a_{1F} , a_{0F} , b_{1F} , and b_{0F} will change accordingly. This is because the filter and window of the PMU are chosen according to the assigned reporting rate, and these parameters are influenced by the filter response.

4.4.2 Magnitude Deviation

The magnitude error in voltage and current is constant in magnitude range test. The error value is linearly dependent on the magnitude of the input signal, shown in Figure 4.5.

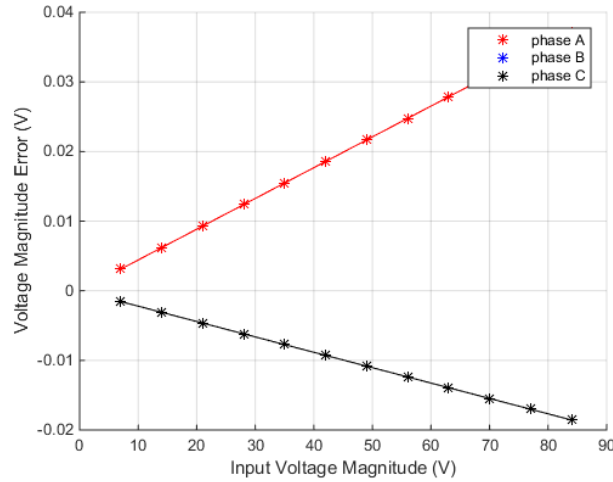


Figure 4.5. Voltage magnitude error in magnitude range test

The magnitude error can therefore be represented by

$$|X(t)|_{err} = (a_{1M}|X| + a_{0M}) \cos(2\theta_0). \quad (4.11)$$

The phase angle error is irrelevant to the magnitude of input signal, and can be calculated by (4.8). The frequency and ROCOF error of magnitude range are 0.

4.4.3 Harmonics Distortion

The magnitude, phase, and frequency error during harmonic distortion are constant over time, and do not show obvious relation between harmonic orders. Without loss of generality, they can be represented in (4.12)-(4.14). Coefficients $a_H(i)$, $b_H(i)$ and $c_H(i)$ can be referred to Table 4.1. ROCOF error is 0.

$$|X|_{err} = \frac{|X|}{|V_0|} \cdot a_H(i) \cdot \cos(2\theta_0) \quad (4.12)$$

$$\phi_{err} = b_H(i) \sin(-2\theta_0) \quad (4.13)$$

$$f_{err} = c_H(i) \quad (4.14)$$

Table 4.1. Coefficients of error in harmonics distortion

Harmonic order (i)	2	3	4	5	6	7	8
$a_H(i)$	6.8e-4	0	6.8e-4	-5.3e-4	0	-5.3e-4	6.6e-4
$b_H(i)$	0.028394	0.023691	0.024181	0.024455	0.025959	0.026307	0.025877
$c_H(i)$	-0.00137	0	0.00137	0.00082	0	-0.00082	0.00055

4.4.4 Interharmonics Distortion

The error of out-of-band interfering signals (interharmonics) are more complicated. Some magnitude error is shown in Figure 4.6. Generally it includes two parts:

- (1) The error caused by the fundamental component. It can be represented by a sinusoidal function $a_{I0} + a_{I1} \cos(2\pi f_{err}t + \theta_{I1})$, which is similar to the result in frequency range test.
- (2) The error caused by the interaction between the fundamental and interharmonic component. It can be described by two components: the sum and the difference of the two frequencies. The function can be represented by $a_{I2} \cos[2\pi(f - f_I)t + \theta_{I2}]$ and $a_{I3} \cos[2\pi(f + f_I)t + \theta_{I3}]$. Notice that these two components can overlap each other when the reporting rate is a factor of the fundamental frequency. E.g., when $f = 60 \text{ Hz}$, $f_I = 29 \text{ Hz}$, and reporting rate $f_s = 60 \text{ Hz}$, both components will be aliased to 29 Hz .

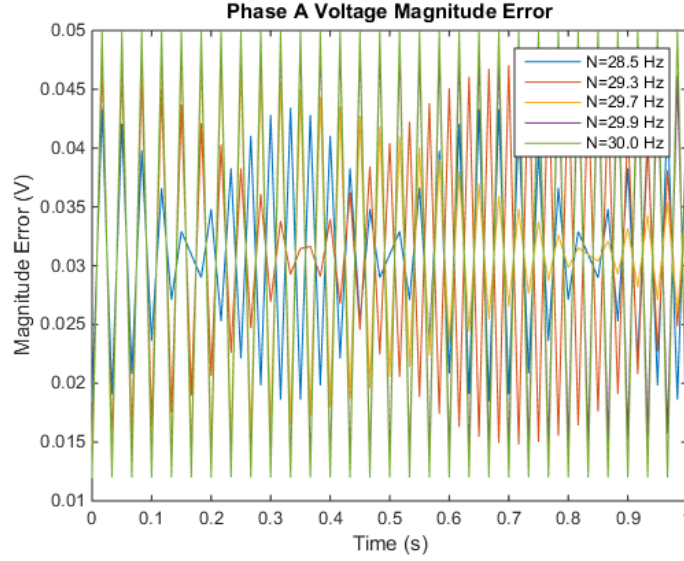


Figure 4.6. Voltage magnitude error in interharmonics test

4.5 Result: Dynamic Error Model

4.5.1 Frequency Ramp Change

The magnitude and phase angle error behavior in frequency ramp is shown in Figure 4.7. The algebra equations of magnitude and phase angle error are very similar to the error of frequency range described in (4.7) and (4.8), except the input signal frequency should be changed to the ramping frequency. Similarly, the frequency and ROCOF error are 0.

$$|X|_{Rerr} = a_{R1} \frac{|X|}{|V_0|} \cos[2\pi \cdot 2(f_0 - f_{ini} - 0.5R_f t) - 2\theta_0] + a_{R0} \quad (4.15)$$

$$\phi_{Rerr} = b_{R1} \cos[2\pi \cdot 2(f_0 - f_{ini} - 0.5R_f t) - 2\theta_0 - 0.5\pi] \quad (4.16)$$

Here f_{ini} is the initial value of frequency and R_f is the frequency ramping rate.

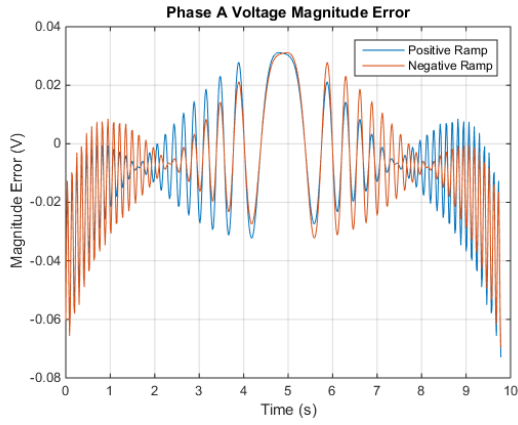
4.5.2 Amplitude Modulation

The magnitude and phase error in the amplitude modulation can be represented by a sinusoidal function whose frequency equals to the modulation frequency, i.e.

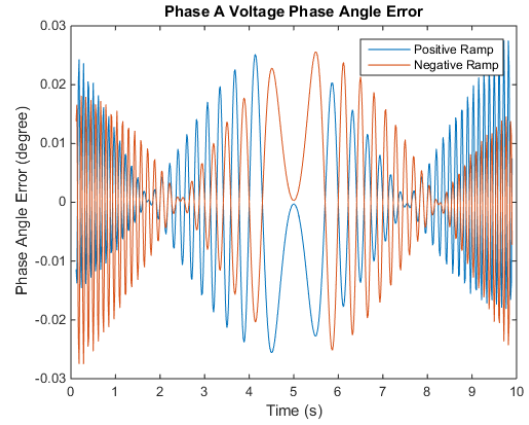
$$|X|_{err} = \frac{|X|}{|V_0|} (a_{AM1} \cos(2\pi f_m t + \theta_{AM1}) + a_{AM0}), \quad (4.17)$$

$$\phi_{err} = b_{AM1} \cos(2\pi f_m t + \delta_{AM1}) + b_{AM0}. \quad (4.18)$$

The frequency and ROCOF error are 0. The magnitude error is shown in Figure 4.8.



(a)



(b)

Figure 4.7. (a) Magnitude and (b) phase angle error in frequency ramp test

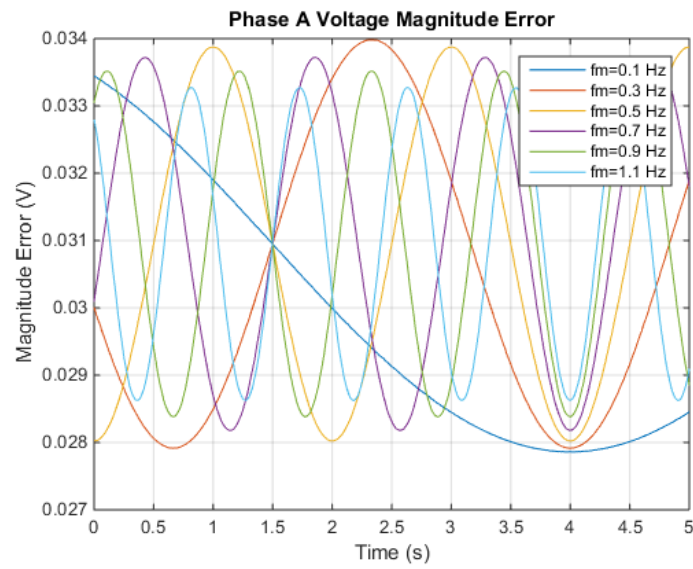


Figure 4.8. Voltage magnitude error in amplitude modulation test

4.5.3 Phase Modulation

Error in phase modulation is similar to the amplitude modulation in the term of including a sinusoidal component whose frequency equals to the modulation frequency. In addition, the magnitude error shows a double frequency component $a_{PM2} \cos(2\pi \cdot 2f_m t + \theta_{PM2})$, and the frequency and ROCOF show a triple frequency component $c_{PM2} \cos(2\pi \cdot 3f_m t + \zeta_{PM2})$.

$$|X|_{err} = \frac{|X|}{|V_0|} (a_{PM1} \cos(2\pi f_m t + \theta_{PM1}) + a_{PM2} \cos(2\pi \cdot 2f_m t + \theta_{PM2}) + a_{PM0}) \quad (4.19)$$

$$\phi_{err} = b_{PM1} \cos(2\pi f_m t + \delta_{PM1}) + b_{PM0} \quad (4.20)$$

$$f_{err} = c_{PM1} \cos(2\pi f_m t + \xi_{PM1}) + c_{PM2} \cos(2\pi \cdot 3f_m t + \xi_{PM2}) \quad (4.21)$$

$$ROCOF_{err} = d_{PM1} \cos(2\pi f_m t + \varepsilon_{PM1}) + d_{PM2} \cos(2\pi \cdot 3f_m t + \varepsilon_{PM2}) \quad (4.22)$$

4.5.4 Amplitude Step Change

In the step change test, the error behaves like the true value passed through the filter. An example is the magnitude error during amplitude step change, shown in Figure 4.9.

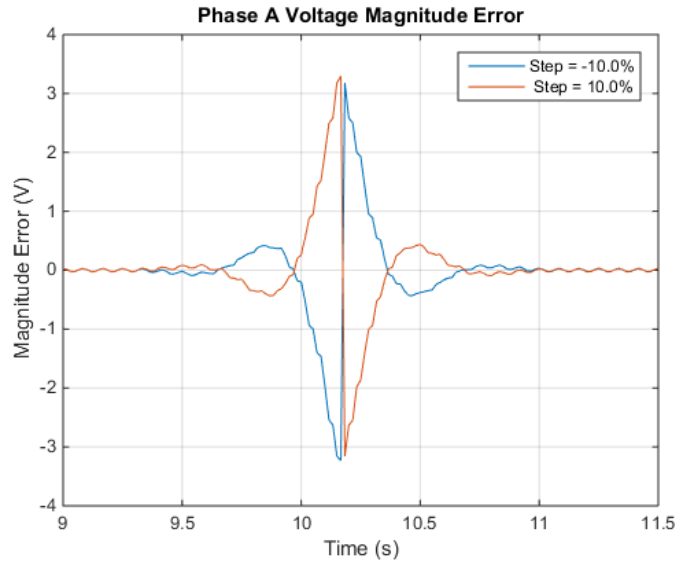


Figure 4.9. Voltage magnitude error in amplitude step change test

Therefore, the convolution of the true value and the impulse response of the filter is used to describe each error. For the magnitude error of amplitude step change, and the phase angle error of phase step change, the true value is represented by the sum of their Fourier

series in a finite order. The magnitude error and phase angle error during angle step change are represented by

$$\begin{aligned} |X|_{err} &= |X|_{step} - c \cdot u(t) \\ &= c \cdot |X| \left(\sum_{i=1}^{250} \frac{2}{\pi} \cdot \frac{1}{2i} \cdot \sin \left(2\pi \cdot \frac{2i}{16} \cdot t \right) \cdot |H(e^{j\omega})| + 0.5 \right) \\ &\quad + |X| - c \cdot u(t), \end{aligned} \quad (4.23)$$

$$\begin{aligned} \phi_{err} &= c \cdot \left(\sum_{i=1}^{250} \frac{2}{\pi} \cdot \frac{1}{2i} \cdot \sin \left(2\pi \cdot \frac{2i}{16} \cdot t \right) \cdot |H(e^{j\omega})| + 0.5 \right) + \theta_0 \\ &\quad - [c \cdot u(t) + \theta_0]. \end{aligned} \quad (4.24)$$

Here c is the step size, $u(t)$ is the step function, and θ_0 is the phase angle before step change. The frequency and ROCOF error are 0.

4.5.5 Phase Step Change

Phase angle error during phase step change can also be represented by the convolution of the true value and the impulse response of the filter.

$$\begin{aligned} \phi_{err} &= \phi_{step} - [c \cdot u(t) + \theta_0] \\ &= c \cdot \left(\sum_{i=1}^{250} \frac{2}{\pi} \cdot \frac{1}{2i} \cdot \sin \left(2\pi \cdot \frac{2i}{16} \cdot t \right) \cdot |H(e^{j\omega})| + 0.5 \right) - c \\ &\quad \cdot u(t) \end{aligned} \quad (4.25)$$

For phase step change, the frequency error is represented by the impulse response of the filter, and the ROCOF error is the differentiation of the frequency error.

$$f_{err} = \sum_{i=1}^{250} \frac{2}{\pi} \cdot \frac{1}{2i} \cdot \sin \left(2\pi \cdot \frac{2i}{16} \cdot t \right) \cdot |H(e^{j\omega})| \quad (4.26)$$

$$\begin{aligned}
ROCOF_{err} = & \frac{600}{1.1} \\
& \cdot \left[0.54 \right. \\
& \cdot \left(\frac{\cos\left(2\pi \cdot \frac{2F_{fr}}{F_{sampling}} \cdot n\right)}{n} - \frac{\sin\left(2\pi \cdot \frac{2F_{fr}}{F_{sampling}} \cdot n\right)}{2\pi \cdot \frac{2F_{fr}}{F_{sampling}} \cdot n^2} \right) \\
& - 0.46 \\
& \cdot \left(\frac{\cos\left(2\pi \cdot \frac{2F_{fr}}{F_{sampling}} \cdot n\right)}{n} - \frac{\sin\left(2\pi \cdot \frac{2F_{fr}}{F_{sampling}} \cdot n\right)}{2\pi \cdot \frac{2F_{fr}}{F_{sampling}} \cdot n^2} \right) \\
& \cdot \left(\frac{2\pi n}{N} + \pi \right) + 0.46 \cdot \frac{\sin\left(2\pi \cdot \frac{2F_{fr}}{F_{sampling}} \cdot n\right)}{2\pi \cdot \frac{2F_{fr}}{F_{sampling}} \cdot n} \cdot \frac{2\pi}{N} \\
& \left. \cdot \sin\left(\frac{2\pi n}{N} + \pi\right) \right]
\end{aligned} \tag{4.27}$$

The ROCOF error and the curve fitting are shown in Figure 4.10.

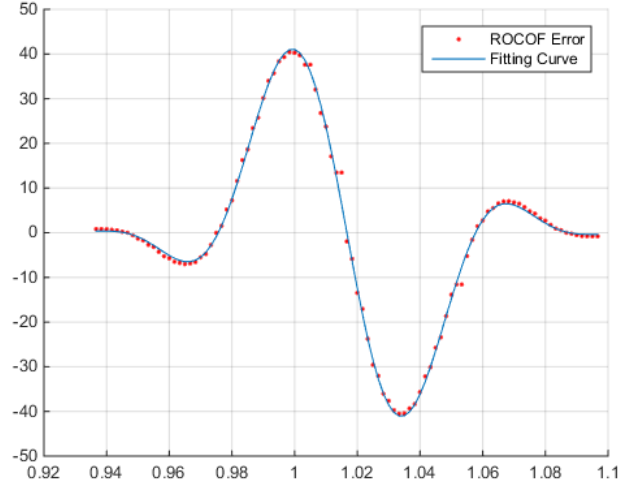


Figure 4.10. ROCOF error and curve fitting in phase step change test

The time interval of step change equals to the window size. Beyond this interval, the input is steady signal and the error behaves the same as during the steady state.

4.6 Discussion

According to the modeling of the PMU measurement error behavior during different working conditions and inputs, several findings can be concluded.

- (1) Much of the measurement error behaves like or includes sinusoidal waveforms over time. This is mainly due to the spectrum leakage and the finite attenuation of the filter. The unattenuated signals therefore, are aliased into the passband of the PMU.
- (2) The filter plays an important role in the accuracy of the PMU algorithm. Generally, a narrower bandwidth filter is able to reject out-of-band interference and improve the accuracy. However, a wider bandwidth filter is required when the fundamental frequency varies in a larger range, such as a low inertial system.
- (3) For phase angle and frequency measurements, which are unique for PMU, are vulnerable to phase modulation and phase step change.

4.7 Conclusion

This chapter investigates the estimation error of PMU. The model of PMU impairment is set up based on the analysis of PMU error in different inputs. Based on analysis and comparison of the PMU error between different PMU types, working conditions and inputs, the model shown in this paper is specific to the IEEE Std. C37.118.1 Annex C reference signal processing model and can be made generic and parameterized by studying the errors of other models of PMUs. It is able to describe the measurement error behavior of PMU in different classes and working parameters. The simulation shows the model fits the real measurement error behavior of the reference signal processing model in time domain when input different kinds of signals. The model is also described using concise algebra equations, which makes it computationally attractive, and simple for implementation. It can be used to simulate the real PMU and generate impaired measurement data for PMU-based application verification in a simple and fast way. The model can also be used for power system simulation which requires accurate PMU models. This method is useful for applying error to ideal data for the purpose of studying PMU application response to PMU error. This work also led to a better understanding of the effect of filtering on PMU error which will result in a future paper on that topic.

Further work is to make the model more generic by focusing on the error due specifically due to the PMU filter. That work will be followed by investigating errors associated with frequency tracking and adaptive filter PMU algorithms.

CHAPTER 5 PMU ACCURACY ANALYSIS

5.1 Introduction

First introduced in 1980s, synchronized phasor measurement units (PMUs) have now become a mature technology and are capable of realizing many applications related to power systems [178]. PMUs are devices which sample voltages and currents through power and current transformers. The devices then estimate the voltage and current phasors referenced to the timing signal from global positioning system (GPS). The phasors are time-stamped using GPS time and transmitted through network. Based on their accurate measured data and synchronized network, many PMUs deployed in a wide area are connected together and able to estimate the status of the whole measured power system. This wide area measurement system is capable of power system stability monitoring, post-mortem analysis, adaptive protection and control, etc. Currently, PMUs are utilized in state estimation, linear optimal control, oscillation control, adaptive protection, event location, dynamic line rating, etc. [142, 179].

Frequency disturbance recorder (FDR) is another kind of synchrophasor, which is based on distribution line measurement. This instrument is low cost and rapidly deployable. These features provide the possibility to build the North American Power Frequency Monitoring Network (FNET/GridEye) [180]. FNET/GridEye measures synchronized results, including frequency, phase angle and voltage, from different places around North American. It is able to aware the system situations and identify significant disturbances based on these data [17, 166, 181].

The wide-area measurement can be utilized to estimate the state, detect the event and protect the power system. Many measurement-based applications have already been developed and implemented. However, all these applications require specific accuracy. If the measurement error is beyond the accuracy limitation, the application may generate fault results or even fail. Therefore, it is essential to know the accuracy of synchrophasors, especially the phase angle and frequency.

In this chapter, the frequency and phase measurement accuracy limitation of synchrophasors is obtained by analyzing the frequency and phase error sources, and synchrophasor algorithm. The analysis results give the theoretical limitation of measurement accuracy and the contribution from each error source. Meanwhile, it provides information to evaluate how accuracy the measurement-based applications could obtain.

5.2 Accuracy Limitation Analysis

Generally, the factors that limit the measurement accuracy can be divided into instrument internal source and measured signal source. The former includes time reference inaccuracy, algorithm flaw and device error. The latter refers to the distortion in the measured power signal. Two main distortions are considered in this research: white noise

and harmonics distortion. Others are usually much smaller than these or could be easily filtered, thus are not considered in this chapter.

5.2.1 Error Source Analysis

5.2.1.1 Time Reference Error

Global Positioning System (GPS) is usually used to provide the time reference for synchrophasors, taking the advantage of its accuracy and synchronicity [159]. The pulse per second (PPS) signal, which is supplied by most GPS receivers, provides a high precision 1 s periodical signal whose rising edge is aligned to the Coordinated Universal Timing (UTC) second boundary. This feature enables the wide-area measurement of PMUs to obtain a precise and synchronized frequency reference. However, this PPS signal is not ideal in reality, due to the transmission delay between GPS satellites and receiver, and the interferences and noise on the receiver. Its rising edge is shown in Figure 5.1 as an example.

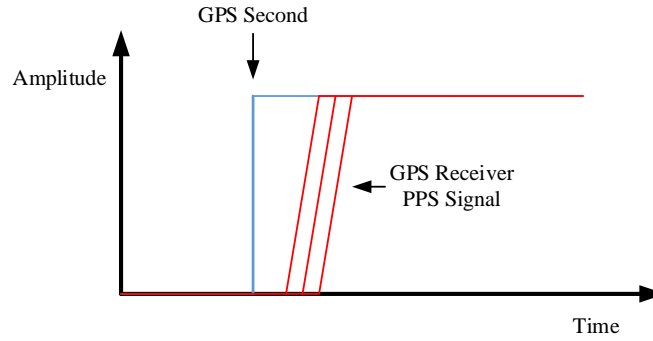


Figure 5.1. GPS PPS signal output

Due to the imperfect of GPS system, GPS receiver, and the disturbance introduced during the GPS signal transmission, the actual PPS signal generated by the GPS receiver includes an error from the edge of UTC second boundary. Regarding this error, two measures of the signal should be considered: accuracy and precision. Accuracy means how close the signal rising edge is to the actual UTC second boundary, or the time shift error. The effect of the time shift error is finally transferred into the phase angle error following the relation

$$\theta_{err} = 2\pi f t_{err}, \quad (5.1)$$

where θ_{err} is the phase angle error derived from the time shift error, f is the power system frequency, and t_{err} is the time shift error. The magnitude is not likely to be influence by this error. The frequency, which is usually calculated by the differentiation of phase angles, will not be impacted either, since θ_{err} is a quasi-constant value regarding to the time.

The time shift error includes the GPS system error and the GPS receiver error. The former indicates the time error between GPS time and UTC time. According to the GPS performance standard and report, it is required to be within 40 ns in 95% time, and in reality it is within 10 ns [182]. This error derives mainly from two sources: the time error of atomic clocks on GPS satellites, and the error in estimating the GPS signal transmitting delay. Considering PMUs in a small geographical area, the GPS satellites locked by the PMUs are generally the same, and the transmitting delay are very close to each other. Therefore, they suffer almost identical time shift error, resulting the same phase angle error. As phase angles are usually used by subtracting the reference angle which is measured on the swing bus, the error is eliminated. For the PMUs deployed in a wide area, this error cannot be ignored. For the GPS receiver, there can often be a few microseconds off from the actual GPS timing, but this error is usually fixed for a given firmware thus can be calibrated and ignored.

Precision is how much the PPS signal edge changes from one second to the other. This change is also called the PPS jitter. The GPS satellite geometry, signal conditions, drift and variation of the oscillator, as well as the internal circuitry of the GPS receiver all contribute to the jitter [183]. Due to the uncertainty of trace delay, interference and oscillator precision, the GPS jitter varies and cannot be eliminated by calibration.

The PPS signal is utilized by PMU as a frequency reference. Sampling of ADC in PMU are aligned and referred to the PPS signal. Usually it can be represented by

$$\frac{1}{f_s} = T_s = \frac{t_{PPS}}{N} \quad (5.2)$$

where f_s is the sampling frequency, T_s is the sampling period, t_{PPS} is the time interval between two neighboring PPS rising edges with a nominal value of 1 sec, and N is the nominal factor determined by the desired sampling frequency. For example, for the desired sampling frequency of 1,440 Hz, N is set to be 1,440. Notice that N is subject to change in some algorithm to improve the accuracy, but it is still calculated under the assumption that $t_{PPS} = 1$ sec [184].

When the PPS jitter exists, an error is introduced to the sampling frequency, thus transferred into the error of phasor and frequency. For most approaches, the measured frequency is proportional to the sampling frequency, i.e.

$$f_x = M f_s \quad (5.3)$$

f_x refers to the measured frequency, and N is the proportion between them. Consider the error of reference frequency, there is

$$f_x + e_x = M(f_s + e_s). \quad (5.4)$$

Here e_x is the frequency measurement error, and e_s is the error of sampling frequency. Therefore, the relative error of measurement result and reference are equal.

$$\frac{e_x}{f_x} = \frac{e_s}{f_s}. \quad (5.5)$$

Given e_t as the jitter of PPS, there is

$$\frac{e_s}{f_s} = \frac{e_t}{1+e_t}. \quad (5.6)$$

$$e_x = \frac{e_t}{1+e_t} f_x. \quad (5.7)$$

Usually the actual frequency of the signal is approximately equal to the nominal frequency, and the jitter is much smaller than 1 second, therefore the frequency error can be calculated by

$$e_x = e_t f_0. \quad (5.8)$$

f_0 represents the nominal frequency.

The phase angle is calculated by

$$\theta = \frac{t}{T_0} \cdot 360^\circ, \quad (5.9)$$

in which θ is the phase angle, t is the measurement time and T_0 is the nominal period. Therefore the phase angle error caused by GPS is

$$e_\theta = 360^\circ T_0 e_t. \quad (5.10)$$

5.2.1.2 Algorithm Error

A synchrophasor measurement algorithm is used to estimate phasor and frequency of power grid signal. Approximations are often utilized by the algorithm for processing simplification and realizable, thus bringing in error. Filter is usually implemented to suppress noise from the power line and the instrumentation channel. Its influence on synchrophasor measurement accuracy should also be considered. Besides the error introduced by algorithm itself, many other error factor, such as noise and harmonics, introduce different level of error depending on the algorithm used by the synchrophasor. Therefore, algorithm is an important factor to be considered for PMU accuracy analysis.

5.2.1.3 Device Error

Device error refers to the error caused by the instrument hardware, including internal noise, analog-to-digital (ADC) error, rounding error, etc. Here the ADC error is considered as the main error source. When an analog signal is sampled and converted to

digital signal by ADC, the continuous values of voltage are rounded to their nearest digital value due to the resolution and accuracy of the ADC, thus error is brought. Furthermore, the offset and nonlinear error of ADC are also added into the total ADC error.

5.2.1.4 White Noise

White noise is inevitable in the real world, nor easily filtered thoroughly. The intensity of noise is evaluated by signal-to-noise ratio (SNR), which is defined as the ratio of the signal power to the noise power and given in the form of logarithm by the following formula

$$SNR_{dB} = 10 \log_{10} \frac{P_{signal}}{P_{noise}}. \quad (5.11)$$

White noises of different SNR levels in actual power grid are added to the signal, and their impacts on accuracy are obtained by simulation.

5.2.1.5 Harmonic Distortion

Harmonic distortion is one of the major noise in the power system, and it affects the accuracy of frequency and phase angle measurement. The total harmonic distortion (THD) factor is the ratio of the r.m.s. values of all of the harmonic components together to the r.m.s. amplitude of the fundamental component as follows [185]:

$$THD(\%) = \frac{\sqrt{\sum_{n=2}^{\infty} i_{sn}^2}}{i_{s1}} \times 100\%. \quad (5.12)$$

5.2.2 Accuracy Limitation Calculation

According to the discussion above, equation (5.1) can be used to calculate the phase angle error caused by the GPS time shift. The GPS commitment of UTC time offset is 40 ns for 95% cases, and the real performance is within 10 ns. Therefore, 10 ns and 40 ns are considered for GPS time shift error.

Due to the uncertainty of GPS jitter, GPS receiver manufacturers usually do not give a quantified performance. Generally speaking, the GPS jitter for most GPS receivers varies from 50 ns to 1 μ s. In some cases where the location of the receiver is fixed and known, it is possible to reduce the error to 10 ns with the assistance of related techniques [186]. Therefore, 10 ns, 50 ns and 1 μ s are considered as typical frequency reference errors.

For other errors sources, simulation is used to evaluate their contributions to the measurement error. This approach is shown in Figure 5.2.

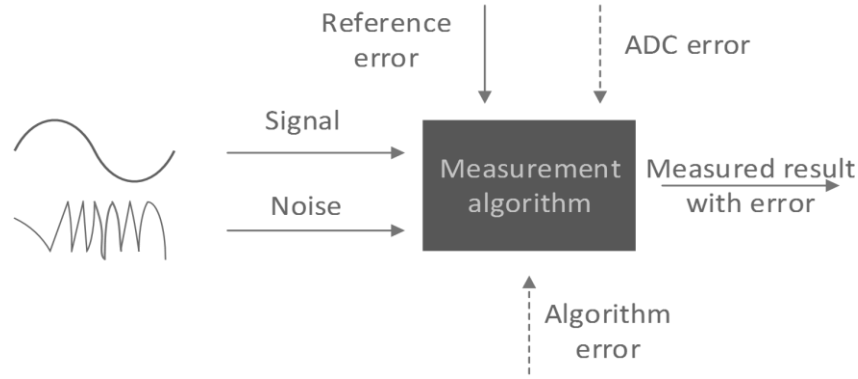
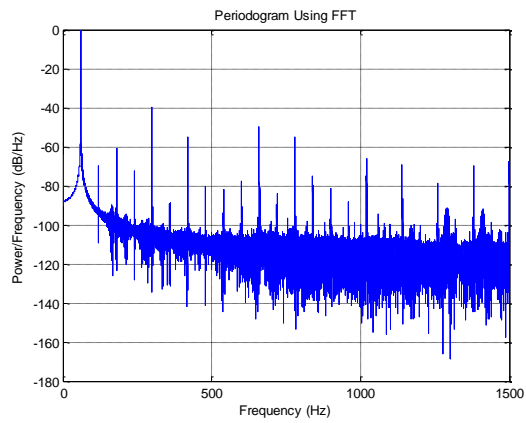


Figure 5.2. Diagram of error estimation simulation

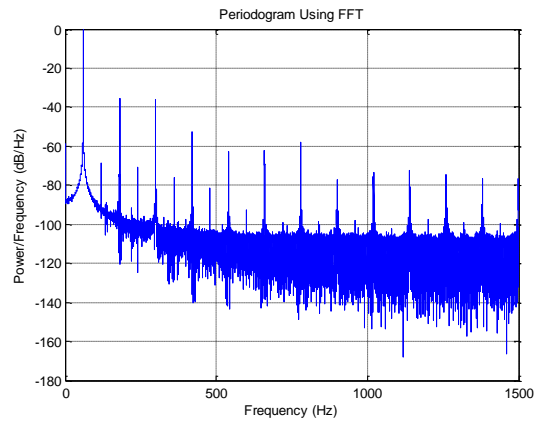
During the simulation, a pure digital sinusoidal signal with a known frequency, angle and amplitude is fed into the measurement algorithm. The estimated frequencies and phase angles of all the sampling points are compared with the true value, obtaining the error of each point. The simulation time, thus the amount of sampling points, is increased until the maximum positive and negative error are converged. Both errors then together indicate the algorithm error boundary. Discrete Fourier Transformer (DFT) is usually utilized for phasor estimation [56]. The algorithm is tested under frequency range conditions. For the frequency of U. S. power grid, the frequency deviation is usually within ± 0.05 Hz, hence the algorithm is evaluated for the actual frequency from 59.95 Hz, to 60.05 Hz. For this algorithm, the farther the actual frequency shifts from the nominal one, the larger phase angle and frequency error the algorithm brings [187]. Therefore, the simulation is able to cover the scenario with largest measurement error.

For an ADC, the higher resolution and accuracy, usually the longer conversion time it takes. Therefore, ADCs with extremely high resolution could not fulfill the dynamic requirement of power grid measurement, especially for synchrophasors. Under the trade-off between dynamic and accuracy, typical 14-bit and 16-bit ADCs are used in PMUs, so they are used for evaluation. The simulation used is similar to that used for algorithm error evaluation, except that the input signal is rounded according to the ADC resolution and accuracy. For instance, when considering the 16-bit ADC with 1 least significant bit (LSB) error, the input signal is rounded into $1/2^{16}$. The related device error is calculated by comparing inputs with outputs.

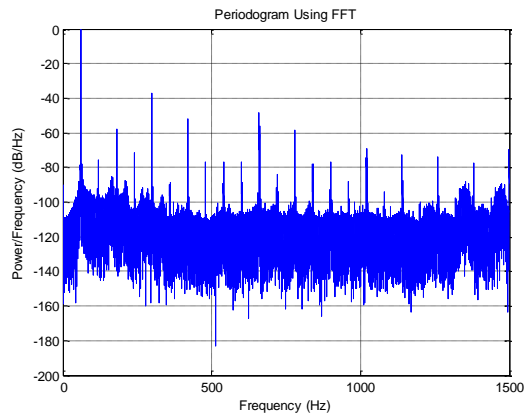
To evaluate the intensity of white noise, electrical signal from four different 120 V outlets are measured, under the sampling rate of 3 kHz and resolution of 16-bit. The related single-side power spectrum densities (PSD) are calculated and shown in Figure 5.3. According to the test, the SNRs of the power grid signals are generally 70 dB to 80 dB. For transmission lines, the SNR is usually lower than distribution line, due to the relatively high voltage and few disturbance sources. 90 dB is used as the boundary of SNR, since it is the typical SNR the standard power source could reach, and the power



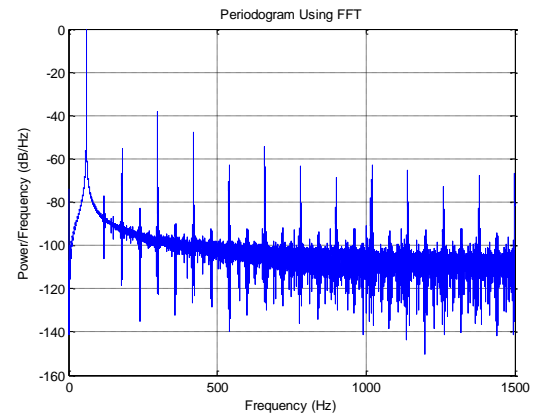
(a)



(b)



(c)



(d)

Figure 5.3. Power spectrum density of electrical signals from different 120 V outlets

source is used for synchrophasors' calibration. All these levels of white noise are added to the pure signal for the measurement accuracy evaluation.

Using DFT algorithm for frequency and angle estimation, the effect of harmonic waves on measurement accuracy is eliminated when the fundamental frequency equals to the nominal frequency. Both the frequency and angle error increase with the frequency deviation.

The harmonic distortion varies from time to time and from place to place. In the four scenarios above, the PSD of harmonic components are measured and shown in terms of dB in Table 5.1, together with their THDs. These harmonic waves with different THDs are recreated by simulation codes and added into the input signal individually for measurement error evaluation.

Table 5.1. Harmonic components of electrical signals from four different outlets

Harmonic Components	Case 1	Case 2	Case 3	Case 4	Harmonic Components	Case 1	Case 2	Case 3	Case 4
2 nd	-69.7	-68.75	-75.61	-76.99	14 th	-75.12	-98.33	-78.28	-93.83
3 rd	-60.78	-35.66	-57.77	-55.11	15 th	-81.33	-77.03	-76.95	-68.83
4 th	-72.33	-70.87	-71.69	-83.01	16 th	-88.35	-98.27	-88.29	-92.29
5 th	-39.63	-35.88	-37.29	-38.14	17 th	-65.97	-73.52	-69.13	-62.8
6 th	-88.49	-75.91	-89.17	-89.8	18 th	-100.3	-102.5	-94.24	-93.32
7 th	-54.94	-52.77	-52.13	-47.74	19 th	-69.17	-72.48	-72.72	-65.12
8 th	-80.1	-81.34	-76.71	-92.37	20 th	-100.1	-97.37	-99.8	-92.61
9 th	-81.93	-62.99	-76.59	-62.73	21 st	-78.79	-74.77	-73.66	-72.64
10 th	-81.54	-92.46	-77.01	-92.55	22 nd	-97.05	-99.28	-97.41	-92.17
11 th	-49.73	-61.98	-48.6	-54.49	23 rd	-69.72	-76.59	-77.24	-67.44
12 th	-83.82	-99.28	-83.72	-92	24 th	-98.94	-99.53	-98.93	-94.13
13 th	-54.98	-57.93	-58.45	-63.43	25 th	-67.37	-76.8	-69.81	-66.54
THD	0.82%	0.91%	0.32%	0.47%					

Notice: Harmonic components are given in term of dB, referred to the fundamental frequency component.

Since the deviation frequency of power grid is usually within ± 0.05 Hz, and the measurement errors are symmetric when the actual frequency lies on either side of the nominal frequency, the errors, especially the error caused by harmonic distortion, are calculated at the fundamental frequency of 59.95 Hz.

Regarding the errors caused by ADC, white noise and harmonic distortion, all the input signals should go through a low-pass filter before measured. The filter is also realized using simulation codes to simulate the amplitude and frequency response of the real filter. It should also be noticed that the algorithm is used in each simulation case, so the calculated errors also include the error caused by the algorithm.

The measurement accuracy limitation is shown in Table 5.2. The results are calculated under 59.95 Hz, except for the algorithm, in which different frequencies in each scenario is indicated.

Table 5.2. Measurement accuracy limitation results

Source	Factor	Scenario	Angle Error (degree)	Frequency Error (Hz)
Instrument	GPS time shift ^a	10 ns	$\pm 2.16\text{E-}04$	0
		40 ns	$\pm 8.63\text{E-}04$	0
		1 μs	$\pm 2.16\text{E-}02$	0
	PPS jitter	10 ns	$\pm 2.16\text{E-}04$	$\pm 6.00\text{E-}07$
		50 ns	$\pm 1.08\text{E-}03$	$\pm 3.00\text{E-}06$
	Algorithm ^b	59.95 Hz	$\pm 1.00\text{E-}03$	$\pm 7.03\text{E-}07$
		59.975 Hz	$\pm 5.62\text{E-}04$	$\pm 3.17\text{E-}07$
		60.00 Hz	0	0
		60.025 Hz	$\pm 5.57\text{E-}04$	$\pm 3.16\text{E-}07$
		60.05 Hz	$\pm 1.00\text{E-}03$	$\pm 7.01\text{E-}07$
	ADC ^{a, c}	14-bit	$\pm 5.50\text{E-}03$	$\pm 2.10\text{E-}04$
		16-bit	$\pm 2.80\text{E-}03$	$\pm 5.30\text{E-}05$
Signal	White Noise ^{a, d}	70 dB	$\pm 1.45\text{E-}02$	$\pm 5.00\text{E-}04$
		80 dB	$\pm 5.90\text{E-}03$	$\pm 1.70\text{E-}04$
		90 dB	$\pm 3.12\text{E-}03$	$\pm 9.07\text{E-}05$
	Harmonic Distortion ^{a, e}	Case 1	$\pm 7.98\text{E-}02$	$\pm 9.10\text{E-}04$
		Case 2	$\pm 3.21\text{E-}02$	$\pm 3.70\text{E-}04$
		Case 3	$\pm 4.85\text{E-}02$	$\pm 5.70\text{E-}04$
		Case 4	$\pm 9.48\text{E-}02$	$\pm 1.07\text{E-}03$

Notes

- ^{a.} The actual frequency is 59.95 Hz.
^{b.} The algorithm here used is DFT.
^{c.} The accuracy is assumed to be 1 LSB.
^{d.} Considering scenarios of different SNRs; no harmonic distortion included.
^{e.} Utilizing the harmonics measured in the four cases in Table 5.1; no white noise included.

According to the results, the GPS error is fairly small, especially when the PPS jitter is less than 50 ns. The DFT algorithm causes $\pm 1.00 \times 10^{-3}$ degree and $\pm 7.00 \times 10^{-7}$ Hz error when the frequency deviation is ± 0.05 Hz. This error decreases when the actual frequency approaches the nominal frequency, and there is no error when the frequency is equal to 60 Hz. For frequency measurement, the algorithm error is much smaller than the error caused by other factors; therefore its influence on measurement accuracy is negligible. For phase angle, the algorithm error is relatively large, thus contributing a non-ignorable part to the results. For the ADC error, part of the results is caused by the algorithm. Both scenarios are based on the assumption that the accuracy equals to 1 LSB. From the results it could be concluded that both 14-bit and 16-bit ADC could fulfill the requirement given by C37.118-2011 [33]. The higher accuracy leaves more tolerance for other error sources.

Among the error sources from the signal, white noise and harmonic disturbance are analyzed separately. Both results include the influence from algorithm error. The frequency and angle errors overpass most instrumental sources errors when the SNR of white noise is 70 dB. Increasing the SNR minimizes both errors.

For the harmonic distortions, the error is equal or larger than the white noise error under the scenario of 70 dB. From Table 5.2 it could be seen that the magnitude of high order odd harmonic components are comparable to the low order components. Due to the cost limitation, the attenuation provided by the low-pass filter is limited, while the high order components contribute more error since their large deviations from the nominal frequency. Both factors conduct the fairly large error. To decrease this error, higher performance filters or notches may be considered to be utilized.

5.3 Impact of Converter-based Energy Sources

5.3.1 Converter-based energy sources analysis

Power electronic converters are used to integrating distributed generations (DG) such as renewable energy sources (wind, solar, etc.), and novel energy (gas turbines, fuel-cells, etc.), and energy storages (battery, flywheel, etc.) into the electric grids [188].

With the increasing focus on the environment and the improved technology to implement renewable energies, many states have mandated the growth rate of renewable energy resources on the electrical power grid. These resources are made up of relatively small power plants distributed across the grid. Historically grid frequency and voltage stability has been maintained by generators consisting of rotating machinery placed far apart from each other. Renewable energy is converted to AC by silicon power devices controlled by software which can change voltage and frequency much more quickly than the rotating generators. It is unclear what key power system parameters will need to be transmitted, how they should be recorded, and how they can be best used. As renewable resources reach high penetration, it is unclear how the important measurements should be standardized, and what traceable test and calibration systems will be required.

The goal of this work is to investigate the disturbance from the renewable energies, and the influence on the PMU measurement. For the sake of the wind gradient and the tower shadow effect, an output of power drop will appear three times per revolution for a three-bladed wind turbine, also called 3p oscillation. Both wind turbine and photovoltaics utilizes power electronic devices to convert DC to AC. All these are possible to influence the measurement result of PMU. We will investigate their influence on the PMU measurement, especially the discrete Fourier transformer (DFT) based phasor estimation algorithm.

5.3.2 Model Construction

The disturbance from the distributed resources is complicated due to the multiple disturbance sources. Some are from the mechanics such as the wind turbine blades, others from different types of inverters and the related control methods. The electronic inverters are usually operated in high frequency; therefore, high speed time-domain simulation is required.

The result of this study will provide a better understanding about the influence of distributed resources on measurement. With this knowledge, it is able to evaluate the reliability of measurement and thus control on distributed renewable energies. It will also benefit for setting the regulations for the power quality of renewable energies, including flicker and harmonics.

To obtain detailed and reliable voltage and current waveform from distributed resources, detailed model needs to be set up and time domain simulation for power system transient is required. In this project, PV and wind generator based power system model with inverters are set up in PSCAD, as shown in Figure 5.4, Figure 5.5, and Figure 5.6. Time domain simulation is implemented. The waveform is input into the PMU model to obtain the influence.

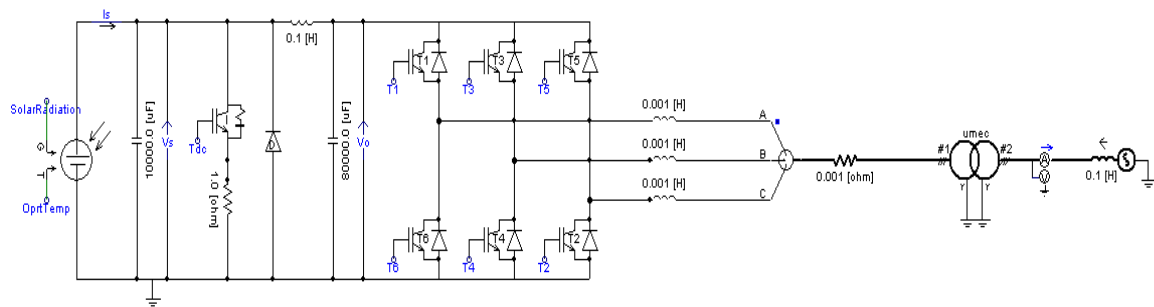


Figure 5.4. System model with PV

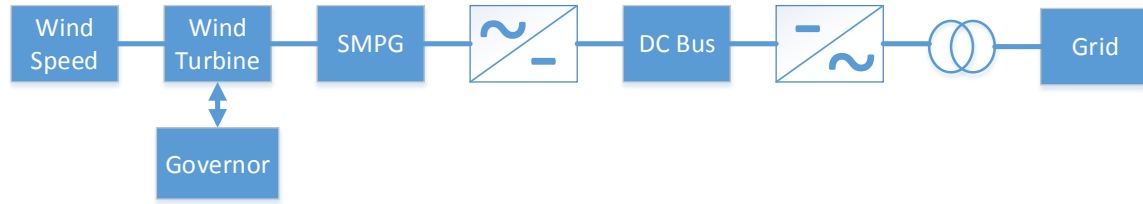


Figure 5.5. System model with wind turbine

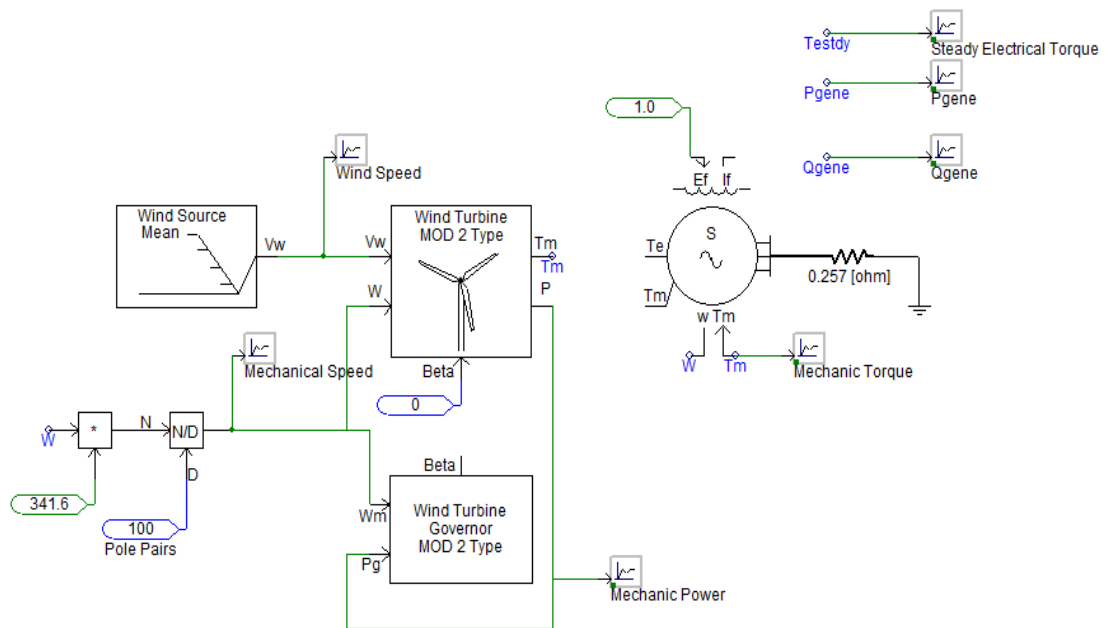


Figure 5.6. Wind turbine model

5.3.3 Impact Analysis

The 3p oscillation of wind turbine is illustrated by the RMS value of its output voltage shown in Figure 5.7.

According to the analysis of PV and wind turbine, it is found that most of the disturbance is from harmonics and interharmonics derived from the switch action of inverters. The harmonics of voltage and current in wind turbine system is listed in Table 5.3. The frequency and phase angle error from these disturbance is listed in Table 5.4.

From the results above, it can be concluded that:

- 1) Power electronics devices of both PV and wind turbine will influence the frequency and phase angle measurement due to the harmonics and interharmonics from the switch action of these devices.
- 2) Filter is useful to suppress the harmonics and interharmonics from the power electronics devices, and thus decrease the measurement error.
- 3) Current suffers more impact than voltage. Therefore, it should pay more attention when using measured current phasor for applications, such as power flow analysis and system parameter estimation.

5.4 Conclusion

In this chapter, the theoretical accuracy limitation of frequency and phase angle measurements on power grid is discussed. The errors caused by time reference, estimation algorithm, instrument devices, white noise and harmonic distortion are analyzed. Based on the normal synchrophasors design and power grid operation conditions, the phase angle and frequency errors caused by each factor are calculated and given out. The result provides references to the synchrophasors improvement. It could also be utilized to analyze the error impact on measurement-based applications.

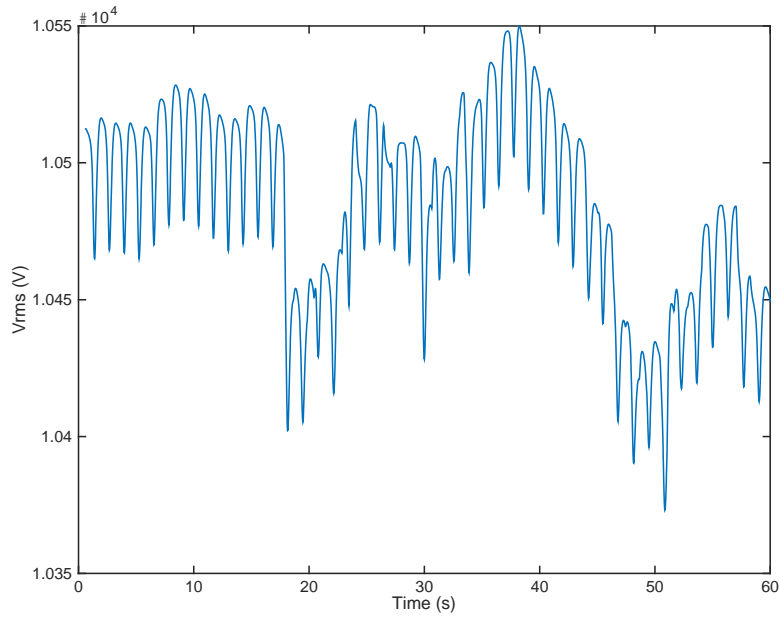


Figure 5.7. 3p oscillation of RMS value of voltage output by wind turbine

Table 5.3. Harmonics of voltage and current in wind turbine system

Harmonics	Voltage (dB)	Current (dB)
1	0	0
2	-73.7119	-25.1818
3	-77.9832	-32.7239
4	-84.2215	-23.4122
5	-74.0905	-15.5738
6	-84.7843	-63.2197
7	-79.2810	-19.1988
8	-92.7623	-30.6668
9	-86.9351	-63.5318
10	-81.9245	-30.4140
11	-86.9097	-26.9853
12	-87.6662	-68.9806

Table 5.4. Simulation result of measurement error from PV and wind turbine

		Frequency error (Hz)	Phase angle error (°)
PV	No filter	-0.0398 ~ -0.0368	-0.0620 ~ -0.0246
	With filter	-0.0391 ~ -0.0377	-0.0510 ~ -0.0114
Wind turbine	No filter	-0.0594 ~ 0.0193	-0.8303 ~ 0.4751
	With filter	-0.0385 ~ -0.0383	-0.0040 ~ 0.0052

CHAPTER 6 FAST RESPONSE PMU DEVELOPMENT

6.1 Introduction

The need of advanced monitoring, protection and control performance of wide area power system has brought the interesting towards synchrophasor measurement and PMU. PMU is able to provide accurate and synchronized data with high data rate. The PMU based wide-area monitoring system is able to provide snapshots of the whole power grid. In the early year, the research of PMU mainly focuses on the steady state monitoring. The related standards also only define the compliance limits of the steady state. It is until late 2011 the new version of the standard, i.e. the IEEE Std. C37.118.1-2011 redefined the compliance limits to include both steady-state and dynamic operating conditions [33]. In this standard, total vector error (TVE) is adopted to combine the effect of magnitude, phase angle, and time-synchronization errors. The maximum TVE allowed in the standard is 3% under dynamic states. However, according to a test of 9 commercial available PMUs by NIST in 2014, almost no devices passed all the accuracy requirement [143]. Furthermore, IEEE SA amended the synchrophasor standard with IEEE Std. C37.118.1a-2014 and adjusted some performance limits, mainly lowered the performance requirement of ROCOF under dynamic operation [35].

Meanwhile, advanced PMUs are demanded to address the problem of ever-increasing fast transient swings in the future grids. More and more inverter-based power sources, such as wind farm, solar energy, small turbine, and energy storage are being connected to the power grid and replace the conventional power generators. As a result, the power grid inertia will keep on decrease, and hence increase the transient swing [189, 190]. As most of numerical protection systems at present depend on the real-time estimation of power system phasors, the performance of synchronized phasor measurements during dynamic operation becomes critical. An advanced PMU with high accuracy and fast responding speeding during the dynamics will be able to provide reliable and timely information for protection and control system to respond to the event and take actions to avoid insecurity of the system.

To improve the dynamic performance of PMUs, the main effort is to improve the algorithm which is used for phasor and frequency estimation. Discrete Fourier Transform (DFT) is the most commonly used algorithm by PMUs, for the sake of simple implementation and harmonics rejection. However, due to the spectral leakage effect, the measurement error increases when the fundamental frequency deviates from the nominal frequency. Furthermore, a data window of one to several cycles is used by DFT algorithm for phasor and frequency estimation. This introduces time delay for dynamic phasor and frequency estimation. Therefore, a new algorithm with good dynamic performance is required to improve the reliability and responding speed of PMU.

The object of the work is to develop an advanced PMU for ultra-fast transient measurement during disturbances. The ultimate objective is to achieve transient stability prediction and control during the critical first swing. In this chapter, an algorithm will be

developed to enable the fast and reliable transient measurement response within a fraction of cycle. The algorithm will then be implemented on advanced hardware platforms to construct a PMU that can detect fast transients while keeping the accuracy within the dynamic performance requirement by the PMU standard.

6.2 Fast Response Algorithm Design

6.2.1 Dynamic Analysis of DFT Algorithm

DFT algorithm is utilized by most commercial PMUs for phasor and frequency estimation, mainly due to its good performance in steady state and simplicity to be realized. Its performance, however, downgrades during dynamic conditions.

First of all, the measurement error of DFT algorithm is considerably large for dynamic input, such as magnitude/phase step change, magnitude/phase modulation, and frequency ramping, compared with steady state. DFT algorithm usually uses samplings in an observation interval (or data window) of 1 to 6 cycles for phasor and frequency estimation, and the phasor and frequency are deemed as constant during this interval. When the parameters of power grid voltage/current start to change and the new waveform samples come into the observation interval, its effect is ‘averaged’ by the old data, hence the estimation error arises. For example, when the magnitude of the input voltage experiences a step change from 1 p.u. to 1.1 p.u., the new samples are from the waveform with 1.1 p.u. magnitude while the old samples from that with 1 p.u.. The estimated magnitude will be between 1 p.u. and 1.1 p.u. until all samples in the data window are from new waveform.

Secondly, this will cause responding time delay. As the step change takes place when the first new sample comes into the window, the estimated magnitude will behavior like a ramp until the window is filled with new samples. The reported step change will be significantly delayed from the step change time, especially when the window length is several cycles.

6.2.2 Analysis of PLL Algorithm

The advanced phase-locked loop (PLL) algorithm simulates the conventional PLL by using the output as feedback and comparing the output with the input. The error (difference from comparison) is then used to correct the output. It estimates the magnitude, phase angle, frequency, and the offset of the input signal. Denote the input signal as $u(t)$, the estimated signal as

$$y = \hat{A} \cos(\hat{\omega}t + \hat{\phi}) + \hat{D} = \hat{A} \cos(\hat{\theta}) + \hat{D}, \quad (6.1)$$

and the error as

$$e = u - y. \quad (6.2)$$

Define objective function as

$$J = e^2 = (u - y)^2. \quad (6.3)$$

To obtain the accurate estimation of the signal, the objective function should be minimized. At the minimum value, the first-order optimality conditions will have to be satisfied. Therefore, there is

$$g(x) = \frac{\partial J}{\partial P} = 0. \quad (6.4)$$

Here P is the estimated variables. Using the steepest descent method, the differentiation of each variable can be obtained.

$$\dot{A} = 2e \cos \hat{\theta} \quad (6.5)$$

$$\dot{\omega} = -2eA \sin \hat{\theta} \quad (6.6)$$

$$\dot{\theta} = \omega \quad (6.7)$$

$$\dot{D} = 2e \quad (6.8)$$

With the differentiation, the variables can be obtained by Newton-Rapson method. To eliminate the steady state error and minimize the convergence time, integration is added to Newton-Rapson method. The structure of the algorithm is shown in Figure 6.1. In this figure, PI represents proportional-integral (PI) controller. There are totally five parameters in this algorithm, two in two PI controllers each, and another in magnitude estimation. They need to be tuned to make the algorithm work.

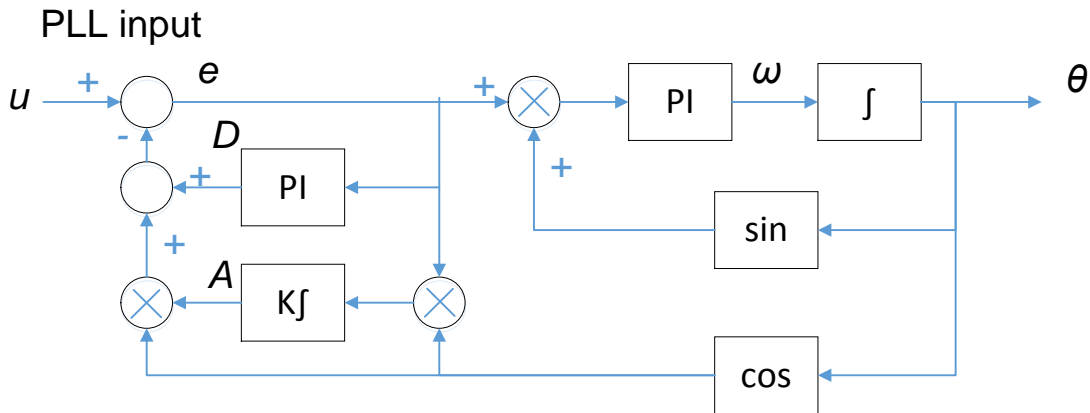


Figure 6.1. Structure of the PLL algorithm

6.2.3 Improvement of PLL Algorithm

Parameters of PI controller in the PLL algorithm introduced in Subsection 6.2.2 needs to be tuned to ensure the algorithm works correctly and stable. Furthermore, a fixed group of parameters can hardly work for both steady state and dynamics. With a strong control it provides fast response to dynamics but also overreacts to fluctuations in steady state. A mild control guarantees the accuracy in steady state, but also decrease the responding speed to dynamics. To solve this problem, the algorithm is improved with a variation. In this variation, the estimation of magnitude, frequency, phase, and dc offset are the same as the first variation. The difference is that the parameters k_1, k_2, k_3, k_4 and k_5 are variable. For each input, after the estimations are done, the parameters k_1, k_2, k_3, k_4 and k_5 update. Then in the next iteration of estimation, the updated coefficients are used for calculation. The coefficients k_1, k_2, k_3, k_4 and k_5 are first calculated using the following equation:

$$k_i'(n) = a_i k_i(n-1) + r_i e(n)^2, (i = 1, 2, \dots, 5) \quad (6.9)$$

Here $0 < a_i < 1$ and $r_i > 1$. They can be determined by the preference of the algorithm performance and the situation of the input signal. One example is:

$$a_1 = 0.9, r_1 = 4 \times 10^{-4}, a_2 = 0.9, r_2 = 4.8 \times 10^{-2}, a_3 = 0.9, r_3 = 6 \times 10^{-2}, a_4 = 0.9, r_4 = 4.8 \times 10^{-3}, a_5 = 0.9, \text{ and } r_5 = 4.8 \times 10^{-4}.$$

In case the disturbance or error causing the algorithm unstable and inaccurate, the boundaries are set for each k_i , i.e.

$$k_i(n) = \begin{cases} k_{imax} & k_i'(n) > k_{imax} \\ k_{imin} & k_i'(n) < k_{imin} \\ k_i'(n) & \text{otherwise} \end{cases} \quad (6.10)$$

One example of the boundaries is:

$$k_{1max} = 2000, k_{1min} = 400, k_{2max} = 0.7, k_{2min} = 0.3, k_{3max} = 60, k_{3min} = 25, k_{4max} = 0.08, k_{4min} = 0.02, k_{5max} = 0.002, \text{ and } k_{5min} = 0.0005.$$

Another variation is to use multiple iterations for each input. When the input signal is highly dynamic, such as during a sudden change of frequency, phase angle, or magnitude, the algorithm has difficulty converging using one iteration for each input. However, when using multiple iterations, the variables are estimated several times and converge closer to the real value. As a result, the algorithm will show a better performance in following with the change of the input signal.

For each iteration, the error is calculated using the equation below.

$$e_i(n) = u(n) - y_i(n) \quad (6.11)$$

Here i indicates the iteration index. The estimated signal $y_i(n)$ is calculated using the variables from estimation of last iteration. For the first iteration of the current input, using the equations below.

$$y_i(n) = \hat{A}_M(n-1) \cos(\hat{\theta}_M(n-1)) + \hat{D}_M(n-1) \quad (6.12)$$

Here M is the maximum iteration number.

With the estimation error, variables can be estimated. The magnitude is first estimated as follows:

$$\hat{A}_i(n) = k_1(n)e_i(n) \cos \theta(n-1) T_s + \hat{A}_{i-1}(n) \quad (6.13)$$

Then the integer part of the angle frequency is updated as follows:

$$\hat{\omega}_{inti}(n) = -k_3(n)e_i(n)\hat{A}_i(n) \sin \hat{\theta}_{i-1}(n) T_s + \omega_{int(i-1)}(n) \quad (6.14)$$

The angle frequency is then estimated as follows:

$$\hat{\omega}_i(n) = -k_2(n)e_i(n)\hat{A}_i(n) \sin \hat{\theta}_{i-1}(n) + \hat{\omega}_{int(i-1)}(n) \quad (6.15)$$

Hence the frequency can be calculated by

$$\hat{f}_i(n) = 2\pi\hat{\omega}_i(n) \quad (6.16)$$

The phase is calculated as follows:

$$\hat{\theta}_i(n) = \hat{\omega}_i(n)T_s + \hat{\theta}_M(n-1) \quad (6.17)$$

Notice that all the phase angle in iteration i are updated based the phase angle of last iteration of the last input, i.e. $\hat{\theta}_M(n-1)$.

The integer part of the dc offset is updated as follows:

$$\hat{D}_{inti}(n) = k_5(n)e_i(n)T_s + \hat{D}_{int(i-1)}(n) \quad (6.18)$$

The dc offset is estimated as follows:

$$\hat{D}_i(n) = k_4(n)e_i(n) + \hat{D}_{int(i-1)}(n) \quad (6.19)$$

In the equations above, n is the time index of variables.

The coefficients $k_i(n)$ ($i = 1, 2, \dots, 5$) can be set as constant in the first variation. For a signal with nominal frequency and magnitude of 60 Hz and 20 V, the parameters' values are $k_1 = 1600$, $k_2 = 0.5$, $k_3 = 40$, $k_4 = 0.04$, and $k_5 = 0.001$.

The coefficients $k_i(n)$ ($i = 1, 2, \dots, 5$) can be also be variable as in the second variation. i.e.

$$k_i'(n) = a_i k_i(n-1) + r_i e(n)^2, (i = 1, 2, \dots, 5) \quad (6.20)$$

Here $0 < a_i < 1$ and $r_i > 1$. They can be determined by the preference of the algorithm performance and the situation of the input signal. One example is

$$a_1 = 0.9, r_1 = 4 \times 10^{-4}, a_2 = 0.9, r_2 = 4.8 \times 10^{-2}, a_3 = 0.9, r_3 = 6 \times 10^{-2}, a_4 = 0.9, r_4 = 4.8 \times 10^{-3}, a_5 = 0.9, \text{ and } r_5 = 4.8 \times 10^{-4}.$$

Also there are boundaries for each k_i , i.e.

$$k_i(n) = \begin{cases} k_{imax} & k_i'(n) > k_{imax} \\ k_{imin} & k_i'(n) < k_{imin} \\ k_i'(n) & \text{otherwise} \end{cases} \quad (6.21)$$

One example of the boundaries are

$$k_{1max} = 2000, k_{1min} = 400, k_{2max} = 0.7, k_{2min} = 0.3, k_{3max} = 60, k_{3min} = 25, k_{4max} = 0.08, k_{4min} = 0.02, k_{5max} = 0.002, \text{ and } k_{5min} = 0.0005.$$

The iteration number M depends on the performance requirement and the computation speed. Larger M will improve the dynamic performance of the algorithm, but increase the computation burden. One example for the value of M is 10.

6.2.4 Testing Result

The performance of the algorithm is evaluated according to the IEEE Standard C37.118.1-2011, and C37.118.1a-2014. P class requirement is chosen for the test, since the proposed PMU is targeting the fast response and transient capture.

6.2.4.1 Steady State

(1) Frequency Range

In the frequency range test, P class PMU is required to work in range of ± 2 Hz deviated from the nominal frequency. The maximum TVE is 1% and the frequency error is 0.005 Hz. The test result is shown in Figure 6.2.

According to the test, the TVE and frequency error are much better than the requirement of the standard.

6.2.4.2 Dynamic State

(1) Amplitude Modulation

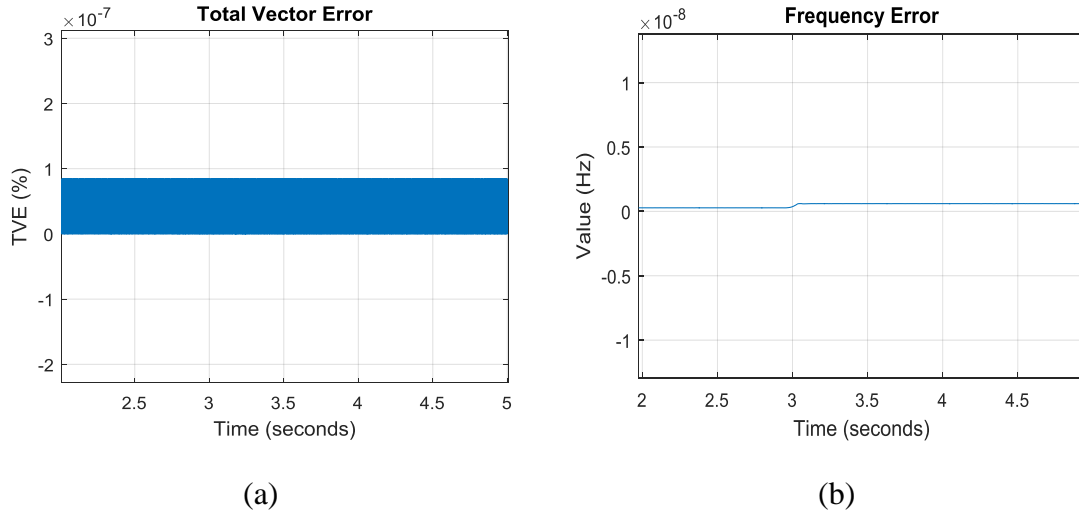


Figure 6.2. Frequency range test, (a) frequency, (b) TVE

In the amplitude modulation test, the input signal may be represented by

$$x = X_m[1 + k_x \cos(\omega_m t)] \cos \omega_0 t \quad (6.22)$$

According to the standard, the maximum modulation frequency required is 2 Hz and the modulation amplitude is 10%. The maximum TVE is 3% and the frequency error is 0.06 Hz. The test result is shown in Figure 6.3. The frequency error is and the TVE are 30 and 200 times better than the standard respectively.

Compare the actual value of magnitude and the estimated value, it can be seen that the maximum delay is about 0.0025 sec, equivalent to 15% cycle, shown in Figure 6.4.

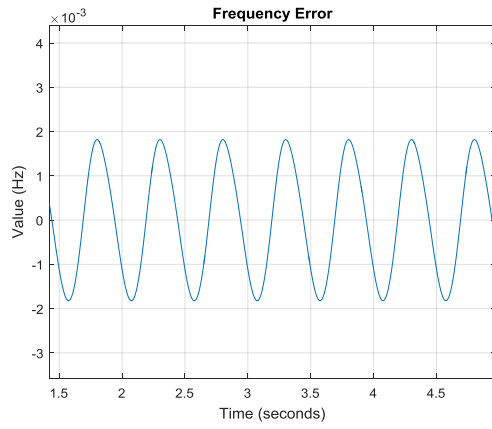
(6) Phase Modulation

In the phase modulation test, the input signal may be represented by

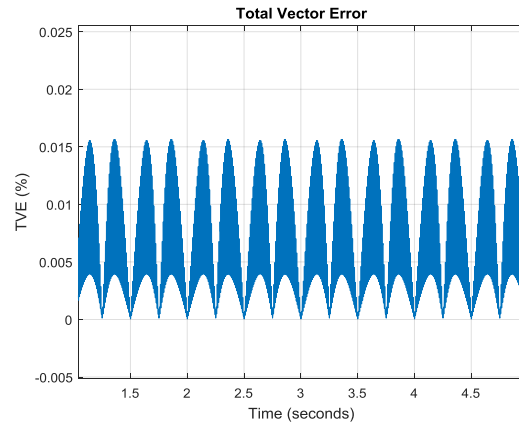
$$x = X_m \cos [\omega_0 t + k_a \cos(\omega t - \pi)] \quad (6.23)$$

According to the standard, the maximum modulation frequency required is 2 Hz and the modulation amplitude is 0.1 rad. The maximum TVE is 3% and the frequency error is 0.06 Hz. The results are shown in Figure 6.5.

Compare the actual frequency and the valued estimated by this algorithm and the 6-cycle DFT algorithm, shown in Figure 6.6. The delay of PLL algorithm is 8 ms, comparing to 77 ms of 6-cycle DFT method.



(a)



(b)

Figure 6.3. Amplitude modulation test, (a) frequency, (b) TVE

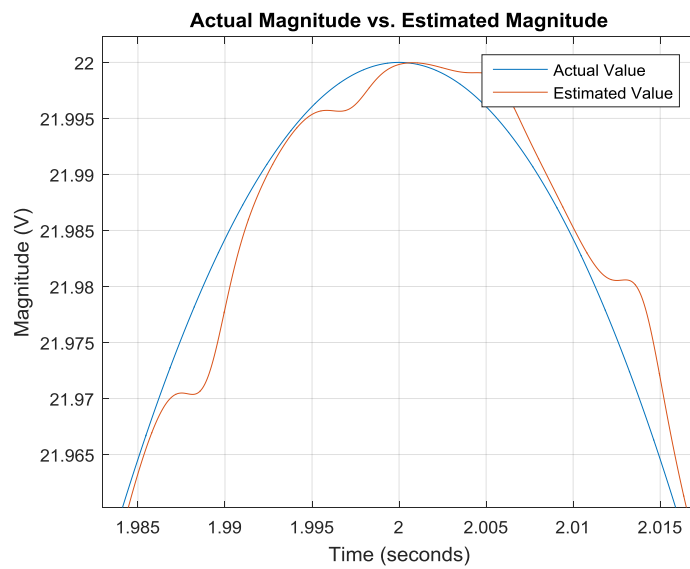
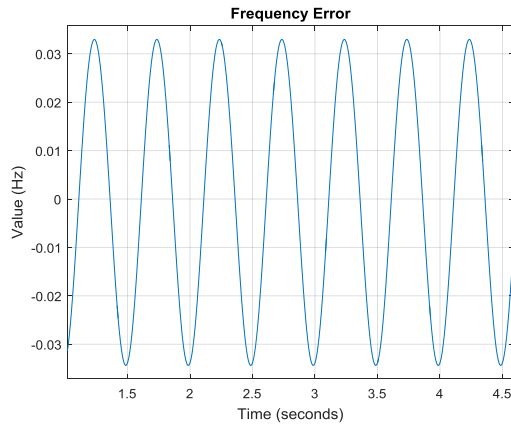
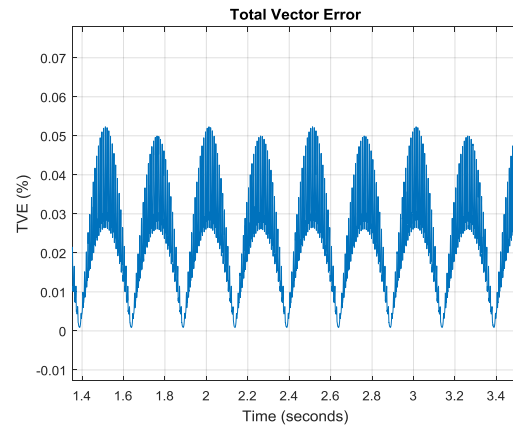


Figure 6.4. Actual magnitude vs. estimated magnitude



(a)



(b)

Figure 6.5. Phase modulation test, (a) frequency, (b) TVE

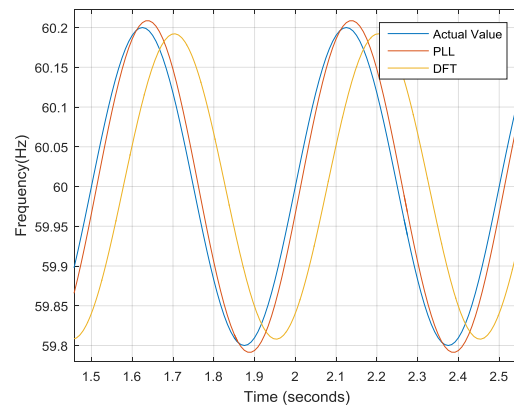


Figure 6.6. Frequency comparison

(7) Frequency Ramp

In the phase modulation test, the input signal may be represented by

$$x = X_m \cos [\omega_0 t + \pi R_f t^2] \quad (6.24)$$

According to the standard, the maximum frequency ramping rate required is $\pm 1 \text{ Hz/s}$ and the ramp range is $\pm 2 \text{ Hz}$. The maximum TVE is 1% and the frequency error is 0.01 Hz . In this test, the frequency of the input signal rises from 58 Hz to 62 Hz at the rate of 1 Hz/s . The results are shown in Figure 6.7.

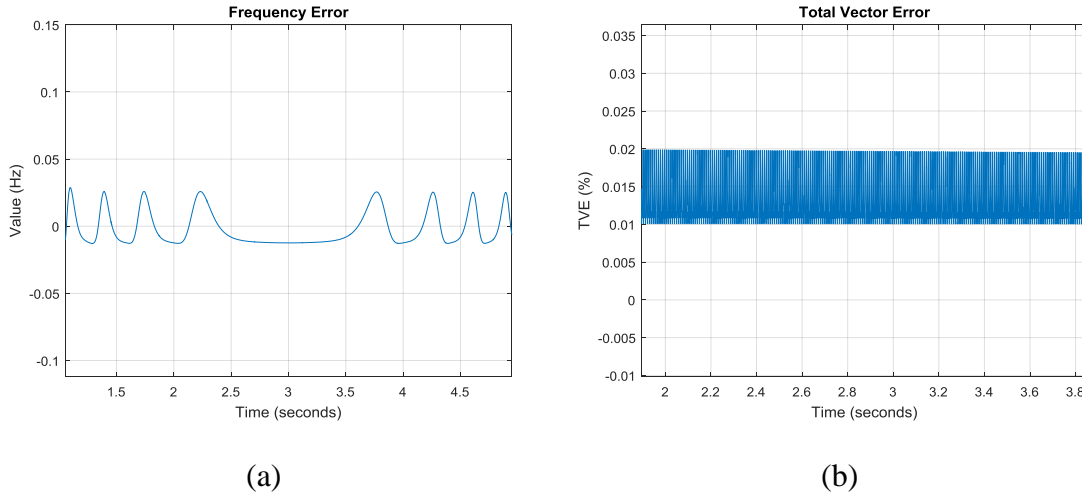


Figure 6.7. Frequency ramp test, (a) frequency, (b) TVE

The comparison between PLL and 6-cycle DFT algorithms are shown in Figure 6.8. It can be seen from that after the frequency ramp change, the PLL algorithm responses faster and then shows smaller error after the frequency ramping. The response delay is about 0.021 s compared to 0.067 s , and PLL algorithm responses about 2.76 cycles faster, as shown in Figure 6.8.

(8) Magnitude Step Change

In the phase modulation test, the input signal may be represented by

$$x = X_m [1 + k_x f_1(t)] \cos \omega_0 t \quad (6.25)$$

According to the standard, the change step is $\pm 10\%$. In the test, a 10% magnitude step change takes place at 1 s . The results are shown in Figure 6.9.

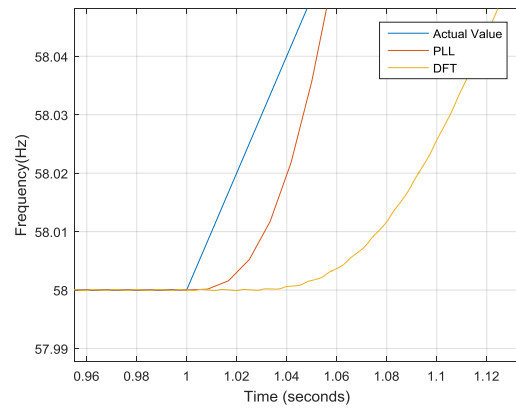


Figure 6.8. Comparison of frequency estimation response during frequency ramp change

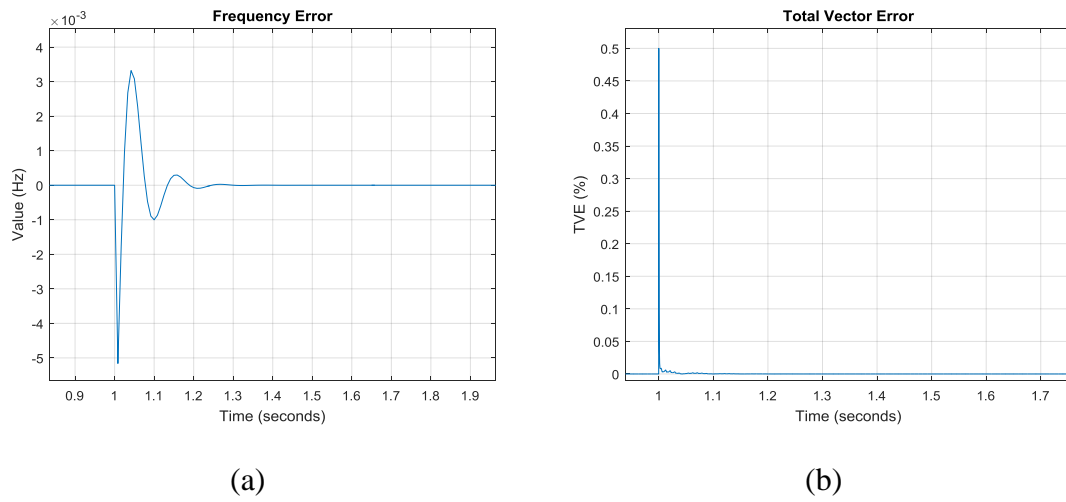


Figure 6.9. Magnitude step test, (a) frequency, (b) TVE

(9) Phase Step Change

In the phase modulation test, the input signal may be represented by

$$x = X_m \cos [\omega_0 t + k_a f_1(t)] \quad (6.26)$$

According to the standard, the change step is $\pm 10^\circ$. In the test, a 10° step change takes place at 1 s. The results are shown in Figure 6.10.

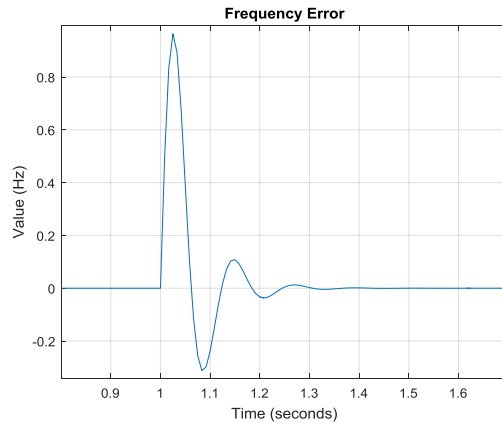
From Figure 6.11 it can be seen that the response time of PLL algorithm is 0.015 s, while the 6-cycle DFT algorithm is 0.045 s.

6.3 High Reporting Rate Design

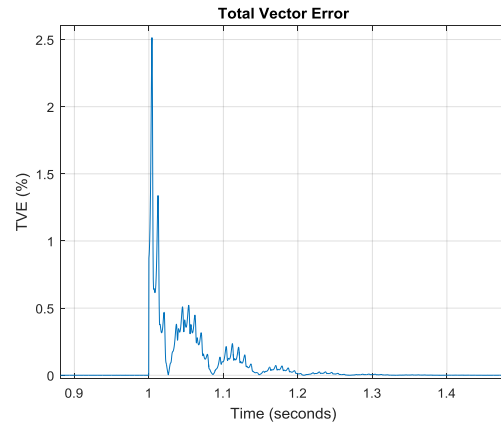
The implementation of the advanced PLL algorithm helped to improve the dynamic performance of the PMU in phasor and frequency estimation, including reducing the measurement error, response time delay, and reporting time delay. However, to fully benefit from the improved dynamic performance of the fast response PMU, there is one more step, i.e. to increase the reporting rate of the PMU.

When the responding speed is low and/or the reporting latency is relatively large compared to the reporting rate, higher the reporting rate does not improve much of the PMU application performance. However, when the response and reporting latency are lower, the low reporting rate becomes the bottleneck to provide timely dynamic information of the power grid. With the decrease of PMU latency and increase of the reporting rate, a lot of PMU based applications will show higher performance thanks to the improved dynamic characteristic and abundant information provided by the fast response PMU. E.g., the linear state estimation will be able to provide a faster and more accurate estimation of the phase angle, voltage, power and reactive power of the power grid; real-time stability analysis application is able to detect the possible insecure status of the power system in a speedy manor. PMU-measurement based control applications will also benefit from it, as time delay is hard to be eliminate in the feed-back control loop and will downgrade the control performance.

Besides the benefit in improving the current application performance, high reporting rate could also help to realize some new applications. For example, the conventional oscillation detection applications use phase angle or frequency measurements to analysis and obtain the oscillation mode, damping ratio, mode shape, and participation factor. Due to the highest reporting rate of conventional PMUs is 60 Hz for a 60 Hz system, and 50 Hz for a 50 Hz system, the highest oscillation mode can be detected and analyzed is 30 Hz and 25 Hz respectively according to Nyquist-Shannon sampling theorem. This bandwidth is wide enough for inter-area oscillation, the oscillation mode of which is usually within 0.2 Hz to 2 Hz. However, the oscillation frequency of subsynchronous resonance (SSR) could goes beyond 30 Hz. This phenomenon becomes obvious as the increasing penetration of wind farm connected to the power system [191]. Therefore, the



(a)



(b)

Figure 6.10. Phase step test, (a) frequency, (b) TVE

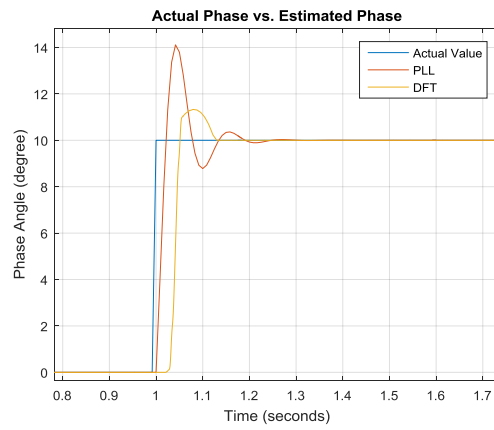


Figure 6.11. Comparison of phase angle estimation response during angle step change

measurement with reporting rate above 60 Hz is needed. Another application is the measurement based power system dynamic prediction, which needs high reporting rate of phasor measurements [192].

In realization of the high reporting rate synchrophasor, one challenge is to provide the correct and useable phase angle. In conventional PMUs, the highest reporting rate equals to the nominal frequency of the power grid. Therefore, there is at most one measurement for each cycle. Denote the waveform as

$$x(t) = \sqrt{2}X_m \cdot \cos(\omega t + \theta_0), \quad (6.27)$$

where $x(t)$ is the voltage/current, X_m is the magnitude, ω is the frequency, t is the time, and θ_0 is the initial phase angle.

When the frequency of the power grid equals to the nominal frequency, the reported phase angle is consistently equal to θ_0 . When the power grid frequency deviates from the nominal value, the angle of synchrophasor changes over time. Taking 60 Hz system as example, the required reporting rates in the standard are 10 Hz, 12 Hz, 15 Hz, 20 Hz, 30 Hz, and 60 Hz [33]. All the reporting intervals of them are integral times of 1 nominal cycle, i.e. 1/60 sec. Denote them as

$$T_r = \frac{1}{f_r} = 2\pi \cdot \frac{M}{\omega_0}, \quad (6.28)$$

where T_r is the reporting interval, f_r is the reporting rate, M is the ratio between the nominal frequency and the reporting rate:

$$M = \frac{\omega_0}{2\pi f_r}. \quad (6.29)$$

It is an integer for the required reporting rates listed above. As the reporting time can be represented by

$$t_r = kT_r \quad (k = 0, 1, 2, \dots). \quad (6.30)$$

The reported phase angle is

$$\theta_r(k) = \omega t_r + \theta_0 = \frac{\omega}{\omega_0} 2\pi k M + \theta_0. \quad (6.31)$$

The difference between two neighboring reported phase angles is

$$\Delta\theta_r = \theta_r(k+1) - \theta_r(k) = \frac{\omega}{\omega_0} 2\pi M. \quad (6.32)$$

Since the frequency deviation is usually very small compared to the nominal value, and M is an integer, $\Delta\theta_r$ will also be very close to 2π . An example of 60.5 Hz frequency at 60 Hz reporting rate is shown in Figure 6.12.

However, when the reporting rate is above 60 Hz, saying 120 Hz or 180 Hz, M is no longer an integer value. Taking 120 Hz reporting rate as example, $M = 0.5$, then (6.32) becomes

$$\Delta\theta_r = \frac{\omega}{\omega_0}\pi. \quad (6.33)$$

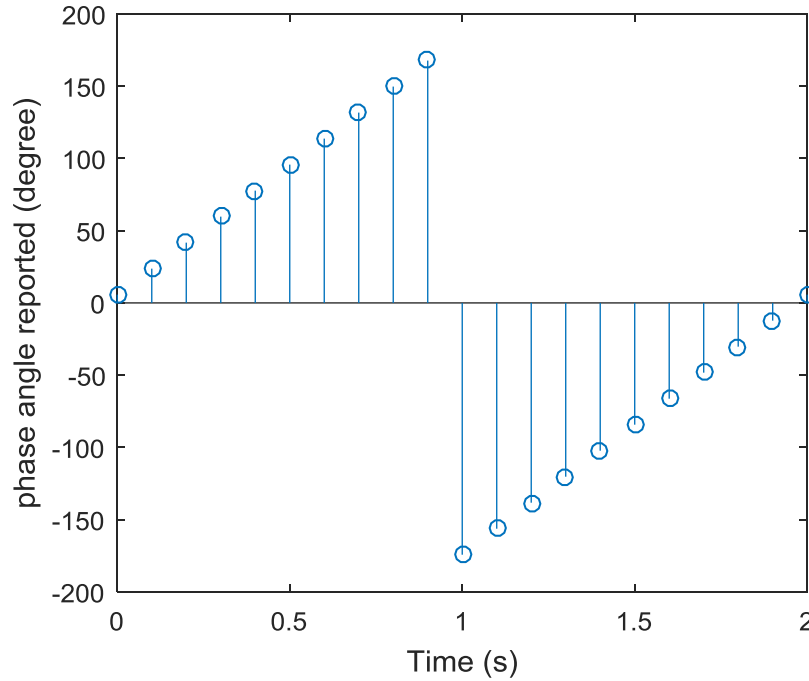


Figure 6.12. Phase angle of 60.5 Hz waveform at 60 Hz reporting rate

That means the two reported angles will have a difference around π . The reported angles will keep on like ‘fluctuation’ as shown in Figure 6.13.

In this fluctuation, there is a jump of about π between adjacent phase angle measurements. If the reporting rate is increase to 180 Hz and 240 Hz, this jump will then become $\pi/3$ and $\pi/4$, respectively. This jump tends to bring inconvenience or even problems in data visualization and applications. Therefore, an intuitive way is to remove this jump by:

$$\theta_r^c(k) = \theta_r(k) - 2\pi kM. \quad (6.34)$$

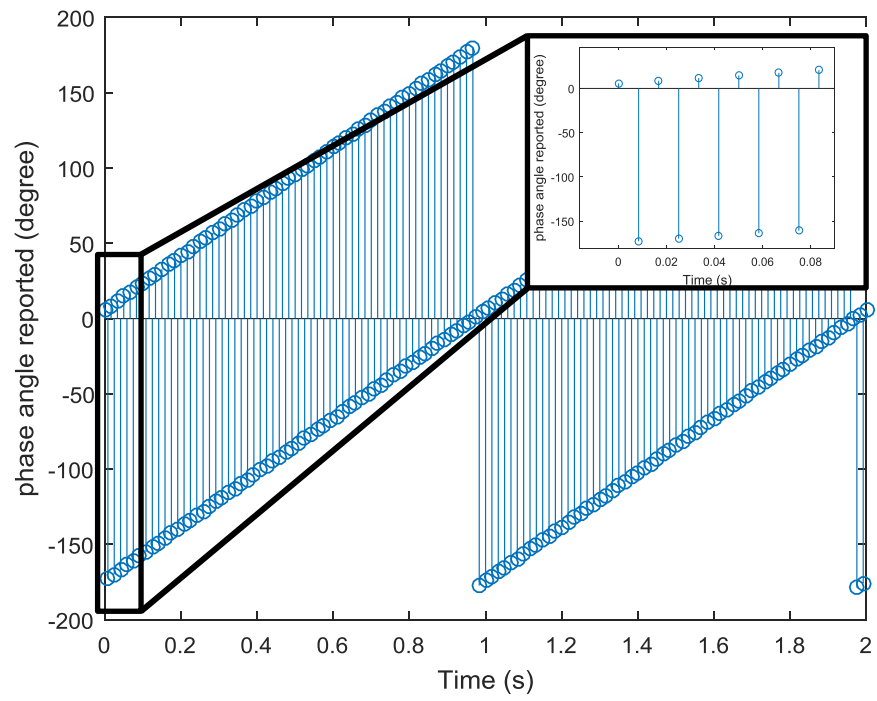


Figure 6.13. Phase angle of 60.5 Hz waveform at 120 Hz reporting rate

Here $\theta_r^c(k)$ is the compensated phase angle achieved by removing the angle jump. Notice that this is a generic equation since it also works for situations where reporting rate is below 60 Hz (i.e., M is an integer). The example of 60.5 Hz waveform at 120 Hz reporting rate after compensation is showing in Figure 6.14.

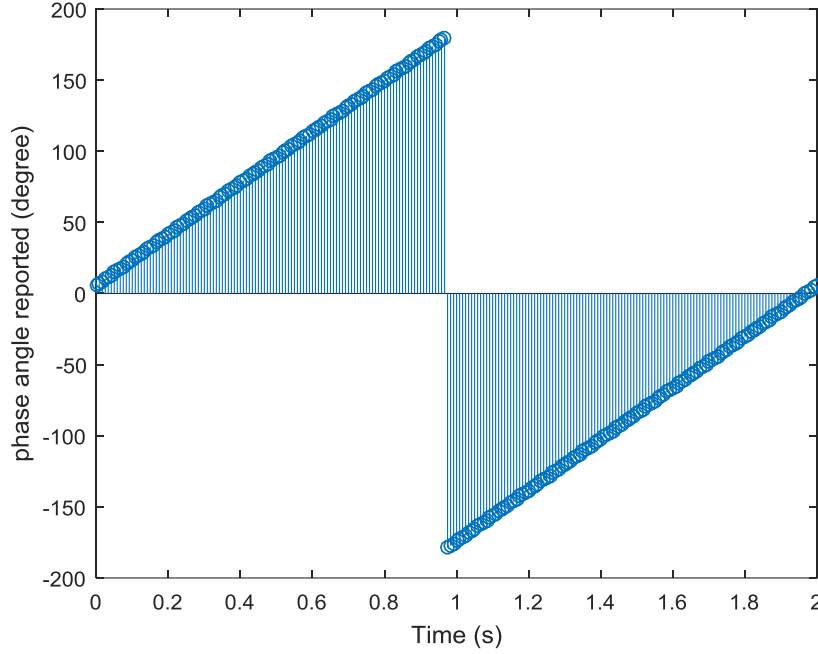


Figure 6.14. Phase angle of 60.5 Hz waveform at 120 Hz reporting rate after compensation

Actually, the compensated results satisfy the definition of synchrophasor, which is given by

$$\mathbf{X}(t) = X_m e^{j((\omega - \omega_0)t + \theta_0)}. \quad (6.35)$$

The phase angle reported by the synchrophasor is $(\omega - \omega_0)t + \theta_0$ if we don't consider measurement error. According to this definition, the angle of synchrophasor can be represented by

$$(\omega - \omega_0)t + \theta_0 = (\omega - \omega_0)t_r + \theta_0 = \frac{\omega}{\omega_0} 2\pi kM - 2\pi kM + \theta_0. \quad (6.36)$$

Comparing (6.36) and (6.34), it can be found that they are equal. Therefore the removing of phase jump not only makes the data processing easier, but also transfers the output to comply with synchrophasor definition.

This phenomenon can be understood by its analogy to the rotating wheel in videos. When the rotation speed of the wheel equals to the sampling rate of the camera, the same spoke remains unmoved in the video. When the rotation speed is slightly higher or lower than

the sampling rate, the spoke is seen slowing forward or backward. The phase angle of the voltage is like the spoke rotating from 0° to 360° . If both the reporting rate and the voltage frequency is 60 Hz, the reported angle is a constant value. If the frequency is higher or lower than 60 Hz, the reported angle will slightly increase or decrease. However, when the sampling rate of camera is twice the speed of rotation speed, the spoke is sampled twice every round, one at the initial position, and the other at a position 180° away. Similarly for the PMU, when the reporting rate is 120 Hz, the angle are reported twice every cycle, and there is a 180° jump between every other reported phase angle.

6.4 PMU Realization

The fast response PMU is realized in the hardware of universal grid analyzer (UGA) – a single-phase voltage synchrophasor to evaluate its performance [193].

The diagram of the hardware is shown in Figure 6.15. Voltage signal from wall outlet is taken by the voltage transducer, downscaled into the acceptable voltage range of ADC. It is then sampled by the ADC after passing the anti-aliasing filter which eliminates the high frequency components. The ADC transforms the analog signal into 16-bit digital form and input into the DSP. Advanced PLL algorithm is realized in the DSP to estimate the phasor and frequency, which are then transmitted to the ARM through Serial Peripheral Interface (SPI) bus. The estimation results are time stamped in the ARM and transmitted to display in the LCD and sent to data server through Ethernet transceiver. The time is provided by the GPS receiver, which also provides PPS signal for synchronous sampling and correct the sampling rate in real-time.

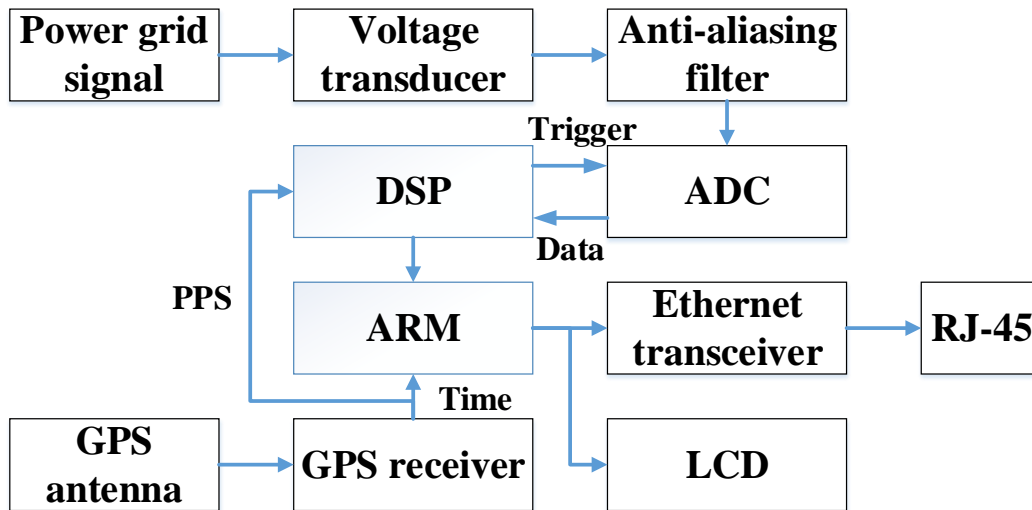


Figure 6.15. Diagram of UGA hardware

A picture of the hardware is shown in Figure 6.16.



Figure 6.16. Picture of UGA hardware

The software of the PMU includes two parts: DSP software and AMR software.

DSP software is realized in TI C6000 serial DSP. It includes 6 modules:

- Control: controls the procedure of the software and the calling of other components;
- Algorithm: advanced PLL algorithm which estimates the phasor and frequency of the input raw data;
- Timer: controls the time to trigger the ADC synchronous sampling; calculates the real time frequency of the oscillator and corrects the sampling rate by tuning the divider factor;
- Universal asynchronous receiver-transmitter (UART): communicates with ADC and GPS receiver;
- Interrupt service route (ISR): responds to the interruptions, including timer and UART.

The procedure of the software is shown in Figure 6.17. After the DSP is powered on, the control module first initializes the variables and peripherals. Then it enters into the infinite loop in which it repeats acquiring data and executing the phasor estimation. Whenever the data sampled by ADC is received, the algorithm module is called for estimation. Each estimation result is used for the next estimation. The data needed to report is only a subset of all the estimation results. The data to be output are packaged and sent to the SPI buffer immediately once available. They are then transmitted to the AMR.

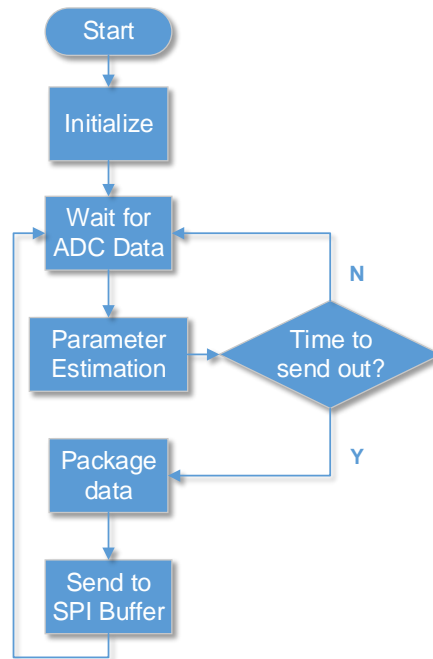


Figure 6.17. DSP software diagram

AMR software is running on an ARM Cortex-M3. It includes 7 modules:

- Control: controls the procedure of the software and the calling of other components;
- GPS: parses the GPS information includes UTC time, geographic coordinator in terms of longitude and latitude, and the GPS accuracy/quality in terms of the number of GPS satellites locked by the receiver;
- SPI: reads and parses phasor and frequency data transmitted from DSP;
- Data Packet: packet time stamp from GPS module and the phasor and frequency estimation results from SPI module according to the corresponding data format; sends to the Ethernet and LCD through UART module and LCD module, respectively;
- Universal asynchronous receiver-transmitter (UART): communicates with GPS receiver and Ethernet transceiver;
- LCD: displays information on LCD including UTC time, GPS satellite number, frequency, and voltage magnitude;
- Interrupt service route (ISR): responds to the interruptions, including timer, SPI and UART.

The procedure of the software is shown in Figure 6.18. After the ARM is powered on, the control module first initializes the variables and peripherals. Then it enters into the infinite loop in which it repeats examining the GPS status and packaging and sending data. Data will not be sent out until enough GPS satellites are captured, to ensure the data quality. Then the time and position are parsed from the GPS data package, and the phasor

and frequency from DSP through SPI. Both contents are packaged and sent out to the Ethernet module. They are also sent to the LCD module to update the display. Every time a data frame is sent, the GPS will be checked to determine the status. After the coordinator is obtained, and the location of the FDR is fixed, accurate time can be obtained even with only one satellite. Therefore, only when the GPS satellite is totally lost for one hour, the FDR will stop sending data, as the oscillator will drift far enough after one hour of GPS loss that the phasor and frequency measurement are beyond the required accuracy for applications.

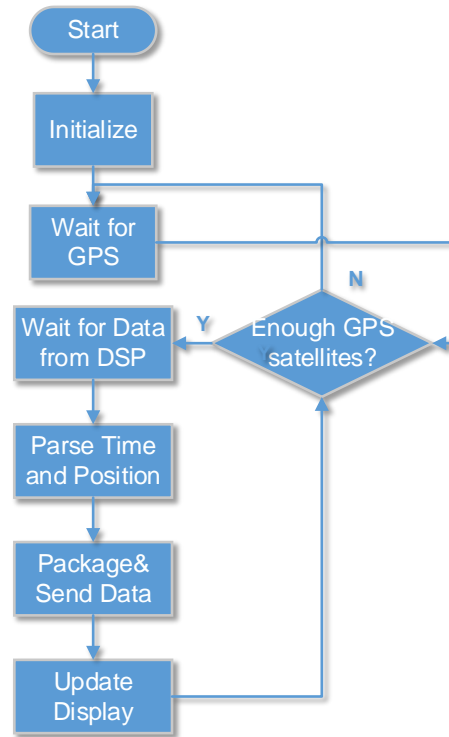
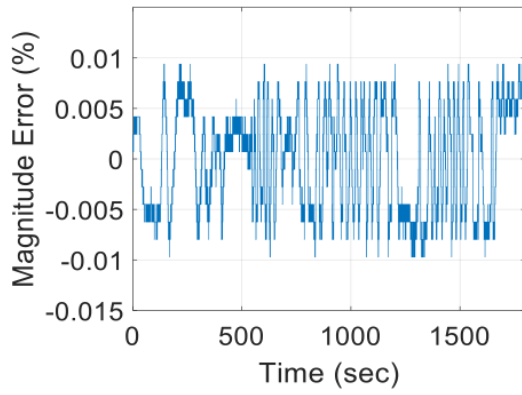


Figure 6.18. ARM software diagram

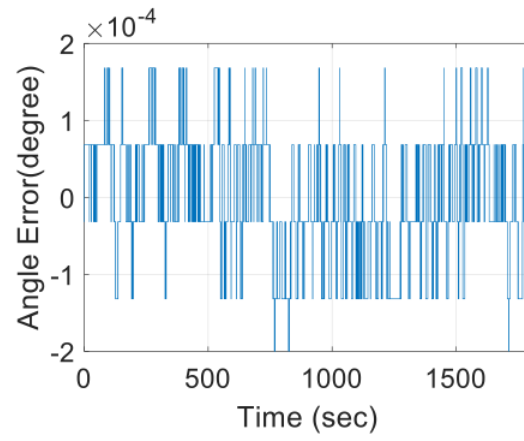
6.5 Performance Testing

The realized fast response PMU is tested using the GPS-synchronized standard power source.

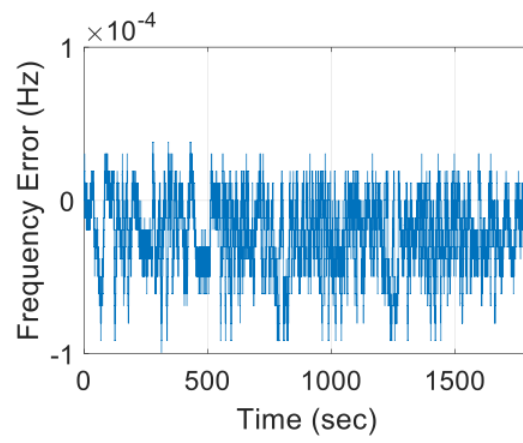
In the steady state, the magnitude error, phase angle error, and the frequency error are shown in Figure 6.19. The testing time is 30 minutes. It can be seen from the figure that the magnitude error is within $\pm 0.01\%$, phase angle error within $\pm 2 \times 10^{-4}^\circ$, and frequency error within ± 0.1 mHz. All are much more accurate than the requirement of the PMU standard.



(a)



(b)



(c)

Figure 6.19. Steady state testing result

For the dynamic test, the magnitude step change is taken as an example. In this test, the magnitude of the input signal takes a step change of 10%. The time of this change is set as time 0, and the testing results are plotted against the true value. The performance of the fast response PMU is also compared with other commercial PMUs reported in [143].

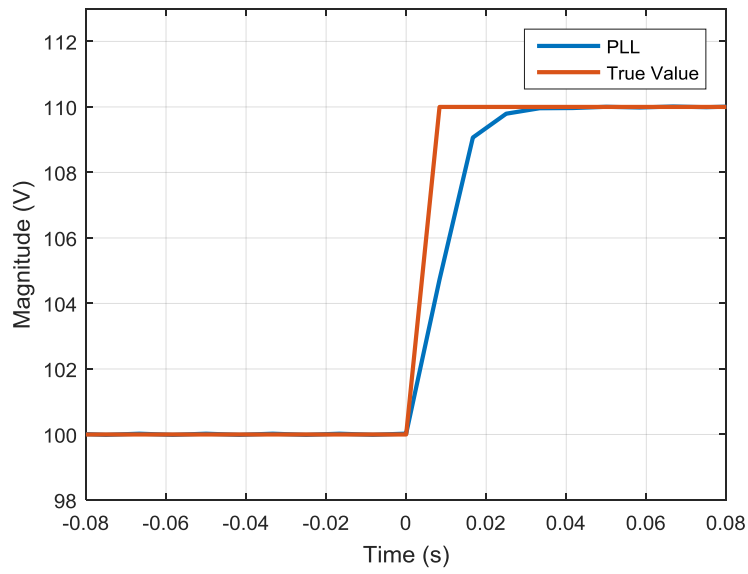
The magnitude performance is plotted in Figure 6.20 (a). The delay time, which is defined as the time interval between the true value and the reporting value at the 50% of the change step, is only 0.0047 sec, much smaller comparing with the commercial PMUs shown in Figure 6.20 (b) and (c). Furthermore, it does not have any overshooting.

The phase angle measurement and TVE are shown in Figure 6.21. The phase angle experiences a -0.3° error during the magnitude step change, but it is still within the 1% TVE range. In the TVE, there is one point jump, which corresponds to the magnitude step change. This is because the magnitude step change cannot be responded by the PMU immediately. However, just after this point, the TVE immediately falls into the range of 1%.

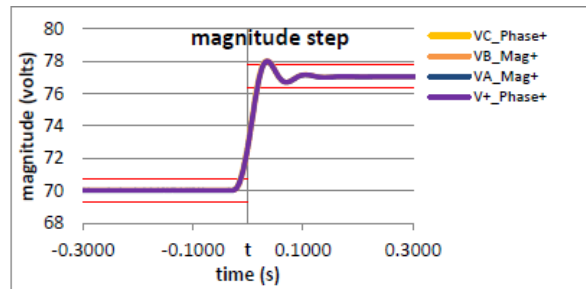
The frequency performance of the fast response PMU is shown in Figure 6.22 (a). It can be seen that only one measurement point is influenced by the magnitude step change and deviates from the true value. However, the error is still within the required frequency error range, i.e. ± 0.005 Hz. From Figure 6.22 (b)-(d) it can be seen that all these commercial PMUs take at least two points to converge back to the true value of frequency and the errors go beyond the allowed range.

6.6 Conclusion

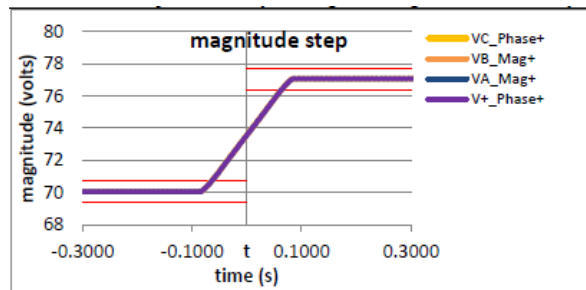
In this chapter, a fast response PMU is developed. The advanced PLL algorithm is proposed and improved. Then the high reporting rate method is designed and a phase angle correction method is proposed regarding to the phase angle fluctuation when the reporting rate surpasses the nominal frequency of the power system. The proposed PMU is realized in hardware. Testing results show that its dynamic performance is better than the commercial PMUs. It can server for the power system applications which require extremely low measurement delay and reliable measurement results during the abrupt changes in power grid.



(a)

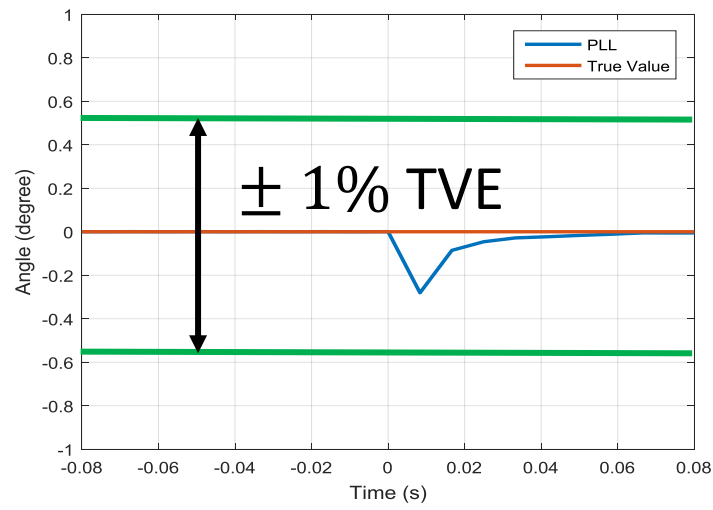


(b)

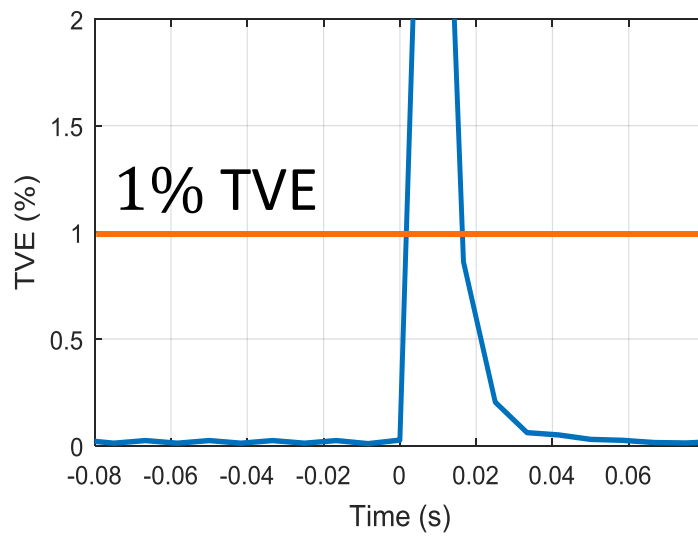


(c)

Figure 6.20. Magnitude result in magnitude step change testing: (a). true value and testing result of fast responding PMU; (b). testing results of a commercial PMU; (c). testing results of another commercial PMU.

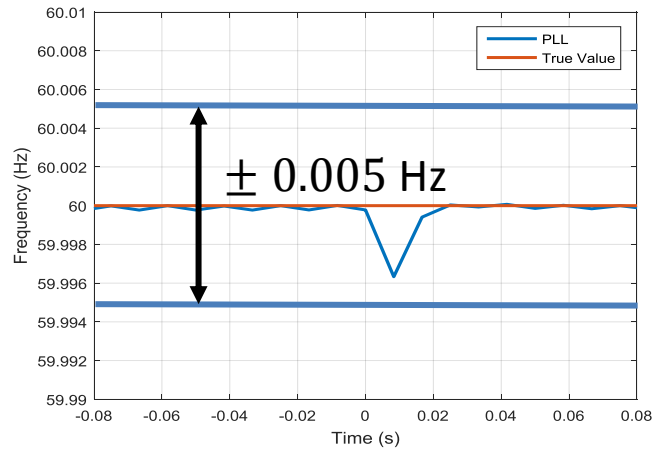


(a)

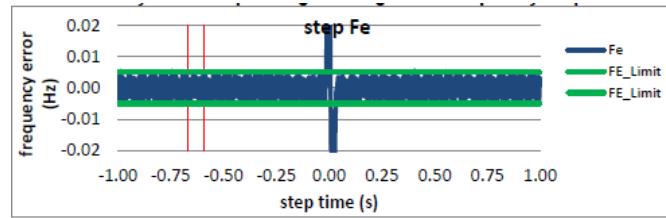


(b)

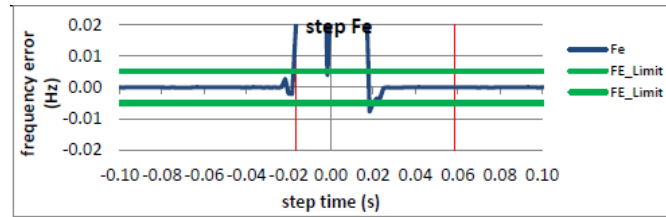
Figure 6.21. Result in magnitude step change testing: (a). phase angle error, the two green lines correspond to the equivalent 1% TVE; (b). TVE, the orange line corresponds to 1% TVE.



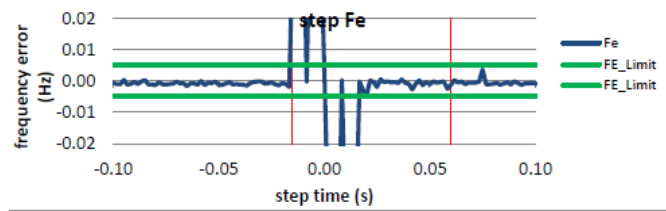
(a)



(b)



(c)



(d)

Figure 6.22. Frequency measurement in magnitude step change testing: (a). true value and testing result of fast responds PMU, the green lines correspond to the ± 0.005 Hz error range allowed by PMU standard; (b). testing results of a commercial PMU; (c), testing results of another commercial PMU; (d), testing results of yet another commercial PMU.

CHAPTER 7 C37.118.2 STANDARD COMPLIED FDR/UGA

7.1 Background

The current Frequency Disturbance Recorders (FDRs) and Universal Grid Analyzers (UGAs) of FNET/GridEye are using the FNET/GridEye communication protocol. Although this protocol works well with FNET/GridEye data server and OpenPDC, it is not compatible with many other data concentrators. This impedes the FNET/GridEye sensors to work with other local and wide area monitoring systems. As the PMU standard for synchrophasor data transfer is published and used by most commercial PMUs [34], it is necessary for FDR and UGA to be able to support this communication protocol. With the C37.118.2 standard compliance, the FDR/UGA can be directly used for almost all phasor data concentrators. For utility companies, the data from FDR/UGA will provide good supplementary for transmission-level PMU data.

Furthermore, the development of microgrid and distributed generators are calling for better monitoring on distribution level. For the sake of, distribution level synchrophasor is a promising sensor in the future. However, there are no synchrophasor standards for distribution level yet. Since FDR/UGA are targeting the distribution grid, applying transmission level PMU standard on it will unify their data with the transmission level PMU. It then provides an easy way to compare the difference between synchrophasors on transmission and distribution level, hence propose proper standards of accuracy on distribution synchrophasors. It also provides the possibility to test the effectiveness of using transmission level PMU communication protocol on distribution level PMUs. Experience can be accumulated on the test, and any necessary changes can therefore be proposed on the present PMU communication protocol to be adapted for distribution level.

The current data communication between FDR/UGA and FNET/GridEye server is a one-way TCT/IP communication. The communication rate equals to the FDR/UGA data rate, which is 10 Hz. For each data packet, the typical data frame is shown in Table 7.1.

There are several drawbacks of this communication protocol.

- 1) Most information are transferred using ASCII. It therefore needs one byte to represent one digit. The efficiency is fairly low.
- 2) Not every field has a constant definition. The second field (space) subjects to be occupied by UnitID if it is a 4-digit index. The field of First Frequency has 4 possible types, i.e. latitude, longitude, locked-on satellite number, and first frequency. These inconsistencies bring difficulty in data processing.
- 3) Fixed data rate. The FNET protocol uses a fixed data rate of 10 Hz. For applications dealing with fast dynamic states such as power system transient and subsynchronous oscillation,
- 4) Cannot response to phasor data concentrator (PDC). A PDC may receive data stream from multiple PMUs or PDCs with different content, rate, format, etc.

Table 7.1 Data frame of the FNET/GridEye protocol

Field	Size (bytes)	Comments
Start Byte	1	Frame starting byte, 0x01
Space	1	If the UnitID is a 4-digit index, it is the highest digit of the index. Otherwise, it is the ASCII space, 0x20.
UnitID	3	The index of FDR/UGA unit. Each byte corresponds to one digit of the index. For 4-digit index, use the space before this field as the highest digit of the index.
Space	1	ASCII space, 0x20
Date	6	Date[5-4] month, in ASCII Date[3-2] day, in ASCII Date[1-0] year, in ASCII
Space	1	ASCII space, 0x20
Time	6	Time[5-4] hour, in ASCII Time[3-2] minute, in ASCII Time[1-0] second, in ASCII
Space	1	ASCII space, 0x20
Convion Number	2	The index of the data frame in that second.
Space	1	ASCII space, 0x20
First Frequency	7	Latitude, if the frame is the first one of that minute Longitude, if the frame is the second one of that minute Locked-on satellite number, if the frame is the third one of that minute Frequency estimated in the first iteration, otherwise.
Space	1	ASCII space, 0x20
Final Frequency	7	Final estimation result of frequency
Space	1	ASCII space, 0x20
Voltage	8	RMS value of voltage
Space	1	ASCII space, 0x20
Angle	6	Voltage phase angle
Stop Byte	1	Stop byte, 0x00
Total	55	

- 5) Therefore, each stream shall include its own configuration and response to the command from PDC.
- 6) No check word. Check word is used to guarantee the data integrity during transmission. It is already observed that FNET/GridEye is vulnerable to the network transmission error. The 16-bit cyclic redundancy check (CRC) implemented by C37.118.2-2011 is helpful to reduce the transmission error.

IEEE Std. C37.118.2-2011 defines a paradigm for PMU data exchange, including a data communication protocol. In this protocol, the PMU data communication is based on the two-way communication. There are totally four types of message frame: data, configuration, header, and command. The first three types are transmitted from the data source, which could be PMU or PDC, and the last type is sent to the data source. Data message includes the measurements. Configuration includes data type, calibration factors, and other configuration information. Header is used to transmit information about the PMU, data sources, scaling, algorithms, or other information. Command frame encompasses the command from the data receiver (PDC), requesting the data source to turn on/off data frames transmission or sending specified frames.

The main challenge of applying C37.118.2 protocol into FDR/UGA includes two parts:

- 1). Dealing with mismatched information. Some information provided by FDR/UGA is not defined in C37.118.2 protocol, such as longitude and latitude information. Some user defined bytes will be used to include these information. Some other information required by C37.118.2, such as time quality and leap second flag is not provided by previous FNET protocol. They will need to be calculated. Furthermore, some information are in different format. For example, the time stamp is given by year, month, date, hour, minute, second, and subsecond in ASCII code, whereas in C37.118.2 it is defined by second-of-century (SOC), fractional second, and time base.
- 2). Two-way communication. The FNET protocol uses a one-way communication from FDR/UGA to PDC. In C37.118.2, the data source will not only stream data to the PDC, but also needs to respond to the command frame from the PDC.

7.2 Data Package Design

In this section, the data package design for FDR/UGA using C37.118.2 is described.

7.2.1 Common Fields

For each frame, there are 6 common fields, i.e. SYNC, FRAMESIZE, IDCODE, SOC, FRACSEC, and CHK, shown in Figure 7.1.

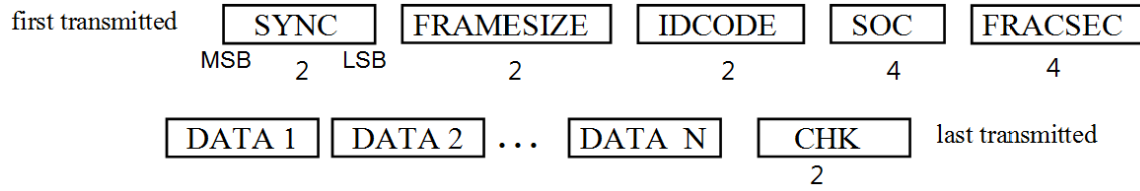


Figure 7.1. Comparison of phase angle estimation response during angle step change

The design of these common fields is described in Table 7.2.

Table 7.2 Common fields of the C37.118.2-2011 frames

Field	Size (bytes)	Comments
SYNC	2	Frame synchronize word. The first byte is 0xAA, the second byte is 0b0xxx_0010. Here xxx indicates the frame type, and the last 4 digits 0010 indicates the protocol version is IEEE Std. C37.118.2-2011.
FRAMESIZE	2	Total number of bytes in the frame.
IDCODE	2	Data stream ID number represented by XXXX_XYYY in decimal. Here XXXX_XX is the device ID of FDR/UGA, and Y is the streaming destination index. For each FDR/UGA there are up to 4 destinations.
SOC	4	Time stamp counting starting at midnight 01-Jan-1970, no leap seconds included.
FRACSEC	4	Fractional of second and time quality. Bits 31-24: Time quality. Bits 23-00: fractional of second in terms of integer number. When divided by time base yields the actual fractional second. The time base is included in the configuration frame.
CHK	2	Check word using CRC-CCITT.

Comparing to the time stamp in absolute time form given by UTC year, month, date, hour, minute, second, and subsecond, the time stamp in C37.118.2-2011 is represented in a relative form which is calculated by the equation below.

$$\text{Time} = \text{SOC} + \text{FRACSEC}[23:0] / \text{TIME_BASE}. \quad (7.1)$$

SOC is the time stamp counting starting at midnight of 01-Jan-1970 and no leap seconds are included. The subsecond part is given by two integer numbers: the lower 24-bit of FRACSEC and the TIME_BASE in configuration frame. Since in most cases the time stamp is evenly distributed over the whole time and the reporting rate is integer, TIME_BASE can be simply filled by the reporting rate and FRACSEC[23..0] by the counting of the reporting measurement in each second.

The higher 8-bit of FRACSEC deals with leap second and time quality. The definition is shown in Table 7.3.

Table 7.3 Bit definition of leap second and time quality of FRACSEC[31..24]

Bit	Comments
7	Reserved
6	Leap second direction 0: add one second 1: delete one second
5	Leap second occurred: set in the first second after the leap second occurs and remains for 24 hours
4	Leap second pending: set between 1 second to 60 second before a leap second occurs, and cleared in the second after the leap second occurs
3-0	Time quality indicator code.

Leap second is a one-second adjustment to the UTC in order to keep the time of UTC day close to the mean solar time. When the leap second arrives, one extra second is added or deducted from the UTC time. It is critical for PMUs to handle the leap second in a correct way, otherwise the PMU may lose synchronous [194]. In the implementation of FDR/UGA, the leap second information will be obtained from the GPS receiver, and indicated in corresponding SOC and FRACSET[6..4].

Time quality indicator code is to indicate the maximum time error. When the FDR/UGA is locked to UTC source, it will be 0x0000. Otherwise, the time uncertainty is calculated according to the time drift rate of the internal oscillator and the time. The information of the indicator is shown in Table 7.4.

Table 7.4 Definition of the time quality indicator

Value	Comments
1111	Clock failure.
1011	Time within 10 s of UTC
1010	Time within 1 s of UTC
1001	Time within 10^{-1} s of UTC
1000	Time within 10^{-2} s of UTC
0111	Time within 10^{-3} s of UTC
0110	Time within 10^{-4} s of UTC
0101	Time within 10^{-5} s of UTC
0100	Time within 10^{-6} s of UTC
0011	Time within 10^{-7} s of UTC
0010	Time within 10^{-8} s of UTC
0001	Time within 10^{-9} s of UTC
0000	Locked to the UTC source

The check word (CHK) is calculated using CRC-CCITT algorithm. The related code is given in Appendix B

7.2.2 Data Frame

The data frame mainly contains the measured data. The single phase voltage magnitude, phase angle, and frequency are included in the corresponding fields, together with first frequency, longitude, latitude, and GPS satellite number in the user-defined ANALOG field. The design of the data frame is shown in Table 7.5.

The PMU time quality in STAT field is different from the time quality indicator shown in Table 7.4. The latter will be 0 when the synchrophasor is locked to the time source, while the former indicates the time error during lock condition. The content of the field is supposed to be provided by the time source when the protocol is designed. Here we use 0b111 to indicate time error unknown since it is not provided by the GPS receiver used here.

7.2.3 Configuration Frame

Configuration frame contains the configuration information of the synchrophasor data stream, and includes parameters used for data processing. There are totally three types of configuration frames specified by the standard.

Configuration frame 1 (CFG-1) mainly denotes the capability of the synchrophasor and indicates all the data can be reported. Configuration frame 2 (CFG-2) indicates the measurements currently being reported in the data frame. Both frames have identical structure, as shown in Table 7.6.

Configuration frame 3 (CFG-3) is similar to CFG-2 but with variable length fields, added synchrophasor and signal information, and extendable frame. The main advantage of this frame is to enable large frame transmission, and expand the phasor and analog scaling to include a multiplier and offset. This frame is optional. As CFG-1 and CFG-2 have already covered all the fields needed for the data transmission between FDR/UGA and the data server, CFG-3 here is not used.

7.2.4 Header Frame

The header frame is to pass human-readable information about the synchrophasor, scaling, algorithms, etc. All the data contents are transmitted in ASCII characters, shown in Table 7.7.

To save the bandwidth and simplify the design, only a short message including device name, ID, and reporting rate is included in the DATA field. The content is restored in MCU.

Table 7.5 Data frame design for FDR/UGA

Field	Size (bytes)	Comments
SYNC	2	Frame synchronize word. 0xAA02
FRAMESIZE	2	Total number of bytes in the frame.
IDCODE	2	Data stream ID number.
SOC	4	Second of century.
FRACSEC	4	Fractional of second and time quality.
STAT	2	Bits 15-14: Data error indicator. 00 for good measurement 10 when PMU in test mode 11 when the check of data received by MCU from DSP indicates error. Bit 13: PMU sync. 1 when locked to GPS, 0 otherwise. Bit 12: 0, data sorting by time stamp. Bit 11: 0, no trigger. Bit 10: usually 0 since no configuration changes during operation, 1 otherwise. Bit 9: 0, no data modified. Bits 8-6: PMU time quality. Bits 5-4: unlocked time. 00: for unlocked time < 10 s 01: $10\text{ s} \leq \text{unlocked time} < 100\text{ s}$ 10: $100\text{ s} \leq \text{unlocked time} \leq 1000\text{ s}$ 11: unlocked time > 1000 s Bits 3-0: trigger reason. 0000 since no trigger by FDR/UGA.
PHASORS	4	In polar format. Magnitude first in 16-bit unsigned integer, followed by angle by 16- bit signed integer, in radians $\times 10^4$.
FREQ	2	Frequency deviation from nominal in mHz, given by the 16 bit integer.
DFREQ	2	ROCOF, in Hz/s $\times 100$, by 16-bit integer.
ANALOG	8	User defined analog word, including 4 values, representing first frequency, longitude, latitude, and satellite number, in sequence by 16-bit integer.
DIGITAL	0	DO NOT USE
CHK	2	Check word using CRC-CCITT.

Table 7.6 Configuration frame 1 and 2 design for FDR/UGA

Field	Size (bytes)	Comments
SYNC	2	Frame synchronize word. 0xAA22 (CFG-1), or 0xAA32 (CFG-2).
FRAMESIZE	2	Total number of bytes in the frame.
IDCODE	2	Data steam ID number.
SOC	4	Second of century.
FRACSEC	4	Fractional of second and time quality.
TIME_BASE	4	Resolution of FRACSEC. Here the reporting rate is used as TIME-BASE. E.g., when reporting rate is 10 Hz, TIME-BASE is 0x000A.
NUM_PMU	2	Number of PMUs. 0x01.
STN	16	Station name in 16 byte ACSII. Do not use this currently since FDR/UGA may subject to relocate. IDCODE is used to determine the station.
IDCODE	2	The same as the IDCODE in the 3 rd field here.
FORMAT	2	Data format in data frame, 0x01. Bits 15-4, unused. Fill with 0. Bit 3:0 indicates FREQ/DFREQ using 16-bit integer. Bit 2: 0 indicates analogs use 16-bit integer. Bit 1: 0 indicates phasor using 16-bit integer. Bit 0: 1 indicates phasor using polar format.
PHNMR	2	Number of phasors: 0x01.
ANNMR	2	Number of analog values: 0x04.
DGNMR	2	Number of digital status words: 0x00.
CHNAM	80	Phasor and channel name, 16 bytes for each channel in ASCII. Phasor: 0x0000_566F_6C74_6267_6520_5068_6173_6F72 (Voltage Phasor) Analog: 0x0000_0000_0000_004C_6F6E_6769_7475_6465 (Longitude) 0x0000_0000_0000_0000_4C61_7469_7475_6465 (Latitude) 0x0053_6174_656C_6C69_7465_4E75_6D62_6572 (Satellite Number)
PHUNIT	4	Conversion factor for phasor channel. 0x0000_2710, (10,000).
ANUNIT	16	Conversion factor for longitude, 0x0000_2710, (10,000). Conversion factor for latidue, 0x0000_2710, (10,000). Conversion factor for satellite number, 0x0000_0001, (1).
DIGUNIT	0	-
FNOM	2	Nominal line frequency code. Bits 15-1, reserved. Fill with 0. Bit 0: 0 – fundamental frequency = 60 Hz; 1 – fundamental frequency = 50 Hz.
CFGCNT	2	Configuration change count. Use 0 if no changes.
DATA_RATE	2	Data rate.
CHK	2	Check word using CRC-CCITT.
Total	154	

Table 7.7 Header frame design for FDR/UGA

Field	Size (bytes)	Comments
SYNC	2	Frame synchronize word. 0xAA12.
FRAMESIZE	2	Total number of bytes in the frame.
IDCODE	2	Data steam ID number.
SOC	4	Second of century.
FRACSEC	4	Fractional of second and time quality.
DATA	1	ASCII character, 1 byte each. Multiple bytes supported.
CHK	2	Check word using CRC-CCITT.

7.2.5 Command Frame

The command frame is usually sent by the PDC to the synchrophasor. The commands include turning on/off transmission of data frames, sending header frame or configuration frame, etc. To enable the FDR/UGA to response to the command frame, the corresponding MCU codes of the FDR/UGA are added, the procedure is shown in Figure 7.2.

The design of the command frame is shown in Table 7.8. Here the 6 commands defined by the PMU standards is realized, as shown in Table 7.9. The commands include starting/stopping data frames transmission, sending header frame, and sending one of the configuration frames. These commands are used by PDC software to communicate with the PMU and control the data streaming. It guarantees the capability of FDRs/UGAs to correctly communicate with PDC and improves their interoperability by realizing these commands.

7.3 Realization and Testing

The C37.118.2-2011 complied communication is realized in MCU/ARM of FDR/UGA including all the data packages designed in 7.2. The diagram is shown in Figure 7.3.

GPS time is streamed to the common field generator to form the common field together with the FDR/UGA ID. Each of the three frames to be streamed out, i.e. data frame, configuration frame, and header frame, uses the common field as the frame head, and fills the SYNC field with the type of the frame. For the data frame, the measurement results parsed from the SPI module and the GPS status including geographic coordinator and satellite number from the GPS module are used to form the frame. Checksum generator is called by each of these three generators to generate the CRC checksum as the end of the frame. The frame streaming control module controls the streaming of all these frames. In default, it streams out every data frame. This control module reads the command sent from PDC and parsed by the command parse module. It executes to each command, such as data frame streaming turn on/off, and configuration frame or header frame streaming. The frames to be send out are fed into the Ethernet module. Command parse module

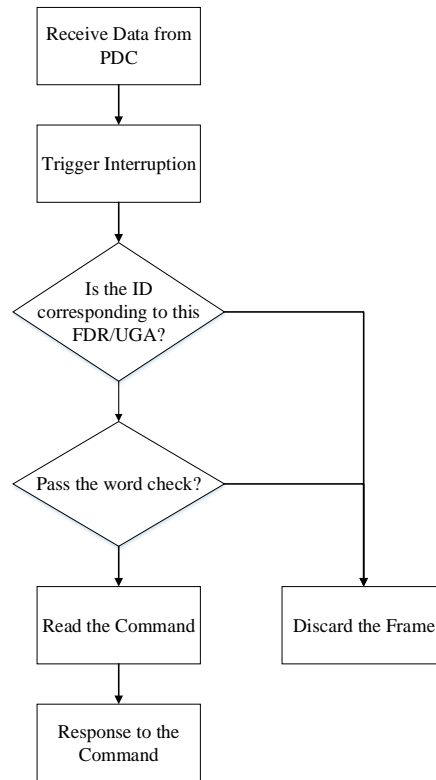


Figure 7.2. Procedure to responding to the command frame

Table 7.8 Command frame design for FDR/UGA

Field	Size (bytes)	Comments
SYNC	2	Frame synchronize word. 0xAA12.
FRAMESIZE	2	Total number of bytes in the frame.
IDCODE	2	Data steam ID number.
SOC	4	Second of century.
FRACSEC	4	Fractional of second and time quality.
CMD	2	ASCII character, 1 byte each. Multiplee bytes supported.
EXTFRAME	0-65518	Extended frame data, 16-bit words, 0 to 65518 bytes as indicated by frame size, data user defined.
CHK	2	Check word using CRC-CCITT.

Table 7.9 Command sent to FDR/UGA

Command word bits	Comments
Bits 15-0 (in Hex):	Corresponds to the CMD field in command frame
0x001	Stop data frames transmission
0x002	Start data frames transmission
0x003	Send header frame
0x004	Send CFG-1 frame
0x005	Send CFG-2 frame

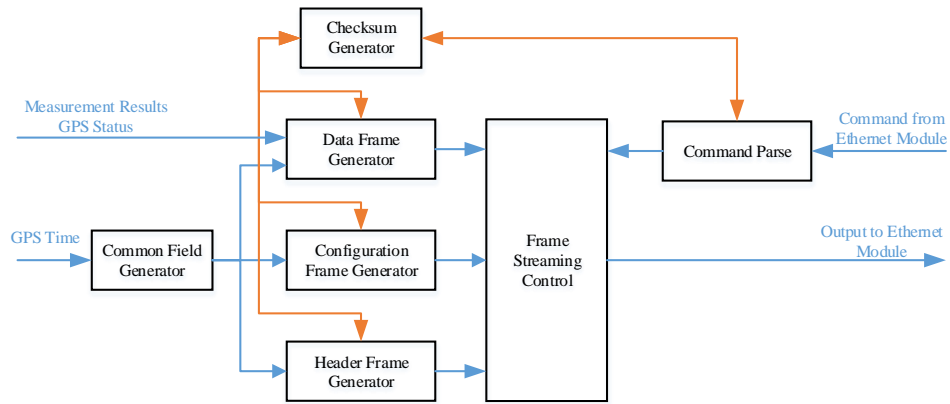


Figure 7.3. Diagram of the C37.118.2 communication module

reads data from the Ethernet module and calls the checksum generator to check the correctness of the command frame.

The realized FDR/UGA are tested with PMUConnectionTester, openPDC, and openHistorian developed by Grid Protection Alliance (GPA). All the commands are responded correctly, and the data are received by these PDC software with no data loss. Long term test shows that the performance of the C37.118.2 complied FDR/UGA are with reliable data streaming.

7.4 Conclusion

In the WAMS and smartgrid, multiple types of synchrophasors from different vendors need to work together with various PDCs, networks, systems, and synchrophasor-based applications. To ensure the security and effectiveness of data communication and information exchange, it is extremely important to ensure the interoperability of different devices and systems. C37.118.2 standard defines the data frame structure protocol and ensures the interoperability of synchrophasors in data communication. In this chapter, the C37.118.2 complied FDR/UGA are developed. The data packages are defined according to the standard requirement and curtailed according to the reality of the FDR/UGA. It is realized in hardware and tested against three commercial available PDC software products. The testing verifies the correctness of data and functions, and the long-term reliability of the communication. It proves that the developed FDR/UGA is compliance with C37.118.2-2011 standard.

CHAPTER 8 PMU MEASUREMENT APPLICATION FOR AUTHENTICATION AND CYBER SECURITY

The electric network frequency (ENF), which is the frequency of the power system fluctuating around the nominal value (50 Hz or 60 Hz), is a sensitive and reliable indicator of the balance between the generation and load. Since this imbalance changes over the time and is non-repeatable, it is with strong temporal character. Meanwhile, the local noise, which is hard to spread out into the whole grid, gives a strong spatial character to the ENF measured at different locations. With these two signatures, the ENF is becoming a useful forensic tool for recorded media authentication. It can also be used for cyber security detection since the attacked data usually lost the spatial and temporal characters hence can be detected.

8.1 Introduction

Though it is not well understood the phenomenology by which sinusoidal grid voltage signals find their way onto recordings made using battery powered digital recorders, it is assured that the signal being observed was actually a grid sinusoidal voltage signal. After Grigoros firstly proposed to use ENF as a signature for multimedia recordings authentication, numerous work are conducted to use ENF to ascertain the created time and location of recordings [195-198]. Past work mainly focused on how to effectively extract the ENF from recordings. The work in this chapter, however, will mainly focus on the method to recognize the time and source location of the recording, with an extracted signal and a database or historical ENF signals acquired in a wide area. Specifically, as WAMSs continuously collect time synchronized frequency and phase angle measurements from a large area with high accuracy and rate, it is a very suitable database for ENF based authentication.

The capability of previous research to determine the recording location is limited to the size of one interconnected grid. It is desirable to have a better spatial resolution. With over 200 data sources widely deployed in North American power grid, FNET/GridEye system provides a great opportunity to look into this topic. The FDR deployment map in the North America is shown in Figure 8.1.

Variations among ENF signals within the same grid are due to the local load characteristics. The responses of turning on and off of large loads, the using of inductance loads and power converters, and the electromagnetic interference introduce noise into the ENF. As the load combination, switching characters, and the topology of distribution lines are different from place to place, these ‘background noises’ have unique spatial characters. They are usually of high frequency and low amplitude, therefore are only observable ‘locally’ and hard to spread out along the power grid. These local characters at different places are recorded by the local frequency measurement devices such as FDRs. Thus by using the noise characteristics, the location of a target frequency signal can be identified by comparing it with historical data from different places. Wide area power grid frequency measurement system, such as FNET, can provide the historical data

with high geography density and long time period, which can be used as a complete dictionary to identify the location of target frequency.



Figure 8.1. FDRs in North American power system

The frequency of the power system mainly depends on the balance between generation and loads, and the system inertia, all of which vary from time to time. Therefore, ENF of each power grid has obvious temporal characteristics. As this feature is extracted and compared with historical data, the timestamp of the target signal can be determined. For the real time signal, the comparison of the tempering feature between multiple ENF measurement sources enables the cyber-attack detection and possible data correction.

In this chapter, the methodology used to extract the spatial and temporal features of the ENF is discussed. Then the spatial and temporal feature based data authentication applications are developed and tested. Finally the conclusion is given.

8.2 Methodology

8.2.1 Spatial Feature Extraction and Pattern Recognition

To determine the location of the target signal, it basically needs two steps: 1) extracting the characteristics of the noise from target frequency, and 2) comparing the extracted characteristics with historical data from different places. Therefore, a method needs to be developed to extract the characteristics of noises while filtering out the common part. In addition, a pattern recognition method needs to be used to identify the location of the target signal.

Here frequency domain analysis is employed to get the characteristics of signals. Due to the location dependent feature, the background noise shows different statistical characteristics in the frequency domain. To extract these characteristics, the “noise” is obtained by removing the common part, and then short-time Fourier transform (STFT) method is performed, as shown in Figure 8.2. The ENF from each measurement unit is first subtracted by the median value of the ENF of all units, then it is divided into many time serial segments. By taking STFT, each segment is converted into a group of features. The ENF of each unit becomes a large amount of samples, each with a group of features.

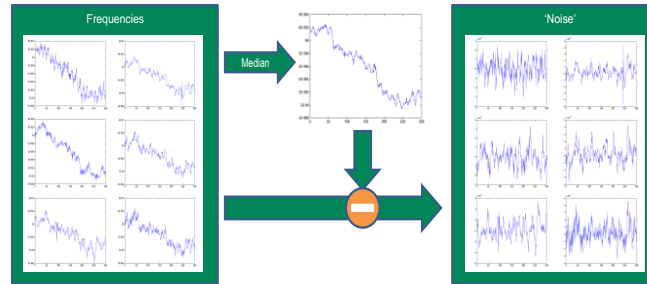


Figure 8.2. STFT based spatial feature extraction

Neural Network, as a powerful and intelligent data analysis tool, can be used for pattern recognition. It is used to predict the ‘label’ of each unknown sample by using its ‘features’. The implementation of Neural Network can be divided into two steps. In the first step, a group of data with labels and features are used to train and validate the Neural Network. Then the features of the target signals are input into this Neural Network and its label is predicted, as shown in Figure 8.3.

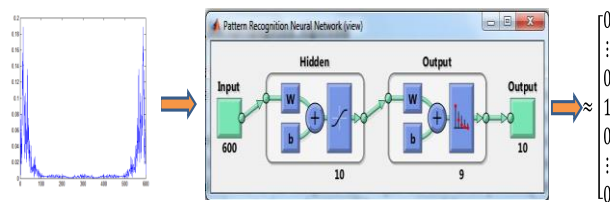


Figure 8.3. Neural network based pattern recognition

In ENF spatial recognition, the features are obtained through STFT, and the labels are their unit IDs, each corresponding to a special location. The samples with features from historical data are used to train the neural network, and the STFT of the target ENF signal is input into the trained network to identify its location. This method can also be used for

PMU ID swap attack, in which sophisticated attackers swap the PMU IDs of each measurement data. The diagram is shown in Figure 8.4.

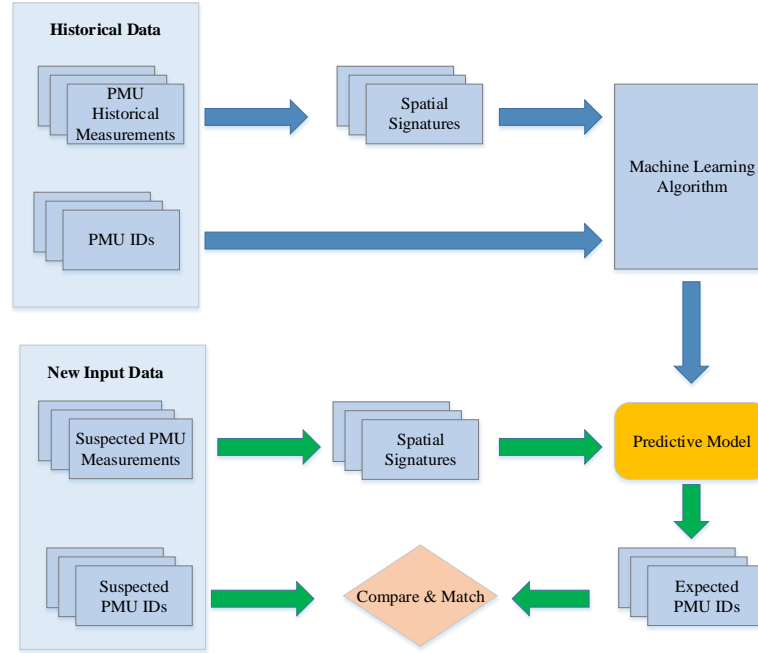


Figure 8.4. Diagram of spatial signature based data authentication using a machine learning method

8.2.2 Temporal Feature Extraction and Pattern Recognition

As the frequency of the interconnected AC power grid is synchronized, the frequency measured in different places contains common trend, which depicts the change of balance between the power generated by plants and consumed by loads in the power grid. This trend includes unique time signature, and therefore can be used for temporal detection.

In this method, temporal signatures of ENF measurements from confirmed units over a common time period can be divided into a lot of segments and used as the benchmark. The temporal signature of the target ENF is extracted and compared with the benchmark segment by segment. Correlation index is used to quantify the mismatch between them. A threshold is used to flag the time tag of the target to be detected.

The STFT again can be used for signature extraction. To reserve the common trend of the signals, average filter is used ahead of the STFT. To fully utilize the features of the signal and minimize the time consumption, a recursive algorithm is used. For each time index, a group of time segments are input into the data window, and the temporal feature is extracted. Then the new segments is fed into the data window, and the oldest segment is excluded. The diagram is shown in Figure 8.5.

Similar to the spatial authentication, this method can be used for temporal data attack detection. When the timestamp of one PMU is distorted, neighboring units can be used as the benchmark to detect the timestamp attack.

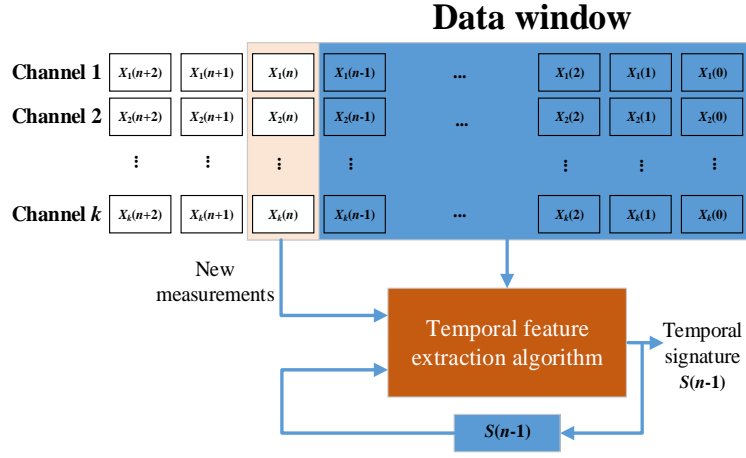


Figure 8.5. Illustration of recursive temporal signature extraction

8.3 Spatial Feature Based Data Authentication

Different scales of the spatial allocation of measurements are tested using the proposed method. In the Case A, five units connected to the same power grid in different states are tested. Distances between them are at the level of hundreds of miles. The locations of these units are shown in Figure 8.6.

In the test, 30 minutes historical data are used for training, and 1 minute target data is used for data source detection. The data rate of the measurements is 10 Hz. It is found that when the target data is 1 day away from the historical data, the match accuracy is about 99.8%. Extending this time interval, the match accuracy decreases, mainly due to the changing of the local signature over time. When the time interval is increased to 1 year, there is still 80% accuracy.

In Case B, the geographical scaled is shrunk to be within the same city. The distances between the five units are just a few miles, as shown in Figure 8.7.

For fair comparison, the amounts of data used for training and testing are the same as Case A. It is found that even when the time interval is 0, meaning the training data is adjacent to the target data, the accuracy rate is 91.6%. Then it dramatically dropped to below 80% when the time interval extends to 1 day. This is probably because the local signature of ENF between these locations are very similar and the method cannot be fully trained to tell the difference.



Figure 8.6. Data source locations of Case A. Yellow marks are the locations where measurement units are installed.

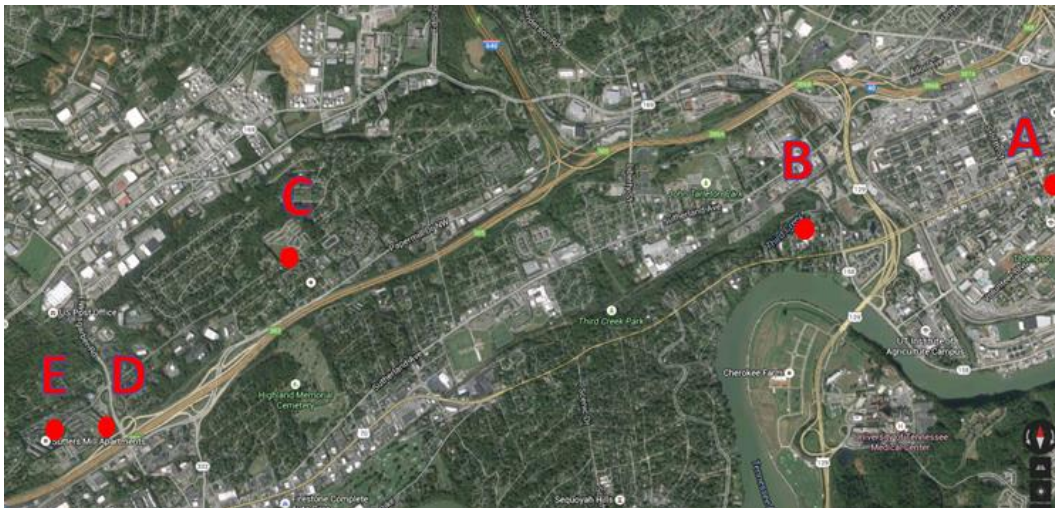


Figure 8.7. Data source locations of Case B. Red dots are the locations where measurement units are installed.

When using the units with reporting rate of 120 Hz, the recognition is raised to 95% for 1 day interval. This is mainly because more information is included as the reporting rate raises, especially those high frequency characteristics which are aliased in low reporting rate. The comparison of different data rates and ENF signal segment lengths are compared in Figure 8.8.

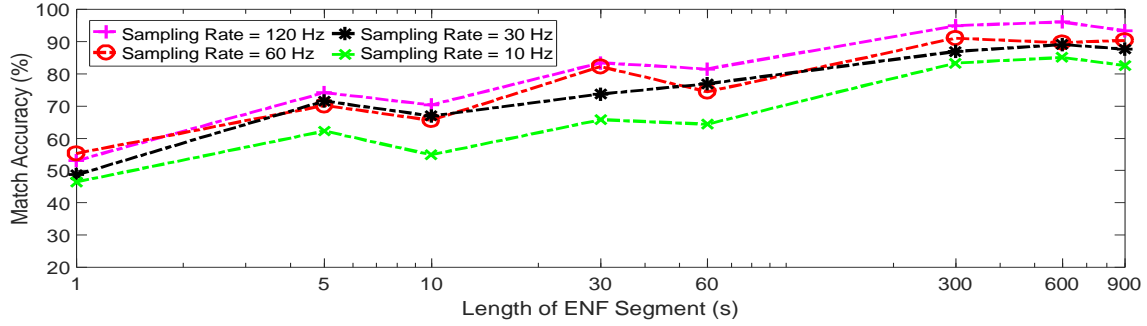


Figure 8.8. Match accuracy comparison of different ENG segments length and sampling rate

Furthermore, it is found that, even in the same building, there are obvious different patterns between each of the three phases. Therefore, they can be told apart, as shown in Figure 8.9. This can also be used for phase identification in distribution systems.

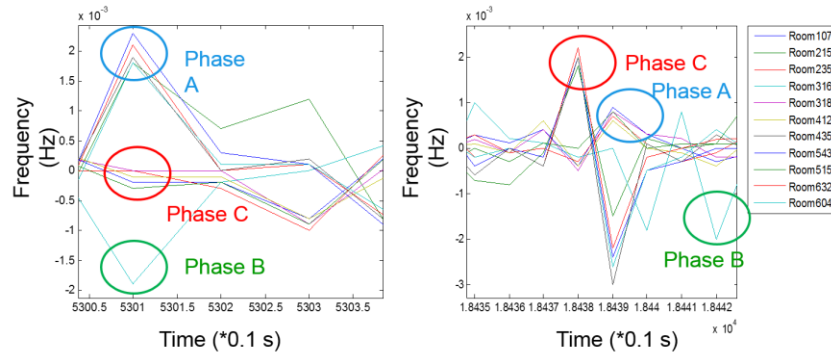


Figure 8.9. Two cases of the ENF measurement in the same building.

8.4 Temporal Signature Based Data Authentication

An example of the temporal signal detection result is shown in Figure 8.10. The correct starting time of the target signal is 100 s. As the data window is sliding, the correlation coefficients between the target and the benchmark are calculated and plotted. It is obvious that at 100 s, a peak is shown, corresponding to the time stamp to be estimated.

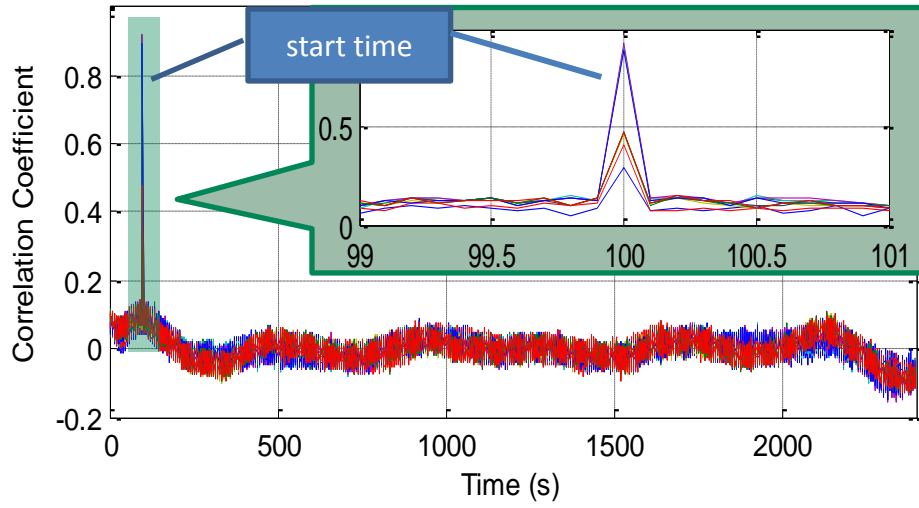


Figure 8.10. Example of temporal signature based authentication.

Testing shows that only 1 s of the target signal is needed to correctly identify its timestamp. With higher reporting rate measurement units, the required time length and the time resolution can be achieved will be even shorter.

8.5 Conclusion

In this chapter, the WAMS based data authentication application is proposed. The spatial and temporal features of the ENF signal obtained from WAMS can be used for data source location and timestamp identification. In source location, the features of historical signals are extracted and used to train a Neural Network model. The model is then used to estimate the location of the target signal. It is found that the location can be corrected told in a range of hundreds miles. With higher reporting rate units, it can be minimized to several miles. For timestamp identification, the features of historical data are compared with the target signal. The timestamp can be correctly identified. These applications can be used to detect sophisticated WAMS cyber-attack, such as PMU ID attack and timestamp attack.

CHAPTER 9 TIME SYNCHRONIZATION INTERVAL ATTACK IN SMART GRID: IMPACT AND DETECTION

9.1 Introduction

Synchrophasor provides essential measurements for smart grid applications. In the measurements, timing plays an important role. First of all, sampling of PMUs are synchronized by the timing signal, to ensure all the measurements are synchronized. Otherwise, the comparison of these timing variables, especially the phase angle, becomes meaningless. Secondly, the measurements are tagged with time. The correct times stamps enables the applications to align the measurements transmitted from multiple remote PMUs without disturbing by different transmission delay and possible data losses. Thirdly, many PMUs relies on the synchronized and precise timing source to discipline its internal clock so as to ensure accurate sampling rate.

Because of the reasons listed above, time-synchronization signal is essential for the data quality of the PMUs. Nowadays, most PMUs relies on GPS directly or indirectly for time synchronization. Some PMUs include GPS receivers and are capable of receiving GPS signals from a GPS antenna. Some others get the timing signal via IRIG-B, a timing synchronization format which is usually provided by a substation clock. The substation clock receives the GPS signals from satellites, transformed the timing into IRIG-B format, and distributed to multiple devices requiring synchronized timing.

GPS signal, however, is vulnerable to short- and long-term outage, space weather interference, malicious attack, etc. Alternative timing sources are proposed. E.g., Precision Time Protocol (PTP) governed by IEEE Std. 1588-2008, provides solution for timing distribution via Ethernet, and the clocks can be synchronized within a microsecond to each other.

PMU network is vulnerable to cyber-attacks in different ways. Many of the attacks are incepted through transmission network, as synchrophasor measurements are streamed out using TCP/IP and/or UDP/IP. These attacks include Denial of Service (DoS) attacks, record and replay attacks, modification attacks, side channel attacks, etc. Cybersecurity technologies are developed to deal with these attacks. Time synchronous attacks (TSAs) is another type of attack which brings concerns recently. This kind of attack spoofs the timing signal achieved by PMUs and results wrong estimation of synchrophasors, finally lead to the false outputs of WAMS. This attack does not alternates any data packets output by PMUs, and therefore can hardly be detected by the usual cybersecurity technologies. However, as timing is critical to WAMS, TSAs are possible to cause large impact on WAMS applications.

In the past researches, it proves that both GPS and PTP are vulnerable to spoofing attacks [199-201]. The studies of TSA mainly focused on consistent timing error injection [202-204]. In these attacks, the synchronized time and time tags are shifted from UTC, and a

phase angle error is introduced. The impact on different WAMS applications are analyzed.

In this chapter, another type of TSA, naming Time Synchronization Interval Attack (TSIA) is investigated. In this attack, the interval of time synchronization signals are under attack. Pulse per second (PPS) signal synchronized to the timing source is used to provide synchronization signal for PMUs. TSIA changes the interval of adjacent PPSs. This change influences the sampling rate and starting time of each synchronized sampling of PMU and introduce errors. Compared to TSAs shifting the time, this type of attack may be harder to detect, as it is possible to introduce a very small error at the beginning of the attack, and then increases to the extent to affect applications.

The arrangement of this chapter is as follows. In Section 9.2, the TSIA model is built up, by studying the possible TSIA types. Then the impact of TSIA is analyzed from aspects of measurement errors and synchrophasor based applications in Section 9.3. The type and parameters of TSIA which could cause serious impacts are then analyzed and the detection methods are provided in Section 9.4. Section 9.5 concludes this chapter.

9.2 TSIA Model

9.2.1 Time Synchronization Interval Overview

PPS signal is either generated by the time receiver, e.g. GPS receiver, or included in the input time signal, e.g. IRIG-B. For the GPS receiver, the on-board oscillator is disciplined by the GPS time. When GPS time is altered due to attack, the oscillator is disciplined by an inaccurate reference and the error is introduced into the PPS. For a GPS receiver, the synchronous time usually refers to the coordinator universal time (UTC) disseminated by GPS and given by

$$t_{UTC} = t_{osc} + t_c, \quad (9.1)$$

where t_{osc} is the time provided by local oscillator inside the GPS receiver, and t_c is the time correction for the GPS receiver's clock calculated from navigation equations.

During GPS spoofing, the incorrect navigation information is provided by the spoofing source, and incorrect t_c is obtained, hence introduces error to t_{UTC} and PPS.

Sophisticated GPS attacker can use a two-step spoofing strategy to lead the GPS receiver track the counterfeit signal [204]. Most GPS receivers use unauthenticated civilian GPS which can be easily mimicked by malicious attacker.

Almost all commercial PMUs support the IRIG-B signal based time synchronization. In many substations, a clock disciplined by GPS generates IRIG-B signal and distributes to time synchronized devices, such as PMU. In the two most common formats of IRIG-B signal, the direct current level shift (DCLS), which is an unmodulated type, is mostly used for substations due to its higher time accuracy at the order of ± 500 ns [202]. The rising edge of the first bit of each IRIG-B frame is aligned to the beginning of each

second. It is used to trigger to rising edge of the PPS signal. If IRIG-B signal is attacked, and replaced by the spoofed signal, it is possible for the attacker to change the time interval between PPS rising edge.

9.2.2 Attack Strategy

There are generally two possible ways to attack the PPS signal, i.e.

1. PPS signal shifting. The length of PPS signal remain unchanged, but the starting time of each PPS is shifted with a delay from the UTC time.
2. Change the PPS length. It also includes the mixture of shifting and changing of PPS interval.

The impact of PPS signal shifting and mitigation are discussed in quite a few of literatures [200, 202, 204, 205]. The changing of PPS length, however, has not been studied according to the best knowledge of the author. In this chapter, the PPS attack in terms of changing PPS interval is discussed. Denote a serial of UTC time $t(n)$, the time impacted TSA can be represented by

$$t_r(n) = t(n) + t_{err}(n) \quad (9.2)$$

where $t_r(n)$ is the time received by synchronous devices, and $t_{err}(n)$ is the time error introduced by attack. If $t_{err}(n)$ is a constant value, it is a PPS signal shifting attack. If $t_{err}(n)$ changes with n , it indicates the PPS length changes.

9.3 Impact Analysis

9.3.1 Measurement Error Derived from TSIA

As the PMU samplings are synchronized to the UTC time, shifting the PPS will introduce a constant error in phase angle estimation, as show in Figure 9.1.

If not considering the intrinsic error of PMU, this phase angle error is proportional to the time shift, given by

$$\theta_{err} = \omega t_{err}, \quad (9.3)$$

where θ_{err} is the phase angle error, ω is the frequency of the input signal, and t_{err} is the time shifting error.

The sampling rate of the PMU is usually generated by its internal oscillator. Most PMUs use synchronous sampling, i.e. the sampling time are aligned between all PMUs, and the sampling interval is a constant value. To achieve this, the sampling clock for ADC is trigger by the PPS signal, and the sampling interval is tuned according to the PPS interval, to conquer the drift of PMU's internal oscillator. Assume the nominal sampling rate is f_{s-nom} , a factor N is used to generate this sampling rate from PPS by using a PLL:

$$\frac{N}{T_{PPS}} = f_{s-nom} \quad (9.4)$$

where T_{PPS} is the time interval of PPS signal, i.e. 1 sec.

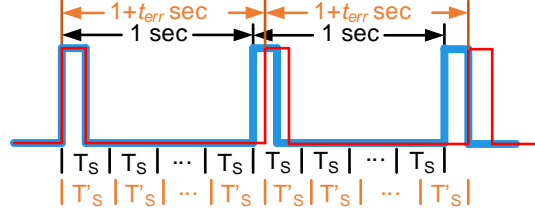


Figure 9.1. Sampling rate changed due to PPS error

When T_{PPS} is altered under attack, the sampling rate will also change.

$$f_{s-atk}(n) = \frac{N}{T_{PPS} + \epsilon_{PPS}(n)} \quad (9.5)$$

$\epsilon_{PPS}(n)$ here represents the PPS error introduced by TSIA. The phase angle, magnitude, and frequency estimated by PMU may all subject to change due to the sampling rate error. The influence on these estimations are evaluated. A signal sampled using the impacted sampling rate is injected into the phasor and frequency estimation algorithm, and the estimation error is obtained.

For the PPS interval with a constant change, the sampling rate is a fixed value deviated from the nominal rate. The impact on magnitude, phase angle, and frequency are shown in Figure 9.2 and Figure 9.3.

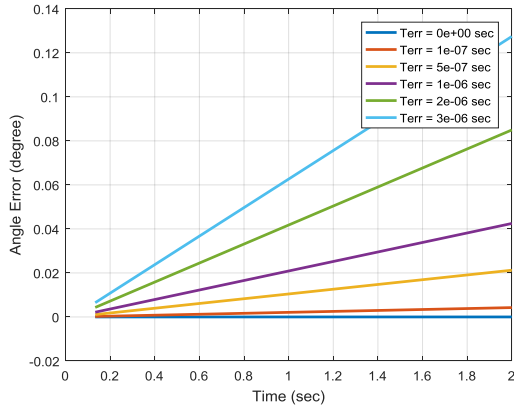
It can be observed that the phase angle changes over time, and its changing rate is proportional to the PPS error.

$$\epsilon_{\theta}(n) = \omega t_{err} = \omega \epsilon_{PPS} n \quad (9.6)$$

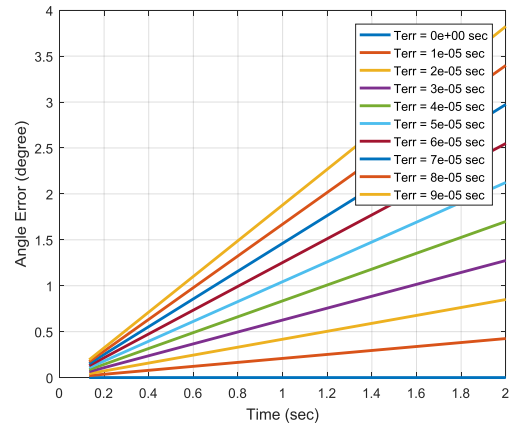
A larger PPS error is able to make the phase angle error reach several degrees in just a few seconds, while a small PPS error causes phase angle error to increase very slowly, but could also reach a large value after enough time length.

The frequency error during constant PPS interval changes is a constant value. This is understandable as frequency is the differentiation of the phase angle. The relation of frequency error and PPS deviation can be represented by

$$\epsilon(\omega) = \omega \epsilon_{PPS}. \quad (9.7)$$

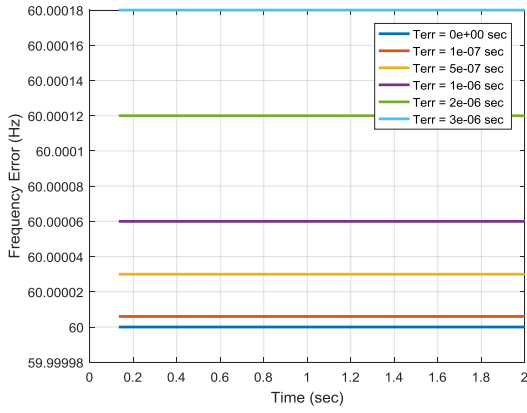


(a)

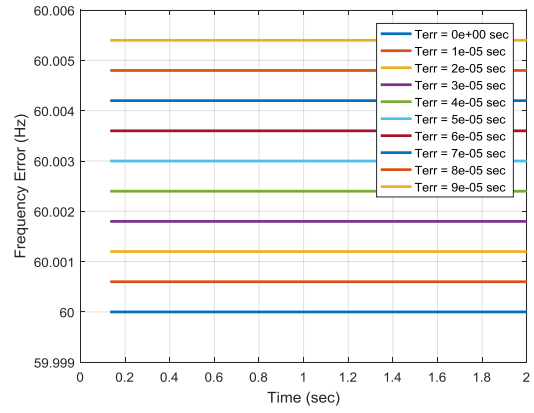


(b)

Figure 9.2. Phase angle error regarding different PPS errors



(a)



(b)

Figure 9.3. Frequency error regarding different PPS errors

9.3.2 Synchrophasor Based Applications Vulnerability to TSIA

A lot of power system applications have been developed or in use based on the synchronous measurement including phase angle, voltage/current magnitude, and frequency. The error induced by the PPS attack, if not eliminated, could downgrade the performance of these applications, and could even cause them failure. In the past researches, the impact of TSA on several applications are studied and listed in Table 9.1.

Table 9.1 Vulnerability of synchrophasor based applications to TSIA

Application	Impact	Notes
Phase angle monitoring [202]	2.7° error causes 12% power flow error (NORDIC)	Depends on the power grid
Anti-islanding protection (angle-based) [202]	8° for 10 cycles activates protection scheme (IEEE 9-Bus system)	Larger mismatch accelerates the action
Oscillation damping control [202]	10.73° error increases 13% over shoot and 15.4% setting time 35.6° error causes negative damping (Kundur system model)	Smaller error, though may not cause negative damping, increases overshoot and setting time
Line fault detection and location [204]	20° error: 50 km error (3Φ-G) 10° error: 220 km error (L-G) 10° error: 50 km error (L-L)	Transmission line dependent
Voltage stability [204]	Decrease the active power delivered margin 10° error: from 7.8 p.u. to 0.8 p.u.	Misleads the system to implement wrong actions of voltage stabilization
Event location (TDOA based) [204]	1 sec error causes 35 km	

It can be seen that most applications will be impacted when the phase angle error surpasses 10°. Therefore, it is critical to detect any attacks which introduce an error larger than 10°. For those attacks inducing slowly increasing angle error, they should be detected before the error is accumulated to 10° so as to prevent the impact on corresponding applications.

9.4 TSIA Detection

For the constant PPS interval change, the time used to achieve specific phase angle error is proportional to the PPS interval error. For a large interval error, it can quickly reach a large phase angle error. Meanwhile, the frequency error is also proportional to the PPS interval error. Therefore, it is possible to detect the large PPS interval change by the change of frequency. The relation of PPS interval error with the time to achieve assigned phase angle error and frequency error are plotted in Figure 9.4.

Considering the small frequency differences between PMUs at different locations of the same power grid, it is possible to detect the PPS interval change if the frequency deviation is large. For the Eastern Interconnection, the frequency difference is usually within 0.004 Hz. To make a conservative assumption, 0.006 Hz is used as the threshold for PPS interval detection, which is corresponding to a 100 μ s attack at $f = 60$ Hz.

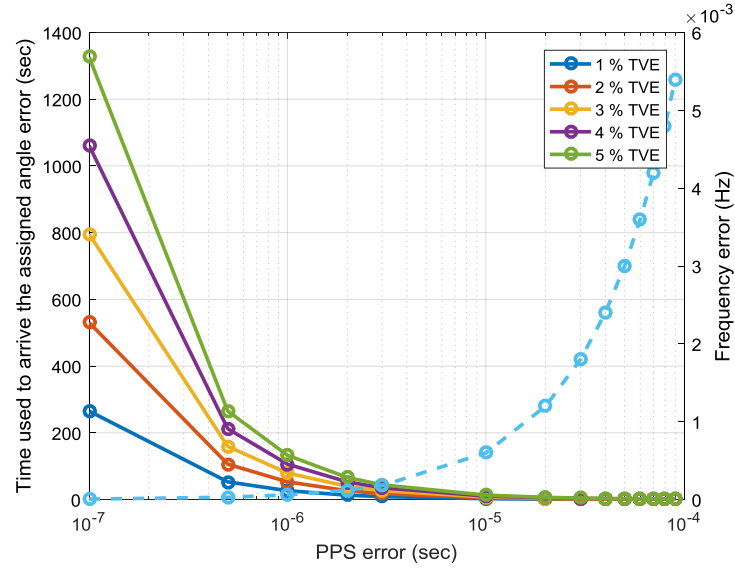


Figure 9.4. Frequency error and the time to achieve specified TVE regarding to different PPS error

For a fixed system frequency, the frequency measured by the PMU under attack shows a step change and then remains an unchanged frequency deviation. As system frequency does not change abruptly, the step change can be told by calculating the rate of change of frequency (ROCOF). At the frequency step change, ROCOF will show a large peak or dip, which can be used to indicate a suspected attack.

This method can be enhanced by comparing the frequency measurement of the suspected PMU with neighboring PMUs. Assume neighboring PMUs are not under attack, the frequency estimated by them will be a useful reference for the attack detection. When the frequency deviation between the suspect PMU and the average frequency of other units abruptly increases or decreases over the preset threshold, it indicates a possible attack.

Practically, the power system disturbance such as generation trip or load shedding is also possible to cause the frequency deviation. During a disturbance, the unbalance of generation and load causes a rising or drop of frequency which propagates from the event location to all the power grid as an electromechanical wave. In this situation, the frequency difference between PMUs may be decreased or increased due to the different time delay with which the electromechanical wave propagates and arrives at the location of each PMU. It is therefore essential to obtain the 'true' frequency deviation during the power system disturbance. As the time of arriving can be achieved with the information of propagation speed and geological distance, it needs to be deducted for the comparison of frequency.

Another possible factor to cause false alarm in practice is oscillation. Large oscillation could result a large frequency deviation. For a low frequency oscillation, the change of frequency is very slow, and can be differentiated from the frequency step change. When the frequency of oscillation is relatively high, the frequency deviation speed could be

close to the step change. For this situation, an integration can be used to tell the frequency step change from the oscillation, as the integration of an oscillated frequency will be much smaller than a step change frequency.

Meanwhile, as the angle is drifting during the attack, its drifting rate can be extracted as an auxiliary method to confirm if a TSIA happens. The diagram of this method is illustrated in Figure 9.5.

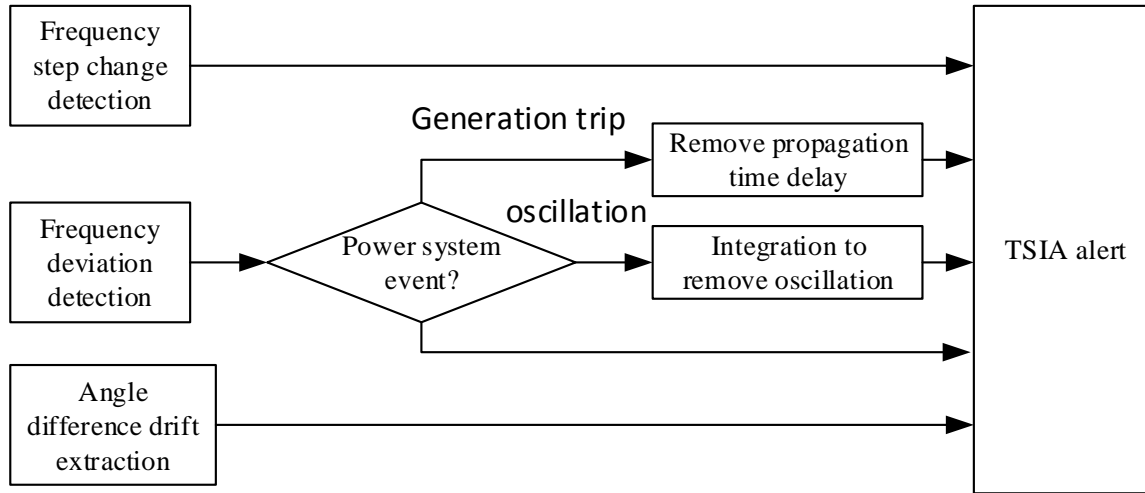


Figure 9.5. TSIA detection method diagram based on frequency deviation

For a smaller PPS error, the frequency deviation is too small to be identified, and the angle drifting is very slow and hard to be observed. In this case, one possible way is to introduce backup timing source for comparison. Some possible methods include using another GPS band, or other GNSS system such as GALILEO, or using GPS-independent timing source such as PTP, eLoran, or chip-scale atomic clocks (CSACs) [206]. However, this will need to redesign the hardware and could considerably increase the cost of PMUs. PTP and eLoran will need even more investment to operate the time distribution system. A possible economic solution is to utilize the onboard oscillator of the microprocessor for PPS interval checking.

Here we take FDR as example. The nominal frequency of the oscillator embedded inside the DSP is 40 MHz. Due to the limited precision in manufacture, it usually has a deviation from the nominal value. The frequency of the oscillator can be measured by using a timer inside the DSP. The timer uses this oscillator as the clock, and increases the counter for every clock period. Using the PPS signal to trigger the starting and ending of the counter, the frequency of this oscillator can be roughly obtained. A measurement of the frequency deviation of one oscillator is shown in Figure 9.6.

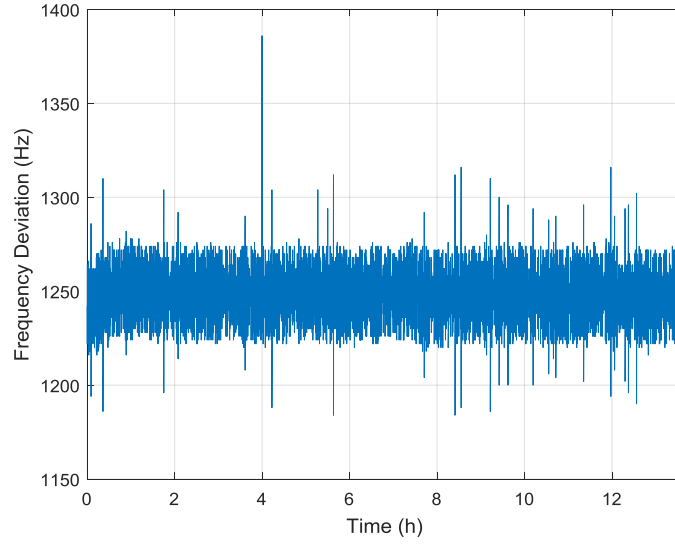


Figure 9.6. Frequency deviation of onboard oscillator

In this case, the mean value of the frequency deviation is about 1,250 Hz, and the residual fluctuation range is about 30 Hz. This is mainly due to the fluctuation of ambient temperature, and supply voltage to which the oscillator frequency is sensitive. After calibration, the measured frequency of the oscillator is within ± 30 Hz. If the PPS interval is increased or decreased due to the malicious attack, the measured oscillator frequency will change accordingly. If the measured frequency suddenly changes a lot, it indicates a suspected PPS attack.

For this case, if the PPS error is larger than $0.75 \mu s$, the measured frequency deviation will surpass ± 30 Hz. A conservative threshold could be set as ± 40 Hz, corresponding to $1 \mu s$. For any PPS error larger than $1 \mu s$, it can be detected by the timer using on-board oscillator. A check of phase angle drift of estimated frequency step change could ensure this and trigger the possible PPS attack alarm.

The diagram of this method is illustrated in Figure 9.7.

9.5 Conclusion

In this chapter, TSIA on PMU is investigated. The attack strategy is analyzed, and the error introduced by TSIA is presented. It indicates that TSIA could be used as a sophisticated cyber-attack for WAMS, and cause false results to WAMS applications. A method based on the PMU internal oscillator is proposed. The study proves that this method is possible to detect TSIA which causes any PPS error larger than $1 \mu s$.

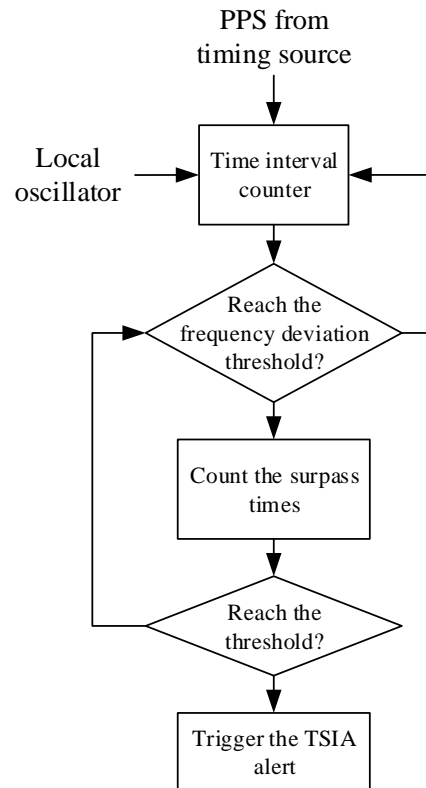


Figure 9.7. TSIA detection method diagram based on internal oscillator

CHAPTER 10 POWER SYSTEM MEASUREMENT FOR GIC DETECTION

10.1 Introduction

Geomagnetic disturbances (GMDs) are serious threats to electronic equipment and even the power grid. The geomagnetic is susceptible to the solar activities such as solar storms or solar flares. During these events, ionized particles carried by the solar wind due to coronal mass ejections or coronal holes at the Sun are captured by Earth's magnetic field [207]. The geomagnetic is therefore disturbed and can be characterized as a very slowly varying magnetic field, usually ranges from 500 nT/min to 5,000 nT/min [208]. The high altitude electromagnetic pulse (HEMP), which could be generated by nuclear weapons, could result in similar phenomenon. Especially in the third component of nuclear EMP, called EMP-E3, could cause the slowly varying of the geomagnetic field very similar to GMD [209].

According to Faraday's law of induction, an electric field at the surface of the Earth is induced due to the slowly varying of the geomagnetic field caused by GMD or EMP-E3. As the long distance transmission line and the ground forms a large closed circuit, the electric field drives a low-frequency (0.1 mHz - 0.1 Hz) in the transmission lines, called geomagnetically induced currents (GICs). The frequency of GIC is significantly lower compared to the power system frequency, therefore it is a quasi-dc.

When GIC flows into the transformers, it will cause half-cycle saturation of transformers, which produces harmonics and leads to transformer overheating, or even damage. The transformer operating in half-cycle saturation absorbs large amount of reactive power and could lead to voltage stability problem. Furthermore, the harmonics generated by the transformer in half-cycle saturation could lead to protection and control devices incorrect operation; the electromagnetic oscillation with capacitor bank or static VAR compensator (SVC), which furtherly added to pressure to the VAR support and voltage stability. Besides, the harmonics, when spread into the generators, could cause generators overheating and tripped the generators, causing even more server power system stability problems.

If the GIC causes high levels of harmonic distortion, there is a risk that the conventional protection system may not provide adequate protection for the capacitors, transformers, and generators. This can cause catastrophic effects, such as possibly months' outage of major portions of the U.S. power grid, since typically transmission owners have very limited number of spare transformers to emergency replacement. Therefore, it is necessary to monitor the GIC impact to prepare or mitigate impact of GIC on equipment and power grid.

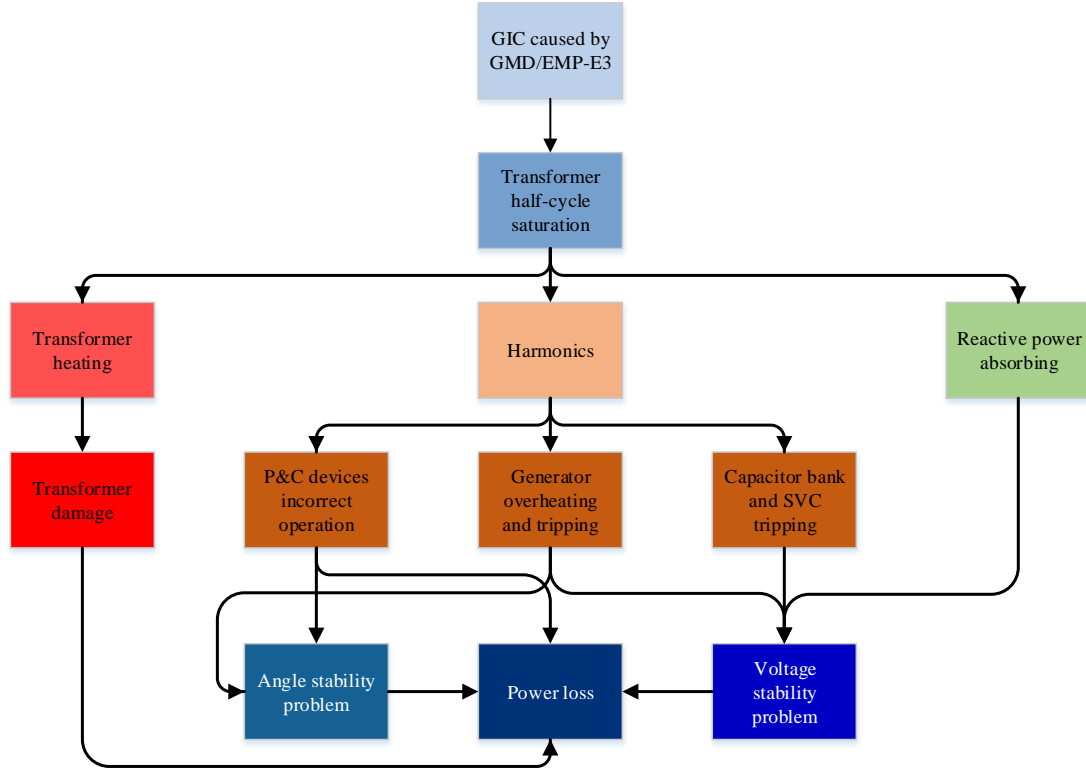


Figure 10.1. Harms of GMD/EMP-3

Basically there are two typical methods to monitor GIC impact:

- Measuring GIC on the power lines or on the neutrals of power transformers;
- Monitoring the changes in the power system environment, such as high harmonic distortion or abnormal reactive flows.

Both methods mentioned above require direct electrical contacts with the power lines or transformers to sense for signal acquisition, making the setup process relatively complex. The physically connection results in high installation and maintenance costs, which limited installation and widespread use of GIC impact monitor. In some locations or areas, it may be difficult or even impossible to set up a GIC impact monitoring devices. The low accessibility and low portability limit the deployment of GIC impact monitoring devices in wide-area electric systems.

Therefore, there is a need for an inexpensive type of non-contact GIC impact monitoring device without significant performance degradation or complex setup processes.

In this chapter, a non-contact GIC detection method is developed. Firstly, the GIC signature is analyzed. Then the theory and the structure of the non-contact transducer is presented. Based on this, a GIC detection algorithm is proposed and tested. Finally the conclusion is given.

10.2 GIC Signature Analysis

It is discovered that GIC will cause the transformers to enter the semi-saturation status. In that case, a lot of harmonics will be generated by the transformer. Among these harmonics, the even harmonic components including 2nd, 4th, and 6th are obvious and much stronger than the normal condition. Therefore, it is possible to develop an algorithm to detect the amplitude of these harmonics and determine if a GIC happens.

As these harmonics are rarely seen during normal conditions, the probability of false alarm will be low. Considering the frequency of harmonics are higher than the fundamental component, they are possible to be estimated even faster than the fundamental frequency.

10.2.1 Effect of GMD /EMP on Transformer

During GMD/EMP-E3, the changing magnetic field on the surface of the Earth induces a slowly changing current into any suitable conductor. Power transmission lines, which are usually long up to kilometers and form a loop with ground, are vulnerable to this effect. The induced current is called GIC, which is almost always direct current since the magnetic field changes slowly. For the cross-section area of the single-turn loop formed by the transmission line and the ground is large, the GIC could be up to 100 amps [210].

As the magnetizing current of even a large transformer is typically 10 amps or less, the large GIC moves the operation point of the transformer core towards magnetic saturation. As the ac of the transmission line then adds to this offset, the transformer experiences saturation in part of the power cycle, which is also known as semi-saturation, as shown in Figure 10.2.

The effect of semi-saturation depends on the structure of the transformer. Usually a three-phase three-limb core design is not likely to be influenced by GIC, since its symmetric structure makes the GIC caused magnetic flux from three windings cancel each other. However, for a single-phase transformer, the net flux from GIC is not zero. Although it is typical for transmission systems to be three-phase, it is common for large transformer banks to use three single-phase units.

10.2.2 Harmonics Analysis

As the GIC is added to the winding and causes the transformer to semi-saturate, the magnetizing current is distorted and becomes asymmetrical. The peak of a positive half-cycle could be several times larger than the waveforms with no GIC. The negative half-cycle, on the other hand, is smaller as the operation point is moved by GIC. This distorted current is rich in harmonics.

It can be seen from Figure 10.3 that the amplitudes of harmonic current are proportional to the amplitude of GIC. Also, the 2nd to 9th harmonics are obvious, and generally the amplitude of the current tends to decrease with increasing harmonics order.

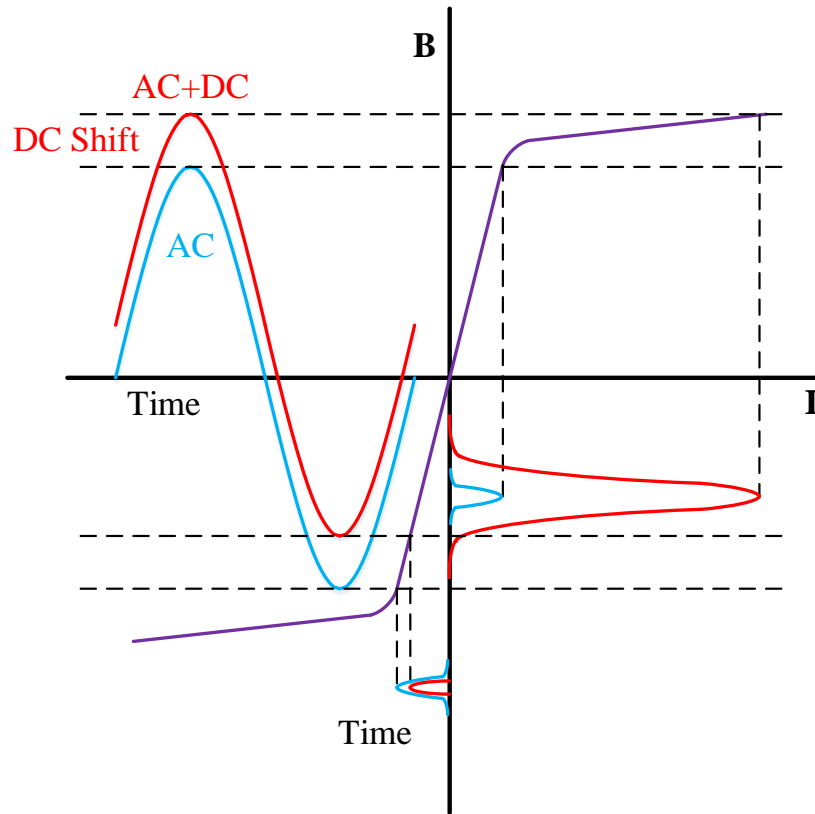


Figure 10.2. DC causes half-cycle saturation of the transformer core

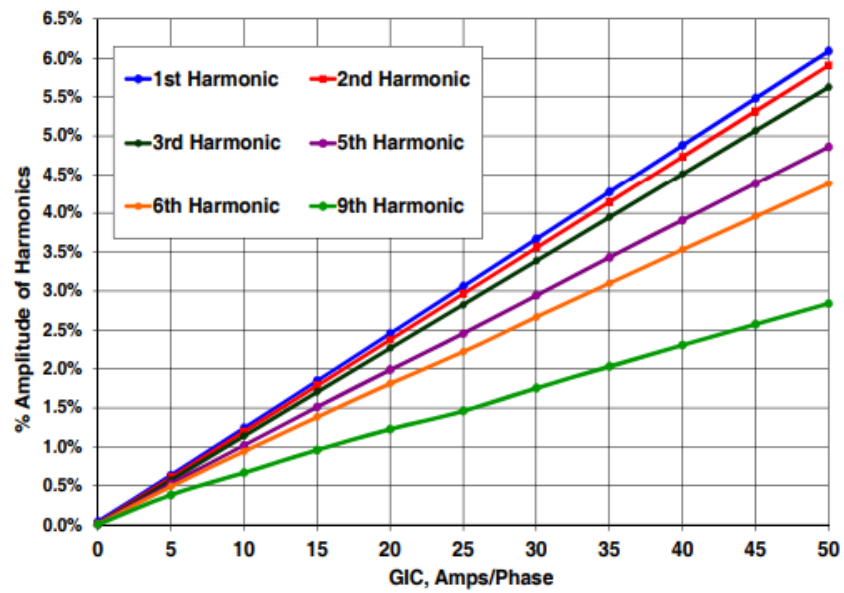


Figure 10.3. Amplitude of harmonics during transformer half-cycle saturation [211]

As even order harmonics are not usual in a normal operated power system, they can be used for GIC detection.

10.3 Non-contact Transducer

Ampere's Law reveals that a magnetic field is produced in the surrounding area of a conductor carrying an AC. During a GMD/EMP-E3 event, the fundamental and harmonics current will generate a corresponding magnetic field. A coil can be used as a magnetic sensor to translate the magnetic field to current.

Denote the current in phase a of the transmission line as I_a , i.e.

$$I_a = \sum_{h=1}^H A_h \sin(2\pi h f_0 t + \phi_h), \quad (10.1)$$

where h is the harmonics order, H is the highest order of the harmonics for which an amplitude is considered, f_0 is the fundamental frequency, t is the time, and A_h and ϕ_h are the amplitude and initial phase angle of the h -th harmonics, respectively.

The magnetic field at one surrounding point generated by the transmission line can be denoted as

$$\mathbf{B}_a = \frac{\mathbf{j}_a \mu I_a}{2\pi l_a}, \quad (10.2)$$

where μ is the magnetic permeability of the medium, \mathbf{j}_a is the unit direction, l_a is the distance from the line to the target point.

For multiple phases and transmission lines, the superposition principle can be applied. For a single circuit three-phase transmission line, the magnetic field can be represented by

$$\mathbf{B} = \mathbf{B}_a + \mathbf{B}_b + \mathbf{B}_c = \frac{\mathbf{j}_a \mu I_a}{2\pi l_a} + \frac{\mathbf{j}_b \mu I_b}{2\pi l_b} + \frac{\mathbf{j}_c \mu I_c}{2\pi l_c}. \quad (10.3)$$

For a balanced three-phase, the proportion of each harmonics will remain unchanged.

Then magnetic flux passes through the coil can be expressed as

$$\Phi = \mathbf{S} \times \mathbf{B} \quad (10.4)$$

where \mathbf{S} is the area of the coil. Using Faraday's induction law, the induced electromotive force in the coil, denoted as EMF , can be represented by

$$EMF = N \frac{d\Phi}{dt}, \quad (10.5)$$

where N is the turns of the coil.

The strength of EMF , according to the equations, is proportional to the turns and cross section area of the coil. A carefully designed coil is able to guarantee the signal strength. Past testing shows that the magnetic field on the ground below high voltage transmission lines is usually larger than $4 \mu\text{T}$ with a horizontal distance of 20 m, and could reach $17 \mu\text{T}$ [212, 213]. The magnetic sensor is designed with 400 turnr, inner diameter of 5 cm and external diameter of 8 cm.

As the magnetic sensor behaviors like a current source, it needs to be transferred to a voltage source with appropriate output range for ADC acquisition and harmonics estimation. A three-stage amplifier circuit is used as I-V converter, voltage amplifier, and filter, as shown in Figure 10.4.

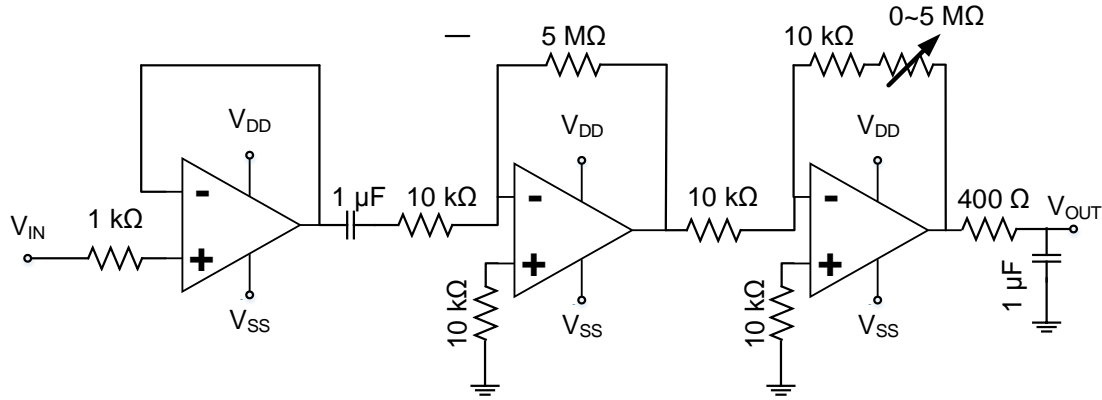


Figure 10.4 Diagram of the amplifier circuit for the non-contact transducer

10.4 GIC Detection Algorithm Design

The harmonic components are usually very weak and tends to be submerged in the noise and fundamental component. Therefore, a sensitive algorithm is required to pick them out and calculate the amplitude. Phase-sensitive detection (PSD) algorithm is used here.

A brief introduction of this algorithm is shown below. When a signal of interest is input into the algorithm, a reference signal with the desired frequency and phase angle will be generated to multiple with this input signal. Then an integration is implemented on the multiplication result. If a component with the same frequency and phase angle as the reference exists in this input, the output will be the multiplication result of the amplitudes of these two signals. Other signal components and noise will be eliminated and will not influence the result. The diagram of this algorithm is shown in Figure 10.5.

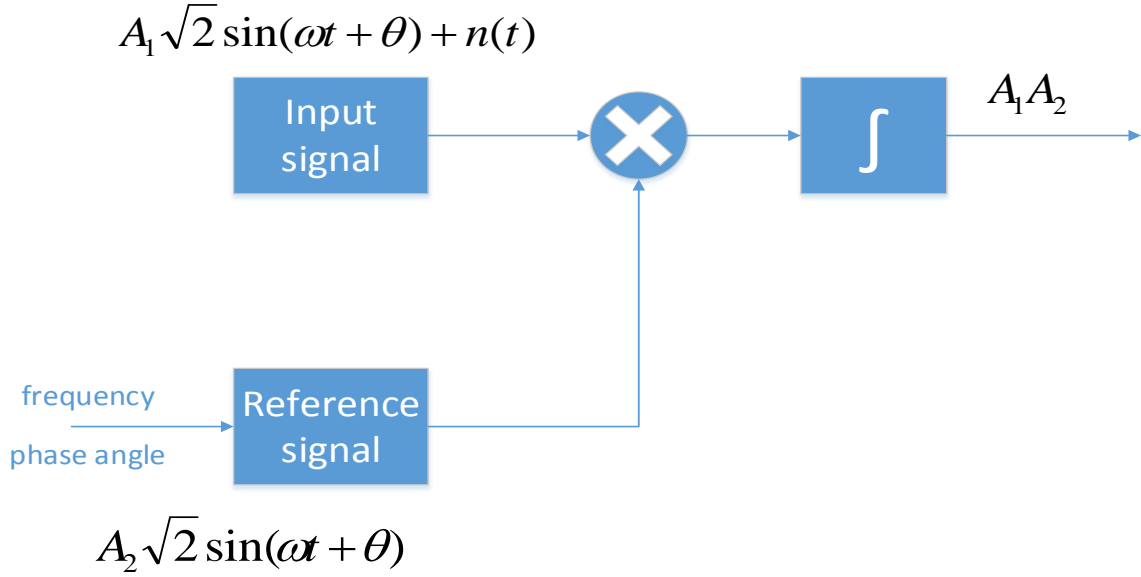


Figure 10.5 Structure of PSD algorithm

Using this method, the reference of even order harmonic can be generated and PSD algorithm will be used to calculate the amplitudes of the harmonic components in the input signal. If their amplitudes are larger than the threshold set for GIC detection, an alarm will be triggered. Protection strategies can be implemented to ensure the corresponding GIC mitigation strategy will be activated to prevent the GIC impact.

10.4.1 Accurate Harmonics Detection Algorithm

Based on PSD algorithm, an accurate harmonics detection algorithm is proposed for GIC/EMP detection. In the first step, the fundamental frequency and phase angle are estimated using a PMU algorithm, denoted as f_0 and θ_0 . Then a sinusoidal reference signal is generated with a frequency equal to hf_0 and an amplitude of A_1 , represented by

$$r(n, \theta) = A_1 \sin(2\pi h f_0 n + \theta_1) \quad (10.6)$$

The reference signal has a frequency equal to the frequency of the harmonic component to be detected. E.g., when the 4th harmonic is to be detected, h is set to be 4.

The input signal, denoted as $x(n)$ is multiplied by $r(n, \theta)$ to produce a demodulated signal denoted as $x_d(n, \theta)$:

$$x_d(n, \theta) = x(n) \cdot r(n, \theta). \quad (10.7)$$

This signal is applied to an integrator by accumulating $x_d(n)$ is a period, typically the integral times of the period of $r(n)$, i.e. $1/(2\pi h f_0)$. Denote the demodulated signal as $y(\theta_1)$.

$$y(\theta) = \sum_{i=1}^M x_c(n, \theta), \quad (10.8)$$

where

$$M = \frac{Nf_s}{2\pi hf_0}. \quad (10.9)$$

In the equation above, f_s is the sampling rate, N is an integer typically in the range of 1 to 10. Using larger N is able to get a more accurate estimation, but will also increase the estimation time.

Iteratively change θ_1 is the range from 0 to 2π and calculate corresponding $y(\theta_1)$, the maximum one is picked, denoted as y_{max} . The amplitude of the h -th harmonic is calculated by

$$A_h = \frac{2y_{max}}{NA_1}. \quad (10.10)$$

The sweeping of θ_1 is usually time consuming, especially when the accuracy is important which requires a small step size for the sweeping of θ_1 . An improving method is to obtain the relation between the phase angle of fundamental component and the harmonic component, then use this relation to estimation the rough value of θ_1 . In the iterations, only sweeping around a small neighboring area is enough to obtain the optimized θ_1 and the corresponding y_{max} .

10.4.2 GIC/EMP-E3 Detection Algorithm

As discussed in last subsection, even harmonics with order 2nd, 4th, and 6th, are significant and unique during GIC/EMP-E3, and can be used to determine if the GIC/EMP-E3 event happens.

Two criterias are used here to determine if the event happens. The first one is the harmonics distortion, denoted as THD and calculated by

$$THD = \sum_{h=2,4,6} \frac{A_h}{A_0}. \quad (10.11)$$

The other criteria is the changing of harmonics distortion, defined by

$$\Delta THD = THD(n+1) - THD(n). \quad (10.12)$$

Two threshold values are set for each of the criteria. When both thresholds are surpassed, the GIC/EMP-E3 detection alert is triggered. The preset protection strategy may enact

appropriate protective actions, such as reducing the amount of load, or activating a neutral blocking device located in the neutral path of a transformer to which the transmission line or bus is connected.

10.4.3 Testing and Result

As the 6th harmonic has the lowest amplitude and highest frequency compared to 2nd and 4th harmonics, it is the most difficult to be detected. Here the detection of 6th harmonics is illustrated, and the detection of the other two will be implemented in the same way.

For the first step, the GIC detection method is tested using simulation. In the simulation, a 6th harmonic with 1% amplitude of the fundamental component is generated as the target signal. To mimic the noise in the transducer, -30 dB SNR is assumed, which is a very poor condition. The waveform in time domain and the power spectrum density are shown in Figure 10.6.

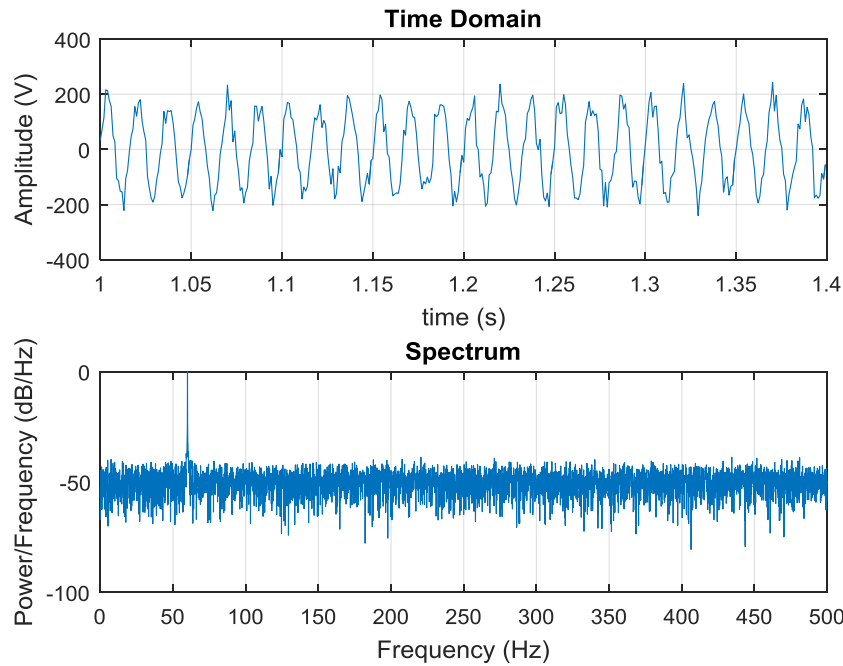


Figure 10.6 Waveform (upper) and power spectrum density (lower) of a signal with 1% 6th harmonic and -30 dB density

From the figure it can be seen that due to the high noise, the waveform is highly distorted, and the 6th harmonics is submerged in the noise and cannot be observed by eyeball.

Implement the harmonics detection algorithm, the 6th harmonic is detected and the estimated 6th harmonic distortion is 0.84%. When there is no harmonics added, the reported 6th harmonics is only 0.12%, which is from the noise. This proves that the

algorithm is able to detect the small harmonic from signal highly distorted by the noise. When the harmonic amplitude is higher, or the SNR is depressed, the detection accuracy will significantly increase.

Furthermore, the detection time is critical to the GIC detection. The faster it is detected, the more time there is for GIC mitigation strategy to take action and prevent device damage and power system event. Detection time of the GIC detection mainly depends on the harmonics estimation, to which the integral time is the critical factor. Different integral time are tested, as shown in Figure 10.7. It is found that with sampling rate of 1,440 Hz, it needs at least 3 sec to get a small estimation error; the time requirement decreased to 1 sec when the sampling rate is increased to 14,400 Hz.

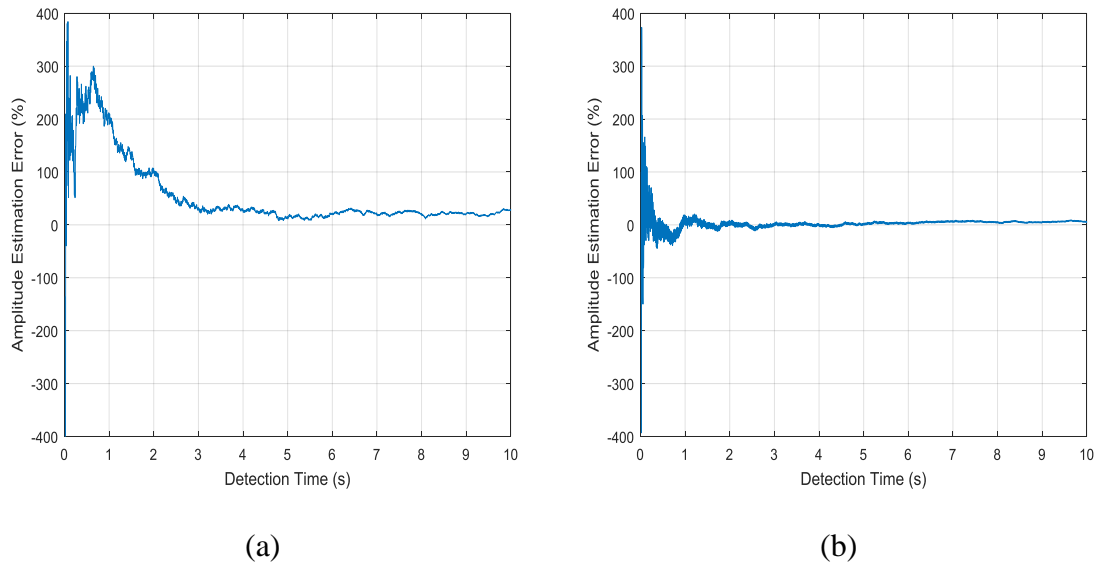


Figure 10.7 The relation between harmonic amplitude estimation error and detection time under sampling rate of (a) 1,440 Hz and (b) 14,400 Hz. Harmonics distortion is 1% and SNR = -30 dB.

An initial study is implemented on a signal mixed with 6th harmonic and large noise distortion. The 6th harmonics can still be detected using PSD method, and the estimation error is less than 8%. Better SNR will help to reduce the error.

A laboratory experiment is implemented to evaluate the proposed GIC detection algorithm. The system setting is shown in Figure 10.8. The signal generator is synchronized to the GPS and output the fundamental 60 Hz signal with harmonic components, simulating the current during transformer half-cycle saturation. It is detected by the magnetic sensor, amplified by the signal transducer, and acquired by the FDR.

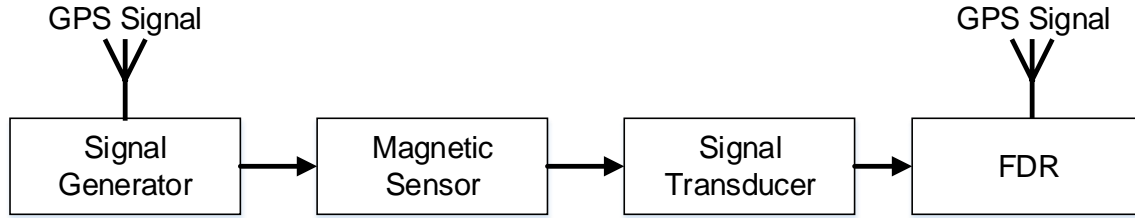


Figure 10.8 Laboratory experiment setting

The samples of simulated GIC aftermath current captured by the FDR through sensor and transducer is shown in Figure 10.9. The signal is highly distorted by noise. Taking 50 kHz as the sampling rate, and the integration time of 0.1 s, the detected 6th harmonic distortion is 0.99%. It proves that with a high sampling rate, the algorithm is able to detect the small harmonic distortion with high accuracy and fast speed.

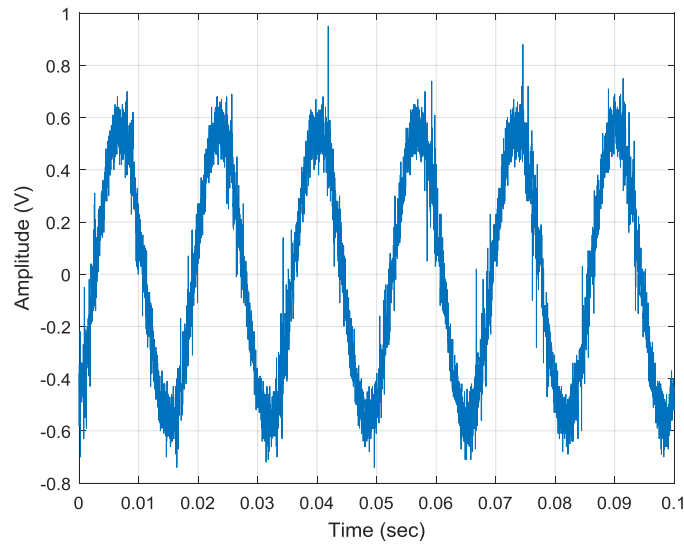


Figure 10.9 A signal sampled with 1% 6th harmonic

10.5 Conclusion

GIC can cause tremendous hazard to power system. It is critical to detection GIC fast and accurately and inform the protection device and system operators to take actions. In this chapter, the cause of GIC and its harm to the power system is introduced. Specifically, the half-cycle saturation of transformers induced by GIC is presented. The even harmonics generated by this phenomenon is utilized as the signature for GIC detection. An algorithm is developed and is able to detect the harmonics submerged in strong noise. A non-contact transducer based on the magnetic field generated by the transmission line is designed and used for signal acquisition. Finally a non-contact GIC detection device is

developed which is able to detect the GIC with fast speed and high accuracy. It can be easily deployed, and provides warnings of GIC for power system protection.

CHAPTER 11 CONCLUSIONS AND FUTURE WORKS

11.1 Conclusions

Situation awareness provides critical information for power system to operate in security and effective condition. The massive Northeast Blackout took place in 2003 disclosed the vulnerability of power system and lack of situation awareness. Afterwards, WAMS, as an important application of real time situation awareness, experienced rapid development and implementation ever since. As the increasing expansion and complexity of the power grid, and the rising of demand of power supply quality, the role of WAMS is critical in the grid modernization. Nowadays, as over 2,000 synchrophasors have been deployed in solely North America, the applications of WAMS being used by utility companies are still limited. The purpose of this dissertation is to explore the potential of WAMS and leverage its functionality in power system. The work of this dissertation mainly focuses on two parts: the improvement of WAMS, and the applications based on WAMS.

One of the main obstacle to implement WAMS is the lack of knowledge of synchrophasor data quality and influence, especially during power system dynamics. To improve WAMS, the work of this dissertation starts from understanding its performance. Firstly, the algorithms of synchrophasors are reviewed. Phasor and frequency estimation algorithm is the core of the synchrophasors. The performance of synchrophasors mainly depends on the algorithm, and the impact of external factors, such as timing accuracy and distortions on the voltage/current also depends on the algorithm. This dissertation is probably the first one to review the phasor and frequency estimation algorithms proposed since the first PMU is proposed in 1983. Algorithms are attributed into mainly eight types. Several common techniques shared by different algorithms are summarized. The algorithms are also compared in terms of accuracy, estimation speed, and computation complexity. The areas to be studied in the future are proposed.

Then the impact of measurement errors on synchrophasor-based are investigated. The measurement errors derive from not only the PMU device itself, but also the instrumentation channel, which is not considered in the PMU standard. To demonstrate the worst possible cases, the largest possible error range is estimated and used to evaluate four synchrophasor-based applications, i.e. power system disturbance location, oscillation detection, islanding detection, and dynamic line rating. It reveals that the impact of measurement errors varies depending on the specific application. Some applications are not likely to be influenced, some are very sensitive to the errors, and the influence on some others depends on the parameters set for those applications.

To fully evaluate the performance of different applications under measurement errors, the real PMUs should be used. However, it is difficult for every application developer to have every type of the PMUs to be used, and it is even harder to use real PMUs to evaluate all the possible inputs the applications are to deal with. Therefore, an alternative way is to develop a tool to mimic the behavior of real PMUs. In this dissertation, a method is proposed to develop parameterized models for real PMUs based on PMU

testing results and operation parameters. A generic model is built for a specific type of PMU. It is capable to represent the error behavior of different combinations of inputs and operation conditions. The error is very close to the real PMU errors. Based on this model, a tool is developed to evaluate the performance of PMU applications without the requirement of real PMUs. Furthermore, it provides a detailed model of PMU for power system simulation.

Besides evaluating and improving the applications, an important and effective method is to provide good quality of measurements. In steady state, the impact of a series of factors contribute to the measurement errors are evaluated. It reveals that time accuracy, ADC accuracy, and the algorithm all contribute to the measurement error. The external distortions mixed in the input voltage/current, such as white noise and harmonics, could bring in even larger error, especially the harmonics during the fundamental frequency being off-nominal. Since power electronic devices are widely used in the increasing renewable energy sources, the harmonics they bring in are worrisome. The models of wind turbine and PV are developed and the harmonics and interharmonics introduced are evaluated. It reveals that it is important to filter out those harmonics, otherwise they could bring large influence on the performance of synchrophasors.

In dynamic state, the current PMUs show response delay and error, mainly because of the algorithms used cannot handle the abrupt change of power signal parameters. A new PMU algorithm is proposed to provide fast response and minimal measurement error during dynamic state. Based on this algorithm, a fast response PMU is developed and realized on hardware platform. Testing results show that it is able to handle fast change of power signal parameters and provide timely and accurate measurement results. Meanwhile, it is able to report at a rate up to 180 Hz, furtherly reduced the reporting delay.

To increase the interoperability of FDR/UGA, the single-phase distribution level synchrophasors used by FNET/GridEye, the C37.118.2 complied data communication protocol is developed. Data packages are designed and curtailed to fit the specific design of FDR/UGA. The testing verified the correctness and reliability of the new communication protocol and embedded software module. The communication interoperability of FDR/UGA is highly improved. It provides the possibility for data from FDR/UGA in distribution level to be merged with the transmission level PMU data on the same platform, and the integral and detailed monitoring of the whole power grid.

To leverage the capability of WAMS, three applications are developed. First of all, a method is proposed to identify the data source from multiple PMUs. In this method, the spatial and temporal features of the synchrophasor measurements are extracted through signal processing. Then a model is developed based on historical data using statistic and machine learning based method. With this model, the unknown data source and starting time of a period of signal can be told. This method can be used for media authentication, cyber-attack detection and correction, and power grid phase identification.

Secondly, an application to detect time synchronization interval attack is developed. Time is critical for WAMS data quality in terms of synchronization and accuracy. GPS is used as the main timing source of WAMS and is vulnerable to attacks. The impact of TSIA is investigated. Using the characters of phase angle and frequency under attack, an application is proposed and developed to detect TSIA. It does need additional hardware resource, and can be realized by upgrading the software and firmware. This application can help to improve the timing security of WAMS.

This dissertation also proposed an application to detect the GIC/EMP, which could cause a large area of power grid outage for up to several months. The method is based on the phenomena of transformers' semi-saturation during GIC/EMP. A synchronous-detection method is used to detect the harmonics caused by semi-saturation of transformers. This method utilizes the measurement results of PMUs and can be easily embedded in the wide deployed PMUs to realize fast detection and reaction to GIC/EMP and secure the power system. It can also be implemented by contactless transducers, so the sensors can be easily deployed in a wide area with minim installation cost.

11.2 Future Works

In the areas presented in this dissertation, some topics can be conducted in the future work.

1. Based on the work of PMU error impact (Chap. 3) and PMU error model (Chap. 4), the applications using realistic PMUs can be conducted. The tolerable accuracy range for each application can be revealed, and the accuracy requirement of each specific application can be set up and used for the PMU selection guidance.
2. The impact of transmission delay and data loss on different PMU applications can be studied. Transmission delay and data loss are not specified in PMU standards, and they are inevitable in real application. An investigation is helpful to set up related standards.
3. PMU accuracy limitation can be extended to more algorithms and the power system dynamic states.
4. It would be useful to develop a uniform frame to integrate synchrophasor data from PMUs in both transmission and distribution level, and with different reporting rates.
5. Realize online application of spatial and temporal feature based methods for cyber-attack detection and data correction.

REFERENCES

- [1] B. B. Mica R. Endsley, Debra G. Jones, "What is Situation Awareness?," in *Designing for Situation Awareness*, ed: CRC Press, 2003, pp. 13-30.
- [2] M. Panteli, P. A. Crossley, D. S. Kirschen, and D. J. Sobajic, "Assessing the Impact of Insufficient Situation Awareness on Power System Operation," *IEEE Trans. Power Syst.*, vol. 28, pp. 2967-2977, 2013.
- [3] V. Terzija, G. Valverde, D. Cai, P. Regulski, V. Madani, J. Fitch, S. Skok, M. M. Begovic, and A. Phadke, "Wide-Area Monitoring, Protection, and Control of Future Electric Power Networks," *Proceedings of the IEEE*, vol. 99, pp. 80-93, 2011.
- [4] T. Xia, "Frequency monitoring network (FNET) algorithm improvements and application development," Doctor of Philosophy, Electrical Engineering, Virginia Polytechnic Institute and State University, 2009.
- [5] I. Kamwa, R. Grondin, and Y. Hebert, "Wide-area measurement based stabilizing control of large power systems-a decentralized/hierarchical approach," *IEEE Trans. Power Syst.*, vol. 16, pp. 136-153, Feb. 2001.
- [6] L. Guoping, J. Quintero, and V. M. Venkatasubramanian, "Oscillation monitoring system based on wide area synchrophasors in power systems," in *2007 iREP Symposium - Bulk Power System Dynamics and Control - VII. Revitalizing Operational Reliability*, 2007, pp. 1-13.
- [7] A. B. Leirbukt, J. O. Gjerde, P. Korba, K. Uhlen, L. K. Vormedal, and L. Warland, "Wide Area Monitoring Experiences in Norway," in *2006 IEEE PES Power Systems Conference and Exposition*, 2006, pp. 353-360.
- [8] A. G. Phadke, "The Wide World of Wide-area Measurement," *IEEE Power and Energy Magazine*, vol. 6, pp. 52-65, 2008.
- [9] I. Kamwa, J. Beland, G. Trudel, R. Grondin, C. Lafond, and D. McNabb, "Wide-area monitoring and control at Hydro-Quebec: past, present and future," in *2006 IEEE Power Engineering Society General Meeting*, 2006, pp. 12 pp.
- [10] P. Korba and K. Uhlen, "Wide-area monitoring of electromechanical oscillations in the nordic power system: practical experience," *IET Generation, Transmission & Distribution*, vol. 4, pp. 1116-1126, Oct. 2010.
- [11] Z. Zhian, X. Chunchun, B. J. Billian, Z. Li, S. J. S. Tsai, R. W. Conners, V. A. Centeno, A. G. Phadke, and L. Yilu, "Power system frequency monitoring network (FNET) implementation," *IEEE Trans. Power Syst.*, vol. 20, pp. 1914-1921, 2005.
- [12] Y. Zhang, P. Markham, T. Xia, L. Chen, Y. Ye, Z. Wu, Z. Yuan, L. Wang, J. Bank, J. Burgett, R. W. Conners, and Y. Liu, "Wide-Area Frequency Monitoring Network (FNET) Architecture and Applications," *IEEE Trans. Smart Grid*, vol. 1, pp. 159-167, Sep. 2010.
- [13] Y. Liu, W. Yao, D. Zhou, L. Wu, S. You, H. Liu, L. Zhan, J. Zhao, H. Lu, W. Gao, and Y. Liu, "Recent developments of FNET/GridEye — A situational awareness tool for smart grid," *CSEE Journal of Power and Energy Systems*, vol. 2, pp. 19-27, 2016.
- [14] Y. Liu, S. You, W. Yao, Y. Cui, L. Wu, D. Zhou, J. Zhao, H. Liu, and Y. Liu, "A Distribution Level Wide Area Monitoring System for the Electric Power Grid—FNET/GridEye," *IEEE Access*, vol. 5, pp. 2329-2338, Feb. 2017.

- [15] D. Zhou, "Wide-Area Synchrophasor Data Server System and Data Analytics Platform," Ph.D. dissertation, Dept. Elec. Eng. and Comp. Sci., University of Tennessee, Knoxville, TN, 2017.
- [16] S. You, Y. Liu, T. Micah, J. Zhao, W. Yao, D. Zhou, L. Wu, Y. Su, X. Zhang, and Y. Liu, "Disturbance Location Determination Based on Electromechanical Wave Propagation in FNET/GridEye -- a Distribution-Level Wide-Area Measurement System," *IET Generation, Transmission & Distribution*, 2017.
- [17] J. Guo, Y. Zhang, M. A. Young, M. J. Till, A. Dimitrovski, Y. Liu, P. Williging, and Y. Liu, "Design and Implementation of a Real-Time Off-Grid Operation Detection Tool from a Wide-Area Measurements Perspective," *IEEE Trans. Smart Grid*, vol. 6, pp. 2080-2087, Sep. 2014.
- [18] T. Yang, H. Sun, and A. Bose, "Transition to a Two-Level Linear State Estimator - Part II: Algorithm," *IEEE Trans. Power Syst.*, vol. 26, pp. 54-62, Feb. 2011.
- [19] A. Monticelli, "Electric power system state estimation," *Proceedings of the IEEE*, vol. 88, pp. 262-282, Feb. 2000.
- [20] P. Kundur, N. J. Balu, and M. G. Lauby, *Power system stability and control* vol. 7: McGraw-hill New York, 1994.
- [21] V. Eckhardt, P. Hippe, and G. Hosemann, "Dynamic measuring of frequency and frequency oscillations in multiphase power systems," *IEEE Trans. Power Del.*, vol. 4, pp. 95-102, Jan. 1989.
- [22] T. W. Cease and B. Feldhaus, "Real-time monitoring of the TVA power system," *IEEE Computer Applications in Power*, vol. 7, pp. 47-51, Jul. 1994.
- [23] M. Begovic, D. Novosel, D. Karlsson, C. Henville, and G. Michel, "Wide-Area Protection and Emergency Control," *Proceedings of the IEEE*, vol. 93, pp. 876-891, May 2005.
- [24] D. E. Bakken, A. Bose, C. H. Hauser, D. E. Whitehead, and G. C. Zweigle, "Smart Generation and Transmission With Coherent, Real-Time Data," *Proceedings of the IEEE*, vol. 99, pp. 928-951, Jun. 2011.
- [25] C. W. Taylor, D. C. Erickson, K. E. Martin, R. E. Wilson, and V. Venkatasubramanian, "WACS-Wide-Area Stability and Voltage Control System: R&D and Online Demonstration," *Proceedings of the IEEE*, vol. 93, pp. 892-906, 2005.
- [26] A. A. Girgis and F. M. Ham, "A New FFT-Based Digital Frequency Relay for Load Shedding," *IEEE Transactions on Power Apparatus and Systems*, vol. PAS-101, pp. 433-439, 1982.
- [27] A. G. Phadke, T. Hlibka, M. G. Adamiak, M. Ibrahim, and J. S. Thorp, "A Microcomputer Based Ultra-High-Speed Distance Relay: Field Tests," *IEEE Transactions on Power Apparatus and Systems*, vol. PAS-100, pp. 2026-2036, 1981.
- [28] A. G. Phadke, J. S. Thorp, and M. G. Adamiak, "A new measurement technique for tracking voltage phasors, local system frequency, and rate of change of frequency," *IEEE Transactions on Power Apparatus and Systems*, vol. PAS-102, pp. 1025-1038, May 1983.
- [29] A. G. Phadke and J. S. Thorp, *Synchronized phasor measurements and their applications*: Springer Science & Business Media, 2008.

- [30] A. G. Phadke, "Synchronized phasor measurements in power systems," *IEEE Computer Applications in Power*, vol. 6, pp. 10-15, Apr. 1993.
- [31] "IEEE Standard for Synchrophasors for Power Systems," *IEEE Std 1344-1995(R2001)*, p. i, 1995.
- [32] *IEEE Standard for Synchrophasors for Power Systems*, 2006.
- [33] *IEEE Standard for Synchrophasor Measurements for Power Systems*, IEEE Standard C37.118.1-2011, 2011.
- [34] *IEEE Standard for Synchrophasor Data Transfer for Power Systems*, C37.118.2-2011, 2011.
- [35] *IEEE Standard for Synchrophasor measurements for Power Systems*, IEEE Standard C38.118.1a-2014, 2014.
- [36] M. M. Begovic, P. M. Djuric, S. Dunlap, and A. G. Phadke, "Frequency tracking in power networks in the presence of harmonics," *IEEE Trans. Power Del.*, vol. 8, pp. 480-486, Apr. 1993.
- [37] C. T. Nguyen and K. Srinivasan, "A New Technique for Rapid Tracking of Frequency Deviations Based on Level Crossings," *IEEE Transactions on Power Apparatus and Systems*, vol. PAS-103, pp. 2230-2236, Aug. 1984.
- [38] O. Vainio and S. J. Ovaska, "Noise reduction in zero crossing detection by predictive digital filtering," *IEEE Transactions on Industrial Electronics*, vol. 42, pp. 58-62, Feb. 1995.
- [39] M. Karimi-Ghartemani and M. R. Iravani, "A nonlinear adaptive filter for online signal analysis in power systems: applications," *IEEE Trans. Power Del.*, vol. 17, pp. 617-622, Apr. 2002.
- [40] R. Weidenbrug, F. P. Dawson, and R. Bonert, "New synchronization method for thyristor power converters to weak AC-systems," *IEEE Transactions on Industrial Electronics*, vol. 40, pp. 505-511, Oct. 1993.
- [41] M. R. Dadash Zadeh and Z. Zhiying, "A new DFT-based current phasor estimation for numerical protective relaying," *IEEE Trans. Power Del.*, vol. 28, pp. 2172-2179, Oct. 2013.
- [42] C. Offelli and D. Petri, "The influence of windowing on the accuracy of multifrequency signal parameter estimation," *IEEE Transactions on Instrumentation and Measurement*, vol. 41, pp. 256-261, Apr. 1992.
- [43] J. Lambert, A. G. Phadke, and D. McNabb, "Accurate voltage phasor measurement in a series-compensated network," *IEEE Trans. Power Del.*, vol. 9, pp. 501-509, Jan. 1994.
- [44] T. Funaki and S. Tanaka, "Error estimation and correction of DFT in synchronized phasor measurement," in *Transmission and Distribution Conference and Exhibition 2002: Asia Pacific. IEEE/PES*, 2002, pp. 448-453 vol.1.
- [45] F. J. Harris, "On the use of windows for harmonic analysis with the discrete Fourier transform," *Proceedings of the IEEE*, vol. 66, pp. 51-83, Jan. 1978.
- [46] A. Nuttall, "Some windows with very good sidelobe behavior," *IEEE Transactions on Acoustics, Speech, and Signal Processing*, vol. 29, pp. 84-91, Feb. 1981.

- [47] L. Salvatore and A. Trotta, "Flat-top windows for PWM waveform processing via DFT," *IEE Proceedings B - Electric Power Applications*, vol. 135, pp. 346-361, Nov. 1988.
- [48] J. A. d. I. O. Serna and K. E. Martin, "Improving phasor measurements under power system oscillations," *IEEE Trans. Power Syst.*, vol. 18, pp. 160-166, Feb. 2003.
- [49] J. A. d. I. O. Serna, "On the use of amplitude shaping pulses as windows for harmonic analysis," *IEEE Transactions on Instrumentation and Measurement*, vol. 50, pp. 1556-1562, Dec. 2001.
- [50] D. Macii, D. Petri, and A. Zorat, "Accuracy Analysis and Enhancement of DFT-Based Synchrophasor Estimators in Off-Nominal Conditions," *IEEE Transactions on Instrumentation and Measurement*, vol. 61, pp. 2653-2664, Oct. 2012.
- [51] I. Kamwa, A. K. Pradhan, and G. Joos, "Adaptive phasor and frequency-tracking schemes for wide-area protection and control," *IEEE Trans. Power Del.*, vol. 26, pp. 744-753, Apr. 2011.
- [52] I. Kamwa, S. R. Samantaray, and G. Joos, "Compliance analysis of PMU algorithms and devices for wide-area stabilizing control of large power systems," *IEEE Trans. Power Syst.*, vol. 28, pp. 1766-1778, May 2013.
- [53] I. Kamwa, S. R. Samantaray, and G. Joos, "Wide Frequency Range Adaptive Phasor and Frequency PMU Algorithms," *IEEE Trans. Smart Grid*, vol. 5, pp. 569-579, Mar. 2014.
- [54] Q. Guo and G. Rui, "An arbitrary-resampling-based synchrophasor measurement algorithm in compliance with IEEE Std C37.118.1a-2014: design, implementation, and validation," in *2016 IEEE/PES Transmission and Distribution Conference and Exposition (T&D)*, 2016, pp. 1-5.
- [55] B. Kasztenny and E. Rosolowski, "Two new measuring algorithms for generator and transformer relaying," *IEEE Trans. Power Del.*, vol. 13, pp. 1053-1059, Oct. 1998.
- [56] J. Chen, "Accurate frequency estimation with phasor angles," Master of Science, Electrical Engineering, Virginia Polytechnic Institute and State University, Blacksburg, VA, 1994.
- [57] T. T. Nguyen and X. J. Li, "A fast and accurate method for estimating power systems phasors using DFT with interpolation," in *Power Engineering Society General Meeting, 2006. IEEE*, 2006, pp. 8.
- [58] J. Xi and J. F. Chicharo, "A new algorithm for improving the accuracy of periodic signal analysis," *IEEE Transactions on Instrumentation and Measurement*, vol. 45, pp. 827-831, Aug. 1996.
- [59] M. Akke and J. S. Thorp, "Sample value adjustment improves phasor estimation at off-nominal frequencies," *IEEE Trans. Power Del.*, vol. 25, pp. 2255-2263, Oct. 2010.
- [60] A. Borghetti, C. A. Nucci, M. Paolone, G. Ciappi, and A. Solari, "Synchronized phasors monitoring during the islanding maneuver of an active distribution network," *IEEE Trans. Smart Grid*, vol. 2, pp. 82-91, Mar. 2011.

- [61] T. Grandke, "Interpolation Algorithms for Discrete Fourier Transforms of Weighted Signals," *IEEE Transactions on Instrumentation and Measurement*, vol. 32, pp. 350-355, Jun. 1983.
- [62] D. Belega and D. Dallet, "Multifrequency signal analysis by Interpolated DFT method with maximum sidelobe decay windows," *Measurement*, vol. 42, pp. 420-426, Apr. 2009.
- [63] D. Belega and D. Petri, "Accuracy Analysis of the Multicycle Synchrophasor Estimator Provided by the Interpolated DFT Algorithm," *IEEE Transactions on Instrumentation and Measurement*, vol. 62, pp. 942-953, May 2013.
- [64] D. Belega, D. Macii, and D. Petri, "Fast Synchrophasor Estimation by Means of Frequency-Domain and Time-Domain Algorithms," *IEEE Transactions on Instrumentation and Measurement*, vol. 63, pp. 388-401, Feb. 2014.
- [65] P. Romano and M. Paolone, "Enhanced interpolated-DFT for synchrophasor estimation in FPGAs: theory, implementation, and validation of a PMU prototype," *IEEE Transactions on Instrumentation and Measurement*, vol. 63, pp. 2824-2836, Dec. 2014.
- [66] Y. Jun-Zhe and L. Chih-Wen, "A precise calculation of power system frequency and phasor," *IEEE Trans. Power Del.*, vol. 15, pp. 494-499, Apr. 2000.
- [67] P. Zhang, H. Xue, and R. Yang, "Shifting window average method for accurate frequency measurement in power systems," *IEEE Trans. Power Del.*, vol. 26, pp. 2887-2889, Oct. 2011.
- [68] P. Zhang, H. Xue, R. Yang, and J. Zhang, "Shifting window average method for phasor measurement at offnominal frequencies," *IEEE Trans. Power Del.*, vol. 29, pp. 1063-1073, Jun. 2014.
- [69] L. Zhan, Y. Liu, J. Culliss, J. Zhao, and Y. Liu, "Dynamic single-phase synchronized phase and frequency estimation at the distribution level," *IEEE Trans. Smart Grid*, vol. 6, pp. 2013-2022, Jul. 2015.
- [70] L. Zhan, Y. Liu, and Y. Liu, "A Clarke Transformation-Based DFT Phasor and Frequency Algorithm for Wide Frequency Range," *IEEE Trans. Smart Grid*, vol. PP, pp. 1-1, 2016.
- [71] F. Dawei and V. Centeno, "Phasor-based synchronized frequency measurement in power systems," *IEEE Trans. Power Del.*, vol. 22, pp. 2010-2016, Oct. 2007.
- [72] R. W. Menzies and G. B. Mazur, "Advances in the determination of control parameters for static compensators," *IEEE Trans. Power Del.*, vol. 4, pp. 2012-2017, Oct. 1989.
- [73] I. Kamwa, M. Leclerc, and D. McNabb, "Performance of demodulation-based frequency measurement algorithms used in typical PMUs," *IEEE Trans. Power Del.*, vol. 19, pp. 505-514, Apr. 2004.
- [74] M. Akke, "Frequency estimation by demodulation of two complex signals," *IEEE Trans. Power Del.*, vol. 12, pp. 157-163, Jan. 1997.
- [75] Z. Yao, "Fundamental phasor calculation with short delay," *IEEE Trans. Power Del.*, vol. 23, pp. 1280-1287, Jul. 2008.
- [76] V. V. Terzija, M. B. Djuric, and B. D. Kovacevic, "Voltage phasor and local system frequency estimation using Newton type algorithm," *IEEE Trans. Power Del.*, vol. 9, pp. 1368-1374, Jul. 1994.

- [77] S. Y. Xue and S. X. Yang, "Power system frequency estimation using supervised Gauss-Newton algorithm," in *2007 IEEE International Conference on Systems, Man and Cybernetics*, 2007, pp. 3761-3766.
- [78] I. Sadinezhad and V. G. Agelidis, "Slow sampling online optimization approach to estimate power system frequency," *IEEE Trans. Smart Grid*, vol. 2, pp. 265-277, Jun. 2011.
- [79] P. K. Dash and S. Hasan, "A fast recursive algorithm for the estimation of frequency, amplitude, and phase of noisy sinusoid," *IEEE Transactions on Industrial Electronics*, vol. 58, pp. 4847-4856, Oct. 2011.
- [80] J. Yang, H. Xi, and W. Guo, "Robust modified Newton algorithm for adaptive frequency estimation," *IEEE Signal Processing Letters*, vol. 14, pp. 879-882, Nov. 2007.
- [81] P. K. Dash, K. R. Krishnanand, and M. Padhee, "Fast recursive Gauss-Newton adaptive filter for the estimation of power system frequency and harmonics in a noisy environment," *IET Generation, Transmission & Distribution*, vol. 5, pp. 1277-1289, Dec. 2011.
- [82] J. Zheng, K. W. K. Lui, W. K. Ma, and H. C. So, "Two simplified recursive Gauss-Newton algorithms for direct amplitude and phase tracking of a real sinusoid," *IEEE Signal Processing Letters*, vol. 14, pp. 972-975, Dec. 2007.
- [83] S. Y. Xue and S. X. Yang, "Power system frequency estimation using supervised Gauss-Newton algorithm," *Measurement*, vol. 42, pp. 28-37, Jan. 2009.
- [84] V. V. Terzija and D. Markovic, "Symmetrical components estimation through nonrecursive Newton-type numerical algorithm," *IEEE Trans. Power Del.*, vol. 18, pp. 359-363, Apr. 2003.
- [85] M. S. Sachdev and M. M. Giray, "A least error squares technique for determining power system frequency," *IEEE Transactions on Power Apparatus and Systems*, vol. PAS-104, pp. 437-444, Feb. 1985.
- [86] M. D. Kusljevic, "A simple recursive algorithm for frequency estimation," *IEEE Transactions on Instrumentation and Measurement*, vol. 53, pp. 335-340, Apr. 2004.
- [87] V. V. Terzija and V. Stanojevic, "STLS algorithm for power-quality indices estimation," *IEEE Trans. Power Del.*, vol. 23, pp. 544-552, Apr. 2008.
- [88] D. W. P. Thomas and M. S. Woolfson, "Evaluation of frequency tracking methods," *IEEE Trans. Power Del.*, vol. 16, pp. 367-371, Jul. 2001.
- [89] P. Castello, J. Liu, C. Muscas, P. A. Pegoraro, F. Ponci, and A. Monti, "A Fast and Accurate PMU Algorithm for P+M Class Measurement of Synchrophasor and Frequency," *IEEE Transactions on Instrumentation and Measurement*, vol. 63, pp. 2837-2845, 2014.
- [90] V. Kaura and V. Blasko, "Operation of a phase locked loop system under distorted utility conditions," *IEEE Transactions on Industry Applications*, vol. 33, pp. 58-63, Jan./Feb. 1997.
- [91] C. Se-Kyo, "A phase tracking system for three phase utility interface inverters," *IEEE Transactions on Power Electronics*, vol. 15, pp. 431-438, May 2000.

- [92] H. Karimi, M. Karimi-Ghartemani, and M. R. Iravani, "Estimation of frequency and its rate of change for applications in power systems," *IEEE Trans. Power Del.*, vol. 19, pp. 472-480, Apr. 2004.
- [93] M. Karimi-Ghartemani and M. R. Iravani, "A method for synchronization of power electronic converters in polluted and variable-frequency environments," *IEEE Trans. Power Syst.*, vol. 19, pp. 1263-1270, Aug. 2004.
- [94] M. Karimi-Ghartemani, B. T. Ooi, and A. Bakhshai, "Application of enhanced phase-locked loop system to the computation of synchrophasors," *IEEE Trans. Power Del.*, vol. 26, pp. 22-32, Jan. 2011.
- [95] M. Karimi-Ghartemani and M. R. Iravani, "Measurement of harmonics/inter-harmonics of time-varying frequencies," *IEEE Trans. Power Del.*, vol. 20, pp. 23-31, Jan. 2005.
- [96] J. R. de Carvalho, C. A. Duque, M. V. Ribeiro, A. S. Cerqueira, T. L. Baldwin, and P. F. Ribeiro, "A PLL-based multirate structure for time-varying power systems harmonic/interharmonic estimation," *IEEE Trans. Power Del.*, vol. 24, pp. 1789-1800, Oct. 2009.
- [97] M. Karimi-Ghartemani, M. Mojiri, A. Bakhshai, and P. Jain, "A phasor measurement algorithm based on phase-locked loop," in *Transmission and Distribution Conference and Exposition (T&D), 2012 IEEE PES*, 2012, pp. 1-6.
- [98] R. E. Kalman, "A new approach to linear filtering and prediction problems," *Journal of Basic Engineering*, vol. 82, pp. 35-45, Mar. 1960.
- [99] M. S. Sachdev, H. C. Wood, and N. G. Johnson, "Kalman filtering applied to power system measurements relaying," *IEEE Transactions on Power Apparatus and Systems*, vol. PAS-104, pp. 3565-3573, Dec. 1985.
- [100] A. A. Girgis and T. L. D. Hwang, "Optimal Estimation Of Voltage Phasors And Frequency Deviation Using Linear And Non-Linear Kalman Filtering: Theory And Limitations," *IEEE Transactions on Power Apparatus and Systems*, vol. PAS-103, pp. 2943-2951, Oct. 1984.
- [101] J. L. Pinto de Sa and L. Pedro, "Modal Kalman filtering based impedance relaying," *IEEE Trans. Power Del.*, vol. 6, pp. 78-84, Jan. 1991.
- [102] A. A. Girgis and W. L. Peterson, "Adaptive estimation of power system frequency deviation and its rate of change for calculating sudden power system overloads," *IEEE Trans. Power Del.*, vol. 5, pp. 585-594, Apr. 1990.
- [103] T. Lobos and J. Rezmer, "Real-time determination of power system frequency," *IEEE Transactions on Instrumentation and Measurement*, vol. 46, pp. 877-881, Aug. 1997.
- [104] J. A. d. I. O. Serna, "Synchrophasor estimation using Prony's method," *IEEE Transactions on Instrumentation and Measurement*, vol. 62, pp. 2119-2128, Aug. 2013.
- [105] I. Kamwa, R. Grondin, V. K. Sood, C. Gagnon, N. Van Thich, and J. Mereb, "Recurrent neural networks for phasor detection and adaptive identification in power system control and protection," *IEEE Transactions on Instrumentation and Measurement*, vol. 45, pp. 657-664, Apr. 1996.

- [106] L. L. Lai, W. L. Chan, C. T. Tse, and A. T. P. So, "Real-time frequency and harmonic evaluation using artificial neural networks," *IEEE Trans. Power Del.*, vol. 14, pp. 52-59, Jan. 1999.
- [107] H. Tao and I. F. Morrison, "The measurement of power system frequency using a microprocessor," *Electric Power Systems Research*, vol. 11, pp. 103-108, Oct. 1986.
- [108] Z. Salcic, S. K. Nguang, and Y. Wu, "An improved taylor method for frequency measurement in power systems," *IEEE Transactions on Instrumentation and Measurement*, vol. 58, pp. 3288-3294, Sep. 2009.
- [109] R. Agha Zadeh, A. Ghosh, G. Ledwich, and F. Zare, "Analysis of phasor measurement method in tracking the power frequency of distorted signals," *Generation, Transmission & Distribution, IET*, vol. 4, pp. 759-769, Jun. 2010.
- [110] T. Xia and Y. Liu, "Single-Phase Phase Angle Measurements in Electric Power Systems," *IEEE Trans. Power Syst.*, vol. 25, pp. 844-852, May 2010.
- [111] D. Dotta and J. H. Chow, "Second harmonic filtering in phasor measurement estimation," *IEEE Trans. Power Del.*, vol. 28, pp. 1240-1241, Apr. 2013.
- [112] G. Benmouyal, "Removal of DC-offset in current waveforms using digital mimic filtering," *IEEE Trans. Power Del.*, vol. 10, pp. 621-630, Apr. 1995.
- [113] M. S. Sachdev and M. Nagpal, "A recursive least error squares algorithm for power system relaying and measurement applications," *IEEE Trans. Power Del.*, vol. 6, pp. 1008-1015, Jul. 1991.
- [114] G. Jyh-Cherng and Y. Sun-Li, "Removal of DC offset in current and voltage signals using a novel Fourier filter algorithm," *IEEE Trans. Power Del.*, vol. 15, pp. 73-79, Jan. 2000.
- [115] N. Soon-Ryul, K. Sang-Hee, and P. Jong-Keun, "An analytic method for measuring accurate fundamental frequency components," *IEEE Trans. Power Del.*, vol. 17, pp. 405-411, Apr. 2002.
- [116] T. S. Sidhu, X. Zhang, F. Albasri, and M. S. Sachdev, "Discrete-Fourier-transform-based technique for removal of decaying DC offset from phasor estimates," *IEE Proceedings - Generation, Transmission and Distribution*, vol. 150, pp. 745-752, 2003.
- [117] T. S. Sidhu, Z. Xudong, and V. Balamourougan, "A new half-cycle phasor estimation algorithm," *IEEE Trans. Power Del.*, vol. 20, pp. 1299-1305, Apr. 2005.
- [118] Y. Chi-Shan, "A discrete Fourier transform-based adaptive mimic phasor estimator for distance relaying applications," *IEEE Trans. Power Del.*, vol. 21, pp. 1836-1846, Oct. 2006.
- [119] G. Yong, M. Kezunovic, and C. Deshu, "Simplified algorithms for removal of the effect of exponentially decaying DC-offset on the Fourier algorithm," *IEEE Trans. Power Del.*, vol. 18, pp. 711-717, Jul. 2003.
- [120] Y. Chi-Shan, "A reiterative DFT to damp decaying DC and subsynchronous frequency components in fault current," *IEEE Trans. Power Del.*, vol. 21, pp. 1862-1870, Oct. 2006.

- [121] R. K. Mai, L. Fu, Z. Y. Dong, B. Kirby, and Z. Q. Bo, "An Adaptive Dynamic Phasor Estimator Considering DC Offset for PMU Applications," *IEEE Trans. Power Del.*, vol. 26, pp. 1744-1754, Jul. 2011.
- [122] Y. S. Cho, C. K. Lee, G. Jang, and H. J. Lee, "An Innovative Decaying DC Component Estimation Algorithm for Digital Relaying," *IEEE Trans. Power Del.*, vol. 24, pp. 73-78, Jan. 2009.
- [123] S. H. Kang, D. G. Lee, S. R. Nam, P. A. Crossley, and Y. C. Kang, "Fourier Transform-Based Modified Phasor Estimation Method Immune to the Effect of the DC Offsets," *IEEE Trans. Power Del.*, vol. 24, pp. 1104-1111, Jul. 2009.
- [124] R. K. Mai, Z. Y. He, L. Fu, B. Kirby, and Z. Q. Bo, "A Dynamic Synchrophasor Estimation Algorithm for Online Application," *IEEE Trans. Power Del.*, vol. 25, pp. 570-578, Apr. 2010.
- [125] G. Barchi and D. Petri, "An improved dynamic synchrophasor estimator," in *Energy Conference and Exhibition (ENERGYCON), 2012 IEEE International*, 2012, pp. 812-817.
- [126] J. A. de la O Serna, "Synchrophasor measurement with polynomial phase-locked-loop Taylor-Fourier filters," *IEEE Transactions on Instrumentation and Measurement*, vol. 64, pp. 328-337, Feb. 2015.
- [127] H. C. Lin and C. S. Lee, "Enhanced FFT-based parametric algorithm for simultaneous multiple harmonics analysis," *IEE Proceedings - Generation, Transmission and Distribution*, vol. 148, pp. 209-214, 2001.
- [128] T. Routtenberg and L. Tong, "Joint Frequency and Phasor Estimation Under the KCL Constraint," *IEEE Signal Processing Letters*, vol. 20, pp. 575-578, Jun. 2013.
- [129] Y. Jun-Zhe and L. Chih-Wen, "A precise calculation of power system frequency," *IEEE Trans. Power Del.*, vol. 16, pp. 361-366, Jul. 2001.
- [130] A. K. Pradhan, A. Routray, and A. Basak, "Power system frequency estimation using least mean square technique," *IEEE Trans. Power Del.*, vol. 20, pp. 1812-1816, Jul. 2005.
- [131] D. Jingyuan, X. Tao, Z. Yingchen, T. Weekes, J. S. Thorp, and L. Yilu, "Monitoring power system disturbances at the distribution level," in *Power and Energy Society General Meeting - Conversion and Delivery of Electrical Energy in the 21st Century, 2008 IEEE*, 2008, pp. 1-8.
- [132] C. Lang, P. N. Markham, and L. Yilu, "Wide-area dynamic model validation using FNET measurements," in *Innovative Smart Grid Technologies (ISGT), 2012 IEEE PES*, 2012, pp. 1-7.
- [133] L. Ying-Hong, L. Chih-Wen, and C. Ching-Shan, "A new PMU-based fault detection/location technique for transmission lines with consideration of arcing fault discrimination-part I: theory and algorithms," *IEEE Trans. Power Del.*, vol. 19, pp. 1587-1593, 2004.
- [134] S. Corsi and G. N. Taranto, "A Real-Time Voltage Instability Identification Algorithm Based on Local Phasor Measurements," *IEEE Trans. Power Syst.*, vol. 23, pp. 1271-1279, Aug. 2008.
- [135] H. Y. Su and C. W. Liu, "An Adaptive PMU-Based Secondary Voltage Control Scheme," *IEEE Trans. Smart Grid*, vol. 4, pp. 1514-1522, Sep. 2013.

- [136] S. Soni, S. Bhil, D. Mehta, and S. Wagh, "Linear state estimation model using phasor measurement unit (PMU) technology," in *Electrical Engineering, Computing Science and Automatic Control (CCE), 2012 9th International Conference on*, 2012, pp. 1-6.
- [137] S. G. Ghiocel, J. H. Chow, G. Stofopoulos, B. Fardanesh, D. Maragal, B. Blanchard, M. Razanousky, and D. B. Bertagnolli, "Phasor-Measurement-Based State Estimation for Synchrophasor Data Quality Improvement and Power Transfer Interface Monitoring," *IEEE Trans. Power Syst.*, vol. 29, pp. 881-888, Mar. 2014.
- [138] L. Zhenzhi, X. Tao, Y. Yanzhu, Z. Ye, C. Lang, L. Yilu, K. Tomsovic, T. Bilke, and W. Fushuan, "Application of wide area measurement systems to islanding detection of bulk power systems," *IEEE Trans. Power Syst.*, vol. 28, pp. 2006-2015, May 2013.
- [139] D. Shi, D. J. Tylavsky, K. M. Koellner, N. Logic, and D. E. Wheeler, "Transmission line parameter identification using PMU measurements," *European Transactions on Electrical Power*, vol. 21, pp. 1574-1588, Nov. 2011.
- [140] S. R. Júlíusson, "Using PMU Measurements to Assess Dynamic Line Rating of Transmission Lines," M. S. thesis, Board of Studies of Energy, Aalborg University, Aalborg, Denmark, 2013.
- [141] H. Liu, L. Zhu, Z. Pan, F. Bai, Y. Liu, Y. Liu, M. Patel, E. Farantatos, and N. Bhatt, "ARMAX-Based Transfer Function Model Identification Using Wide-Area Measurement for Adaptive and Coordinated Damping Control," *IEEE Trans. Smart Grid*, vol. 8, pp. 1105-1115, 2017.
- [142] J. De La Ree, V. Centeno, J. S. Thorp, and A. G. Phadke, "Synchronized Phasor Measurement Applications in Power Systems," *IEEE Trans. Smart Grid*, vol. 1, pp. 20-27, 2010.
- [143] A. Goldstein, "2014 NIST Assessment of Phasor Measurement Unit Performance," National Institute of Standards and Technology, 2014, <http://nvlpubs.nist.gov/nistpubs/ir/2016/NIST.IR.8106.pdf>.
- [144] Z. Huang, B. Kasztenny, V. Madani, K. Martin, S. Meliopoulos, D. Novosel, and J. Stenbakken, "Performance evaluation of phasor measurement systems," in *2008 IEEE Power and Energy Society General Meeting - Conversion and Delivery of Electrical Energy in the 21st Century*, Pittsburgh, PA, USA, 2008, pp. 1-7.
- [145] A. P. S. Meliopoulos, F. Zhang, S. Zelingher, G. Stillman, G. J. Cokkinides, L. Coffeen, R. Burnett, and J. McBride, "Transmission level instrument transformers and transient event recorders characterization for harmonic measurements," *IEEE Trans. Power Del.*, vol. 8, pp. 1507-1517, 1993.
- [146] J. Zhao, J. Tan, L. Wu, L. Zhan, W. Yao, Y. Liu, J. R. Gracia, and P. D. Ewing, "Impact of measurement errors on synchrophasor applications," in *IEEE Power & Energy Society General Meeting*, Chicago, IL, 2017.
- [147] L. Zanni, D. Colangelo, R. Cherkaoui, and M. Paolone, "Impact of synchrophasor measurement types and uncertainties on the accuracy of distribution system linear state estimators," in *2015 IEEE Eindhoven PowerTech*, Eindhoven, Netherlands, 2015, pp. 1-6.

- [148] S. Chakrabarti and E. Kyriakides, "PMU Measurement Uncertainty Considerations in WLS State Estimation," *IEEE Trans. Power Syst.*, vol. 24, pp. 1062-1071, 2009.
- [149] M. Asprou, E. Kyriakides, and M. Albu, "The effect of parameter and measurement uncertainties on hybrid state estimation," in *2012 IEEE Power and Energy Society General Meeting*, San Diego, CA, USA, 2012, pp. 1-8.
- [150] J. Tang, J. Liu, F. Ponci, C. Muscas, and S. Sulis, "Effects of PMU's uncertainty on voltage stability assessment in power systems," in *2011 IEEE International Instrumentation and Measurement Technology Conference*, Binjing, China, 2011, pp. 1-5.
- [151] J. Tang, J. Liu, F. Ponci, A. Monti, C. Muscas, and S. Sulis, "Impact of synchrophasor measurement uncertainty on detecting voltage stability margin in power systems," in *2012 3rd IEEE PES Innovative Smart Grid Technologies Europe (ISGT Europe)*, Berlin, Germany, 2012, pp. 1-6.
- [152] A. Perez, J. Møller, H. Jóhannsson, and J. Østergaard, "Uncertainty in real-time voltage stability assessment methods based on Thévenin equivalent due to PMU's accuracy," in *IEEE PES Innovative Smart Grid Technologies, Europe*, Istanbul, Turkey, 2014, pp. 1-6.
- [153] A. Perez, H. Jóhannsson, J. Østergaard, and K. Martin, "Improved method for considering PMU's uncertainty and its effect on real-time stability assessment methods based on Thévenin equivalent," in *2015 IEEE Eindhoven PowerTech*, Eindhoven, Netherlands, 2015, pp. 1-5.
- [154] T. Becejac, P. Dehghanian, and M. Kezunovic, "Impact of the errors in the PMU response on synchrophasor-based fault location algorithms," in *2016 North American Power Symposium (NAPS)*, Denver, CO, USA, 2016, pp. 1-6.
- [155] C. Chen, J. Wang, and H. Zhu, "Effects of Phasor Measurement Uncertainty on Power Line Outage Detection," *IEEE Journal of Selected Topics in Signal Processing*, vol. 8, pp. 1127-1139, 2014.
- [156] J. Zhao, A. Goldstein, and Y. Liu, "Model of parameterized PMU estimation error," in *IEEE Power & Energy Society General Meeting*, Chicago, IL, 2017.
- [157] A. P. S. Meliopoulos, G. J. Cokkinides, F. Galvan, and B. Fardanesh, "GPS-Synchronized Data Acquisition: Technology Assessment and Research Issues," in *Proc. 2006 System Sciences International Conf.*, Kauia, HI, USA, 2006, pp. 244c.
- [158] A. S. Meliopoulos and G. J. Cokkinides, "Visualization and animation of instrumentation channel effects on DFR data accuracy," in *Proceedings of the 2002 Georgia Tech Fault and Disturbance Analysis Conference*, Atlanta, GA, USA, 2002.
- [159] A. P. Meliopoulos, V. Madani, D. Novosel, G. Cokkinides, R. Alaileh, B. Fardanesh, H. Huang, M. Ford, F. Mekic, U. Manmandhan, R. Hayes, J. Hackett, and S. Widergren, "Synchrophasor Measurement Accuracy Characterization," North American Synchrophasor Initiative Performance & Standards Task Team, 2007.
- [160] *American National Standard Requirements for Power-Line Carrier Coupling Capacitors and Coupling Capacitor Voltage Transformers (CCVT)*, ANSI C93.1-1999, 1999.

- [161] *A Guide for PMU Installation, Commissioning and maintenance*, NASPI Performance and Standard Task Team (PSTT), 2007.
- [162] *PMU installation and configuration requirements*, MISO, 2012.
- [163] *IEEE Synchrophasor Measurement Test Suite Specification*, IEEE Standard C37.242-2015, 2015.
- [164] J. S. Thorp, C. E. Seyler, and A. G. Phadke, "Electromechanical wave propagation in large electric power systems," *Circuits and Systems I: Fundamental Theory and Applications*, *IEEE Transactions on*, vol. 45, pp. 614-622, Jun. 1998.
- [165] R. M. Gardner, Y. Liu, and Z. Zhong, "Location determination of power system disturbances based on frequency responses of the system," U.S. Patent 7 519 454, Apr. 14, 2009.
- [166] Y. Ye, "Wide-area Situational Awareness Application Developments," Ph.D. dissertation, Dept. Elec. Eng. and Comp. Sci., Univ. Tennessee, Knoxville, Knoxville, TN, USA, 2011.
- [167] T. Xia, Y. Zhang, L. Chen, Z. Yuan, P. N. Markham, Y. Ye, and Y. Liu, "Phase angle-based power system inter-area oscillation detection and modal analysis," *European Transactions on Electrical Power*, vol. 21, pp. 1629-1639, Nov. 2011.
- [168] A. Michiorri, H.-M. Nguyen, S. Alessandrini, J. B. Bremnes, S. Dierer, E. Ferrero, B.-E. Nygaard, P. Pinson, N. Thomaidis, and S. Uski, "Forecasting for dynamic line rating," *Renewable and Sustainable Energy Reviews*, vol. 52, pp. 1713-1730, Dec. 2015.
- [169] J. Zhao, J. Tan, L. Wu, L. Zhan, L. Yilu, J. R. Gracia, and P. D. Ewing, "Impact of Measurement Error on Synchrophasor Applications," Oak Ridge National Laboratory, Oak Ridge, TN, USA, 2015, www.osti.gov/servlets/purl/1212367/
- [170] *IEEE Standard for Calculating the Current-Temperature Relationship of Bare Overhead Conductors*, IEEE Standard 738-2012, 2013.
- [171] P. Mahat, C. Zhe, and B. Bak-Jensen, "Review of islanding detection methods for distributed generation," in *2008 Third International Conf. on Electric Utility Deregulation and Restructuring and Power Technologies*, 2008, pp. 2743-2748.
- [172] T. Yang, S. Hongbin, and A. Bose, "Transition to a Two-Level Linear State Estimator-Part I: Architecture," *IEEE Trans. Power Syst.*, vol. 26, pp. 46-53, 2011.
- [173] J. Chai, J. Zhao, Y. Wenxuan, J. Guo, and Y. Liu, "Application of wide area power system measurement for digital authentication," in *2016 IEEE/PES Transmission and Distribution Conference and Exposition (T&D)*, 2016, pp. 1-5.
- [174] L. Guoping, J. Quintero, and V. Venkatasubramanian, "Oscillation monitoring system based on wide area synchrophasors in power systems," in *Bulk Power System Dynamics and Control - VII. Revitalizing Operational Reliability, 2007 iREP Symposium*, 2007, pp. 1-13.
- [175] J. Zhao, L. Zhan, Y. Liu, H. Qi, J. R. Gracia, and P. D. Ewing, "Measurement Accuracy Limitation Analysis on Synchrophasors," in *IEEE Power & Energy Society General Meeting*, Denver, 2015.

- [176] D. Yi, L. Hua, A. G. Phadke, S. Shukla, J. S. Thorp, and L. Mili, "Communication network modeling and simulation for Wide Area Measurement applications," in *Innovative Smart Grid Technologies (ISGT), 2012 IEEE PES*, 2012, pp. 1-6.
- [177] *IEEE Standard for Synchrophasor Measurements for Power Systems, Amendment 1: Modification of Selected Performance Requirements*, C37.118.1a-2014, 2014.
- [178] A. G. Phadke, "Synchronized phasor measurements-a historical overview," in *Transmission and Distribution Conference and Exhibition 2002: Asia Pacific. IEEE/PES*, 2002, pp. 476-479 vol.1.
- [179] E. O. Schweitzer, D. Whitehead, G. Zweigle, and K. G. Ravikumar, "Synchrophasor-based power system protection and control applications," in *Protective Relay Engineers, 2010 63rd Annual Conference for*, 2010, pp. 1-10.
- [180] Z. Yingchen, P. Markham, X. Tao, C. Lang, Y. Yanzhu, W. Zhongyu, Y. Zhiyong, W. Lei, J. Bank, J. Burgett, R. W. Conners, and L. Yilu, "Wide-Area Frequency Monitoring Network (FNET) Architecture and Applications," *IEEE Trans. Smart Grid*, vol. 1, pp. 159-167, 2010.
- [181] Z. Ke, Y. Yanzhu, C. Lang, Z. Yingchen, R. M. Gardner, and L. Yilu, "FNET observations of low frequency oscillations in the eastern interconnection and their correlation with system events," in *Power and Energy Society General Meeting, 2011 IEEE*, 2011, pp. 1-8.
- [182] B. A. Renfro, A. Terry, and N. Boeker, "An analysis of global positioning system (GPS) standard positioning system (SPS) performance for 2016," The University of Texas at Austin, Austin, TX, May 2017.
- [183] "TI GPS PPS Timing Application Note," Texas Instruments, 2012.
- [184] W. Yao, L. Zhan, Y. Liu, M. Till, J. Zhao, L. Wu, Z. Teng, and Y. Liu, "A Novel Method for Phasor Measurement Unit Sampling Time Error Compensation," *IEEE Trans. Smart Grid*, vol. PP, pp. 1-1, 2016.
- [185] L. Hsiung Cheng, "Intelligent Neural Network-Based Fast Power System Harmonic Detection," *Industrial Electronics, IEEE Transactions on*, vol. 54, pp. 43-52, 2007.
- [186] D. Chou, L. Heng, and G. X. Gao, "Robust GPS-Based Timing for Phasor Measurement Units: A Position-Information-Aided Approach," in *ION GNSS+ 2014*, Tampa FL, 2014.
- [187] X. Zhang, "High precision dynamic power system frequency estimation algorithm based on phasor approach," Master of Science, Electrical Engineering, Virginia Polytechnic Institute and State University, Blacksburg, VA, 2004.
- [188] F. Katiraei, M. R. Iravani, and P. W. Lehn, "Micro-grid autonomous operation during and subsequent to islanding process," *IEEE Trans. Power Del.*, vol. 20, pp. 248-257, Jan. 2005.
- [189] S. You, Y. Liu, G. Kou, X. Zhang, W. Yao, Y. Su, S. Hadley, and Y. Liu, "Non-Invasive Identification of Inertia Distribution Change in High Renewable Systems Using Distribution Level PMU," *IEEE Trans. Power Syst.*, vol. PP, pp. 1-1, 2017.
- [190] S. You, G. Kou, Y. Liu, X. Zhang, Y. Cui, M. J. Till, W. Yao, and Y. Liu, "Impact of High PV Penetration on the Inter-Area Oscillations in the U.S. Eastern Interconnection," *IEEE Access*, vol. 5, pp. 4361-4369, 2017.

- [191] R. K. Varma, S. Auddy, and Y. Semsedini, "Mitigation of Subsynchronous Resonance in a Series-Compensated Wind Farm Using FACTS Controllers," *IEEE Trans. Power Del.*, vol. 23, pp. 1645-1654, 2008.
- [192] C. Li, Y. Liu, K. Sun, Y. Liu, and N. Bhatt, "Measurement based power system dynamics prediction with multivariate AutoRegressive Model," in *T&D Conference and Exposition, 2014 IEEE PES*, 2014, pp. 1-5.
- [193] L. Zhan, Z. Jianyang, J. Culliss, Y. Liu, Y. Liu, and G. Shengyou, "Universal Grid Analyzer design and development," in *2015 IEEE Power & Energy Society General Meeting*, 2015, pp. 1-5.
- [194] A. Goldstein, D. Anand, and Y.-S. Li-Babound, "Investigation of PMU Response to Leap Second: 2015," National Institute of Standards and Technology, 2015.
- [195] C. Grigoras, "Forensic analysis of the digital audio recordings-The electric network frequency criterion," in *Forensic Science International*, 2003, pp. 368-369.
- [196] C. Grigoras, "Applications of ENF criterion in forensic audio, video, computer and telecommunication analysis," *Forensic Science International*, vol. 167, pp. 136-145, 2007/04/11/ 2007.
- [197] R. Garg, A. L. Varna, A. Hajj-Ahmad, and M. Wu, "'Seeing' ENF: power-signature-based timestamp for digital multimedia via optical sensing and signal processing," *IEEE Transactions on Information Forensics and Security*, vol. 8, pp. 1417-1432, 2013.
- [198] K. L. V. Iyer, X. Lu, Y. Usama, V. Ramakrishnan, and N. C. Kar, "A Twofold Daubechies-Wavelet-Based Module for Fault Detection and Voltage Regulation in SEIGs for Distributed Wind Power Generation," *IEEE Transactions on Industrial Electronics*, vol. 60, pp. 1638-1651, 2013.
- [199] S. B. Andrade, M. Pignati, G. Dan, M. Paolone, and J. Y. L. Boudec, "Undetectable PMU Timing-Attack on Linear State-Estimation by Using Rank-1 Approximation," *IEEE Trans. Smart Grid*, vol. PP, pp. 1-1, 2017.
- [200] Y. Fan, Z. Zhang, M. Trinkle, A. D. Dimitrovski, J. B. Song, and H. Li, "A Cross-Layer Defense Mechanism Against GPS Spoofing Attacks on PMUs in Smart Grids," *IEEE Trans. Smart Grid*, vol. 6, pp. 2659-2668, 2015.
- [201] B. Moussa, M. Debbabi, and C. Assi, "A detection and mitigation model for PTP delay attack in a smart grid substation," in *2015 IEEE International Conference on Smart Grid Communications (SmartGridComm)*, 2015, pp. 497-502.
- [202] M. S. Almas, L. Vanfretti, R. S. Singh, and G. M. Jonsdottir, "Vulnerability of Synchrophasor-based WAMPAC Applications' to Time Synchronization Spoofing," *IEEE Trans. Smart Grid*, vol. PP, pp. 1-1, 2017.
- [203] A. Khalajmehrabadi, N. Gatsis, D. Akopian, and A. Taha, "Real-Time Rejection and Mitigation of Time Synchronization Attacks on the Global Positioning System," *IEEE Transactions on Industrial Electronics*, vol. PP, pp. 1-1, 2018.
- [204] Z. Zhang, S. Gong, A. D. Dimitrovski, and H. Li, "Time Synchronization Attack in Smart Grid: Impact and Analysis," *IEEE Trans. Smart Grid*, vol. 4, pp. 87-98, 2013.
- [205] J. Wang, W. Tu, L. C. K. Hui, S. M. Yiu, and E. K. Wang, "Detecting Time Synchronization Attacks in Cyber-Physical Systems with Machine Learning

- Techniques," in *2017 IEEE 37th International Conference on Distributed Computing Systems (ICDCS)*, 2017, pp. 2246-2251.
- [206] L. Zhan, Y. Liu, W. Yao, J. Zhao, and Y. Liu, "Utilization of Chip-Scale Atomic Clock for Synchrophasor Measurements," *IEEE Trans. Power Del.*, vol. 31, pp. 2299-2300, 2016.
 - [207] J. Kappenman, "Geomagnetic storms and their impacts on the US power grid," Metatech, Jan. 2010.
 - [208] T. Hutchins, "Geomagnetically induced currents and their effect on power systems," Electrical and Computer Engineering, University of Illinois at Urbana-Champaign, 2012.
 - [209] M. W. Wik and W. A. Radasky, "Development of high-power electromagnetic (HPEM) standards," *IEEE Transactions on Electromagnetic Compatibility*, vol. 46, pp. 439-445, 2004.
 - [210] R. Pirjola, "Geomagnetically Induced Currents as Ground Effects of Space Weather," in *Space Science*, H. J. M. Cuesta, Ed., ed: InTech, 2012, pp. 27-44.
 - [211] R. Girgis and K. Vedante, "Methodology for evaluating the impact of GIC and GIC capability of power transformer designs," in *2013 IEEE Power & Energy Society General Meeting*, 2013, pp. 1-5.
 - [212] G. B. Iyyuni and S. A. Sebo, "Study of transmission line magnetic fields," in *Proceedings of the Twenty-Second Annual North American Power Symposium*, 1990, pp. 222-231.
 - [213] S. R. Azzuhri and W. N. L. Mahadi, "Power transmission line magnetic fields: a survey on 120 kV overhead power transmission lines in Malaysia," in *2004 IEEE Region 10 Conference TENCN 2004.*, 2004, pp. 421-424 Vol. 3.

APPENDIX

Appendix A Dynamic Line Rating of Overhead Transmission Line

The thermal current rating of a conductor is the maximum current which meets the design, security and safety criteria of a particular line on which the conductor is used. The algorithm is originally introduced in IEEE Standard 738-2012 [170].

The ampacity of an overhead transmission line is determined by the dissipation of its heat produced by Joule effect into the environment. The heat balance of per unit length of the conductor can be represent by:

$$m \cdot C_p \cdot \frac{dT_c}{dt} = q_j + q_s - q_c - q_r, \quad (\text{A.1})$$

where $m[\text{kg} \cdot \text{m}^{-1}]$ is the mass per unit length of conductor material, $C_p[\text{J} \cdot \text{kg}^{-1} \cdot \text{K}]$ is the heat capacity of conductor material, $T_c[\text{K}]$ is the conductor temperature, $q_j[\text{W} \cdot \text{m}^{-1}]$ is the heat produced by Joule effect, $q_s[\text{W} \cdot \text{m}^{-1}]$ is the solar heating, $q_c[\text{W} \cdot \text{m}^{-1}]$ is the convective cooling, and $q_r[\text{W} \cdot \text{m}^{-1}]$ is the radiative cooling.

The steady state ampacity of the transmission line is represented by the maximum current satisfying the heat balance where conductor heat gain equals to conductor heat loss:

$$q_j = q_c + q_r - q_s \quad (\text{A.2})$$

$$I_{\max_steady}^2 R(T_{\max}) = q_j \quad (\text{A.3})$$

where $I_{\max_steady}[\text{A}]$ is the ampacity and $R(T_{\max})[\Omega \cdot \text{m}^{-1}]$ is the AC resistance of conductor per unit length at the maximum allowed conductor temperature $T_{\max}[\text{K}]$.

When the feeding current I_{in} is larger than the allowable value I_{\max_steady} , the final temperature will surpass T_{\max} after a period of time. This dynamic process can be represented by the differential equation derived from (A.1) and (A.3) as

$$m \cdot C_p \cdot \frac{dT_c}{dt} = I_{in}^2 \cdot R(T_c) + q_s - q_c - q_r, \quad (\text{A.4})$$

It is safe as long as the conductor temperature T_c is less than T_{\max} . Given a time period, the maximum current I_{\max} to guarantee this safety can be calculated from (A.4).

To solve I_{\max} , the following variables are also needed: m , C_p , present conductor temperature T_p , $R(T_c)$, q_s , q_c , and q_r . Among them m and C_p can be obtained according to the conductor material characteristics. The calculation of the others are introduced below.

A.1 Conductor Temperature and Resistance

Present conductor temperature T_p can be calculated from the conductor AC resistance. For the nominal π model of a medium length transmission line, the circuit equations can be obtained by Kirchhoff's voltage and current laws and represented by:

$$\begin{bmatrix} V_s \\ I_s \end{bmatrix} = \begin{bmatrix} 1 + \frac{YZ}{2} & Z \\ Y \left(1 + \frac{YZ}{4}\right) & 1 + \frac{YZ}{2} \end{bmatrix} \begin{bmatrix} V_r \\ I_r \end{bmatrix}, \quad (\text{A.5})$$

where $Z[\Omega]$ is the series impedance and $Y[\text{S}]$ is the shunt admittance; V_s , I_s , V_r , and I_r are the voltages and currents measured on both ends of the transmission line by PMUs. The AC resistance $R(T_p)$ is the real part of Z , and can be calculated by:

$$R(T_p) = \text{Re}(Z) = \text{Re} \left(\frac{V_s^2 - V_r^2}{V_s I_r + V_r I_s} \right). \quad (\text{A.6})$$

With the knowledge of conductor resistance, the temperature can be calculated according to the tabular resistance values of the transmission line. E.g., the conductor resistance at a high temperature $T_{high}[\text{K}]$ and a low temperature $T_{low}[\text{K}]$ are taken from the corresponding handbook or provided by the manufacture, the present temperature $T_p[\text{K}]$ of resistance $R(T_p)$ can be calculated by linear interpolation:

$$T_p = \left[\frac{R(T_p) - R(T_{low})}{R(T_{high}) - R(T_{low})} \right] \cdot (T_{high} - T_{low}) + T_{low}. \quad (\text{A.7})$$

The resistance $R(T_c)$ at a given temperature T_c can also be calculated according to (A.7).

A.2 Solar Heating

Solar heating q_s is calculated by:

$$q_s = \alpha \cdot Q_{se} \cdot \sin(\theta) \cdot A', \quad (\text{A.8})$$

where α is solar absorptivity, Q_{se} is the solar heat intensity at the earth's surface, θ is the effective angle of incidence of sun's rays, and A' is the projected area of the conductor.

A.3 Convective Cooling

Convective cooling is the greater of the nature convection cooling and the forced convention heat loss. The nature convection cooling q_{cn} is calculated by:

$$q_{cn} = 3.645 \cdot \rho_f^{0.5} \cdot D_0^{0.5} \cdot (T_s - T_a)^{0.5}, \quad (\text{A.9})$$

where $\rho_f[\text{kg}\cdot\text{m}^{-3}]$ is the air density, $D_0[\text{m}]$ is the conductor diameter, $T_s[\text{K}]$ is the conductor surface temperature, and $T_a[\text{K}]$ is the ambient temperature.

The forced convection is given by the larger of the following two equations:

$$q_{c1} = K_{angle} \cdot [1.01 + 1.35 \cdot N_{Re}^{0.52}] \cdot k_f \cdot (T_s - T_a), \quad (\text{A.10})$$

$$q_{c2} = K_{angle} \cdot 0.754 \cdot N_{Re}^{0.6} \cdot k_f \cdot (T_s - T_a). \quad (\text{A.11})$$

In both (A.10) and (A.11), k_{angle} is the wind direction factor given by:

$$K_{angle} = 1.1194 - \cos(\phi) + 0.194 \cdot \cos(2\phi) + 0.368 \sin(2\phi), \quad (\text{A.12})$$

where ϕ is the angle between the wind direction and the conductor axis. Reynolds number, N_{Re} is given as

$$N_{Re} = \frac{D_0 \cdot \rho_f \cdot V_W}{\mu_f}, \quad (\text{A.13})$$

where V_W is the wind velocity; μ_f is the dynamic viscosity of air, calculated by

$$\mu_f = \frac{1.458 \cdot 10^{-6} \cdot T_{film}^{1.5}}{T_{film} + 110.4}. \quad (\text{A.14})$$

The air density is

$$\rho_f = \frac{1.293 - 1.525 \cdot 10^{-4} \cdot H_e + 6.379 \cdot 10^{-9} \cdot H_e^2}{1 + 0.00367 \cdot T_{film}}. \quad (\text{A.15})$$

where $H_e[\text{m}]$ is the elevation of conductor above sea level.

Thermal conductivity of air is

$$k_f = 2.424 \cdot 10^{-2} + 7.477 \cdot 10^{-5} \cdot (T_{film} - 273) - 4.407 \cdot 10^{-9} \cdot (T_{film} - 273)^2. \quad (\text{A.16})$$

Average temperature of the boundary layer T_{film} is given by

$$T_{film} = \frac{T_s + T_a}{2}. \quad (\text{A.17})$$

where the current density is less than $1 \text{ A}\cdot\text{mm}^{-2}$ (as the scenario used in this paper), the radial temperature different of the conductor can be neglected and the surface temperature T_s can be represented by conductor temperature T_c .

A.4 Radiative Cooling

Radiative cooling is calculated by:

$$q_r = 17.8 \cdot D_0 \cdot \varepsilon \cdot \left[\left(\frac{T_s}{100} \right)^4 - \left(\frac{T_a}{100} \right)^4 \right]. \quad (\text{A.18})$$

where ε is the emissivity and equals to 0.8.

Appendix B Implementation of CRC-CCITT

The code of CRC-CCITT is realized below.

```
unsigned int ComputeCRC(char *Message, int MessLen)
{
    unsigned int crc = 0xFFFF;
    unsigned int temp;
    unsigned int quick;
    int i;
    for (i = 0; i < MessLen; i++)
    {
        temp = (crc >> 8) ^ Message[i];
        crc <<= 8;
        quick = temp ^ (temp >> 4);
        crc ^= quick;
        quick <<= 5;
        crc ^= quick;
        quick <<= 7;
        crc ^= quick;
    }
    return crc;
}
```

Appendix C Time Accuracy and Reliability of Synchrophasors

C.1 Introduction

Synchrophasors relies on an accuracy timing source, such as GPS to synchronously acquire voltage/current data from power grid, and assign precise time stamp to the estimated parameters such as phasor and frequency. The data quality of synchrophasors highly depends on the performance of timing source. This is because 1) the samplings are evenly distributed along the time and are required to be aligned with the UTC time; 2) the sampling interval is usually disciplined by the timing source; 3) the time stamp assigned to the measurements are from the timing source. Therefore, the availability and accuracy of the timing source is critical to the synchrophasor measurements.

C.2 Problems

When the timing source is unavailable, the synchrophasor relies on the internal oscillator of the GPS receiver to provide time stamp and PPS signal. As the output frequency of oscillator suffers from aging and drifting, and also depends on the ambient parameters such as temperature and humidity, the time stamp and PPS signal it provides gradually fluctuates and drifts away from the UTC time, and introduces measurement error of synchrophasor.

Even when the time source is accessible, it also includes error which will be transferred into the synchrophasor measurements. Here GPS is taken as an example, since it is the most widely used timing source by synchrophasors deployed. The position and time of the GPS receiver is calculated through navigation equations which are generally based on the fact that the distance equals to the multiplication of speed and travel time. The speed here is the speed of electromagnetic wave which is broadcasted from GPS satellites and received by the GPS receiver. The travel time is the time period during which the broadcasting signal travels from GPS satellites to the receiver, also known as time of flight (TOF). The positions of GPS satellites can be parsed from the ephemeris include in GPS navigation messages in terms of coordinator. Therefore, the distances from the receiver and each satellite can be represented by the coordinators of the receiver and GPS, which includes three unknown variables corresponding to the coordinator of the receiver. The TOF is calculated by the time of transmission (TOT) in code of the navigation message, and the time of arrival (TOA) which is measured by the clock of the receiver. To solve these three variables, theoretically at least three GPS satellites are needed. Due to the uncertainty of TOA is relatively large, a fourth variable is set to indicate the time deviation between the receiver clock and the UTC time. Therefore, a GPS receiver requires at least four satellites to obtain an accurate coordination and time.

As the coordinator of GPS satellites and TOT, which are assumed as absolute accurate, are not ideal, usually more satellites can be used to solve the optimized solution of receiver position and time, and thus improve the accuracy. However, such a large number of GPS satellites are not always available by the GPS receiver, especially considering that

GPS antenna sometimes have to be installed near the window and the scope of the view of sky is quite limited.

Furthermore, another assumption in the navigation equations is that the speed of the electromagnetic wave is constant and equals to the speed of light in vacuum. In reality, this speed is inconsistent and impacted by multiple ambient factors. One of the most significant factor is the ionosphere around the earth, which introduces a delay when the electromagnetic wave pass through it. This delay is called ionospheric delay which depends on both the condition of the ionosphere and the frequency of the microwave signal.

Yet another assumption is that the wave from satellites travel through a direct path to the GPS receiver. In reality, as there exists buildings, canyon walls, or hard ground nearby, the radio signal will reflect off surrounding terrain and cause multipath issue. As signals reach the receiver include both directly and bouncing off one or multiple times, they arrive with slightly different time differences. They tend to overlap and add up to form a sort of signal blob. The receiver is looking for the peak of that blob as the TOA and an error is generated. The messier the blob, the less accurate the TOA and hence the final calculated time and position.

Besides the GPS satellite availability and GPS time error, another factor which could influence the time accuracy and reliability is GPS attack. The attack includes 1) GPS jamming, which intentionally block, jam, or interfere the GPS signal; 2) GPS spoofing, which deceive the GPS receiver by mimic one or more GPS satellite(s) and broadcasting incorrect GPS signals. Both could highly influence the time accuracy and reliability of synchronphasors.

C.3 Mitigation

An alternative or backup timing source is a solution to timing source loss or detected timing source error. Some of the proposed and/or tested candidate timing sources include: Network Time Protocol (NTP), Precision Time Protocol (PTP), eLoran, Iridium, WWVB, etc.

For the timing sources use GPS receiver, there are several methods to improve the accuracy. For the ionospheric delay, which is the largest error, ionospheric model is step up and the parameters are measured by spacecraft and broadcasted for ionospheric delay estimation. However, some errors remain. A solution is to use different radio frequencies. GPS II broadcasts on two frequencies: L1 (1575.42 MHz) and L2 (1227.60 MHz). As ionospheric delay is a well-defined function of frequency and the total electron content (TEC) along the path. The receiver which can receive and parse both frequencies is therefore able to measure the arrival time difference between the two frequencies and determine TEC thus the precise ionospheric delay at each frequency. L2, which is previously reserved for military, is open to civil in GPS III named L2C. Dual-frequency can not only help to measure and remove the ionospheric delay error and improve the

timing accuracy, it also increases the system redundancy and the resistance to GPS jamming. However, it also increases the cost of hardware.

Another solution is to utilize augmentation systems, which were based on ground-based or space-based stations to aid GPS by providing accuracy, integrity, availability, or other improvements on positioning and timing. This type of system includes Nationwide Differential GPS System (NDGPS), Wide Area Augmentation System (WAAS), Continuously Operating Reference Stations (CORS), Global Differential GPS (GDGPS), International GNSS Service (IGS), etc.

In dealing with the multipath reflection error, it is found that the new frequency signal, namely L5, could help to decrease this error. This new civil GPS signal is firstly tested in the Block IIR-M satellite SVN49 in 2009 and will be standard on the GPS III. The frequency selected for L5 is 1176.45 MHz, which is in a protected aeronautical radionavigation services (ARNS) band. This makes L5 signal in the radio spectrum officially protected from interference by other users of the spectrum, and it can be used for safety-of-life applications such as navigating aircraft. Besides this, one advantage of L5 signal is that it is much less prone to distortions from the multipath reflection than L1. This is especially beneficial in cities where multipath reflection is severe. Although multipath reflection still happens on L5 signals, they are sharp enough that the most direct signal is unlikely to overlap with the reflection signals. The receiver chip, therefore, can simply ignore any signal after the first one it receives, which is the shortest path. In this way, the multipath reflection error is greatly decreased. The L5 signal has this characteristic is generally because its transmitted power is increased to be twice as L1 signal and the chip rate is 10 times higher compared to the L1 code signal.

Although various techniques are developed to help improve the accuracy of GPS timing and positioning, a lot of civil GPS receiver products are still using only the L1 signal mainly due to the cost. As the expansion of the GPS market and the increase of the requirement of high precision, more GPS receiver manufacturers will participate in the market and the price is expected to decrease. It is expected that advanced GPS receivers will be used in future synchrophasors to improve the time accuracy and reliability.

Appendix D FDR Troubleshooting

This section is to provide a guide line for FDR troubleshooting. Most FDR and/or PMU users are familiar with how to set them up and receive the data stream. However, some abnormal operations may happen during the usage. Without the knowledge of internal design and the mechanism of each components, they may have no idea what cause the problem.

In this section, various factors which could cause the abnormal operation of FDR during testing or after deployment are analyzed, and the solutions are given. A flowchart of troubleshooting is then given for fast solution. It provides not only helpful guides to the FDR operators, but is also a useful reference for users of other PMU.

D.1 GPS Issue

GPS issues are very common among all the FDR abnormal operations. As almost all FDRs are installed indoor without a roof-mounted GPS antenna, the GPS signal is a big problem. Most GPS antennas are placed near a window with a clear view of sky, as it is stated in the installation guidance. However, there are several cases where the GPS signal is weak or without access.

First of all, some glasses are of ‘low emissive type, a.k.a. low-E glass. This is typical for modern buildings, as this kind of glass can effectively lower the heat emission from inside, and save the energy. However, it also blocks the GPS signal. The GPS antenna for FDR can hardly get GPS signal when located near this kind of glass.

Solution: relocate the FDR to a building without low-e glass. Or put the antenna outside the window.

Secondly, some windows do not have a clear view of the sky. As high buildings, old or new, may locate very close to where the FDR is located, the GPS signal can be blocked.

Solution: relocate the FDR to another place with a clear view of sky

Thirdly, the location of the antenna is too far away from the window. In this situation, the GPS antenna cannot form a direct path towards the antenna.

Solution: relocate the GPS antenna to be close to the window or outside the window.

D.1.1 No GPS

The FDR is designed to pending streaming until it gets enough GPS satellites. When the FDR is powered on, the LCD screen will first show welcome information, then remain on ‘Acquiring...’ until it gets 4 GPS satellites. The time of this period changes depending on several factors. Usually if the FDR is powered off only a few minutes, it just needs less than 1 minute to regain enough GPS satellites and recover streaming, should there are

enough satellites locked before it is powered off. If it is at least several days since the FDR is powered on last time, or the FDR is relocated, it usually needs several hours to days to get enough GPS signal, depending on the quality of the signal it received.

If the FDR is powered on for more than 10 days, but still sticking to ‘Acquiring...’, it is most likely the GPS signal is no good enough. Considering relocate the GPS antenna.

After the FDR got enough GPS satellites, it starts to stream data and display date, time and measurement of frequency and voltage on the screen. It needs at least one GPS satellite to keep on operating. If the GPS is loss at this time, it will take a while to wait for GPS recovering. During this time, it continues to work as normal. The coast time is 1 hour or 2 hours, depending on the MCU software version. If no GPS is found during this period, the FDR stops streaming, because the measurement error is too large and the data cannot be trusted. The FDR at this time is still updating the time and measurement on the screen. The number of GPS satellites the FDR is locked to is displayed as the 2-digit number on the right-upper corner of the LCD screen. During the GPS loss, this number is displayed as ‘00’. For this circumstance, first try to restart the FDR. If it does not work, consider relocate the GPS antenna.

D.1.2 Weak GPS

Compared to totally no GPS, some FDRs obtain 1~2 GPS satellites for a few hours, then lost GPS for another a few hours. This is named as ‘weak GPS’. Firstly, if the GPS loss time during weak GPS is longer than the coast time, the FDR will stop streaming data, until the GPS is recaptured. This will cause data loss. Secondly, if an FDR is always in weak GPS status since it is installed in a new place, it does not have enough time to calculate its coordinator. Although it streams data, the coordinator it reports is still the one it restored during the last time it gets enough GPS satellites to calculate its location. E.g., if an FDR is fully tested in UTK. The coordinator of Knoxville, TN is recorded in its GPS receiver. When it is deployed in a new place, but is in weak GPS ever since it is powered on, it will keep on sending the coordinator of Knoxville, TN although it is actually in a new place. There is also possibility that it reports a coordinator of (0,0) or one with large error and keeps on drifting. In all these status, there exists large time error, since the time is calculated according to the navigation equation and using the coordinator. A wrong coordinator will generate an inaccurate time, therefore error in timestamp, and even the measurement data.

Solution: first try to restart the FDR. If it does not work, consider relocate the GPS antenna.

D.2 Ethernet Issue

Ethernet issue is the second most common issue, and is sometimes hard to distinguish. Data output by MCU are first fed into MOXA, the Ethernet module, and then stream to all the destined data servers. The MOXA works in client mode, and uses TCP/IP

communication. The data streaming is a one-way transmission, and there is no data or command comes from outside to MOXA.

D.2.1 Loose Cable Connection

Sometimes the connection of Ethernet cable become loose, either one the wall/router side or on the FDR side. When the connection is loose, the green LED named 'Network' on the front panel of FDR is off.

Solution: reconnect the cable, if it does not work, try another cable.

D.2.2 Loose Ethernet Module

MOXA is mounted on the mother board of FDR by pin and socket. It is slightly possible for it to become loose during the shipping, especially if it experienced strong vibration and collision. The phenomenon of a loose MOXA is the same as loose cable.

Solution: open the FDR case and reinstall the MOXA. Make sure the triangle mark on the MOXA is facing the rear side of the FDR.

D.2.3 Incorrect IP Configuration

It is required that the IP configuration of FDR should be the same as the Ethernet port it is connected to. If the configuration information is incorrect, or the FDR is connected to a wrong port, or the FDR is relocated to another place with a different IP configuration, the Ethernet connection cannot be set up.

Solution: reconfigure the IP setting.

D.2.4 DHCP Compatibility

Old firmware of MOXA has some compatible issues with some router or WLAN devices. When configured as DHCP mode, it fails to respond to the WLAN device and cannot be assigned an IP.

Solution: upgrade the firmware, or use statistic IP.

D.2.5 Firewall

Some companies or universities have strict firewall rule. E.g., white list is used to control the outbound data streaming. In this case, it is possible the data streaming, or even the TCT/IP connection cannot be set up between FDR and the data server.

Solution: contact the IT department and allow the FDR data streaming. Also need to notice the port number since sometimes only specific ports are allowed by the firewall rules.

D.2.6 Data Loss

Although TCP/IP track the packets sent to guarantee no data loss or corruption, in reality data loss still happens. This is typically due to the network congestion. When the data streaming rate is greater than the send out rate of a network segment, some of the data packets have to be dropped. This mainly happens during the limited bandwidth or the boost of pay load of the local communication network.

Solution: In lab test, data loss within 1% is tolerable. If the data loss rate is large, try to exchange another Ethernet model and redo the test. For a FDR in field, data loss within 10% is generally tolerable. For a larger data loss rate, the local Ethernet status has to be checked.

D.3 Power Issue

Wall outlet is used to provide both the power and signal for FDR to work and measure. This is different from most commercial PMUs which are powered by a different source from measurement feeder. Depending on the specified hardware and firmware, each FDR is generally among one of the four types according to its acceptable corresponding power: 120V/60Hz, 120V/50Hz, 240V/60Hz and 240V/50Hz. When the power supply is provided correctly and the power circuit is normal, the LED of power on the front panel is on, and status is displayed on the LCD screen. When the power LED is off or the LCD does not display anything, it is possible to be a power issue.

D.3.1 Fuse

Fuse is used to protect the FDR device from overcurrent. If the input power voltage is much higher than the rated value, or large power surge occurs and passes the fuse, the fuse will melt and breaks the circuit.

Solution: First, check if the input voltage is in the same range of rated voltage. Then check if the fuse is melted. Change the melted fuse with one of the same type. If it still melts, there is possible internal issue of the FDR device.

D.3.2 Voltage Regulator

Voltage regulator is used to step down the higher DC voltage from rectifiers to the lower and stable voltage, which are used to power other devices. There are several voltage regulators in the FDR, to provide various levels of DC voltage for corresponding chips. Due to the surge, over voltage, unintentional short circuit, chip quality, etc. factors, the voltage regulator could be outage. Using a multimeter to check the input and output voltage of the suspected voltage regulator can evaluate if it is outage.

Solution: change the corresponding chip or board.

D.3.3 Transformer Noise

Transformer hums due to the magnetostriction, which refers to the back and forth of the magnetic sheet steel extending itself when magnetized and contracting when the magnetization being taken away. It is a normal phenomenon.

Solution: no action needed.

D.4 Display Issue

D.4.1 Program Issue

Due to some design flaw, when a FDR is turned on and off very frequently or for many times, it is possible that the MCU program is lost. In this case, there is garbled display on LCD and no data streaming. Rebooting the device does not clear this problem. Now the only known solution is to redownload the MCU code.

Solution: redownload the MCU code and calibration.

D.4.2 LCD Issue

When there is no display on LCD, there are generally two possible reasons. First is the connection cable between MCU board and the LCD is loose. The second possibility is the outage of LCD. If only LCD display is abnormal but the data streaming is still on, it proves the issue is only within LCD.

Solution: check the cable connection. If it does not solve the problem, change the LCD.

D.5 Input Signal Issue

D.5.1 Incorrect Voltage/Frequency

There are generally two versions of FDR circuit, for 120V or for 240V. If the input voltage is much higher than the rated voltage, e.g. input 240 V for the 120 V unit, it is potential to damage the FDR. For this damage, usually the fuse is blown up. On contrary, if the input voltage is much lower than the rated voltage, e.g. input 120 V for the 240 V unit, there will be no display in LCD, very dim LED and the chip will not work. However, the FDR will not be damaged.

Input a frequency far from the rated frequency will introduce large measurement error.

Solution: check the parameter of the outlet and FDR. Use the correct configuration.

D.5.2 Islanded Power Source

Some buildings and houses are equipped with backup power source, such as uninterruptible power supply (UPS) or backup generator. When the backup power source

kicked in during a power outage, the FDR powered by the backup power source is no longer connected to the main power grid and the measurement is usually far from what is reported by neighboring FDRs still connected to the grid. As there is no information indicating it is using the backup power source, the application server may deem that islanding happens in that area, which is not true. Therefore, it is strongly not recommended to connect FDR to any backup power source.

Solution: remove FDR from backup power source, or turn it off before using backup power source.

D.5.3 Local Disturbance

Disturbance exists in local area may interference the signal fed into FDRs and cause disturbance in the measurement results, such as oscillations or spikes in voltage magnitude, phase angle, and/or frequency.

Solution: relocate the FDR.

D.6 Troubleshooting Chart

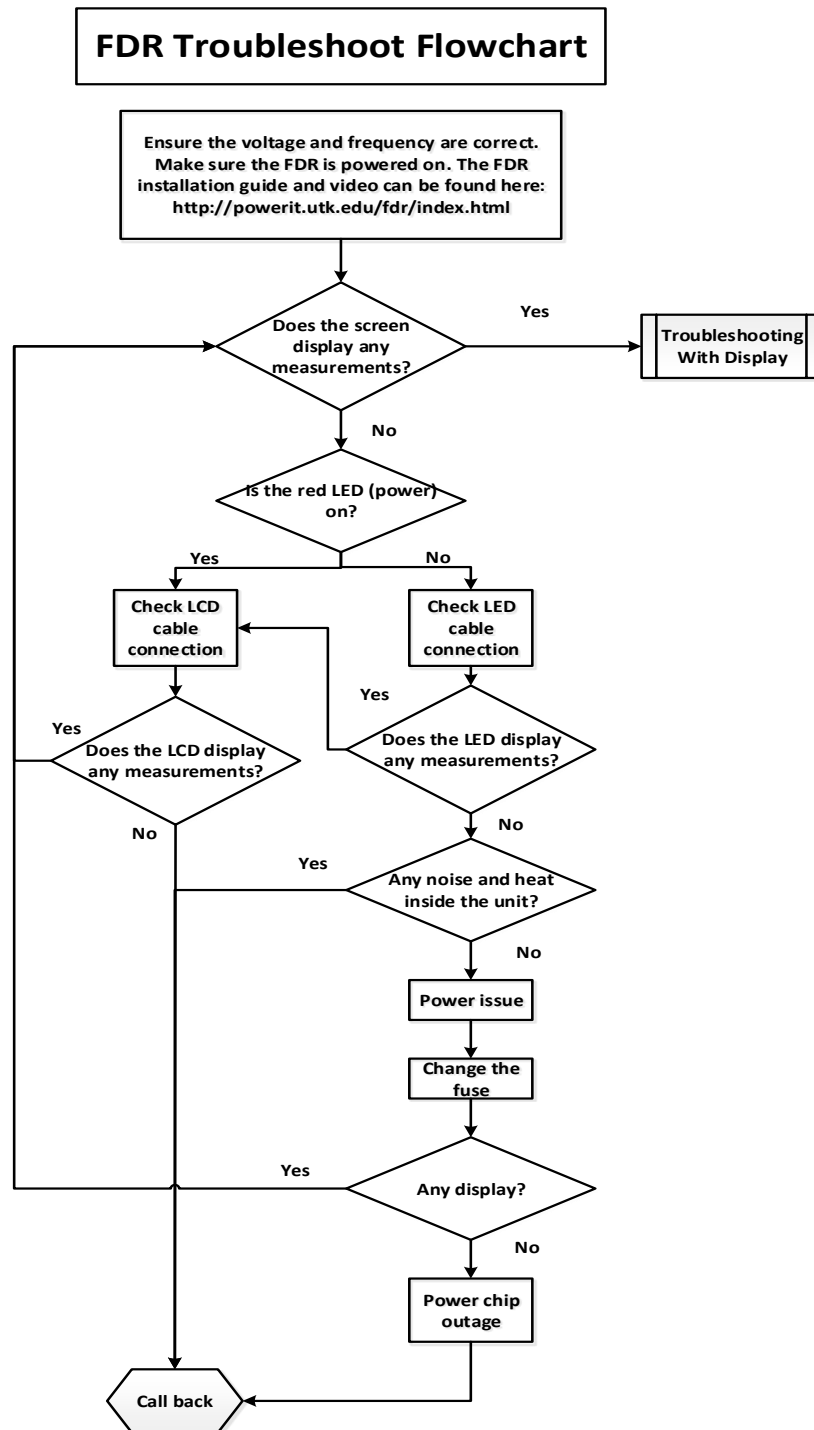


Figure D. 1. Troubleshooting Chart 1

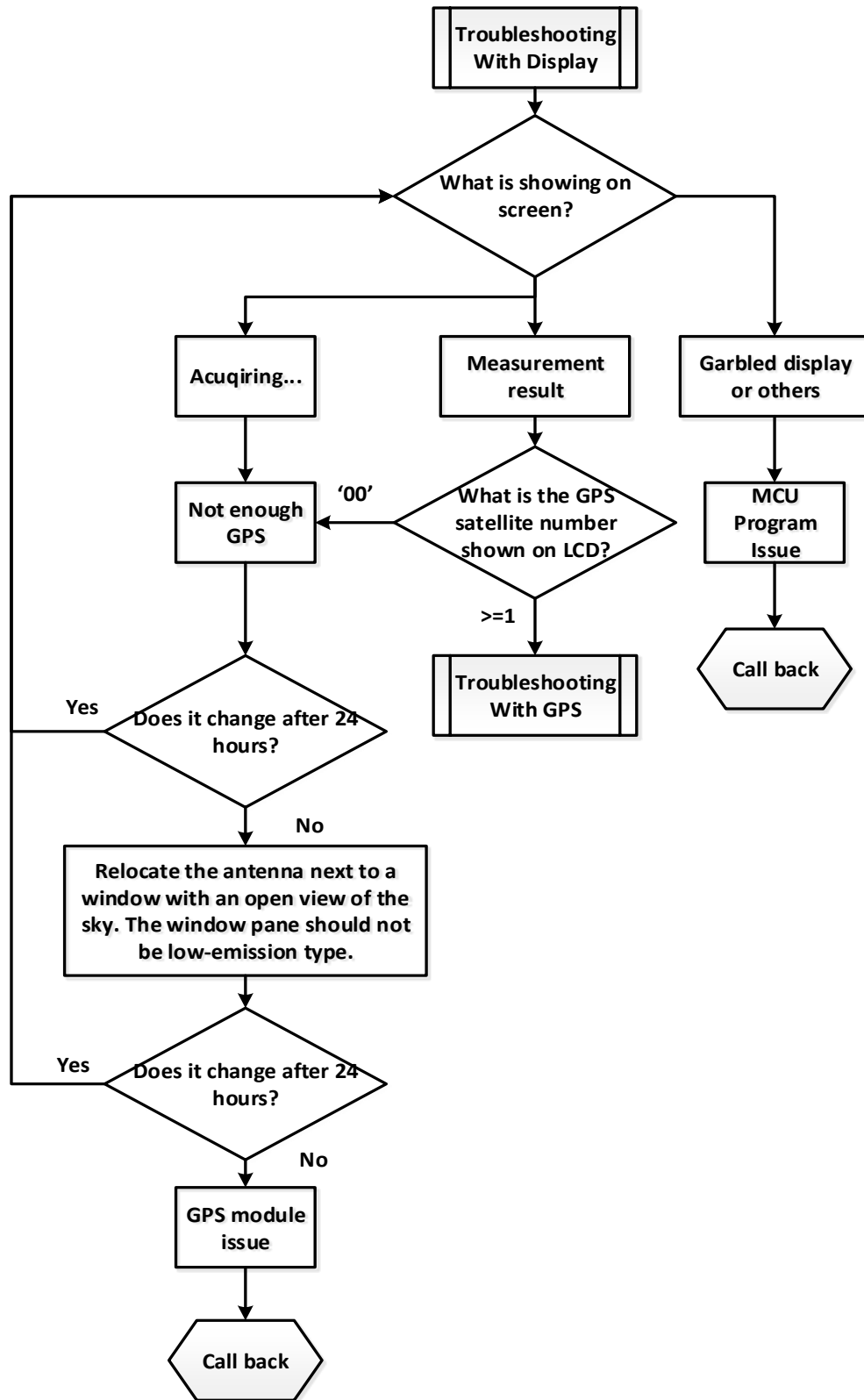


Figure D. 2. Troubleshooting Chart 2

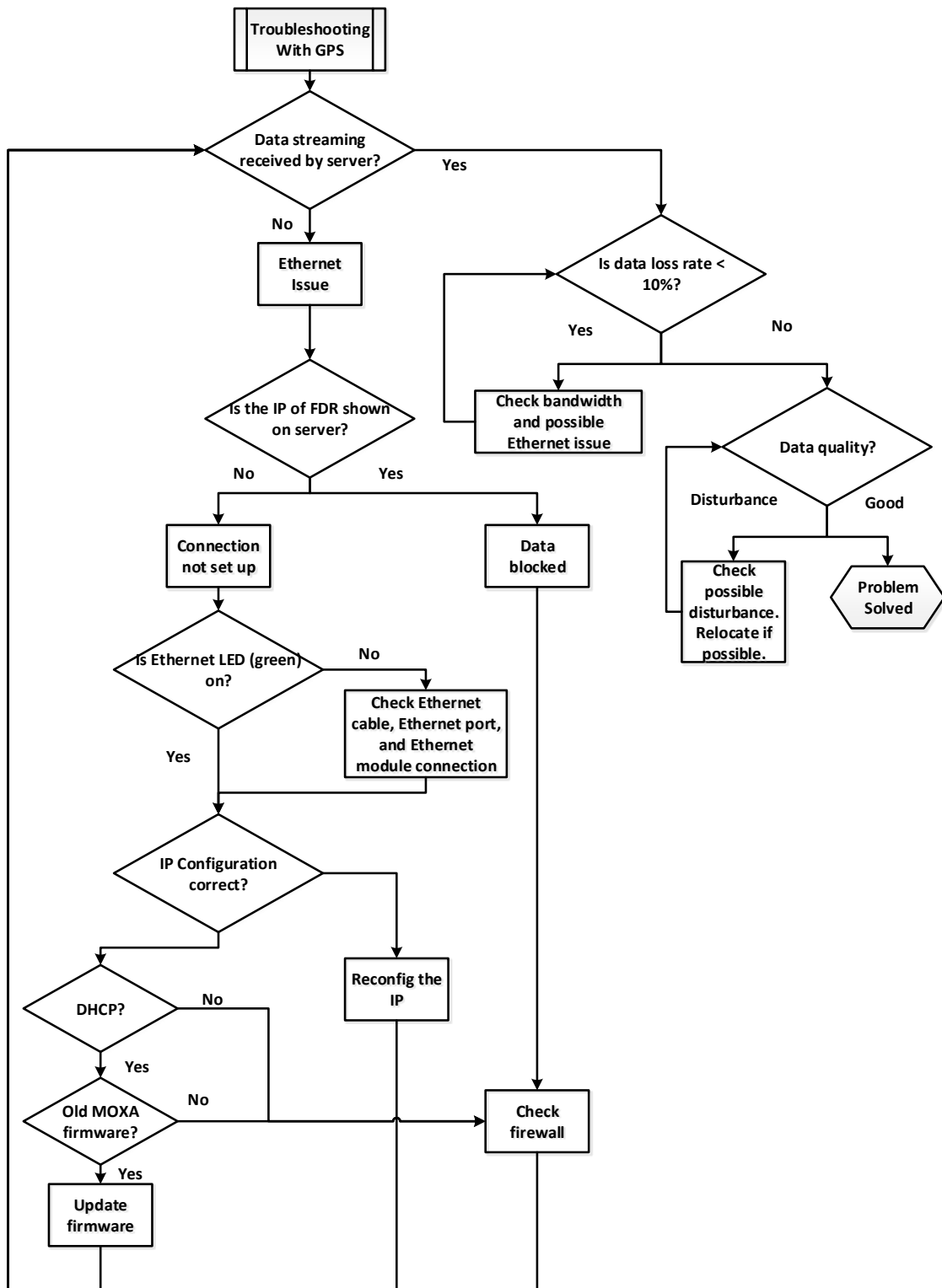


Figure D. 3. Troubleshooting Chart 3

Appendix E FDR Time Delay Issue and Impact

For some historical reasons, the time stamps of FDRs are intentionally shifted 10 sec before the UTC time. As this time stamp is fixed and consistent for all the units, it has no influence on FNET/GridEye applications. The applications only need to shift the time stamps back by 11 sec.

However, this time shift of some FDR units, due to the version of firmware, becomes 10 sec. The difference is uneasy to be observed during the steady state, due to the delay is submerged by the ambient fluctuation of phasor and frequency, and the noise. However, when the event such as generation trip or load shedding happens, this time delay difference is obvious and could cause problems.

An example of the frequency measured by these two clusters of units in EI is plotted in Figure E. 1. It can be seen from the figure that the four units are divided into two groups. The first group includes FDR 818 and FDR 914, both are with 11 sec delay; FDR 724 and FDR 709 belongs to the second group with 10 sec delay.

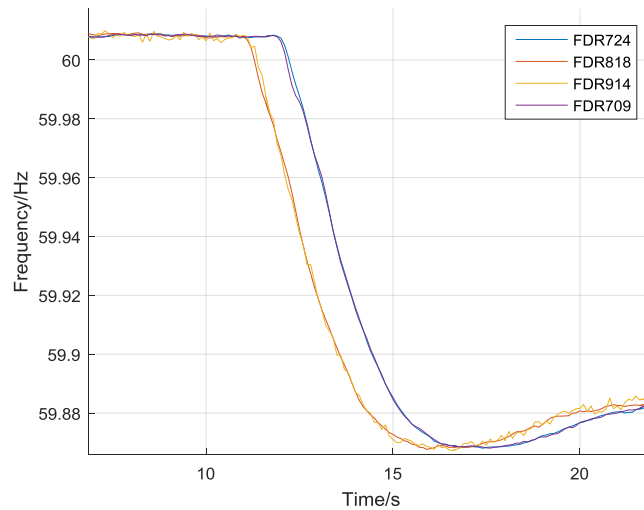


Figure E. 1. Frequency of a generation trip in EI with 2 clusters of FDR units with different time stamp shift

For the application of event location estimation, the 6 first responding units are usually used to estimate the event location by triangulation algorithm. For a power grid with many FDRs, such as EI, the first 6 responding units are usually all the FDRs of 11 sec delay. Therefore, those with 10 sec delay, cannot be used for the location estimation, even though they might be closer to the event place and enhance the accuracy of the estimation. Furthermore, in grids with less units, the two clusters of units are potential to be used together for the algorithm. Similar to the phenomenon shown in 3.4, this could cause failure of the location estimation.

Besides, this delay could cause false alarm of oscillation detection. As the oscillation detection algorithm uses phase angle differences between a reference FDR and all other FDRs in the same power grid, the 1 sec time delay between the reference FDR and another FDR is potential to cause an oscillation in the calculated phase angle difference, when the phase angle loops from π to $-\pi$. When the frequency deviations away from the nominal value, the amplitude of this ‘oscillation’ will become large, and could surpass the threshold set by the oscillation detection algorithm and trigger the alarm.

This issue is solved by identifying the units of these two clusters, and tuning the time shift on the application server, to make their time shifts consistent.

Appendix F Specification of Universal Grid Analyzer

This section is to provide the specification of universal grid analyzer (UGA). The UGA is an embedded microprocessor system with GPS time synchronization and Ethernet communications capability. The UGA measures power system voltage from 57.7V – 240V outlets commonly located in homes, offices, factories and substations. It takes voltage measurements with high sampling rate and calculates phasors, harmonics (up to 15th order), voltage sag, swell, and noise (SNR in dB) of power system voltage signal. Locally measured results are time-stamped using a highly accurate GPS clock and streamed to UGA servers at a reporting rate of 10 Hz (Up to 60 Hz). The system enables researchers to study behaviors within interconnected power systems, and monitor power grid quality in real-time. Moreover, the noise analysis function allows researchers to analyze the measurement accuracy of phasor measurements in real power grid environment.

F.1 General Requirements

This section describes the general requirements of the UGAs.

F.1.1 Input Channels

The UGA measures power system voltage from 57.7V - 240V outlets commonly located in homes, offices, factories and substations.

F.1.2 Communication Channel

Communication interface should be provided through a minimum of one Ethernet network data communication port.

F.1.3 GPS Synchronization Channel

GPS-time synchronization should be provided through GPS antenna offering an effective time synchronization within 1 micro second.

F.2 Functional Requirements

This section describes the minimum functional requirements of the time synchronized Universal Grid Analyzer. Additional functional requirements may be needed for special cases and should be added to this document.

F.2.1 Measurement Accuracy Specifications

The measurement accuracy specification is shown in Table F.1.

F.2.2 Time synchronization requirements

All analog channels should be synchronized to UTC with accuracy sufficient to meet the phasor measurement accuracy requirement of the IEEE C37.118-2011 Standard. The UGA requires 1 micro second GPS time synchronization accuracy for highly accurate phasor measurement.

Table F. 1 Measurement accuracy specifications

Specification	Accuracy
Voltage range	57.7 V to 220V, single-phase input from wall outlets at 60 Hz (a 50 Hz, 240V version is also available)
GPS	GPS synchronized data collection using UTC time
Data reporting rate	10 Hz (Up to 60 Hz)
Frequency measurement accuracy	± 0.001 Hz
Phase angle measurement accuracy	0.005 degree
Harmonics measurement accuracy (up to 15 th order)	1%
Noise measurement accuracy	5 dB
Other specifications	Outputs: frequency, absolute phase angle, UTC time, location, voltage magnitude, satellites number, at a rate of 10 Hz (up to 60 Hz); Harmonics (3 rd , 5 th , 7 th , 9 th , 11 th , 13 th , 15 th), THD, SNR of noise at a rate of 10 Hz (up to 60 Hz). Continuous data transmission with local LCD display Ethernet-enabled; data are transmitted via the Internet to the UGA servers; Higher data rate available when direct connected available

F.3 Communication Requirements

UGAs shall support TCP/IP protocols. Data transmission can also be implemented with separate ports as long as the same reporting capabilities and options are available in both ports.

F.4 Data Format

The newest UGA transmits data through IEEE C37.118-2011 Standard. Two example frame types, i.e., configuration and data frames, are shown in Table F.2 and Table F.3. The configuration frame introduced the frame settings and data format for data frames. The data frames contains the detailed real-time data. The detailed frame format is available in IEEE C37.118-2011 Standard. For the “Harmonics, THD, noise”, the unit of the harmonics and THD measurement is percent, and the unit of noise is dB.

Table F. 2 Configuration Frame of UGA

No	Field	Size (bytes)	Description
1	SYNC	2	Configuration 2
2	FRAMESIZE	2	294bytes
3	IDCODE	2	No. 1197
4	SOC	4	SOC time stamp
5	FRACSEC	4	Fraction of second
6	TIME_BASE	4	Resolution of FRACSEC:1000000 us
7	NUM_PMU	2	The number of PMUs: 1
8	STN	16	Station Name: "U.S. TN KV 1197"
9	IDCODE	2	No. 1197
10	FORMAT	2	Data format within the data frame: FREQ/DFREQ: 16-bit integer; Analog: 16-bit integer; Phasors: 16-bit integer; Magnitude and angle (polar)
11	PHNMR	2	1 phasor
12	ANNMR	2	12 analog values
13	DGNMR	2	0 digital status words
14	CHNAM	16*12	Phase and channel names (16 bytes each) "Voltage" "Latitude" "Longitude" "Satellite" "HAR 3rd" "HAR 5th" "HAR 7th" "HAR 9th" "HAR 11th" "HAR 13th" "HAR 15th" "THD" "Noise"
15	PHUNIT	4	Conversion factor for phasor channels: voltage, 100000
16	ANUNIT	4*12	No information
17	FNOM	2	60 Hz
18	CFGCNT	2	0 configuration change
19	DATA_RATE	2	Rate of data transmissions (from 10 to 60 frames/s)
20	CHK	2	CRC-CCITT

Table F. 3 Data Frame of UGA

No	Field	Size (bytes)	Description
1	SYNC	2	Data frame
2	FRAMESIZE	2	
3	IDCODE	2	No. 1197
4	SOC	4	SOC time stamp
5	FRACSEC	4	Fraction of second
			Good measurement data:
			PMU in sync;
			Data sorting by time stamp;
	STAT	2	No PMU trigger;
			No data modified;
			No PMU time quality used;
			Unlocked time < 10s;
			No trigger reason
6	PHASORS	4	Voltage magnitude and angle
7	FREQ	2	Frequency
8	DFREQ	2	ROCOF in Hz/s
9	ANALOG	2*12	Analog data
20	CHK	2	CRC-CCITT

VITA

Jiecheng Zhao was born in Zhenjiang, Jiangsu, P. R. China. He received his Bachelor's degree in automatic control from Huazhong University of Science and Technology in 2008, and the Ph.D. degree in radio physics from the University of Chinese Academy of Sciences, Beijing, China, in 2013. He joined the University of Tennessee, Knoxville in 2015. His current research interests include power system monitoring, power system measurement method and device, WAMS applications, and renewable energies.